DESIGN, CONTROL AND ENERGY OPTIMIZATION OF A RAPID-PROTOTYPING HYBRID POWERTRAIN RESEARCH PLATFORM

A DISSERTATION
SUBMITTED TO THE FACULTY OF THE GRADUATE SCHOOL
OF THE UNIVERSITY OF MINNESOTA
BY

Yu Wang

IN PARTIAL FULFILLMENT OF THE REQUIREMENTS
FOR THE DEGREE OF
DOCTOR OF PHILOSOPHY

Professor Zongxuan Sun, Advisor

January, 2014

Acknowledgements

I would like to express my sincere gratitude to the people who made significant contributions in the successful completion of my doctoral study at the University of Minnesota.

First and foremost, I would like to thank my advisor, Professor Zongxuan Sun, for the thoughtful and inspirational guidance and comprehensive training he gave to me throughout the whole period when I worked on this doctoral thesis. Especially, what I gained and learnt from his keen insight, broad vision, profound knowledge, and dedication and enthusiasm to the academic work has already become my invaluable asset for my academic and professional life.

I would also like to extend my thanks to my other committee members, Professor Rajesh Rajamani, Professor Kim Stelson, and Professor Peter Seiler for their relevant comments and constructive suggestions that all affiliate me to greatly improve the quality of my thesis.

Also, I want to thank all my labmates and colleagues in my research group, with whom I had the privilege to work or study together on the cutting-edge academic topics, including but not limited to Xingyong Song, Hu Zhang, Joe Sweeny, Meng Wang, Pradeep Gillella, Zhen Zhang, Ali Sadighi, Azrin Zulkefli, Ke Li, Chien-Shin Wu and so on. I am grateful for their contributions in our cooperative research projects, as well as their friendships which made my life easier, happier, and warmer.

Last but certainly not least, I would like to acknowledge the technical supports from the Center of Compact and Efficient Fluid Power and the Diesel Engine Research Lab at University of Minnesota. Especially I would like to express my sincere gratitude to Professor Perry Li, Professor David Kittelson, Mr. Mike Gust and Dr. Darrick Zarling for all their helps in technical, operational and instrumental aspects for my research projects. In addition, I would like to acknowledge the National Science Foundation for the financial support under the grant number CMMI-0959741.

Dedication

This dissertation is dedicated to my dear parents Yanmin Wang and Jinhong Wang, for the huge love and great support they gave to me in my whole life.

Abstract

As one of the most promising approaches for reducing automotive fuel consumption and emissions, the emergence of the powertrain hybridization technology, has inspired extensive research efforts on hybrid vehicle architecture design, parameter optimization and hybrid energy management strategy development. However, the high complexity and considerable economic and time cost of constructing or physically modifying a complete hybrid powertrain system seriously limit the experimental investigation of the hybrid powertrain dynamics and hence, greatly deter the systematic testing, analysis and characterization of the hybrid powertrain operational performance. As a result, the deficiency and inflexibility of the experimental means or environment has already slowed down the continuous innovations on hybrid powertrain system design, control and optimization. To provide an accurate and flexible hybrid powertrain emulation and experimental tool, a rapid-prototyping hybrid powertrain research platform, which employs a transient hydrostatic dynamometer that emulates the dynamics of various hybrid power sources and hybrid architectures, is proposed. This design will greatly expedite the research on various hybrid architectures and control methodologies, without physically building the complete hybrid powertrain system. To accomplish the design and control of this hybrid powertrain research platform, research work in three levels (low level, middle level and high level) has been proposed and carried out.

First, in the low level system, as the basic physical hardware ingredient in the research platform, a hydrostatic dynamometer with an electronically controlled load sensing mechanism was designed and implemented. For the model-based control design,

the high-order, physics-based dynamic models of the dynamometer system were formulated, identified and validated with experimental data. To control the dynamometer-engine system to follow the desired speed/torque profiles, systematic nonlinear tracking control strategies (nonlinear model-based inversion control, and state feedback control via feedback linearization) were investigated and implemented. Less than 3-5% tracking errors for engine speed control have been realized in experiments.

Second, with the well-controlled transient dynamometer as a flexible torque source, the hybrid powertrain simulation and control architecture was designed for experimentally realizing the hardware-in-the-loop (HIL) hybrid powertrain operation emulation. Particularly, corresponding to the middle-level system (hybrid powertrain control and HIL simulation system), the system-decoupling based hybrid powertrain SISO control was first designed, and further integrated with an adaptive driver model, a dynamic programming (DP) energy optimization strategy (high-level system control), and a nonlinear dynamometer torque controller (low-level system control). The driving-cycle HIL experimental results have demonstrated that the overall control system based on the SISO mid-level control is capable to realize the relatively accurate operation emulation of the targeted hybrid powertrain system. Further, the overall dynamics of the power-split hybrid powertrain system were analyzed and consequently, the most important characteristics of its dynamic behaviors were extracted. On this basis, to overcome the inherent limitations of the SISO mid-level control on transient response and further improve the transient engine operation (speed/torque tracking), a multivariable controller was designed to strategically coordinate the engine torque control and hybrid

torques control during the hybrid powertrain operation emulation. The experimental results have validated that the design and implementation of the multivariable mid-level control is capable to develop a good balance of the optimized engine speed/torque profiles tracking during fast transients in the hybrid powertrain system.

Third, on the basis of precise hybrid operation emulation, the high-level system design in this research platform focuses on the hybrid energy management strategy development. The research emphases are laid on making use of the real-time optimal controls to compensate the transient loss of both the fuel efficiency and emissions, which are induced by the dynamic model simplification (order reduction) to fit for the usage of the DP/SDP algorithms, including: 1) On the one hand, to develop a fast and more accurate hybrid energy management strategy for the real-time fuel consumption optimal control, a stochastic dynamic programming - extremum seeking (SDP-ES) optimization algorithm, was developed with both the system states and outputs feedback. First, this SDP-ES algorithm utilized a SDP state-feedback control as a reference feedback term for the approximate global energy optimality and battery's state of charge (SOC) sustainability. Then, more importantly, this algorithm injected a "local" feedback term via the ES, which is a non-model-based nonlinear optimization means, to compensate the control commands from the SDP by leveraging the real-time measurement of system output (fuel consumption). Consequently, this SDP-ES optimization algorithm generated more fuel-efficient engine operation points along the specific battery SOC sustaining line. 2) On the other hand, targeted at achieving the transient emissions reduction without significant loss on the global energy optimality, a "two-mode" hybrid energy

management strategy was designed based on a control-oriented autoregressive (AR) diesel engine emission model. In the “fuel efficiency improving” mode, a DP algorithm was used to seek the global optimization of the fuel economy and ensured the battery SOC sustainability; while in the “emission reducing” mode, the management strategy utilized a linear quadratic regulator (LQR) to locally optimize the surging emissions due to undesired engine torque transients. At the end of the “emission reducing” mode, the locally optimized engine operation was driven back to match the globally optimized trajectory, i.e., the initial states of the next “fuel efficiency improving “mode. This seamless integration of the two modes has realized the reduction of the high local emissions without losing the global fuel efficiency optimality and battery SOC sustainability.

Table of Contents

List of Tables

List of Figures

Chapter 1

Introduction and Research Outline

This chapter presents the research background, motivation and the overall research achievements. In Section 1.1, the basic concept and characteristics of the automotive powertrain hybridization will be introduced and our research objective will be presented. In Section 1.2, by analyzing the challenges of the hybrid powertrain technology development, our proposed solution of developing a rapid prototyping hybrid research platform will be presented. Around this solution, Sections 1.3, 1.4, 1.5 and 1.6 will review the existing results, and provide an overview of our research objectives and contributions in three levels: low level, middle level and high level, respectively. Finally, the research achievements in every chapter will be outlined in Section 1.7.

1.1 BACKGROUND

With the rapid growth of personal transportation all over the world, improving fuel efficiency and reducing emissions has become the main target for automotive powertrain research [1]. In recent years, the ever increasing demand for reducing fuel consumption and emissions has strongly driven the research of new powertrain concepts and technologies, including hybrid powertrain, advanced combustion, efficient and compact transmission, alternative fuels, gaseous and particulate emission reduction, and so on. Those new concepts and technologies greatly increase the degrees of freedom to optimize or even, completely transform the design, operation and control of the automotive propulsion system. However, the dynamic behaviors of the proposed innovations and their interactions with the vehicle are often much more complicated than those in today's automobiles. As a result, it becomes very difficult to precisely quantify the associated benefits and limitations of these innovations in a realistic operating environment.

Powertrain hybridization has been widely accepted as one of the most promising solutions for addressing the energy and environmental issues in both personal and

commercial transportation [2]. The basic idea of a hybrid powertrain is to introduce an alternative power source besides the traditional internal combustion engine (ICE) and further, to coordinate the operation of the ICE and the alternative power source so as to improve the fuel efficiency and driving performance of the overall system [3]. These powertrain systems are usually referred to as electrical variable transmission (EVT) [4] or hydro-mechanical transmission (HMT) [5] since they replace the conventional mechanical transmission by adding electrical or hydraulic actuators that form the hybrid transmission. In recent years, in terms of the types of the alternative power source, various hybrid vehicle (HV) concepts have been proposed, including hybrid electric vehicles (HEVs) [6]-[7], hydraulic hybrid vehicles (HHVs) [5], [8]-[9], and pneumatic hybrid vehicles (PHVs) [10]-[11]. Typically in the HEVs, the alternative power source refers to the electric generator/motor fed by the battery; while in the HHVs, the hydraulic pump/motor fed by the hydraulic accumulator is employed as the alternative power source. Compared with the only ICE system, the hybrid powertrain system can reduce the fuel consumption by means of [2], [12]-[13]:

- ***Engine downsizing***: since the alternative power source can provide part of the traction power during the acceleration phases so as to reduce the demand of peak power of the ICE, the engine in a hybrid vehicle can be designed to be of a smaller size and thus, with a better fuel efficiency.
- ***Operation optimization***: since the alternative power source has the capability of storing (or, supplementing) the excess (or, deficient) power, the operating points (torque/speed) of the ICE can be adjusted and maintained around the high-efficiency area in the engine map to maximize the fuel efficiency.
- ***Regenerative braking***: the alternative power source can capture part of the vehicle kinetic energy when the vehicle is decelerating/braking, so as to reduce the waste energy.

However, it is worth noting that, as a typical case of the advanced automotive technologies listed above, the multidisciplinary nature and complex dynamic behaviors of the hybrid powertrain make it difficult to accurately quantify and therefore, leverage its

inherent advantages and eliminate its potential disadvantages. For example, within a hybrid vehicle, the engine may shut down and restart much more frequently than a conventional vehicle to save fuel [13]; however, the frequent restart of the engine may have a negative impact on emissions and driveline vibration [14].

Consequently, to realize the desired benefits of the novel powertrain technologies without losing the gains in other aspects, accurate performance analysis based on experimental investigation becomes especially important, which in turn asks for a rapid, flexible and precise research platform for testing, measurement and analysis. With developing the advanced hybrid powertrain as a final target, to develop such a research platform is exactly the focus of this thesis.

1.2 RESEARCH OBJECTIVES

1.2.1 Challenges of the Hybrid Powertrain Research

Driven by the great expectation for the powertrain hybridization technology, extensive investigations on hybrid powertrain design and control have been conducted in recent years, and various technical solutions have been proposed (see Section 1.4.1 and 1.5.1 for details). However, as introduced in the last section, the seamless usage of the powertrain hybridization technology in the vehicle is challenging due to the effect of the complex system dynamics. Derived from this fact, two technical barriers that seriously limit the capability of accurately testing and further researching new hybrid architectures and control methodologies, include:

- **Transient and Interconnected Dynamics**

Under real driving environments, the transient and interconnected dynamics of the hybrid powertrain system (typically, the dynamic interactions between the ICE and the alternative power sources, dynamic interactions between the ICE and the driveline, the internal combustion dynamics of ICE, and so on) have significant impacts on the fuel efficiency, emissions and driving performance. These interconnected dynamics usually cannot be captured with low order models, which make it difficult to precisely control and optimize the real-world hybrid powertrain operation only with the purely simulation-

based investigation. Thus, the experimental validation and investigation become especially important for the improvement of the hybrid powertrain technologies.

- **Complexity and Cost of Constructing a Physical Hybrid System**

Conventionally, a physical hybrid powertrain test bed includes the whole powertrain system: ICE, alternative power sources, energy storage unit, hybrid transmission, driveline and vehicle load. Usually, only the vehicle load is replaced with a dynamometer. Obviously, it is very time-consuming and costly to build such a complicated testing system. Any further modification of the architecture or sizing of the hybrid system (for example, the size or power of the electric motor, the gear ratio of the planetary gear set) will require significant redesign and reconstruction of the testing system. This barrier seriously slows down the experimental investigation of various hybrid powertrain architecture designs and optimizations. Thus, the experimental investigation based on a purely physical system is also proved to be inefficient for the rapid improvement of the hybrid powertrain technologies.

1.2.2 Proposed Solution: Rapid Prototyping Hybrid Powertrain Research Platform

Based on the analysis in Section 1.2.1, on the one hand, the research based on the "fully virtual" hybrid powertrain (which is, to purely simulate the whole powertrain system including the engine, transmission and driveline dynamics by means of some software packages) cannot provide accurate enough feedback to guide the research activities on the hybrid powertrain; on the other hand, the research based on the "fully real" hybrid powertrain is actually inefficient and too costly to a large extent. Then, to greatly expedite the investigation of hybrid powertrain control, a "semi-virtual" hybrid rapid prototyping concept is proposed in this thesis, by which the hybrid powertrain design and optimization procedure can be significantly simplified.

As we know, the combustion dynamics of the IC engine, which directly determine the engine fuel efficiency and emissions, are too complicated to be modeled with a low-order mathematic approximation; to the contrary, the dynamics of the alternative power

sources, hybrid transmission, driveline and vehicle load can be described with well-developed models. Therefore, it is feasible to replace all the hybrid power source, hybrid transmission, driveline and vehicle load with a high-bandwidth emulation tool. Here we refer the test bed of this kind as "semi-virtual hybrid". By construction, the semi-virtual hybrid testing is based on the actual engine, real-time measurement of fuel consumption and emissions, and high-fidelity mathematical models of hybrid power sources and power transmission systems.

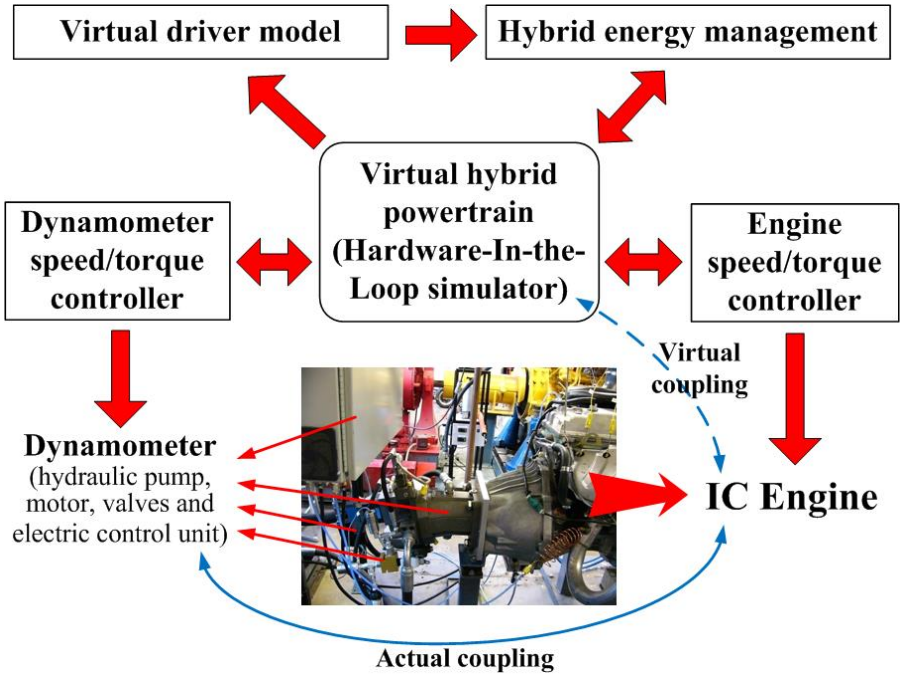

Fig. 1.1 Structure diagram of the hybrid powertrain research platform

Following the concept of the "semi-virtual hybrid", a rapid prototyping hybrid powertrain research platform based on a transient hydrostatic dynamometer is designed, as shown in Fig.1.1. Since a hydrostatic dynamometer system (see Section 1.3) has superior power density and higher bandwidth, it is an ideal candidate to enable the transient emulation capability, so as to precisely track fast-varying torque/speed profiles. This research platform employs a high-bandwidth hydrostatic dynamometer to emulate the dynamic behaviors of the alternative power sources, driveline and vehicle loads, and interact with a multi-cylinder IC engine in real-time. In this platform, the engine fuel

efficiency and emissions can be measured in real-time and hence, the associated benefits and limitations of various hybrid powertrain architectures and control methodologies can be precisely quantified and systematically investigated by means of experiments.

The design of the rapid-prototyping hybrid powertrain research platform successfully overcomes the two technical barriers discussed in Section 1.2.1, with some unique advantages as follows:

- **Cost-effective and Time-efficient**

Without building most of the physical systems, an important advantage of the rapid prototyping research platform is that it is much more cost-effective and time-efficient.

- **High Precision**

In contrast to a "fully virtual" hybrid powertrain, the proposed research platform is capable of ensuring high fidelity and precision in experiments as a result of retaining the engine, the combustion control system and other relevant instrumentation for precise characterization of the fuel efficiency and emissions.

Based on the design logic described above, the control architecture of this hybrid powertrain research platform is built, as shown in Fig. 1.2. With the hydrostatic dynamometer and engine (in red in Fig. 1.2) as the control target, the overall hybrid powertrain control and simulation system (in black in Fig.1.2) is the core part of the research platform. The control flow within the research platform is given by:

First, the driver model will produce a desired output power corresponding to the desired cycle, as the driver's control command for the vehicle. Then, in the high level system, with this desired power as the reference, the hybrid powertrain energy management system will generate an optimal engine operating trajectory based on the real-time fuel consumption and the SOC (state of charge) of the energy storage unit.

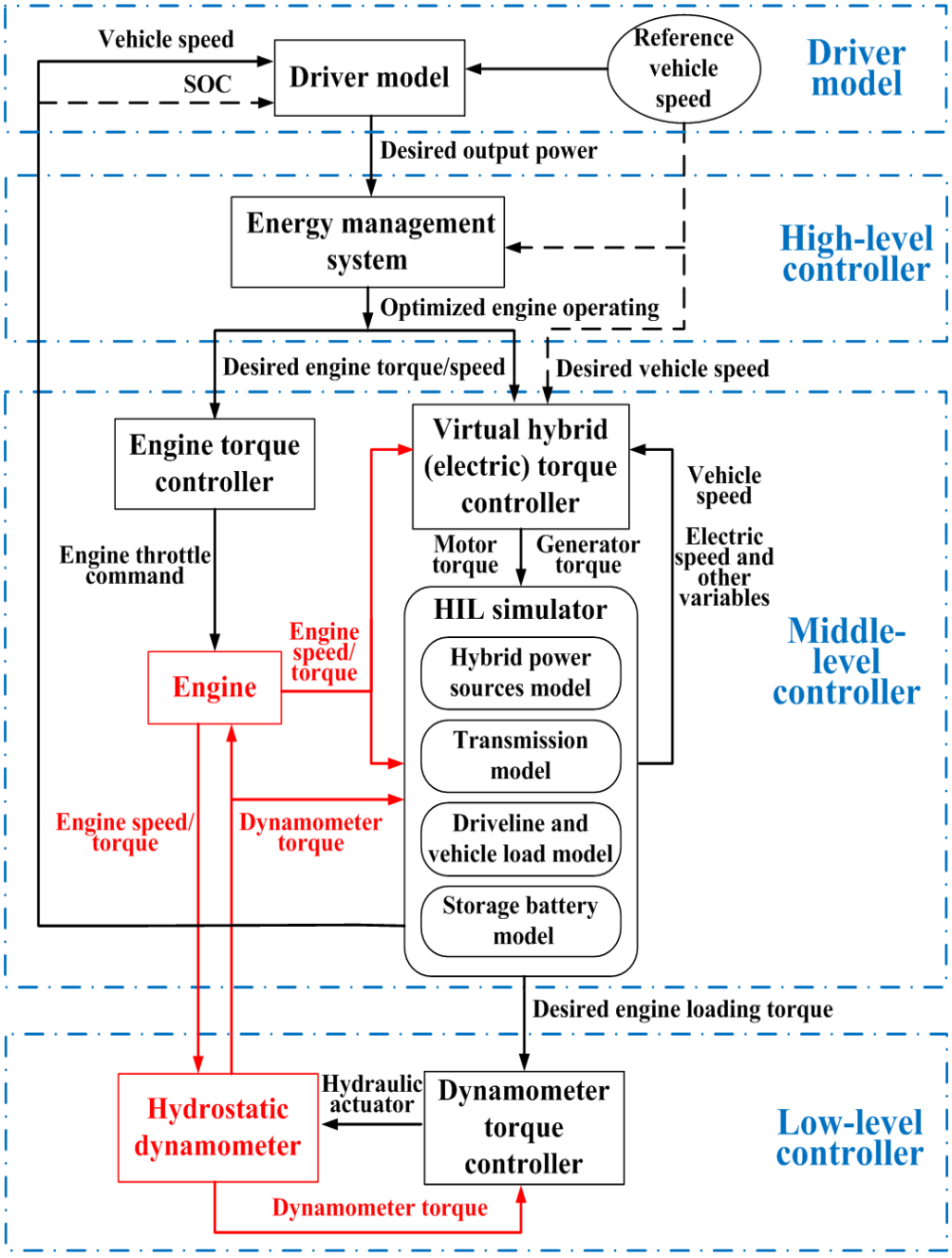

Fig. 1.2 Control architecture of the rapid prototyping hybrid powertrain research platform

In the middle level system, given the optimized engine torque and speed as the reference, the virtual hybrid torque controller manipulates the virtual hybrid torques (electric generator/motor torques) to drive the engine to operate along the optimized torque and speed trajectory. Meanwhile, the hybrid transmission/driveline hardware-in-

the-loop (HIL) simulator is simulating the target hybrid system using the well-developed dynamic models (including the alternative power sources, hybrid transmission, driveline and vehicle load), to produce the high-fidelity dynamic responses (primarily, the engine loading torque) like a real-world powertrain system. In the low level system, given the virtual engine loading torque produced by the HIL simulator as the reference, the dynamometer torque controller will control the dynamometer to emulate the desired engine loading torque, so as to drive the engine-dynamometer system to track the optimized engine torque and speed profiles. With the combination of the well-controlled engine torque and engine loading (dynamometer) torque, the engine will operate at the virtual hybrid modes.

To construct the designed hybrid research platform, three levels of research tasks need to be achieved, including: 1) Low level: design and control of the transient hydraulic dynamometer, which will provides the hardware ingredient for the designed platform and essentially ensure the dynamics emulation capability of the whole system; 2) Middle level and system integration: control and HIL testing of the semi-virtual hybrid powertrain, and also, control integration of the inter-connected low/middle/high level systems in the research platform; 3) High level: design and experimental validation of the optimal hybrid energy management strategy for fuel consumption and emission optimization, which can be considered as a demonstration of the designed hybrid powertrain research platform and more significantly, an advanced study in the core area of the hybrid powertrain development.

1.3 LOW LEVEL: DESIGN AND CONTROL OF A TRANSIENT HYDRAULIC DYNAMOMETER

The transient hydrostatic dynamometer is the basic hardware ingredient and critical dynamic emulation tool of the proposed hybrid powertrain research platform. Whether this dynamometer has the sufficient transient torque/speed tracking capability to emulate the dynamic behavior of the real-world hybrid powertrain will be crucial to the implementation of the proposed platform. Thus, with the target of developing a precise

and fast-response hybrid dynamics emulating tool, the emphasis of the research in the low level is laid on the design, modeling and control of the hydrostatic dynamometer [15]-[17], which will be summarized in Section 1.3.2.

1.3.1 Literature Review

Dynamometers have long been used to test automotive powertrain systems by emulating the loading conditions that may be experienced in real-world driving scenarios [18]. As a loading/motoring unit, the dynamometer "absorb" (or "provide", if necessary) torque from (or to) the engine. Driven by the combustion force and the dynamometer torque, the engine can follow desired speed and acceleration profiles, and hence, operating at desired torque-speed conditions for fuel efficiency, emissions and performance testing. Traditionally automotive powertrain research has been conducted with electromagnetic dynamometers. However, an important constraint that degrades the transient tracking capability of the electromagnetic dynamometer exists, which is, the limited power or torque to weight ratio. As the torque or power of a dynamometer increases so does the inertia of the electromagnetic dynamometers. This fact makes it very difficult to precisely emulate the transient behaviors of the powertrain systems that are experienced in the real-world driving scenario. The bulky size also makes it hard for reconfiguration for different testing purposes.

As mentioned before, a lot of rapidly-emerging innovations on the automotive propulsion system require significant flexibilities and transient capabilities of the testing tool. This calls for a new generation of transient dynamometers that are fast, precise and flexible. Given its superior power density, low inertia, and high bandwidth, the hydrostatic dynamometer is an ideal candidate for the next generation dynamometers. The hydrostatic dynamometer drives the engine with the hydrostatic torque generated by the fluid pressure, which provides it with large traction torque but very small angular moment of inertia (which is, much less than the electromagnetic dynamometer with similar output torque) [19]. Some studies on the design, control and implementation of the hydrostatic dynamometers have been reported, as follows:

Existing Hydrostatic Dynamometer Architectures

The research on the high-bandwidth hydrostatic dynamometer started from late 1980s [20]-[21]. The development of the dynamometer architecture design is mainly demonstrated by various actuation methods for the hydraulic torque control, and the increasing complexity of the hydraulic loop design. In early 1990s, Schenck Pegasus [21] designed a hydrostatic dynamometer composed of a primary flow compensation pump/motor and a secondary torque absorbing pump/motor. Given a constant pressure drop, the dynamometer torque was only controlled by modulating the displacement of the secondary pump/motor [22]. Ghaffarzadeh, et al. [23] proposed a hydrostatic dynamometer, which employed a variable pump displacement control unit and a relief valve that controls the pump outlet pressure, with a fixed inlet pressure control; while Dorey and Wang [20] proposed another hydrostatic dynamometer which employed a two-stage servo-controlled load valve for pump outlet pressure control and a two-stage boost relief valve for pump inlet pressure high/low adjustment, with a fixed pump displacement. Both of the two dynamometers employed two variables (including at least one pressure control) to establish the hydraulic torque as engine loads, which improves the flexibility and bandwidth for the dynamometer torque control.

In [22],[24]-[25], Babbit et al. presented a high bandwidth hydrostatic dynamometer for powertrain transient testing. A pressure relief valve and servo valves are employed to control the pump/motor inlet and outlet pressures respectively. On this basis, as a single-cylinder engine testing tool, another transient hydrostatic dynamometer was designed by Lathi et al. in [26]-[28]. Specifically, with a high-bandwidth servovalve, it separated the system into a motor circuit and a pump circuit to generate the high/low inlet pressure corresponding to motoring/absorbing torque conditions respectively, so as to optimize the power efficiency and dynamic response. This dynamometer aims to drive a single-cylinder engine to produce the instantaneous speed trajectory as a multi-cylinder engine. Recently, a hydrostatic absorption dynamometer incorporating a two-section gear pump and a pressure relief valve has been developed in [29] for testing small to medium sized engines.

Existing Hydrostatic Dynamometer Control Designs

Rapid and precise control of the dynamometer torque/speed is the primary requirement of the hydrostatic dynamometer control design. This requirement presents a serious technical challenge since the system involves multivariable nonlinear dynamics, which cannot be easily modeled with a linear approximation. In addition, the system variables (torque, pressure, speed and flow rate) are closely coupled, and therefore a simple reduction in their dynamic interactions is not feasible. Some research work on control design for electromagnetic dynamometers has been reported [18],[30]-[32]. However, few papers have been published on the modeling and control of hydrostatic dynamometers. Dorey and Wang [20] proposed a model reference adaptive controller for the hydraulic torque control. It simplified the system model by designing a proper PID controller to lead to a closed-loop system response like a first order system, and then, designed the adaptive control law with respect to the simplified model to achieve the torque control. Babbit, et al. [22] designed a PID controller for the hydraulic torque control with the linearized model around some typical operating points. Moskwa and Lathi [28] designed cascaded feedforward plus PI/PD controllers for the hydraulic torque control with the cascaded nonlinear model.

1.3.2 Research Summary

The design and control of the hydrostatic dynamometer that meet the needs of the proposed hybrid powertrain research platform have been achieved. Some unique or significant contributions in the low-level system design are summarized as follows:

1) Unique architecture design, modeling and system decoupling of the hydrostatic dynamometer

Different from the existing dynamometer architectures reviewed in the last section, a three-control-variables hydraulic system with an electronically controlled load sensing mechanism is designed [16]-[17], as shown in Fig. 1.3, to provide more control flexibilities and maintain a good balance between system controllability and response. On this basis, a physics-based 9th-order nonlinear model is constructed and validated with

experiments. The decoupling of this system, which is critical to the successful implementation of the nonlinear controls, is realized by leveraging its unique structure.

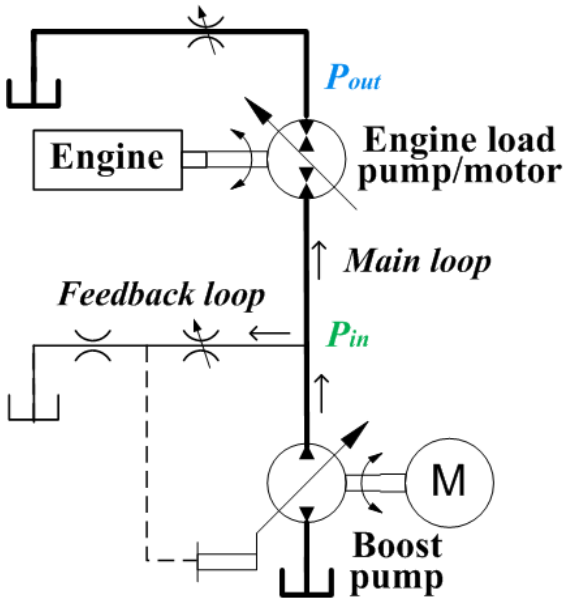

Fig. 1.3 Schematic diagram of the designed hydrostatic dynamometer

2) Systematic nonlinear controls for the transient hydrostatic dynamometer

We develop a state feedback control via feedback linearization to achieve precise and fast response tracking control for the engine speed. As a benchmark, a nonlinear inversion plus PID control is also implemented. Moreover, we apply Kalman filtering to obtain smooth signals of engine speed/acceleration, which is more effective than the low pass filter or other type of observers for this application.

1.4 MIDDLE LEVEL: HYBRID POWERTRAIN RESEARCH PLATFORM ARCHITECTURE DESIGN AND HYBRID POWERTRAIN CONTROL INTEGRATION

With the transient dynamometer and its related control system as the basic torque tool, the hybrid powertrain platform design focuses on constructing a whole set of virtual hybrid powertrain simulation and control system, and integrating it with the

dynamometer control system and engine control system in the physical level, to realize the hybrid powertrain dynamics emulation and hence, enable the experimental investigation of the targeted hybrid architecture and control strategies [33]-[34]. Particularly, the experimental investigation of a power-split hybrid architecture (Toyota THS) using the rapid prototyping platform has been conducted.

1.4.1 Literature Review

Existing Hybrid Powertrain Architectures

Various hybrid architectures can be accurately modeled and HIL simulated in the hybrid powertrain research platform. In terms of the mechanical architecture, HVs can be divided into three categories: parallel hybrids, series hybrids, and power-split hybrids [2].

The series hybrid architecture [35]-[36], as shown in Fig. 1.4 (a), converts the overall mechanical energy from the ICE into the electric energy stored in the storage battery, and further, converts the electric energy into the traction power by a traction motor to drive the vehicle. It is actually equivalent to add an ICE/generator to a battery powered pure electric vehicle (EV) as the primary energy source. The prominent advantages of the series hybrid architecture includes: 1) mechanical decoupling between the ICE and the vehicle which provides the absolute flexibility for the engine to operate at the very narrow optimal area with high fuel efficiency; 2) better torque-speed characteristic of the electric traction motor, especially in the launching phase. However, an obvious drawback for the series architecture exists, which is, the double energy conversions induces more energy loss to reduce the overall powertrain efficiency. In addition, a large energy storage element is need.

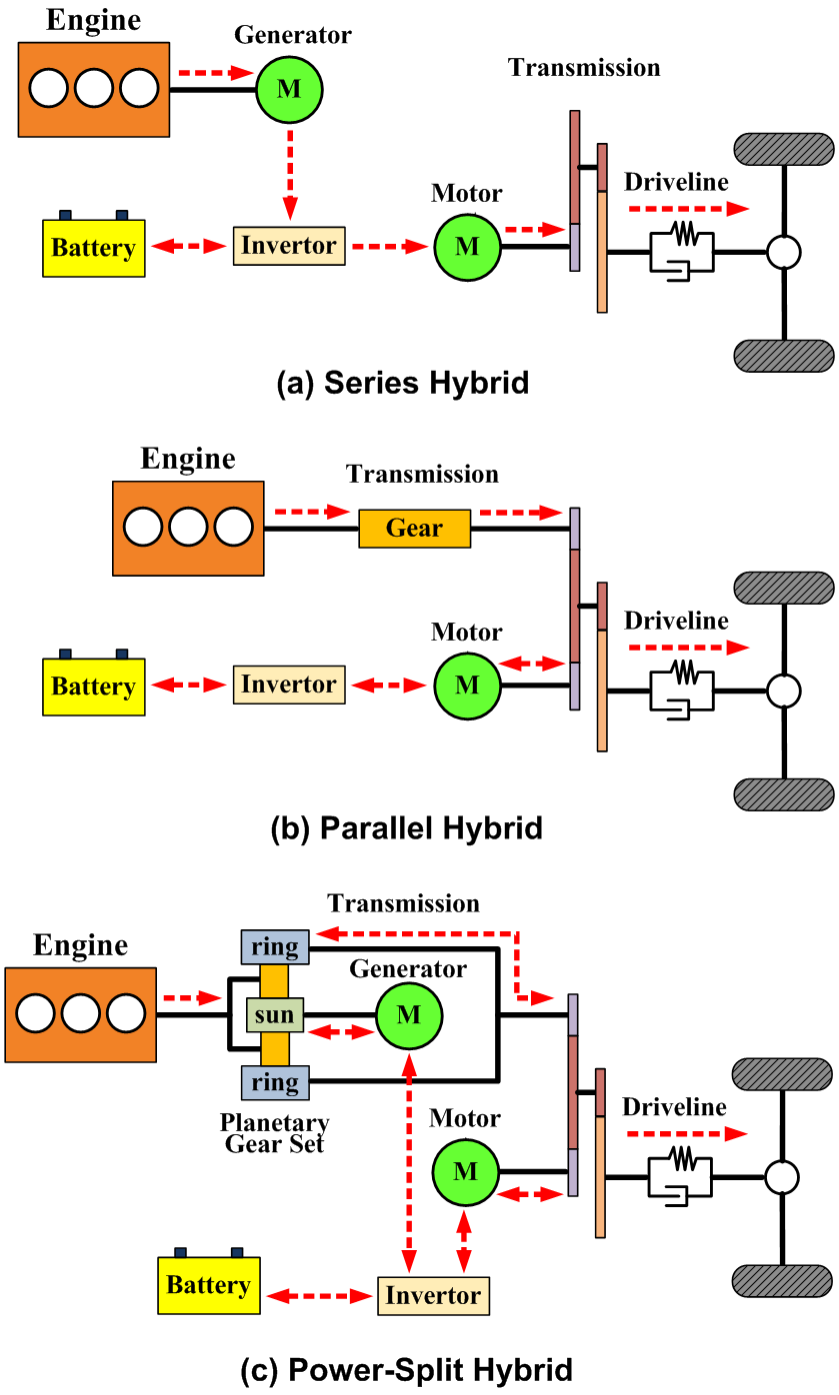

Fig. 1.4 Diagram of the typical hybrid powertrain architectures

The parallel hybrid architecture [37], as shown in Fig. 1.4 (b), allows both the ICE and electric motor to supply the traction power to the vehicle through a mechanical coupling. Either the mechanical and electric power path can drive the vehicle individually

or collaboratively. This parallel design greatly reduces the energy loss due to unnecessary energy conversion from the ICE to electric motor. However, it cannot maintain the engine operating points in the optimal high-efficiency area because of the mechanical coupling (i.e., speed coupling) between the engine and the vehicle.

The power-split hybrid architecture [12], also known as series-parallel hybrid, as shown in Fig. 1.4 (c), combines the advantages of both the two previous architectures. It employs a planetary gear set to split the engine power into two parts: one part is transferred to the driveline directly and the other part passes the "generator-battery-motor" path to the driveline. With the specific mechanical configuration of the planetary gear set, the engine speed and vehicle speed are completely decoupled, which allows to flexibly adjust the engine operating point to an arbitrary position in the engine map, to improve the powertrain fuel efficiency.

Among the three typical hybrid architectures, the power-split transmission has some more distinguished advantages, but also brings more complex control problems due to its higher degree of freedom. In this thesis, we dedicate to emulate the operation of the Toyota THS power-split hybrid architecture and on this basis, investigate the characteristics of the various hybrid architectures and control methodologies.

Existing Hybrid Powertrain Control Algorithms

In the power-split hybrid powertrain system, the desired vehicle speed and optimized engine speed/torque will be realized by controlling both the engine torque and hybrid torques (usually, torques from the electric machines). The design of this hybrid powertrain control will decide whether the optimized engine operation and designed vehicle operation can be simultaneously satisfied and further, to a large extent determine the energy optimality and drivability of the hybrid vehicles. Therefore, the study of the hybrid powertrain control will be significant in the hybrid powertrain development.

Reference [38] first proposed the system-decoupling-based control strategy (SISO controls) of the electric hybrid torques, which makes use of the electric generator to control the generator speed (equivalently, engine speed) and the electric motor to compensate the driving power of the whole vehicle. In [12] the SISO based controls were further improved and applied to cooperate with different energy management strategies.

Further, the limitations of the SISO based controls ("non-minimum phase" issues) in the automotive powertrain was indirectly unveiled in [39], and a MIMO control was designed to overcome the undesired dynamic responses on vehicle speed control based on a continuously variable transmission (CVT) system. On this basis, reference [40] discussed some similar "non-minimum-phase zero" phenomena in the power-split hybrid powertrain system, and designed a centralized (MIMO) torque controllers to eliminate the transient inverse electric generator torque.

1.4.2 Research Summary

1) Architecture design and controllers integration of the hybrid powertrain research platform

In order to achieve the real-time hybrid powertrain emulation, we developed the control architecture to integrate the physical systems (dynamometer, engine, etc) and the virtual hybrid powertrain simulator and controllers. The control flow is well-designed to not only guarantee the operation of the research platform close to the real-world hybrid powertrain operation, but also make the whole system consistent and stable. In terms of control design, corresponding to the each level in the hybrid powertrain research platform, an adaptive driver model, a DP based energy management strategy, a system-decoupling based middle-level control, and a feedback-linearization based dynamometer torque control are designed and integrated, respectively.

2) Dynamic analysis of the hybrid powertrain system and multivariable middle-level control design

The analysis of the dynamic interactions between the hybrid powertrain system outputs and inputs concludes that, the decoupling-based SISO hybrid powertrain controls have some inherent limitations on transient engine speed tracking, due to the existence of the electric constraints and some negative interactions within the system dynamics. To solve this problem and further improve the transient engine operation, a multivariable middle-level controller is designed to make full use of the transient engine torque to compensate the deficiency of the drive torque when the engine jumps from one operating point to another, so as to produce a good balance of the engine transient speed and torque

tracking, with relatively moderate usage of the electric power.

1.5 HIGH LEVEL (ENERGY OPTIMIZATION): DESIGN OF THE REAL-TIME SDP-ES ENERGY MANAGEMENT STRATEGY

Among the various related technologies on hybrid powertrain, the energy management strategy plays a critical role. The main objective of the energy management strategies is to minimize the fuel consumption and other significant performance index (for example, emissions) by determining the power split between the ICE and the alternative energy sources. In essence, the energy management is a global optimization problem along a finite time horizon (driving cycle). In principle, it is not necessary to minimize the fuel mass-flow rate at each instant of time, but rather the total fuel (emissions) consumed during the whole driving mission. In order to leverage the existing model-based global optimization tool (stochastic dynamic programming) and the non-model-based real-time optimization tool (extremum seeking), a SDP-ES energy management algorithm is designed [41] and introduced in Section 1.5.2.

1.5.1 Literature Review

In recent years, most of the researchers on the hybrid powertrain area lay their emphasis on the optimal algorithm/strategy of energy management and extensive simulation or experimental investigations in this area have been conducted [12]-[13], [37]-[45]. The existing optimal approaches are grouped into three categories.

Rule-based management strategies

Many existing energy management strategies are rule-based [42]-[46], because of the ease of the switching control among various operating modes, without huge computational burdens. The rule-based control employs a set of event-triggered rules to on-line manipulate the operation of the hybrid powertrain with respect to different driving scenarios, for example, “start”, “cruise”, “hard acceleration”, “regeneration” and so on,

which are defined by the values of current speed/torque and the driver's command on the brake pedal and accelerator pedal. The decision about the power-split ratio depends on the pre-defined rules corresponding to the current driving scenarios and the state of charge (SOC) of the storage unit [42]. The rule-based control strategy usually produces relatively high but not absolute optimal fuel efficiency.

Infinite (finite) horizon optimal management strategies

As the most important optimization tool for the global hybrid powertrain energy control problem, dynamic programming (DP) which globally optimizes the fuel efficiency and reduce the emissions by searching through all feasible control actions backwards along the given driving cycle, for all the states which presents the energy status and operating situations. Because of the huge computational burden and requirement for the future information, the DP based algorithm loses the capability for real-time implementation. Thus, extensive compromised suboptimal algorithms for real-time implementation are introduced. Lin et al. [43] designed a DP based rule-based strategy that extracted the near-optimal rules from the DP optimal results for some typical driving cycles. Kolmanovsky, et al. [47] and Lin, et al. [48] proposed a stochastic dynamic programming (SDP) energy management strategy, which extracts the optimal control policy based on the power demand statistics of multiple driving cycles, with an assumption that the power demand of the driver can be presented by a underlying Markov process. Liu, et al. [45] developed the SDP algorithm for the two-degree-of-freedom power-split HEV, Meyer, et al. [49] developed the SDP algorithm for the HHV application, and Moura, et al. [50] applied the SDP algorithm to the plug-in hybrid electric vehicles (PHEV). Further, Tate, et al. [51]-[52] proposed the shortest-path stochastic dynamic programming (SP-SDP), which introduced some more states that represent a "terminal" condition into the original SDP algorithm, so as to absorb the system dynamics to this terminal ("key off") condition in the iterative process but without discounted future cost, and quantify the penalty for the deviation of the final SOC from a set point only at key off condition. This kind of improved SDP algorithm offers a more natural formulation of the optimal control problem. Moreover, Opila, et al. [53] further incorporate the drivability metrics into the SP-SDP optimal strategy.

As an alternative of the real-time optimal algorithm, Borhan, et al. [54] proposed a model predictive control (MPC) based optimal algorithm for minimizing the fuel consumption based on an iterative prediction of the model outputs along a finite future time horizon, for the HEV application. Dappen, et al. [55] improve this MPC optimal algorithm for the HHV application.

Instantaneous optimal management strategies

Compared with the infinite (finite) horizon optimal algorithm, the instantaneous optimal algorithm focuses on locally optimizing the instantaneous energy efficiency point by point, instead of the global optimization. Paganelli, et al. [56] proposed an equivalent consumption minimization strategy (ECMS), which converses the instantaneous electric power into estimated equivalent fuel consumption, so as to realize the instantaneous minimization of the gross fuel consumptions. On this basis, Musardo, et al. [57] improved an adaptive ECMS (A-ECMS) algorithm which adaptively estimates the power equivalent factor with the record for the past information and the prediction for the future conditions, to fit for various driving conditions. Theoretically, Serrao, et al. [58] proved ECMS can be treated as a realization of Pontryagin's minimum principle for hybrid powertrain control. Liu, et al. [12] improved the ECMS algorithm for the two-degree-of-freedom power-split HEV and compared the optimal results with the SDP algorithm.

In addition, many other optimal algorithms, for example, the variable structure control based on Pontryagin's minimum principle [59], fuzzy logic [60], artificial neural networks [61], are also published in recent years.

1.5.2 Research Summary

Based on the existing hybrid energy optimal algorithms, some studies on the advanced optimal control are achieved. The main contributions are summarized as:

Design and development of the real-time SDP-ES energy optimization algorithm

A state-plus-output-feedback SDP-ES energy management strategy has been developed, to get a better balance between optimality and real-time control behaviors. This strategy combines a state-feedback based global energy optimization tool (SDP)

[62]-[64] as a reference controller to ensure the approximate global energy optimality and battery SOC sustainability, and a output-feedback based local energy optimization (ES) as a compensation controller to compensate the control commands from the SDP and generate more fuel-efficient operation points along the specific SOC sustaining line. This design actually "loosens" the precision limitations of the SDP, so as to offer larger space to reduce the computation burden by model simplification.

1.6 HIGH LEVEL (EMISSION OPTIMIZATION): TRANSIENT EMISSIONS MODELING AND DESIGN OF THE TWO-MODE ENERGY MANAGEMENT STRATEGY

Due to the complex physical/chemical nature of the engine combustion process, the engine power conversion and the gaseous/particulate emissions generation have quite different dynamics. Therefore, it is difficult to simultaneously and precisely optimize both the engine fuel efficiency and emissions, especially when we realize that the transient engine behaviors have significant influence on the emissions. This issue is especially amplified by the potential wide application of the diesel engine in the hybrid vehicles design, because of its higher fuel efficiency but more serious emissions (mainly, NOx and soot) [65] at both steady-states and transients (the latter, in particular, is worth studying) [66]. Targeted at achieving both the global energy optimization and transient emissions reduction based on a diesel hybrid electric vehicle, a "two-mode" hybrid energy management strategy is designed based on a data-driven diesel engine emissions dynamic model [67], as introduced in Section 1.6.2.

1.6.1 Literature Review

Large amount of work has been reported on optimizing the fuel efficiency or steady-state emissions in the hybrid powertrain system. However, relatively fewer studies are conducted to reduce the transient emissions of the diesel engine or diesel HEVs. Typical transient emissions control methods include: 1) controlling the temperature effect (for example, limiting the "engine off" time to prevent the engine from cooling down) and 2)

controlling the torque effect (smoothing the engine torque trajectory to avoid the sharp torque changes). The latter method has already been used in the hybrid vehicle supervisory strategy design. In [68], the abrupt engine dynamic behaviors are reduced by compensating the torque demand with an electric motor in a rule-based strategy. Reference [69] optimized the soot emission of an ISG diesel HEV by using a transient emission model-based optimal control strategy, in which a model predictive control algorithm was designed to realize the optimization for fuel efficiency and emissions. Recently, a self-learning neuro-dynamic programming algorithm is proposed to minimize the fuel consumption and transient NOx/soot emissions for a series hybrid hydraulic vehicle, based on the high-order transient emission dynamic models [70]. Recently, reference [71] investigates and demonstrates the NOx and Soot emission optimization performance with the quasi-static and transient emission models considered in the dynamic programming. In Ref [72], by correcting the engine torque based on mean value models for the engine EGR dynamics and NOx formation, the transient engine torque is limited so as to produce a significant NOx reduction with limited increase in the fuel consumption.

1.6.2 Research Summary

As a significant attempt on the development of the hybrid energy management strategy for reducing both the fuel consumption and the (dynamic) emissions, some contributions have been achieved as follows

Formulation, identification and validation of a control-oriented engine emission dynamic model

A control-oriented diesel engine emission model is first investigated based on large amounts of experimental data. Different from the static-mapping-based fuel consumption model, the emission model must involve transient dynamics to reflect the complex physical/chemical process during combustions. To meet the needs of the model-based emission control and optimization, a relative low-order, control-oriented mathematic model with well-selected input variables is designed by employing an autoregressive (AR) modeling approach, based on the usage of the experimental data.

Design and experimental investigation of the "Two-Mode" energy management strategy for emission control

On the basis of the data-driven engine emission dynamic model, a "Two-Mode" hybrid energy management strategy is designed, implemented and analyzed in experiments. In the "fuel efficiency improving" mode, a dynamic programming (DP) algorithm is used to seek the global optimization of the fuel economy and ensure the battery SOC sustainability; while in the "emission reducing" mode, the management strategy utilizes a linear quadratic regulator (LQR) to locally optimize the surging emissions due to undesired engine torque transients. At the end of the "emission reducing" mode, the locally optimized engine operation is driven back to match the globally optimized trajectory, i.e., the initial states of the next "fuel efficiency improving "mode. The seamless integration of the two modes will realize the reduction of the high local emissions without losing the global fuel efficiency optimality and battery SOC sustainability.

1.7 RESEARCH OUTLINE

In the following chapters of the thesis, all the research achievements will be presented in details, as follows:

Chapter 2 (low level design): This chapter presents the design, modeling, control and experimental validation of a transient hydrostatic dynamometer, as the physical-level task of the proposed research platform. Based on the detailed dynamic models, two nonlinear controllers and a Kalman filter based observer are designed and the experimental results demonstrate that the designed nonlinear controllers are capable of fast and precise tracking of the desired engine speed profile. The low level control system design in this chapter provides a set of fundamental control tools for the research in the succeeding chapters.

Chapter 3 (middle level design and system integration): This chapter presents the architecture design, control development and experimental investigation of the hybrid powertrain control system, as the system-level task of the proposed research platform.

To facilitate the hardware-in-the-loop experiment, the detailed dynamic models of the virtual hybrid powertrain system are built. On this basis, with an adaptive driver model, a closed-loop control system consists of three level controllers is designed and the experimental results demonstrate the capability of the proposed hybrid powertrain control system for the hybrid operation emulation. On this basis, the transient dynamics of the power-split hybrid powertrain system is fully analyzed and some unique dynamic characteristics: inverse transient dynamics and transient engine speed tracking issues are investigated. In order to better improve the transient performance of the control system, a multivariable middle level controller is designed to pursue a good balance of fast transient engine speed/torque tracking and moderate usage of the electric torque/power within the capabilities of the electrical system.

Chapter 4 (high level design: real-time energy optimization): This chapter presents the design of a SDP-ES energy management strategy which synthesizes a SDP state-feedback control as a "global" feedback term, and an ES output-feedback optimization as a "local" feedback term to generate more fuel-efficient operating points by leveraging the real-time measurement of fuel flow and emissions. The simulation results show the SDP-ES algorithm can provide desirable improvement of fuel economy based on the original SDP.

Chapter 5 (high level design: transient emission optimization): This chapter presents the control-oriented diesel engine emission modeling and design of a two-mode model-based hybrid energy management strategy. In the "fuel efficiency improving" mode, the management strategy makes use of a dynamic programming (DP) algorithm to seek the global optimization of the fuel efficiency, while in the "emission reducing" mode, the management strategy utilizes a linear quadratic regulator (LQR) to locally optimize the operating trajectory generated by the DP in a short time horizon, to reduce the high transient emissions induced by the sharp engine torque changes. The experimental results demonstrate that the proposed modeling and control strategy can considerably reduce the local soot emissions but still maintain the high fuel efficiency and battery SOC.

Chapter 6 (Conclusion): This chapter discusses and concludes all the research

work achieved in this thesis, and based on the current accomplishments, analyzes the possible improvements and potential innovations in the future.

Chapter 2

Transient Hydrostatic Dynamometer Design, Modeling, Control and Experimental Validation

2.1. RESEARCH OBJECTIVE

Aimed at building a hybrid powertrain rapid prototyping and research platform, a hydrostatic dynamometer is designed, controlled and experimentally investigated in this chapter. With its low inertia and fast response, the dynamometer can be used as a virtual power source or loading unit to emulate the torque-speed profile of any hybrid power sources (e.g. electrical motor or generator), so as to support the research of various hybrid powertrain architectures [6]-[11] and control methodologies [12]-[13], [37]-[61] without building the actual hybrid system, as shown in Fig. 2.1. This will be extremely cost-effective and time-efficient for the hybrid powertrain research.

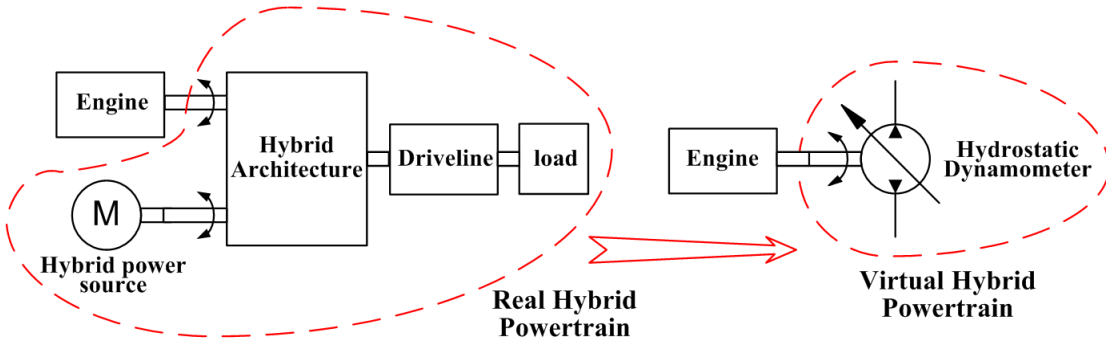

Fig. 2.1 Diagram of the hybrid powertrain research platform

Section 2.1 presents the hydraulic system design, which is characterized with the application of an electronically controlled load sensing mechanism. Load sensing is essentially a self-feedback loop with the load pressure as the feedback signal to adjust the

supply pump displacement to meet the load demand. Then, to realize the precise tracking performance of such a nonlinear and multivariable hydrostatic dynamometer system, this section presents a detailed nonlinear model and two systematic nonlinear control designs. In Section 2.2-2.4, a 9th order physics-based model for the system was developed and further, decoupled into two sub-systems for the operating pressure control and the power output control, by leveraging the unique architecture of the hydrostatic dynamometer. Furthermore, the system parameters are identified and validated with experimental data. In Section 2.5, for the power output control subsystem, a state feedback nonlinear controller is designed, which employs feedback linearization to offset the nonlinearity of the system and a state feedback stabilizer to achieve the system stabilization and precise tracking performance. As a benchmark, a nonlinear model-based inversion plus PID controller is also designed and implemented. For the operating pressure control subsystem, a PID regulator is designed to control the operating (inlet) pressure. In addition, a Kalman filter based observer is designed to estimate and smooth the engine speed and acceleration trajectories in real-time. In Section 2.6, extensive tests have been conducted to demonstrate the precise tracking performance of the proposed transient hydrostatic dynamometer.

2.2. SYSTEM DESIGN

The architecture of the hydrostatic dynamometer is shown in Fig.2.2. The system includes three parts: the hydraulic system and accessories (including the fluid power transmission components and actuators), the test engine and accessories, and the control system (including the real-time control unit and multiple sensors).

The host computer employs Matlab/SIMULINK® for designing, compiling and downloading the control algorithm to the control target, as well as, the real-time data monitoring and parameter regulation. A UEI® real-time control module is utilized as the real-time control target. The hydraulic system includes the hydraulic pump/motor/valves, electric motor, oil tank and cooling system. An IC engine is connected to the hydraulic pump/motor as the test engine. In our project, a Ford Falcon 6-cylinder 4.0L gasoline engine and a John Deere 4-cylinder 4.5L diesel engine are successively used as the test

engine. A speed/torque transducer is mounted on the engine shaft for torque/speed measurement. A group of pressure/temperature sensors are placed at both the hydraulic system and the test engine for parameter measurement and operation monitoring. A detailed picture of the main actuators and sensors is shown in Fig.2.3.

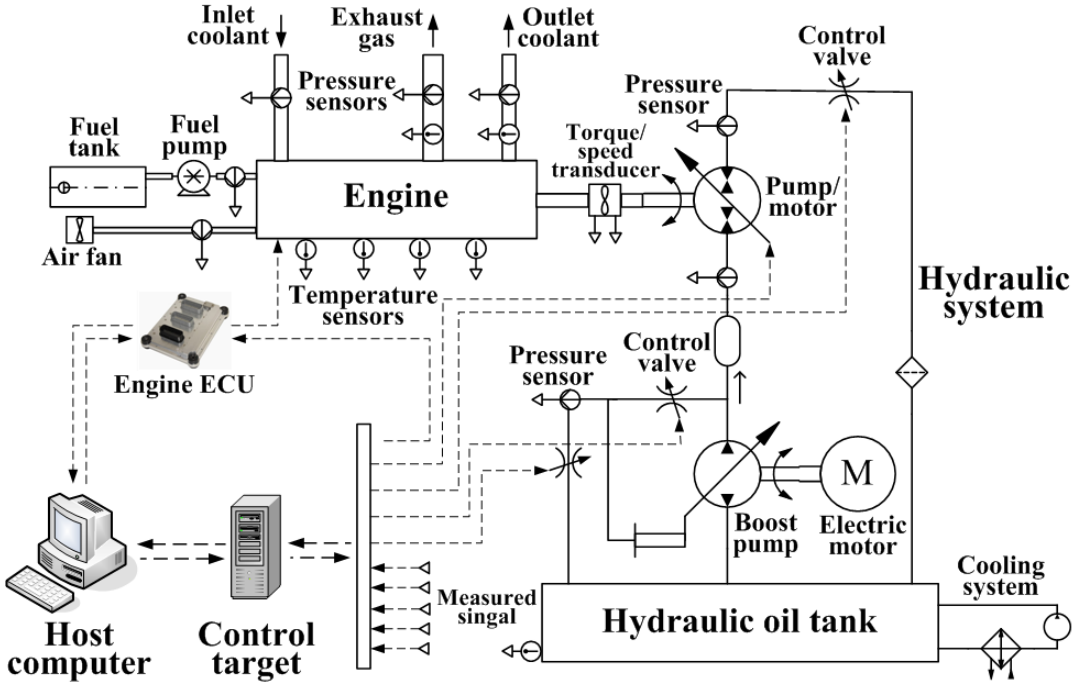

Fig. 2.2 Diagram of the hydrostatic dynamometer

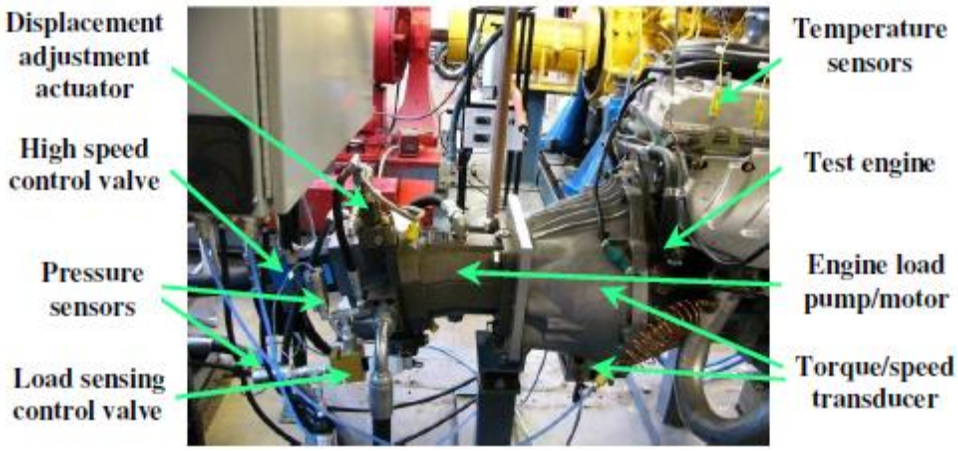

Fig. 2.3 Picture of the main actuators and sensors

The hydraulic system is the most important part of the hydrostatic dynamometer, as shown in Fig. 2.4. The main hydraulic components include: a boost pump and an engine load (EL) pump/motor (both are variable displacement piston pumps), a load sensing control (LSC) valve (proportional valve), and a high speed control (HSC) valve (two stage valve, shown in the bottom right corner of Fig. 2.4).

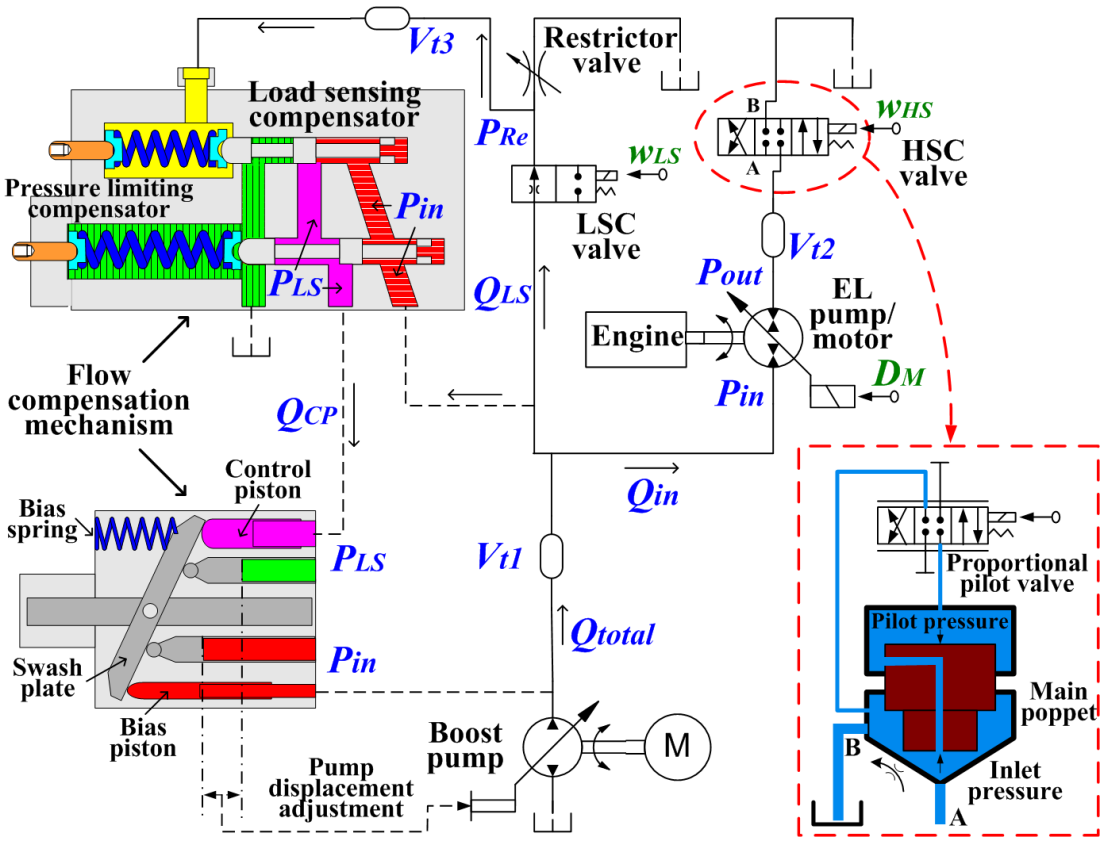

Fig. 2.4 Architecture of the hydraulic system for the dynamometer

As shown in Fig. 2.4, the hydraulic system consists of one fluid supply (Q_{total}) and two loops: the engine loading and motoring loop (Q_{in}) and load sensing feedback loop (Q_{LS}). Powered by an electrical motor, the boost pump provides fluid Q_{total} for both loops. The majority of the fluid, Q_{in} enters the main loop as the engine load, while a small portion of the fluid, Q_{LS} flows into the feedback loop to generate a feedback pressure for the boost pump displacement control.

In the load sensing feedback loop, the LSC valve generates a proper feedback pressure P_{re} as an input to the flow compensation mechanism. This mechanism, consisting of two flow compensators, is integrated into the boost pump. The pressure limiting compensator is used for limiting the operating pressure P_{in} under the safety threshold. More importantly, the load sensing compensator is used to adjust the swashplate angle, and hence, regulate the boost pump displacement, to ensure that the supplied fluid meets the engine demand, and regulate the inlet pressure of the EL pump/motor, P_{in}.

In the engine loading/motoring loop, the HSC valve controls the outlet pressure of the EL pump/ motor P_{out}, while the displacement adjustment mechanism controls the displacement of the EL pump/motor D_M. Since the dynamometer torque is a function of the displacement D_M and pressure drop $P_{out} - P_{in}$, we can manipulate the dynamometer torque to "counteract" the engine torque by controlling the above actuators and further, drive the engine to precisely track the desired speed profile.

There are two main characteristics for this hydraulic circuit design:

1) Torque Control with Three Independent Control Variables

For the main torque input/output component, the engine loading (EL) pump/motor, the torque output can be controlled with three independent control variables (the inlet pressure P_{in}, the output pressure P_{out}, and the displacement D_M). The output pressure P_{out} is controlled by the HSC valve, as a primary control variable for high-bandwidth torque control; the inlet pressure P_{in} is controlled by the load sensing mechanism, for the flexible adjustment of the pressure drop $P_{out} - P_{in}$ with different dynamometer operating modes (loading or motoring); the displacement D_M is further independently controlled, for the flexible adjustment of the pump/motor displacement to coordinate the relationship between the flow rate and output pressure under some mechanical constraints, especially at some extreme operating phases (low speed with high torque, or high speed with low torque).

2) Introduction of the Load Sensing Mechanism for Inlet Pressure Control

Load sensing is essentially a self-feedback loop which utilizes the load pressure as the feedback signal to adjust the supply pump displacement to meet the load demand. Different from the conventional application with the load sensing mechanism, which usually places the load sensing control (LSC) valve in the main loop to control the hydraulic flow rate, the design in this thesis adds a bypass loop (feedback loop) in parallel with the main loop, and places the LSC valve in the bypass loop. In this case, the load sensing mechanism will control the inlet pressure of the main loop instead of the flow rate. In terms of the special research objectives of the dynamometer system in this thesis, this load-sensing based hydraulic loop design has a series of advantages, including:

- ***Pressure Control***: this design replaces the hydraulic flow control with the pressure control, which meet the needs of the EL pump/motor torque control.
- ***Self-feedback Control***: compare with the direct valve control for the inlet pressure [22], the load sensing mechanism configuration provides us a better balance between system controllability and response. This design makes use of the self-feedback characteristic of the hardware system to regulate the inlet pressure corresponding to the constant command from the LSC valve. It avoids the possible conflicts between the inlet and outlet pressure controls, and further, provides a unique structure for the model decoupling in the next section [16]-[17].
- ***Low Power Loss***: since the LSC valve is settled at the bypass loop through which a very small portion of hydraulic fluid passes, the power loss is relatively smaller than the case when the LSC valve is settled at the main loop.

With regards to the power efficiency, a typical case study can be used to demonstrate the special advantage of the modified load sensing feedback loop. When the inlet pressure is regulated at 70 *bars*, which means the loading sensing feedback pressure is around 50 *bars*, the flow rate passing through the load sensing feedback loop will be 2-3 L/min based on the valve specifications. Meanwhile, if the EL pump/motor operates at the speed range of 800-2000 *rpm* with a maximum displacement of 107*cc/rev*. the flow rate passing through the main loop will be 85.6-246 *L/m*. Then, the total flow rate

provided by the boost pump will be 87.6-214 *L/m*, and the waste flow in the load sensing feedback loop is only 1.2% - 2.8% of the total flow. This is much more efficient than the regular loop design based on the application of the relief valve.

2.3 SYSTEM MODELING

2.3.1 Dynamic Models

1) Dynamic Model of the Fluid Supply System

As the fluid power supply, the boost pump provides the flow Q_{total} for both hydraulic loops. The majority part Q_{in} enters the engine loading/motoring loop, while the other part Q_{LS} flows into the feedback loop. The operating pressure-flow dynamics in the hydraulic fluid supply are given by:

$$\frac{V_{t1}}{\beta_e}\dot{P}_{in} = Q_{total} - Q_{LS} - Q_{in} \tag{2.1}$$

where,

$$Q_{total} = n_P D_{P\max} \phi_P \eta_{PV} \tag{2.2}$$

$$Q_{LS} = C_d A_{LS} w_{LS} \sqrt{\frac{2}{\rho}(P_{in} - P_{Re})} \tag{2.3}$$

V_{t1} is the volume between the hydraulic power supply and the two hydraulic loops, β_e is the effective bulk modulus, n_P is the rotational speed of the electric motor, $D_{P\max}$ is the maximum displacement of the boost pump, ϕ_P is the percentage of the actual displacement to the maximum displacement of the boost pump, η_{PV} is the volumetric efficiency of the boost pump, C_d is the discharge coefficient, ρ is the mass density of the fluid, A_{LS} is the maximum orifice area of the LSC valve, w_{LS} is the open area ratio of the LSC valve, i.e., the ratio of the open orifice area to the maximum orifice area, and P_{Re} is the outlet pressure of the LSC valve, i.e. the inlet pressure of the restrictor valve. Q_{in} is the flow entering the engine loading/motoring loop, which will be formulated in the next

section.

2) Dynamic Model of the Engine Loading/Motoring Loop

The engine loading/motoring loop consists of the EL pump/motor, the HSC valve and the test engine.

Because the test engine is rigidly connected with the EL pump/motor, the shaft dynamics is neglected due to its high stiffness. Then, the torque-speed dynamics of the engine-dynamometer system are given by:

$$J_e\dot{\omega} = T_e - T_f - T_{dyno} \tag{2.4}$$

where ω is the engine rotational speed, J_e is the total moment of inertia of the engine and EL pump/motor, and T_e, T_f and T_{dyno} are the engine combustion torque, engine friction torque and dynamometer torque, respectively.

The engine friction torque is represented as:

$$T_f = T_{cou} + f_{vis}\omega \tag{2.5}$$

where T_{cou} is the Coulomb friction torque and f_{vis} is the viscous friction coefficient.

The dynamometer torque, i.e., the fluid torque from the EL pump/motor, is given by:

$$T_{dyno} = \frac{D_M}{2\pi}\left(P_{out} - P_{in}\right)\eta_{MM} \tag{2.6}$$

where $\frac{D_M}{2\pi}\left(P_{out} - P_{in}\right)$ is the ideal torque generated by the EL pump/motor, and η_{MM} is the mechanical efficiency of the EL pump/motor, derived as in [73]:

$$\eta_{MM} = 1 - C_{da}\mu\frac{\omega}{P_{in} - P_{out}} - C_f\frac{P_{in} + P_{out}}{P_{in} - P_{out}} \tag{2.7}$$

where C_{da} is the dimensionless damping coefficient, μ is the absolute viscosity of the hydraulic fluid and C_f is the internal friction coefficient of the EL pump/motor. The second term in the above equation describes the torque loss for shearing the viscous fluid, which is proportional to the pump/motor rotational speed. The third term describes the torque loss due to the friction force in the bores of the piston opposing the motion of the piston, which is proportional to the pressure acting on the piston area.

The flow-pressure dynamics of the HSC valve are given by:

$$\frac{V_{t2}}{\beta_e}\dot{P}_{out} = Q_{EL} + Q_{im} - Q_{em} - Q_{HSC} \tag{2.8}$$

where, V_{t2} is the volume between the outlet of the EL pump/motor and the HSC valve, Q_{EL} is the ideal flow rate passing through the EL pump/motor, Q_{im} is the internal (cross-port) leakage flow rate, Q_{em} is the external leakage flow rate which is going from the pump/motor outlet chamber, past the pistons and to the case drain, and Q_{HSC} is the flow rate passing through the HSC control valve, i.e., the outlet flow rate from the volume V_{t2}. These flow rates are further written as:

$$Q_{EL} = \frac{D_M}{2\pi}\omega \tag{2.9}$$

$$Q_{im} = C_{im}\left(P_{in} - P_{out}\right) \tag{2.10}$$

$$Q_{em} = C_{em}P_{out} \tag{2.11}$$

$$Q_{HSC} = C_d A_{HS} w_{HS}\sqrt{\frac{2}{\rho}P_{out}} \tag{2.12}$$

where C_{im} and C_{em} are the internal and external leakage coefficients of the EL pump/motor, respectively, w_{HS} is the open area ratio of the HSC valve, A_{HS} is the maximum orifice area of the HSC valve. Due to the relatively high bandwidth of the HSC valve (for the pilot valve, about 155 Hz as measured), the valve dynamics can be temporarily neglected in the pressure dynamic model.

As the connection between the dynamics of the hydraulic fluid supply and the engine loading/pumping loop, the relationship:

$$Q_{in} = Q_{EL} + Q_{im} + C_{em}P_{in} = \frac{D_M}{2\pi}\omega + C_{im}\left(P_{in} - P_{out}\right) + C_{em}P_{in} \tag{2.13}$$

describes the interactions between the flow rates, rotary speed and pressures in the engine loading/pumping loop.

3) Dynamic Model of the Load Sensing Feedback Loop

The load sensing feedback loop consists of the flow compensation mechanism inside

the boost pump (including the load sensing compensator, pressure limiting compensator and swashplate), the LSC valve and the restrictor valve.

As mentioned before, a small portion of the fluid from the boost pump, Q_{LS} passes through the LSC valve and the restrictor valve in series in the feedback loop. The flow-pressure dynamics of the two valves are given by:

$$\frac{V_{t3}}{\beta_e}\dot{P}_{Re} = Q_{LS} - Q_{Re} \tag{2.14}$$

where V_{t3} is the volume of the pipes/connectors that connect the LSC valve, the restrictor valve and the load sensing compensator. The flow rate passing through the restrictor valve Q_{Re} satisfies that:

$$Q_{Re} = F\left(P_{Re}, I_{Re}\right) \tag{2.15}$$

where, the function F is obtained by the numerical fitting of the measured characteristic curve of the restrictor valve. I_{Re} is the current command to the restrictor valve.

Furthermore, the dynamics of the spool in the load sensing compensator is given by:

$$m_c\ddot{L}_{sp} = -f_c\dot{L}_{sp} - k_cL_{sp} + \left(P_{in} - P_{Re} - P_{sb}\right)S_c \tag{2.16}$$

where, L_{sp} is the load sensing spool displacement from the neutral position to the left hand side of the chamber, m_c, f_c, k_c and S_c are the mass of the spool, the viscous friction coefficient, the spring rate and the chamber's cross sectional area, respectively. P_{sb} is the load sensing standby pressure, i.e., the ratio of the spring force to the chamber area S_c at the neutral position ($L_{sp} = 0$). As a default factory setting, P_{sb} is designed to be 20 *bars*.

Besides the spool dynamics, the flow-pressure dynamics of the load sensing compensator are given as follows. The compensator flow rate Q_{CP} flows from the internal chamber of the compensators to the control piston. Since the chamber volume of the compensators can be neglected when compared to the volume of the control piston, the flow-pressure dynamics are:

$$\frac{L_{pis}S_{P-control}+V_{p0}}{\beta_e}\dot{P}_{LS}=Q_{CP}-S_{P-control}\dot{L}_{pis} \tag{2.17}$$

where,

$$Q_{CP}=\begin{cases} C_d A_c \dfrac{L_{sp}}{L_{or}}\sqrt{\dfrac{2}{\rho}\left(P_{in}-P_{LS}\right)} & L_{sp}>0 \\ C_d A_c \dfrac{L_{sp}}{L_{or}}\sqrt{\dfrac{2}{\rho}P_{LS}} & L_{sp}\le 0 \end{cases} \tag{2.18}$$

L_{pis} is the displacement of the control piston from the right end to the left hand side, $S_{P-control}$ is the cross sectional areas of the control piston, V_{p0} is the initial piston volume when $L_{pis}=0$, and $S_{P-control}\dot{L}_{pis}$ denotes the rate of change of the control piston volume. L_{or} and A_c are the maximum width and maximum area of the main orifice of the load sensing compensator, respectively. Specially, when the spool of the load sensing compensator is to the left of the neutral position, i.e. $L_{sp}>0$, the central port of the compensator is open to the right chamber (the area filled with horizontal bars in Fig. 2.4 , with the pressure P_{in}), so the first orifice equation in (2.18) is used to describe the flow-pressure relationship; when the spool is to the right of the neutral position, i.e. $L_{sp}\le 0$, the central port is open to the left chamber (the area filled with vertical bars in Fig. 2.4, connected to the tank), so the second orifice equation in takes effect instead.

In (2.17) and (2.18), the flow-pressure dynamics in the pressure limiting compensator is neglected, because it almost never affects the flow rate Q_{CP} and pressure P_{LS}, unless the operating pressure P_{in} exceeds the safety threshold.

Finally, the dynamics related to the boost pump displacement adjustment is analyzed. The dynamics of the rotary motion of the swashplate around its pivot are given by:

$$\begin{aligned} I_P\ddot{\theta}=&-f_P\dot{\theta}+d_P\left[k_P d_P\left(\tan\theta_m-\tan\theta\right)\right] \\ &+d_P\left(-P_{LS}S_{P-control}+P_{in}S_{P-bias}\right) \end{aligned} \tag{2.19}$$

where θ and θ_m are the current and maximum swashplate angles, d_P is the distance

between the central axis of the control piston and swashplate pivot, S_{P-bias} is the cross sectional area of the bias piston, f_P, I_p and k_P are the equivalent angular viscous friction coefficient, rotary moment of inertia, and bias spring rate of the swashplate, respectively.

Since θ is relatively small, it is reasonable to assume that:

$$L_{pis} = d_P\left(\tan\theta_m - \tan\theta\right) \approx d_P\left(\tan\theta_m - \theta\right) \tag{2.20}$$

Substituting (2.20) into (2.19) yields:

$$\ddot{L}_{pis} = -\frac{f_P}{I_P}\dot{L}_{pis} + \frac{d_P^{\,2}}{I_P}\left(-k_P L_{pis} + P_{LS}S_{P-control} - P_{in}S_{P-bias}\right) \tag{2.21}$$

Furthermore, the percentage of the actual displacement to the maximum displacement of the boost pump is given by:

$$\phi_P = 1 - \frac{L_{pis}}{d_P \tan\theta_m} \tag{2.22}$$

The variables ϕ_P and Q_{LS} are the connections between the dynamics of the fluid supply system and the load sensing feedback loop.

Based on the inherent physical properties and multiple measurements of the hydrostatic dynamometer, as well as the data from the related literature about the components in use, the majority of the parameters in the dynamic models can be determined with relatively high fidelity, as shown in Table 2.1.

2.3.2 Experimental Identification of the System Parameters

Besides the known or measurable parameters, there are some important parameters which cannot be directly obtained. These parameters are identified with experimental data. To simplify the experiments, dynamometer motoring mode is used, where the fluid power motors the engine at the desired speed, i.e., $T_e = 0$.

1) Engine Friction Torque Related Parameters

From (2.4) and (2.5), in steady state, the Coulomb friction torque T_{cou} and viscous friction coefficient f_{vis} satisfy:

TABLE 2.1 Determinate parameters in the dynamic model

Symbo		Quantity
J_e	engine inertia	0.15 ($kg \cdot m^2$)
β_e	effective bulk modulus	1.3×10^9(pa)
R_{HS}	HSC valve coefficient	1.05×10^{-5}(m^3/sec/$pa^{1/2}$)
	where, $R_{HS=}C_dA_{HS}(\rho)^{1/2}$	
R_{LS}	LSC valve coefficient	5×10^{-7}(m^3/sec/$pa^{1/2}$)
	where, $R_{LS=}C_dA_{LS}(\rho)^{1/2}$	
V_{t1}	pipe volume	6.9×10^{-4} (m^3)
V_{t2}	pipe volume	2×10^{-4} (m^3)
V_{t3}	pipe volume	9.6×10^{-5} (m^3)
n_P	electrical motor speed	1770(rpm)
η_{PV}	boost pump volumetric efficiency	0.95
d_p	specific distance in swashplate	0.0945 (m)
θ_m	maximum swashplate angle	30(degree)
D_{Pmax}	boost pump displacement	131(cc/rev)
m_c	mass of spool (LS)	9.718×10^{-3} (kg)
f_c	viscous friction coefficient (LS)	26.19 (N/(m/sec))
k_c	spring rate (LS)	36000 (N/m)
S_c	cross-sectional area (LS)	3.1619×10^{-5} (m^2)
I_p	swashplate rotary inertia	0.021 ($N \cdot m \cdot sec^2$)
f_p	angular viscous friction coefficient	1.458×10^{-3} ($N \cdot m^2$/(m/sec))
k_p	spring rate (bias piston)	31250 (N/m)
L_{or}	orifice width (LS)	0.0018 (m)
$S_{P\text{-}control}$	cross-sectional area (control piston)	10^{-3} (m^2)
$S_{P\text{-}bias}$	cross-sectional area (bias piston)	3.674×10^{-4} (m^2)
V_{p0}	initial control piston volume	10^{-5}(m^3)

$$T_f = -T_{dyno} = T_{cou} + f_{vis}\omega \tag{2.23}$$

Since the parameters T_{cou} and f_{vis} appear linearly in the parametric model, a standard least square algorithm is used to estimate the unknown parameters.

Based on a set of experimental data of T_f and ω, with the least square fitting, the friction torque related parameters are obtained as: $T_{cou} = 17.569\, N{\cdot}m$ and $f_{vis} = 0.1490$ *N·m/(rad/sec)*, as shown in Fig. 2.5.

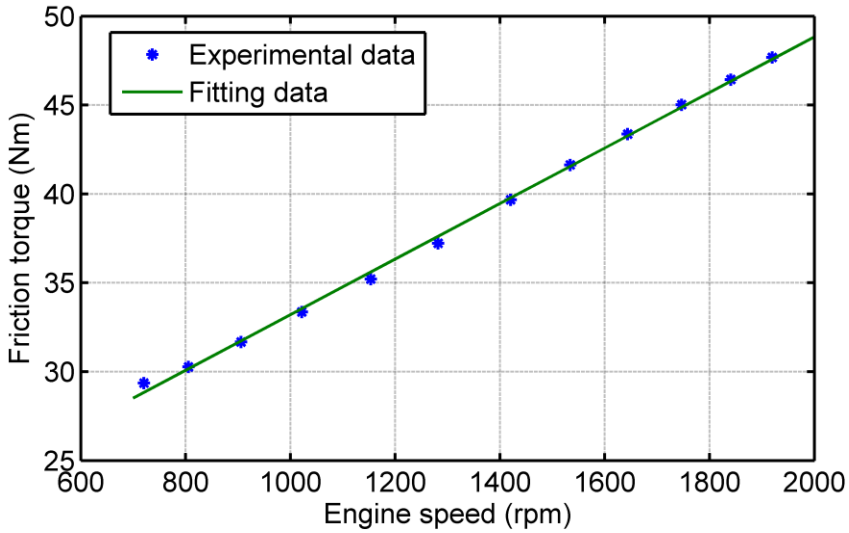

Fig. 2.5 Least square fitting for engine friction torques vs. engine speed

2) Pump/motor Mechanical Efficiency Related Parameters

From (2.4)-(2.7), in steady state, the relationship between the viscous damping coefficient $C_{da}\mu$ and the internal friction coefficient C_f is given by:

$$a_0 = C_f + a_1 C_{da}\mu \tag{2.24}$$

where

$$a_0 = -\frac{2\pi T_f}{D_M\left(P_{in} + P_{out}\right)} + \frac{P_{in} - P_{out}}{P_{in} + P_{out}} \tag{2.25}$$

$$a_1 = \frac{\omega}{P_{in} + P_{out}} \tag{2.26}$$

With the least square algorithm, the mechanical efficiency related parameters are

solved as: $C_{da}\mu = 7269.2\,Pa/(rad/sec)$ and $C_f = 0.0310$, as shown in Fig. 2.6.

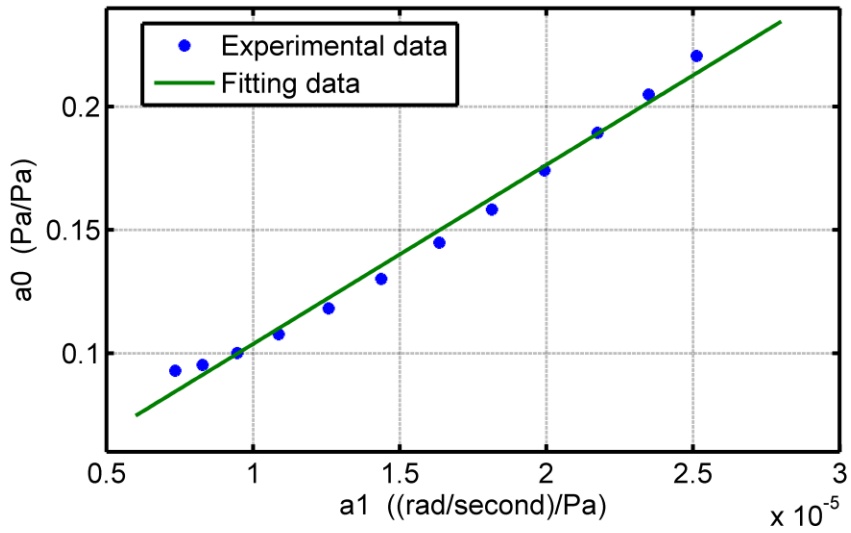

Fig.2. 6 Least square fitting for the mechanical efficiency related parameters

3) Pump/motor Volumetric Efficiency Related Parameters

From (2.8)-(2.12), in steady state, the relationship between the internal and external leakage coefficients of the EL pump/motor, C_{im} and C_{em} is given by:

$$b_0 = -C_{em} + b_1 C_{im} \tag{2.27}$$

where

$$b_0 = \frac{R_{HS} w_{HS}}{\sqrt{P_{out}}} - \frac{D_M}{2\pi P_{out}}\omega \tag{2.28}$$

$$b_1 = \frac{P_{in} - P_{out}}{P_{out}} \tag{2.29}$$

Based on a set of experimental data, we still adopt the least square algorithm to identify the parameters, $C_{im} = 2.46\times10^{-12}\ m^3/sec/Pa$ and $C_{em} = 6.46\times10^{-12}\ m^3/sec/Pa$, as shown in Fig. 2.7.

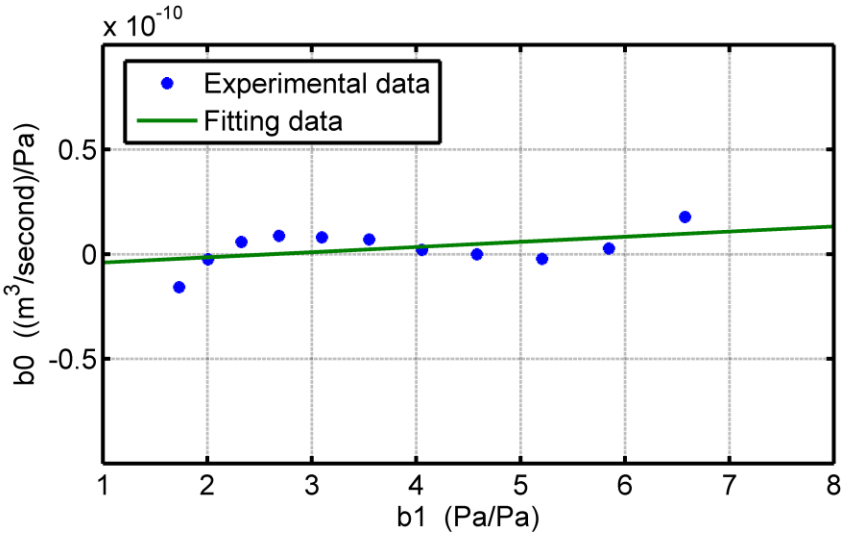

Fig.2.7 Least square fitting for the volumetric efficiency related parameters

The experimental data show some nonlinear effects, which cannot be completely captured with a linear relationship. Nevertheless, since the system dynamics are not very sensitive to the variations of C_{im} and C_{em}, the identified values are acceptable, as shown by the system validation in the following section.

2.3.3 Experimental Validation of the System Model

To validate the developed mathematical models, experimental data at both steady state and transient operations are compared with the model predictions.

1） Model Validation in Steady State

For these experiments, we maintain the inlet pressure at 64 *bars*. Then, a series of engine speeds corresponding to different outlet pressures are obtained. Fig.2.8 shows that the model prediction matches the experimental data very well.

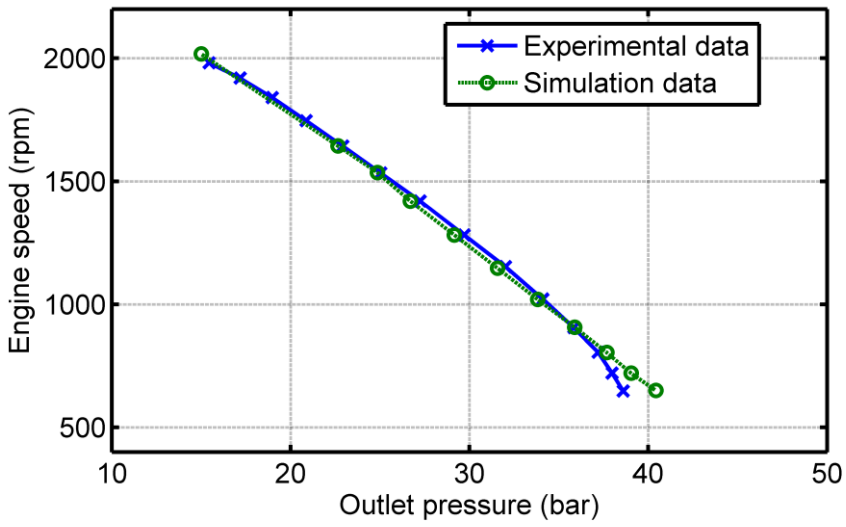

Fig. 2.8 Comparison of the speed vs. outlet pressure in the steady state

2） Model Validation during Transients

Not only in steady state, comparisons of step responses and frequency responses are also used to validate the system model during transient operations. For this nonlinear system, the frequency responses are obtained around a specific operating point (about 1150 *rpm*).

Fig. 2.9 shows the step responses in both experiments and simulations, for a step input of 0.1 *volt* (control command of the HSC valve). Compared with the simulation data, a slight delay and under-damped characteristics can be observed from the experimental data. It is mainly due to the unmodeled dynamics (the shaft dynamics, variations of fluid compressibility, etc.). In addition, dynamics of the Kalman filter (see Section 2.5) also contribute to this phenomenon.

The frequency responses are shown in Fig. 2.10, for a set of sinusoidal inputs with amplitude of 0.1 *volt* (control command of the HSC valve) at a frequency range from 0.06 *Hz* to 4 *Hz*, around the given operating point.

Based on the experimental validation, the developed mathematical model is shown to be an accurate representation of the actual system dynamics both at steady state and during transients, and will be used for control system design in Section 2.6.

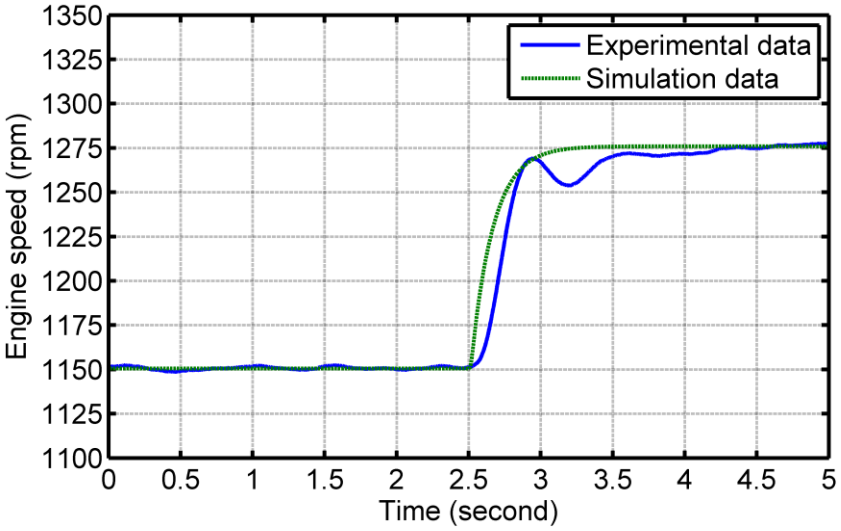

Fig. 2.9 Comparison of the step responses

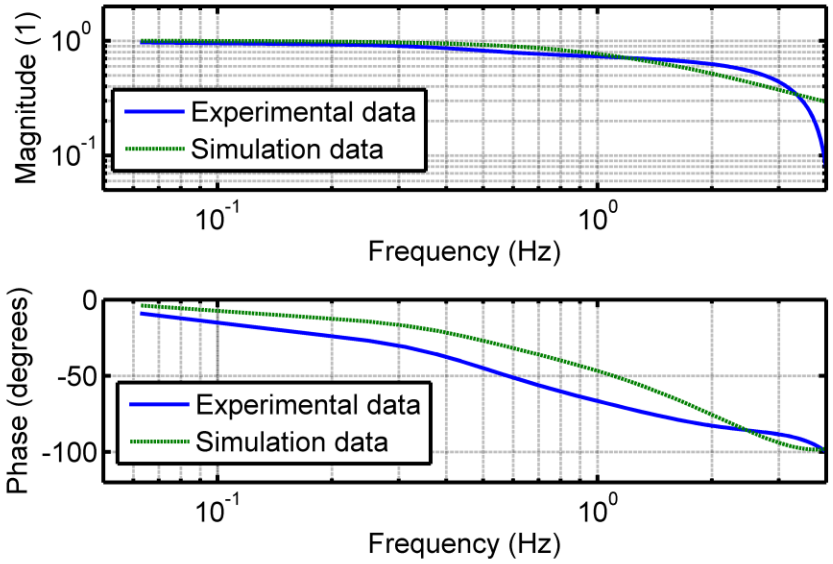

Fig. 2.10 Comparison of the frequency responses

2.4 DYNAMICS ANALYSIS AND SYSTEM DECOUPLING

Precise speed profile tracking of the hydrostatic dynamometer is required as the primary control target. This presents a serious technical challenge since the system involves multivariable nonlinear dynamics, which cannot be easily modeled with a linear

approximation. In addition, the system variables (torque, pressure, speed and flow rate) are closely coupled, and therefore a simple reduction in their dynamic interactions is not feasible.

By analyzing the unique structure, a system decoupling approach is accessed without losing the main dynamic interaction among the important system variables. Although the overall system model is 9^{th} order, the dynamics of the engine loading/pumping loop are only connected to the fluid supply system and the load sensing feedback loop through variables Q_{in} and P_{in}. Furthermore the operating (inlet) pressure P_{in} can be measured directly and Q_{in} can be calculated based the measurement of P_{in}, P_{out} and ω. This will allow us to decouple the dynamometer into two subsystems: the operating pressure control subsystem (including the hydraulic fluid supply and load sensing feedback loop) and the power output control subsystem (including the engine loading/motoring loop) , as shown in Fig. 2.11.

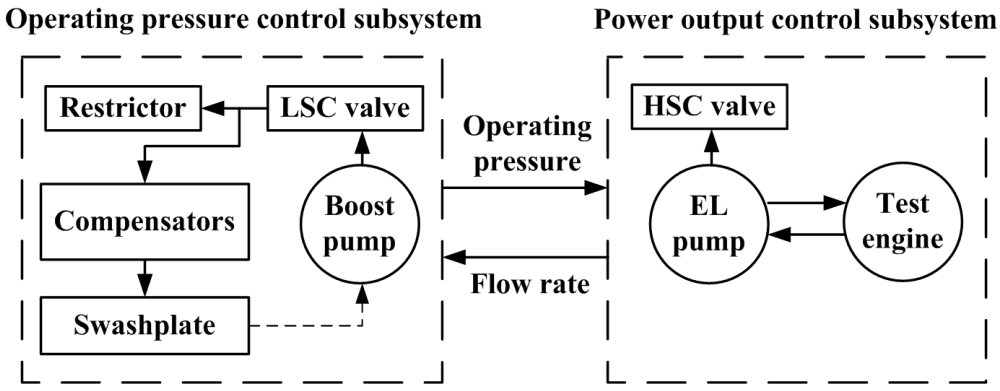

Fig. 2.11 Schematic diagram of the decoupled systems

For the operating pressure control subsystem, the seventh-order dynamic model is:

$$\dot{P}_{in} = \frac{\beta_e}{V_{t1}} n_P D_{P\max} \left(1 - \frac{L_{pis}}{d_P \tan\theta_m}\right) \eta_{PV} - \frac{\beta_e}{V_{t1}} R_{LS} w_{LS} \sqrt{P_{in} - P_{Re}} - \frac{\beta_e}{V_{t1}} Q_{in}$$

$$\dot{P}_{Re} = \frac{\beta_e}{V_{t3}} R_{LS} w_{LS} \sqrt{P_{in} - P_{Re}} - \frac{\beta_e}{V_{t3}} Q_{Re}$$

$$\ddot{L}_{sp} = -\frac{f_c}{m_c} \dot{L}_{sp} - \frac{k_c}{m_c} L_{sp} + \left(P_{in} - P_{Re} - P_{sb}\right) \frac{S_c}{m_c}$$

$$\dot{P}_{LS}=\frac{\beta_e C_d A_c \frac{L_{sp}}{L_{or}}\sqrt{\frac{2}{\rho}\left(\frac{L_{sp}+\left|L_{sp}\right|}{2\left|L_{sp}\right|}P_{in}-\frac{L_{sp}}{\left|L_{sp}\right|}P_{LS}\right)}-\beta_e S_{P-control}\dot{L}_{pis}}{L_{pis}S_{P-control}+V_{p0}}$$

$$\ddot{L}_{pis}=-\frac{f_P}{I_P}\dot{L}_{pis}+\frac{{d_P}^2}{I_P}\left(-k_P L_{pis}+P_{LS}S_{P-control}-P_{in}S_{P-bias}\right) \tag{2.30}$$

For the power output control subsystem, the second-order dynamic model is:

$$\dot{\omega}=-\frac{C_{da}\mu D_M(t)}{2\pi J_e}\omega-\frac{\left(1+C_f\right)D_M\left(t\right)}{2\pi J_e}P_{out}+\frac{T_E(t)}{J_e}+\frac{\left(1-C_f\right)D_M\left(t\right)}{2\pi J_e}P_{in}\left(t\right)$$

$$\dot{P}_{out}=\frac{\beta_e D_M\left(t\right)}{2\pi V_{t2}}\omega-\frac{\beta_e C_d A_{HS}}{V_{t2}}w_{HS}\sqrt{\frac{2}{\rho}P_{out}}-\frac{\beta_e}{V_{t2}}\left(C_{im}+C_{em}\right)P_{out}+\frac{\beta_e}{V_{t2}}C_{im}P_{in}\left(t\right) \tag{2.31}$$

where, $T_E(t)=T_e-T_{cou}-f_{vis}\omega$ is the net torque from the engine, which includes both the engine's combustion torque and internal friction torque.

2.5 CONTROLLER DESIGN

Fast and accurate tracking of the desired engine speed via precise control of the dynamometer torque, is the primary control target for the hydrostatic dynamometer. As a result of the system decoupling in Section 2.4, only the dynamics of the power output control subsystem in (2.31) needs to be considered for the engine speed tracking, as long as the inlet pressure can be measured as a time-varying input.

The operating (inlet) pressure control subsystem is only concerned with the regulation of the inlet pressure. It is a high-order nonlinear dynamic system described by (2.30). However, with the benefits of the self-feedback characteristics of the load sensing control mechanism, the stability of this nonlinear system has been guaranteed by mechanical design itself. On this basis, a PID controller is designed to regulate the operating pressure (i.e., adjust the equilibrium point of the nonlinear system).

In the power output control subsystem, although there are two actuators available for the dynamometer torque control, the bandwidth of the solenoid for displacement control of the EL pump/motor is much lower than the bandwidth of the HSC valve. Therefore, we choose the HSC valve as the primary actuator. Meanwhile, the solenoid for

displacement control works as the secondary actuator, which is only used to regulate the steady state relationship between the engine speed and the outlet pressure, if necessary [15]. Thus, with the open area ratio of the HSC valve w_{HS} as the input u, the engine speed ω and outlet pressure P_{out} as the states x_1 and x_2, the model is given as:

$$\begin{aligned}
\dot{x}_1 &= -\frac{C_{da}\mu D_M(t)}{2\pi J_e}x_1 - \frac{(1+C_f)D_M(t)}{2\pi J_e}x_2 + \frac{T_E(t)}{J_e} + \frac{(1-C_f)D_M(t)}{2\pi J_e}P_{in}(t) \\
\dot{x}_2 &= \frac{\beta_e D_M(t)}{2\pi V_{t2}}x_1 - \frac{\beta_e C_d A_{HS}}{V_{t2}}\sqrt{\frac{2}{\rho}}\sqrt{x_2}u - \frac{\beta_e}{V_{t2}}(C_{im}+C_{em})x_2 + \frac{\beta_e}{V_{t2}}C_{im}P_{in}(t) \\
y &= x_1
\end{aligned} \tag{2.32}$$

To achieve precise tracking of the above nonlinear system, two types of nonlinear controllers, a nonlinear model-based inversion plus PID control and a state feedback control via feedback linearization are designed and implemented. In order to provide smooth engine speed and acceleration signals for control implementation, a Kalman estimator is first designed.

2.5.1 Kalman Estimator for Engine Rotational Speed and Acceleration

Engine speed and acceleration are important system states and feedback variables for the tracking controller. As mentioned in section 2.2, an optical-encoder-based speed transducer is used to generate the pulse string whose frequency represents the engine rotational angle. However, it is impossible to obtain the exact and smooth speed and acceleration by numerically differentiating the measured rotational angle.

Because of the engine inertia, the engine speed profile is relatively smooth in the time domain. Assuming that the third derivative of the engine speed (snap) is normally distributed around zero and remains constant between sampling steps [74], the engine dynamics can be expressed in the following discrete form:

$$\begin{bmatrix} \theta(t_k+T) \\ \omega(t_k+T) \\ a(t_k+T) \\ j(t_k+T) \end{bmatrix} = \begin{bmatrix} 1 & T & \frac{1}{2}T^2 & \frac{1}{6}T^3 \\ 0 & 1 & T & \frac{1}{2}T^2 \\ 0 & 0 & 1 & T \\ 0 & 0 & 0 & 1 \end{bmatrix} \begin{bmatrix} \theta(t_k) \\ \omega(t_k) \\ a(t_k) \\ j(t_k) \end{bmatrix} + \begin{bmatrix} \frac{1}{24}T^4 \\ \frac{1}{6}T^3 \\ \frac{1}{2}T^2 \\ T \end{bmatrix} d(t_k)$$

Or,
$$x(t_k+T) = A_K x(t_k) + G_K w(t_k) \tag{2.33}$$

where $\theta(t_k)$, $\omega(t_k)$, $a(t_k)$, $j(t_k)$ and $d(t_k)$ are the rotational angle, speed, acceleration, second derivative and third derivative of speed (which are, jerk and snap) at time t_k, respectively. T is the sampling time.

Since $d(t_k)$ is assumed to be normally distributed around zero, it can be considered as the process noise $w(t_k)$ with the covariance matrix Q [74]; while the measurement noise will be defined as $v(t_k)$ with the covariance matrix R. In this case, state $x(t_k)$ can be estimated using a Kalman filter/estimator. Since the rotational angle is the only available measurement, the output is defined as:

$$\begin{aligned} y(t_k) &= \begin{bmatrix} 1 & 0 & 0 & 0 \end{bmatrix} x(t_k) + v(t_k) \\ &= C_K x(t_k) + v(t_k) \end{aligned} \tag{2.34}$$

The Kalman filter/estimator is described by:

$$\begin{aligned} \hat{x}(t_k+T/t_k) &= \left[A_K - LC_K\right]\hat{x}(t_k/t_k-T) + Ly(t_k) \\ \hat{x}(t_k/t_k) &= \left[I - A_K^{-1}LC_K\right]\hat{x}(t_k/t_k-T) + A_K^{-1}Ly(t_k) \end{aligned} \tag{2.35}$$

where, $\hat{x}(t_k+T/t_k)$ and $\hat{x}(t_k/t_k-T)$ are the predicted states at time t_k and t_k-T, respectively. $\hat{x}(t_k/t_k)$ is the current state estimate at time t_k. The gain matrix L is determined by solving a matrix Riccati equation [75].

The ratio of Q and R will decide the performance of the Kalman estimator. A high value of Q/R will result in a faster but not so smooth state estimate. Since the magnitude of the process noise is much higher than measurement noise in the real world, a large

Q/R (about 10^8) is adopt to get a compromise between the smoothness and the response time of the Kalman estimator.

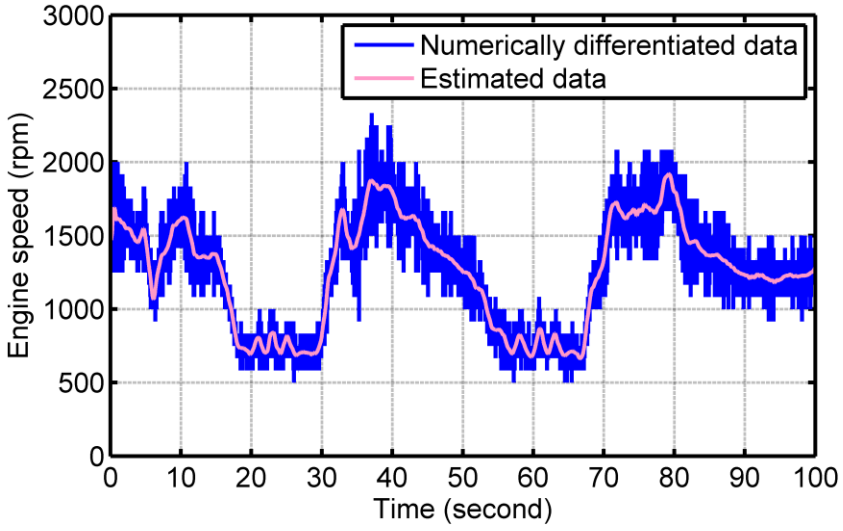

Fig. 2.12 Estimated and numerically differentiated engine speed

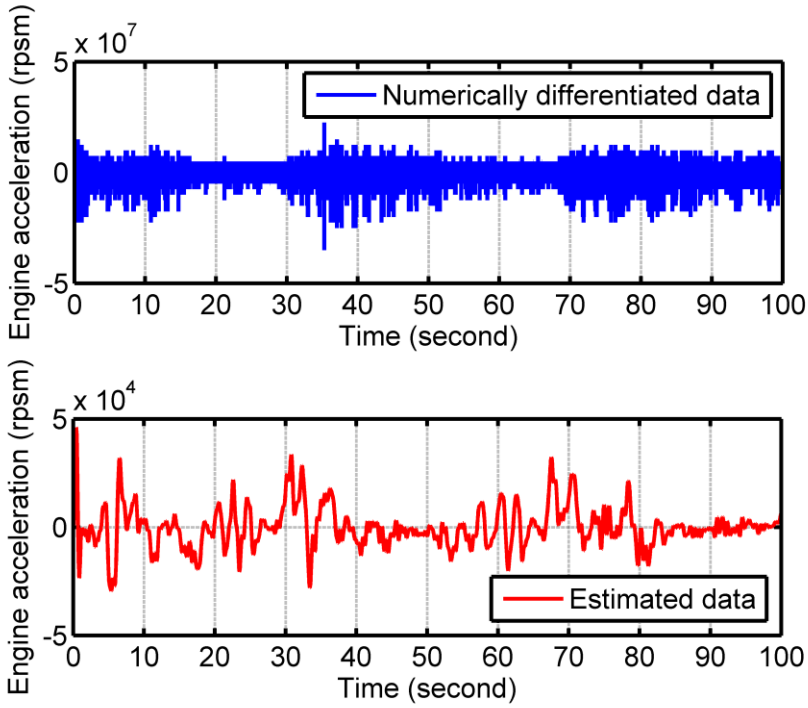

Fig. 2.13 Estimated and numerically differentiated engine acceleration

Fig. 2.12-2.13 show the estimated speed and acceleration signals using the above

Kalman estimator. Obviously, the estimated speed and acceleration signals become much smoother than the numerically differentiated data, which is critical for control implementation. Moreover, there is no significant time delay between the estimated data and the numerically differentiated data.

2.5.2 Nonlinear Model-based Inversion plus PID Control

At first, a nonlinear model-based feedforward plus PID controller is designed based on the nonlinear inversion [76]. With regards to the minimum-phase nonlinear system described in (2.32), the idea of the feedforward control is to make use of the dynamic model to calculate the desired state x_2 with the known reference speed $r(t)$ (i.e., the desired state x_1), and furthermore, to calculate the desired control input u with the calculated state x_2 and x_1. With respect to the controller implemented in this project, the necessary preconditions for feedforward control are satisfied, as follows:

1) $r(t)$ and its time derivatives $\dot{r}(t)$ and $\ddot{r}(t)$ are bounded for $t \geq 0$, and $\ddot{r}(t)$ is a piecewise continuous function of t;

2) $r(t)$, $\dot{r}(t)$ and $\ddot{r}(t)$ are all available.

By replacing the state x_1 with the reference $r(t)$ in the first equation of the dynamic model in (2.32), we get the desired state corresponding to the reference:

$$x_{2\_des} = \frac{\frac{2\pi}{D_M(t)}\left[T_E(t) - J_e\dot{r}(t)\right] - C_{da}\mu r(t) + \left(1 - C_f\right)P_{in}(t)}{1 + C_f} \tag{2.36}$$

Furthermore, substituting (2.36) into the second equation in (2.32) yields the desired input:

$$u = \frac{-\frac{V_{t2}}{\beta_e}\dot{x}_{2\_des} + \frac{D_M(t)}{2\pi}r(t) + C_{im}\left(P_{in}(t) - x_{2\_des}\right) - C_{em}x_{2\_des}}{C_d A_{HS}\sqrt{\frac{2}{\rho}x_{2\_des}}}$$

$$= \Big\{ \frac{2\pi V_{t2}}{\beta_e D_M(t)\left(1+C_f\right)}\left[J_e\ddot{r}(t) - \dot{T}_E(t)\right] - \frac{V_{t2}}{\beta_e}\frac{1-C_f}{1+C_f}\dot{P}_{in}(t)$$

$$+ \left[\frac{V_{t2}C_{da}\mu}{\beta_e\left(1+C_f\right)} - \frac{2\pi V_{t2}J_e\dot{D}_M(t)}{\beta_e {D_M}^2(t)\left(1+C_f\right)} + \frac{2\pi J_e\left(C_{im}+C_{em}\right)}{D_M(t)\left(1+C_f\right)}\right]\dot{r}(t)$$

$$+ \left[\frac{2\pi V_{t2}\dot{D}_M(t)}{\beta_e {D_M}^2(t)\left(1+C_f\right)} - \frac{2\pi\left(C_{im}+C_{em}\right)}{D_M(t)\left(1+C_f\right)}\right]T_E(t) + \left[\frac{D_M(t)}{2\pi} + \frac{C_{da}\mu\left(C_{im}+C_{em}\right)}{1+C_f}\right]r(t)$$

$$+ \left[C_{im} - \left(C_{im}+C_{em}\right)\frac{1-C_f}{1+C_f}\right]P_{in}(t) \Big\} / \left[C_d A_{HS}\sqrt{\frac{2}{\rho}x_{2\_des}}\right] \tag{2.37}$$

Equations (2.36)-(2.37) represent the feedforward control law. Since the actual system has unmodeled dynamics, and there also exist some input/output disturbances, a PID controller is added in parallel to reduce the tracking error both in transient and steady state, defined as:

$$C_{ff}(s) = K_{P\_ff}\left(1 + \frac{1}{T_{I\_ff}s} + T_{D\_ff}s\right) \tag{2.38}$$

Finally, the diagram of the nonlinear model-based inversion plus PID controller is shown in Fig. 2.14.

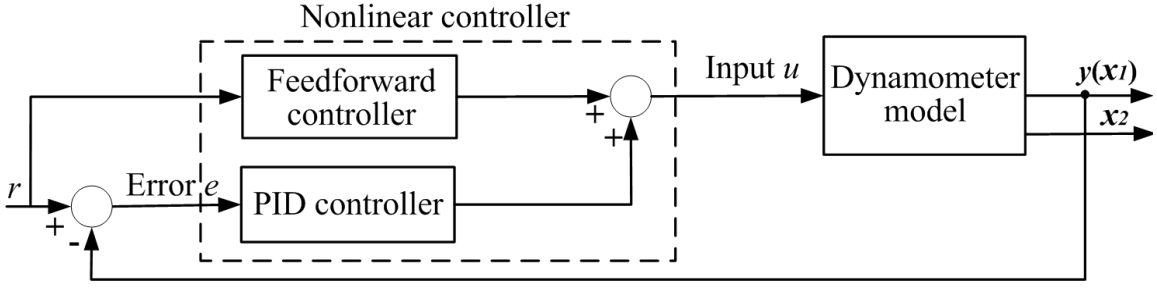

Fig. 2.14 Schematic diagram of the nonlinear model-based inversion plus PID controller

In the actual experiments, the PID parameters are tuned as: $K_{P\_ff} = 1.8\times10^{-6}$ *1/rpm*,

$T_{I\_ff} = 0.044\,sec$ and $T_{D\_ff} = 0.055\ sec.$

2.5.3 State Feedback (Feedback Linearization) Control

As an alternative to the nonlinear model-based inversion plus PID control, a state feedback control via feedback linearization is designed to make the nonlinear system more tractable and further, to use the well-developed linear control methodologies to realize the system stabilization and reference tracking.

1) Feedback Linearization

Unlike the Jacobian linearization (local linearization), the feedback linearization is a global representation of the original nonlinear model over the entire set of operating conditions [77]. This method has been applied to various applications involving nonlinear systems [78]-[80].

The main idea behind feedback linearization is to formulate a nonlinear state feedback law that in effect transforms the original nonlinear system into a linear form. At first, the nonlinear system in (2.32) will be rewritten in the form of,

$$\dot{x} = f(x) + g(x)u, \qquad y = h(x) \tag{2.39}$$

where

$$f(x) = \begin{pmatrix} -\dfrac{C_{da}\mu D_M(t)}{2\pi J_e}x_1 - \dfrac{\left(1+C_f\right)D_M(t)}{2\pi J_e}x_2 + \dfrac{T_E(t)}{J_e} + \dfrac{\left(1-C_f\right)D_M(t)}{2\pi J_e}P_{in}(t) \\ \dfrac{\beta_e D_M(t)}{2\pi V_{t2}}x_1 - \dfrac{\beta_e}{V_{t2}}\left(C_{im}+C_{em}\right)x_2 + \dfrac{\beta_e}{V_{t2}}C_{im}P_{in}\left(t\right) \end{pmatrix},$$

$$g(x) = \begin{pmatrix} 0 \\ -\dfrac{\beta_e C_d A_{HS}}{V_{t2}}\sqrt{\dfrac{2}{\rho}}\sqrt{x_2} \end{pmatrix},$$

$$h(x) = x_1 \tag{2.40}$$

In order to build the normal form, the coordinate transformation is given by the Lie algebra operation:

$$\phi(x) = \begin{pmatrix} \phi_1(x) & \phi_2(x) \end{pmatrix}^T = \begin{pmatrix} h(x) & L_f h(x) \end{pmatrix}^T \tag{2.41}$$

where the Lie algebra is defined by:

$$L_f h(x) = \begin{pmatrix} \dfrac{\partial h(x)}{\partial x_1} & \dfrac{\partial h(x)}{\partial x_2} \end{pmatrix} f(x) \tag{2.42}$$

In the new coordinates, the states are defined as:

$$\xi_i = \phi_i(x) = L_f^{\,i-1} h(x) \qquad 1 \le i \le 2 \tag{2.43}$$

Then, we can get the normal form as:

$$\xi_1 = h(x) = x_1$$

$$\xi_2 = \dot{\xi}_1 = L_f h(x) = -\frac{C_{da}\mu D_M(t)}{2\pi J_e} x_1 - \frac{\left(1+C_f\right) D_M(t)}{2\pi J_e} x_2 + \frac{T_E(t)}{J_e} + \frac{\left(1-C_f\right) D_M(t)}{2\pi J_e} P_{in}(t)$$

$$\begin{aligned}
\dot{\xi}_2 = {} & \frac{\left(1+C_f\right)\beta_e R_{HS} D_M(t)\sqrt{x_2}}{2\pi J_e V_{t2}} u + \frac{\left(1-C_f\right) D_M(t)}{2\pi J_e} \dot{P}_{in}(t) + \frac{\dot{T}_E(t)}{J_e} \\
& - \left(\frac{1+C_f}{2\pi J_e} x_2 - \frac{1-C_f}{2\pi J_e} P_{in}(t) + \frac{C_d \mu}{2\pi J_e} x_1 \right) \dot{D}_M(t) - \frac{C_{da}\mu D_M(t) T_E(t)}{2\pi {J_e}^2} \\
& - \frac{\left(1+C_f\right)\beta_e C_{im} D_M(t)}{2\pi J_e V_{t2}} \left(P_{in}(t) - x_2 \right) + \frac{{C_{da}}^2 \mu^2 D_M(t)^2}{4\pi^2 {J_e}^2} x_1 + \frac{\left(1+C_f\right) C_{da}\mu D_M(t)^2}{4\pi^2 {J_e}^2} x_2 \\
& - \frac{\left(1-C_f\right) C_{da}\mu D_M(t)^2}{4\pi^2 {J_e}^2} P_{in}(t) - \frac{\left(1+C_f\right)\beta_e D_M(t)^2}{4\pi^2 J_e V_{t2}} x_1 + \frac{\left(1+C_f\right)\beta_e C_{em} D_M(t)}{2\pi J_e V_{t2}} x_2 \\
= {} & a\left(x, T_E, D_M, P_{in}\right) + b\left(x_2, D_M\right) u
\end{aligned} \tag{2.44}$$

where $a\left(x, T_E, D_M, P_{in}\right)$ and $b\left(x_2, D_M\right)$ are both functions of the original states and time-varying parameters.

Now the transformed system can be represented as:

$$\begin{bmatrix} \dot{\xi}_1 \\ \dot{\xi}_2 \end{bmatrix} = \begin{bmatrix} 0 & 1 \\ 0 & 0 \end{bmatrix} \begin{bmatrix} \xi_1 \\ \xi_2 \end{bmatrix} + \begin{bmatrix} 0 \\ 1 \end{bmatrix} \left[a + bu \right], \qquad y = \begin{bmatrix} 1 & 0 \end{bmatrix} \begin{bmatrix} \xi_1 \\ \xi_2 \end{bmatrix}$$

Or,

$$\begin{aligned} \dot{\xi} &= A\xi + B\left(bu + a\right) \\ y &= C\xi \end{aligned} \tag{2.45}$$

2) State Feedback Controller for the Transformed System

With the reference tracking as the control target, it is more convenient to replace the transformed state ξ with the speed tracking error e, which is [81]:

$$\begin{aligned} e &= y - r = \xi_1 - r \\ \dot{e} &= \dot{\xi}_1 - \dot{r} \end{aligned} \tag{2.46}$$

where, r is the desired engine speed reference.

Then, the normal form in (2.45) can be further transformed to the tracking error dynamics, as follows:

$$\begin{bmatrix} \dot{e} \\ \ddot{e} \end{bmatrix} = \begin{bmatrix} 0 & 1 \\ 0 & 0 \end{bmatrix} \begin{bmatrix} e \\ \dot{e} \end{bmatrix} + \begin{bmatrix} 0 \\ 1 \end{bmatrix} \left[a + bu - \ddot{r} \right]$$

Or,

$$\begin{aligned} \dot{E} &= AE + B\left(bu + a - \ddot{r} \right) \\ &= AE + Bv \end{aligned} \tag{2.47}$$

where, the state $E = \begin{bmatrix} e & \dot{e} \end{bmatrix}^T$, and v is the control input for the transformed linear system.

With regard to the control target, the feedback controller should include a linearizing component $u = \frac{1}{b}\left(v - a + \ddot{r} \right)$ and a stabilizing component $v = -KE = -k_1 e - k_2 \dot{e}$. In other words, the state feedback control law is given by:

$$u = \frac{1}{b}\left(-k_1 e - k_2 \dot{e} - a + \ddot{r} \right) \tag{2.48}$$

where, k_1 and k_2 are both positive.

Substituting the state feedback control law into the tracking error dynamics in (2.47) yields:

$$\dot{E} = \left(A - BK \right) E \tag{2.49}$$

It is not difficult to show that $A - BK$ is Hurwitz when k_1 and k_2 are both positive. Then, the transformed system is globally asymptotically stable. Consequently, $y(t) \to r(t)$ as $t \to \infty$.

However, for practical applications, unmodeled dynamics are unavoidable. To further reduce the tracking error, the state feedback control law is modified as:

$$u = \frac{1}{b}\left(-k_1 e - k_2 \dot{e} - \lambda \int e - a + \ddot{r}\right) \tag{2.50}$$

where, λ is a positive gain. The integral term $-\lambda \int e$ is added into the nominal control law in (2.48) to reduce the tracking error e in steady state.

Finally, the diagram of the state-feedback-based nonlinear controller is shown in Fig. 2.15.

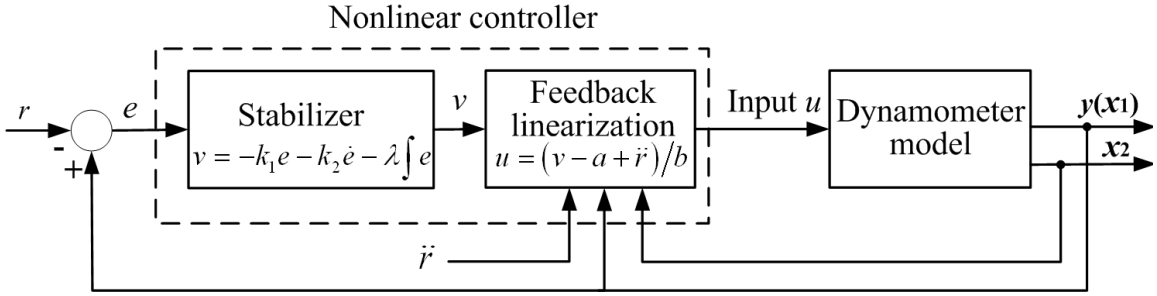

Fig.2.15 Schematic diagram of the nonlinear controller based on feedback linearization

In the actual experiments, the controller parameters are tuned as: $k_1 = 10050\, sec^{-2}$, $k_2 = 250.2\, sec^{-1}$ and $\lambda = 2000\, sec^{-3}$.

2.6 EXPERIMENTAL RESULTS

To demonstrate the transient capability of the dynamometer, extensive engine speed tracking experiments have been conducted. For the engine speed tracking experiments, the federal testing procedure (FTP), which is a typical engine operating speed trajectory for evaluating the automotive fuel economy and emissions, is used as the reference speed profile.

Test Case 1: Partial FTP driving cycle, gasoline engine

First, the speed tracking experiments for part of the FTP cycle are conducted based on the low-inertia gasoline engine. Fig. 2.16-2.18 show the engine speed tracking performance with the nonlinear model-based inversion plus PID controller. To compare the tracking performance in different operational modes, the dynamometer is running in the "dyno motoring" mode (where the dynamometer torque, but no combustion torque

drives the engine to track the desired speed) and "dyno loading" mode (where both the dynamometer torque and the combustion torque drive the engine; the dynamometer torque mainly serves as the loading torque), respectively. Correspondingly, Fig. 2.19-2.21 show the engine speed tracking performance with the state feedback (feedback linearization) controller in different operational modes.

Based on the experimental results in Fig. 2.18, it is clear that the nonlinear model-based inversion plus PID controller can achieve fast and precise reference profile tracking. In most cases, the magnitude of the tracking errors is less than 3% of the reference signal. The tracking errors in the "dyno loading" mode are obviously larger than those in the "dyno motoring" mode. That is mainly because in the former mode, the combustion torque from the engine is not as smooth as the torque from the hydraulic system, which brings in engine speed oscillations, and thus, extra tracking errors both in the transient and steady state. From Fig. 2.21, it can be concluded that the state feedback control via feedback linearization can also achieve fast and precise reference profile tracking (with less than 5% tracking errors). The characteristics of the transient tracking errors are very similar to the case with the nonlinear inversion controller.

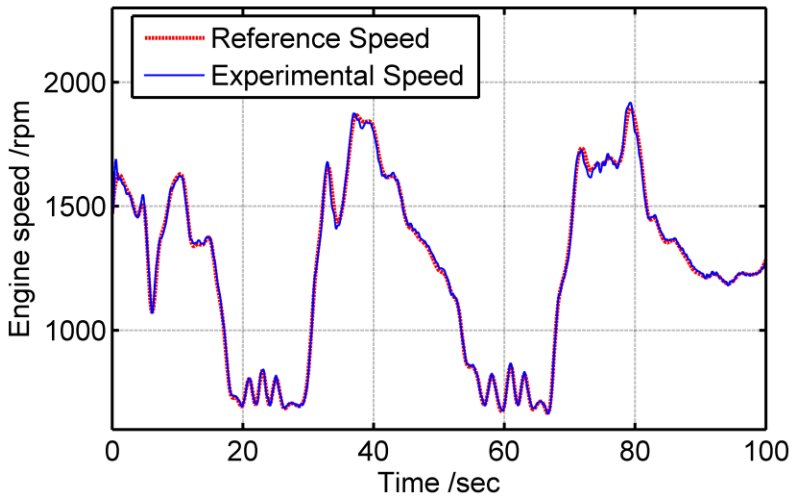

Fig. 2.16 Engine speed tracking trajectory (Nonlinear inversion plus PID controller, "dyno motoring" mode)

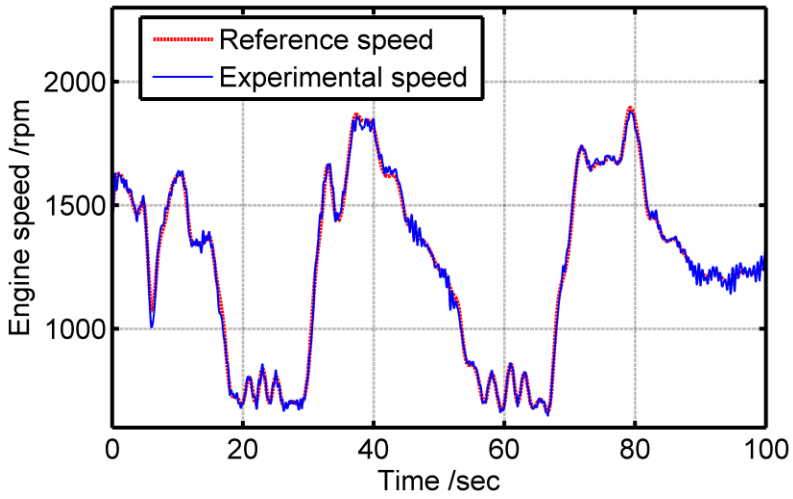

Fig. 2.17 Engine speed tracking trajectory (Nonlinear inversion plus PID controller, “dyno loading” mode)

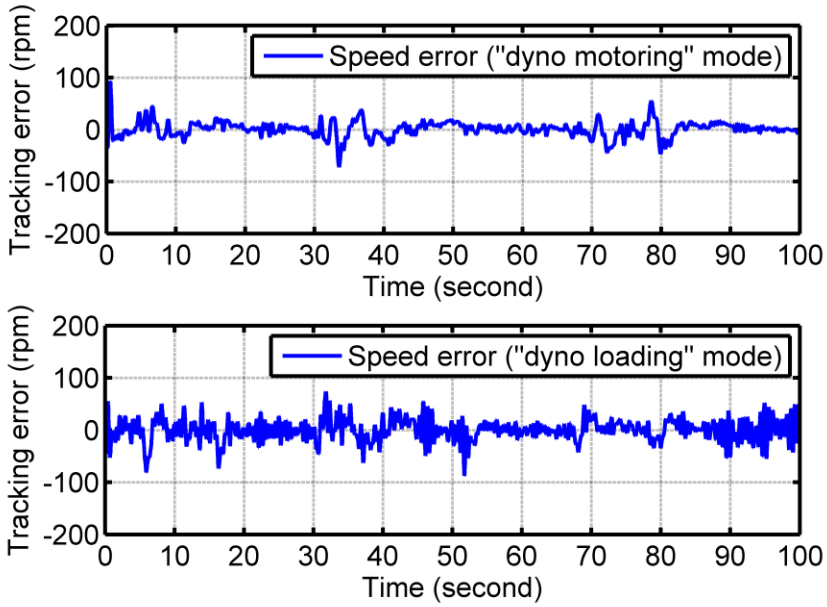

Fig. 2.18 Engine speed tracking error (Nonlinear inversion plus PID controller)

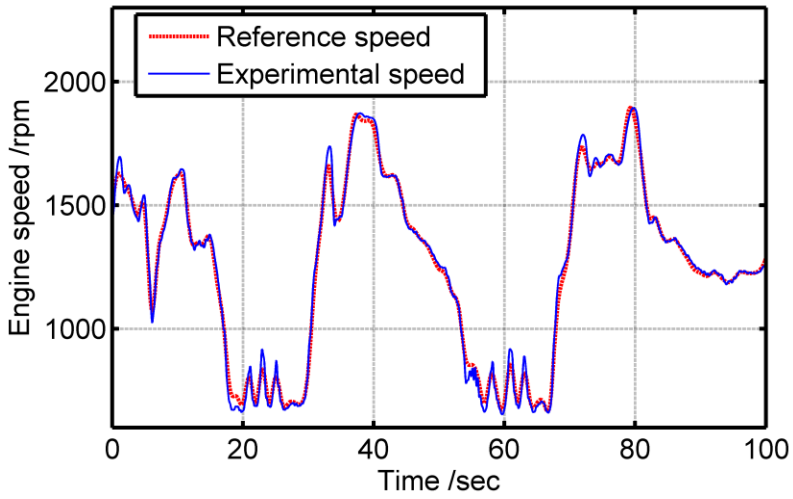

Fig. 2.19 Engine speed tracking trajectory (Feedback linearization controller, “dyno motoring” mode)

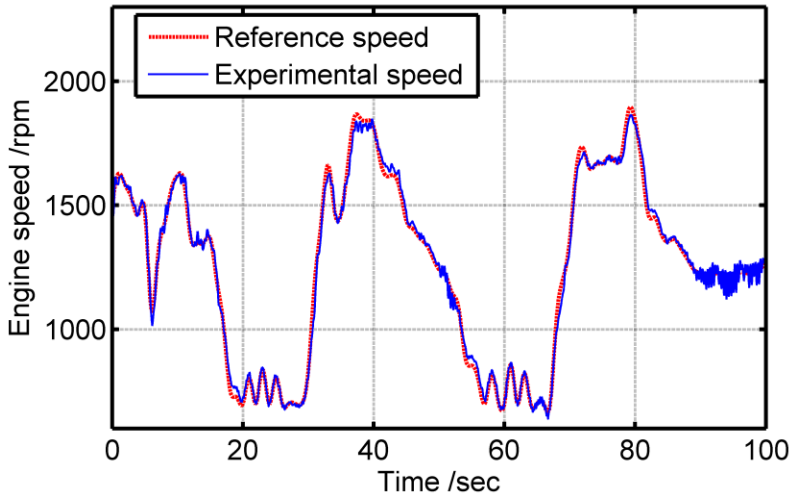

Fig. 2.20 Engine speed tracking trajectory (Feedback linearization controller, “dyno loading” mode)

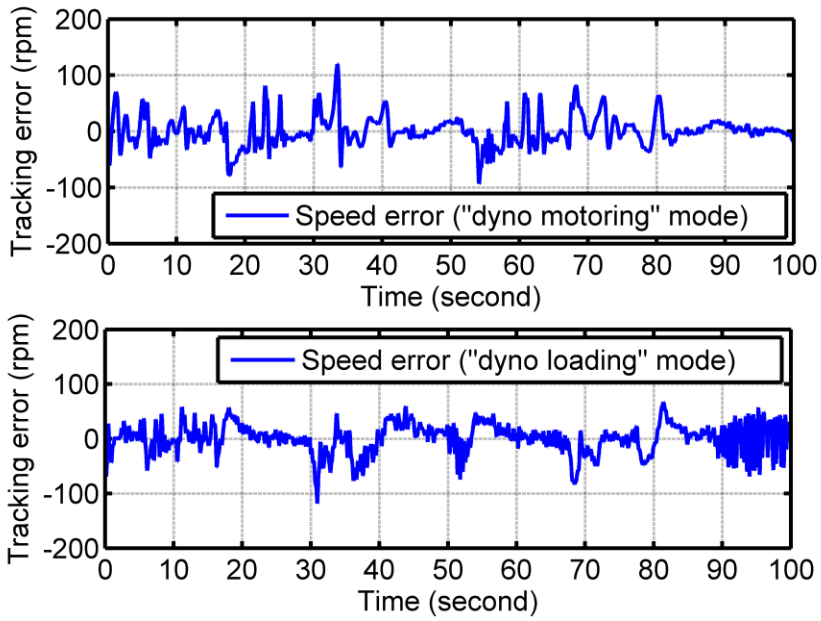

Fig. 2.21 Engine speed tracking error (Feedback linearization controller)

However, the transient tracking errors with the state feedback controller are slightly larger than those with the nonlinear model-based inversion plus PID controller. The main factor that results in this phenomenon is the unmodeled dynamics in the system. Even though there are not obvious advantages for the tracking control via feedback linearization from the current experimental results, the effort on this area is still significant and promising. The introduction of the feedback linearization provides opportunities to apply the well-developed linear and robust control methodologies, so as to provide the greater possibility to further improve the tracking accuracy in both transient and steady states.

Test Case 2: Complete FTP driving cycle, diesel engine

With a high-inertia diesel engine, the speed tracking experiments along a complete FTP cycle are also conducted, with the real-time fuel consumption measurement. The characteristics of the tracking performance are similar to the case with gasoline engine. Thus, only the tracking performance and fuel consumption with the nonlinear inversion based control at “dyno loading” mode are shown in Fig. 2.22-2.24.

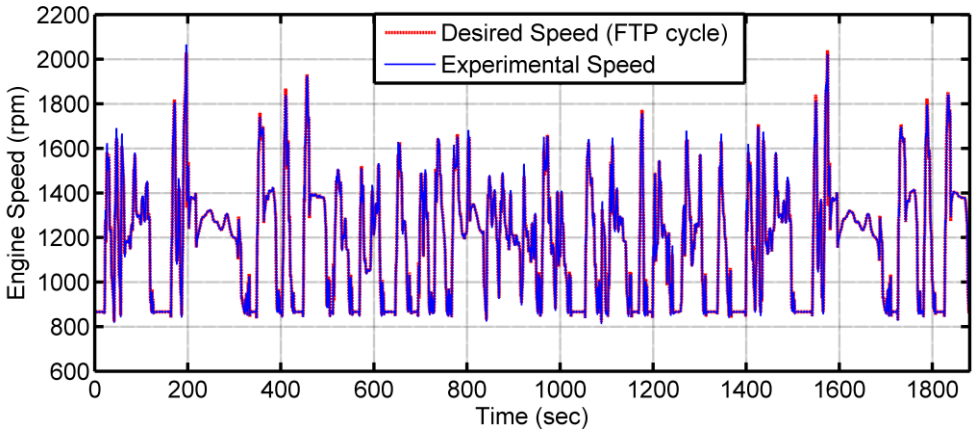

Fig. 2.22 Engine speed tracking trajectory for the complete FTP cycle

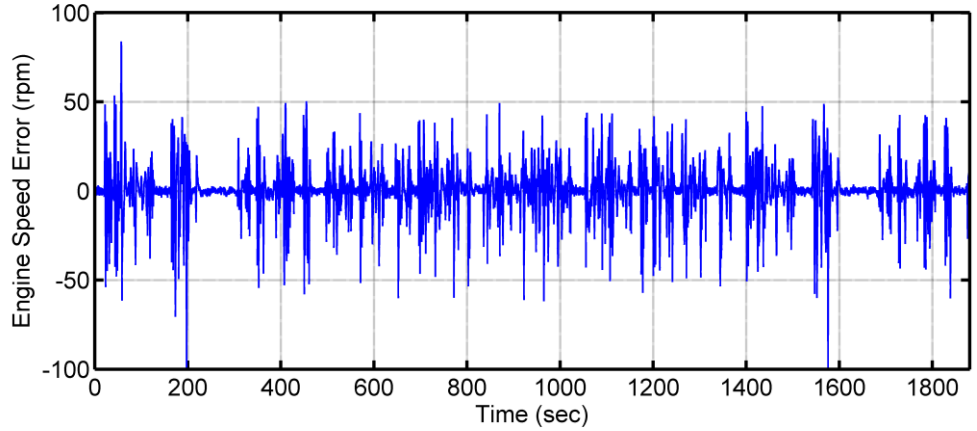

Fig. 2.23 Engine speed tracking errors for the complete FTP cycle

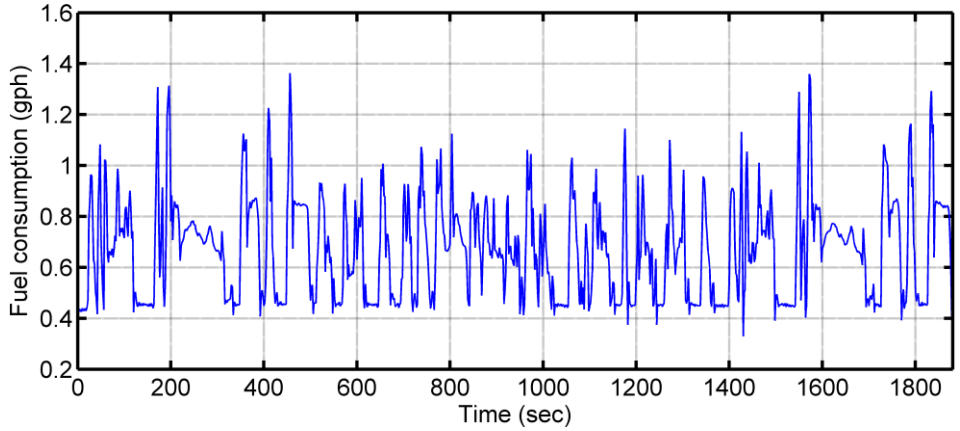

Fig. 2.24 Engine fuel consumption trajectory for the complete FTP cycle

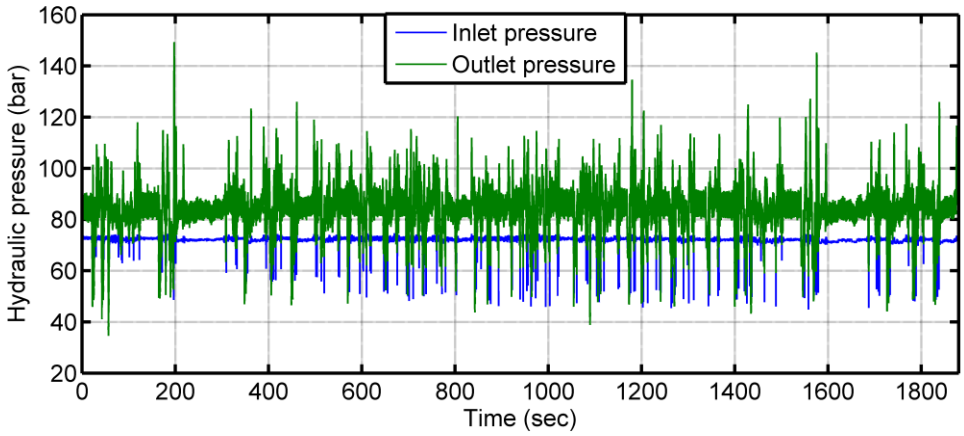

Fig. 2.25 Hydraulic pressure trajectories for the complete FTP cycle

2.7. CONCLUSION

This chapter presents the design, modeling, control and experimental validation of a transient hydrostatic dynamometer. A 9^{th}-order nonlinear model is constructed, and the system parameters are identified and validated by experiments. Based on its unique architecture, the dynamometer system is decoupled into two subsystems to simplify the control design. Model-based nonlinear controllers and a Kalman filter based observer are designed to enable the transient capability of the dynamometer. The experimental results demonstrate that the nonlinear model-based inversion plus PID controller and the state feedback controller via feedback linearization are capable of fast and precise tracking of the desired engine speed profile.

Chapter 3

Hybrid Powertrain Research Platform Architecture Design and Hybrid Powertrain Control

3.1. RESEARCH OBJECTIVE

To greatly expedite the investigation of hybrid powertrain control, a rapid prototyping hybrid powertrain research platform based on a transient hydrostatic dynamometer is proposed in this thesis, as shown in Fig. 3.1. The combustion dynamics of the engine is too complicated to be modeled with a low-order approximation; to the contrary, the dynamics of the alternative power sources, hybrid transmission, driveline and vehicle load can be described with well-developed models. Thus, this research platform employs a high-bandwidth hydrostatic dynamometer to emulate the dynamic behaviors of the hybrid power sources (e.g., electric motor/generator) and vehicle loads, and interact with a multi-cylinder IC engine in real-time. In this platform, the engine fuel efficiency and emissions can be measured in real-time and hence, the associated benefits and limitations of various hybrid powertrain architectures and control methodologies can be precisely quantified and systematically investigated by means of experiments, without building the complete physical hybrid powertrain system.

Hardware-in-the-loop (HIL) testing has been applied in the study of both the traditional or advanced powertrain. In recent years, some systematic research efforts on the engine-in-the-loop testing for a parallel hybrid powertrain system using an AC electric dynamometer have been reported [82], for evaluating hybrid propulsion concepts and transient emissions. For this work, with a high-bandwidth hydrostatic dynamometer

as the torque tool, our research is targeted at experimentally investigating the torque-control based hybrid powertrain operation, for a typical power-split hybrid vehicle. However, to realize the targeted hybrid powertrain dynamics emulation is actually very challenging, since it combines a series of complex dynamic systems (engine, dynamometer and simulated alternative power sources, hybrid transmission, etc.) which brings in great difficulty to realize the precise system control, especially for the engine torque or engine loading torque control. Also, the two degree of freedom of a power-split hybrid system further increases the complexity of the powertrain control.

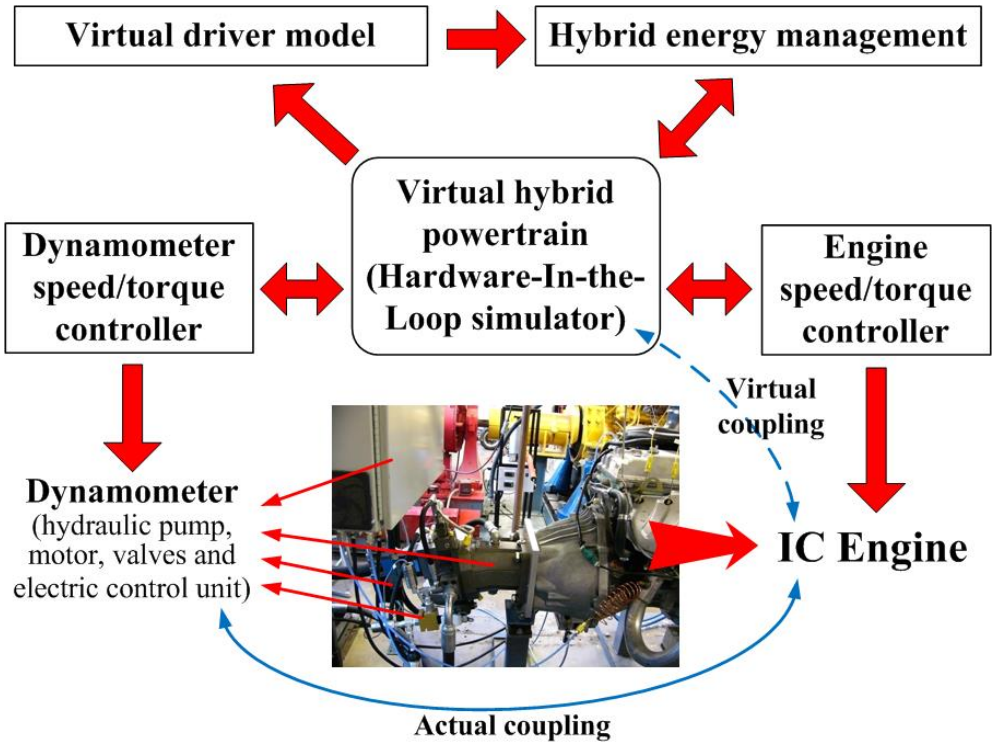

Fig. 3.1 Structure diagram of the research platform

In order to overcome the above technical challenges and fully realize the hybrid powertrain emulation based on the proposed rapid prototyping research platform, Section 3.2 presents the design and function analysis of the control architecture of the research platform. With the power-split hybrid architecture, in Section 3.3, a Toyota electric hybrid vehicle is modeled as an emulating target for the HIL simulator. Section 3.4 presents the control design for every level of the research platform. At first, an adaptive

driver model is designed to manipulate the required power to match the desired vehicle speed. Then, the controllers for three-level system are designed, including a high-level controller for hybrid powertrain energy management, a middle-level controller for engine torque control, hybrid (electric) torques control and hybrid transmission/driveline HIL simulation, and a low-level controller for dynamometer torque control. Correspondingly, in Section 3.5 the experimental results show that this hybrid powertrain rapid prototyping and control system is capable to emulate the dynamics of the targeted hybrid powertrain system for both the partial and full driving cycle. Then, Section 3.6 and Section 3.7 analyze the dynamic interactions of the whole closed-loop system and on this basis, analytically validate the effectiveness of the SISO middle level controller design and more importantly, unveil the dynamic issues connected with the current middle level controller design under transients. To solve these dynamic issues and better coordinate the transient engine speed and torque tracking, Section 3.8 presents a new multivariable controller for the redesign of the middle-level control system, to reach a good balance of transient engine operation (speed/torque) control. Finally, in Section 3.9, the experimental results demonstrate the improvements on transient engine operation control of the multivariable mid-level controllers compared with the SISO mid-level control.

3.2. ARCHITECTURE DESIGN

The architecture of the overall hybrid powertrain rapid prototyping and research platform is shown in Fig. 3.2. With the hydrostatic dynamometer and engine (in red in Fig. 3.2) as the control target, the hybrid powertrain control and simulation system (in black in Fig.3.2) is the core part of the research platform. It is built as three-level closed-loop control architecture.

Given an desired vehicle speed trajectory, the driver model will produce a corresponding powertrain output power as the driver's control action for the vehicle; then, in the high level system, with this desired power as the reference, the hybrid powertrain energy management system will generate an optimal engine operating trajectory based on the real-time fuel consumption and the SOC (state of charge) of the energy storage unit. This optimized operating trajectory is further used as the reference

for the mid-level control.

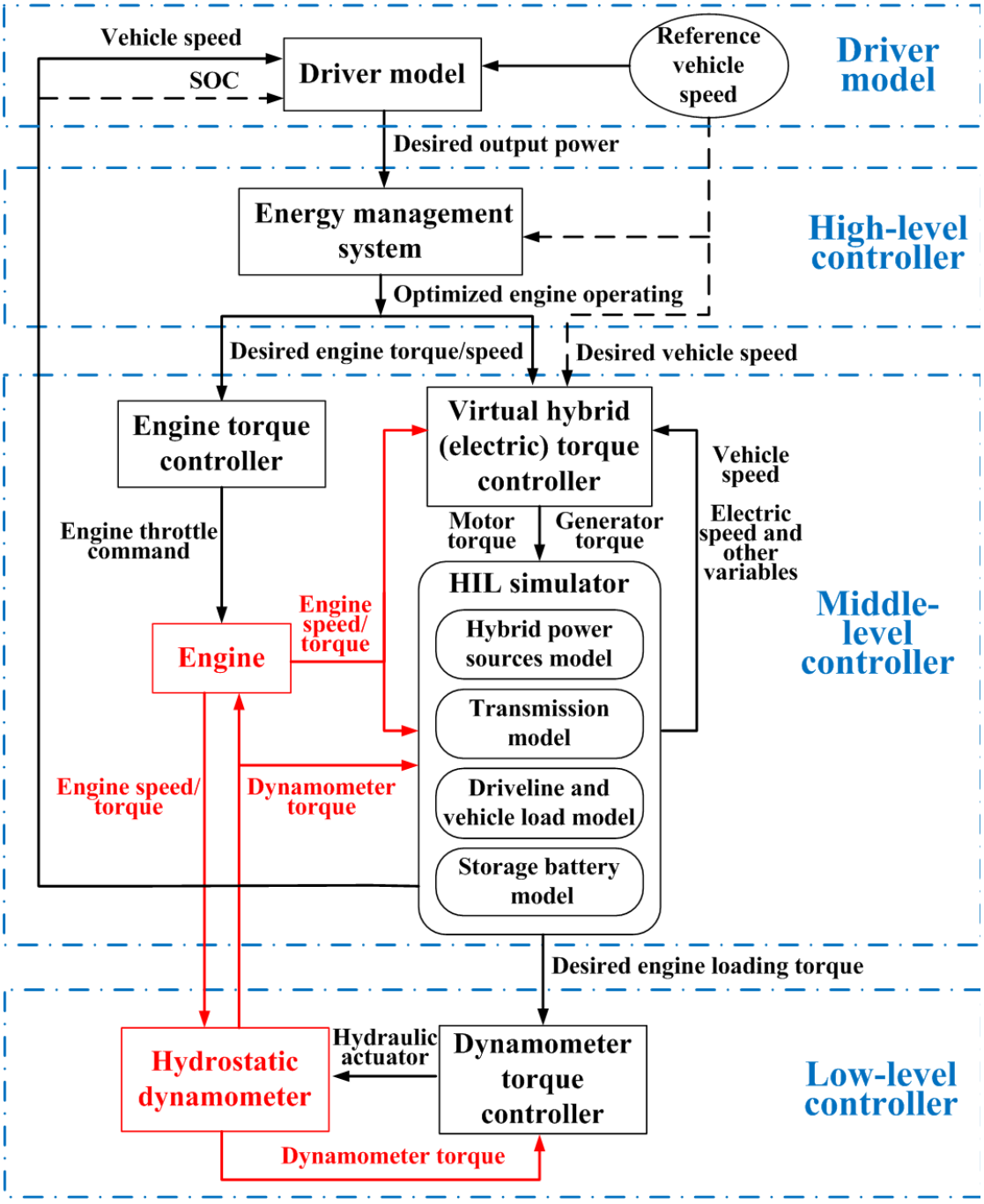

Fig. 3.2 Architecture of the rapid prototyping hybrid powertrain research platform

In the middle level system, given the optimized engine torque and speed as the reference, the virtual hybrid torque controller manipulates the virtual hybrid torques

(electric generator/motor torques) to drive the engine to operate along the optimized torque and speed trajectory. Then, the virtual electric machine controller and engine throttle controller will control both the hybrid power sources (electric machines) and engine to produce the desired torques. Meanwhile, the hybrid transmission/driveline HIL simulator is simulating the target hybrid system using the well-developed dynamic models, to produce the high-fidelity dynamic responses (primarily, the engine loading torque) like a real-world powertrain system.

In the low level system, given the virtual engine loading torque produced by the HIL simulator as the reference, the dynamometer torque controller will control the dynamometer to emulate the desired engine loading torque, so as to drive the engine-dynamometer system to track the optimized engine torque and speed profiles. With the combination of the well-control engine torque and engine loading (dynamometer) torque, the engine will operate at the virtual hybrid modes. Consequently, measurement and analysis of the fuel consumptions and emissions will give an accurate evaluation for the performance of the proposed hybrid architecture or energy management strategy.

3.3 SYSTEM MODELING

To ensure the dynamics running in the HIL testing can be viewed as a good substitute of the real hybrid powertrain system, precise dynamic modeling for the hybrid powertrain systems is crucial. Among the existing hybrid vehicle prototypes, the Toyota THS system [6], [83]-[84], is used as a typical power-split electric hybrid configuration, as shown in Fig. 3.3.

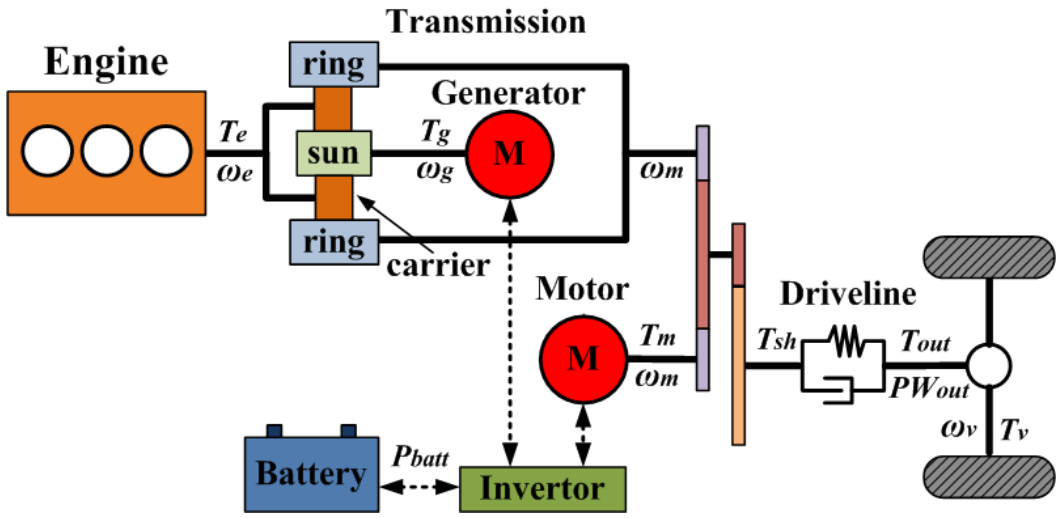

Fig. 3.3 Architecture of the power-split powertrain system

3.3.1 Power-split Transmission Dynamics

The dynamics of the power split transmission is the most important part in the hybrid powertrain, where the planetary gear set is applied as the core mechanism. The dynamic models for the power-split transmission and driveline have been well-studied, which can be given by:

$$J_{ec}\dot{\omega}_e = T_e - T_c \tag{3.1}$$

$$J_{gs}\dot{\omega}_g = T_s - T_g \tag{3.2}$$

$$J_{mr}\dot{\omega}_m = T_r + T_m - \frac{T_{sh}}{K_{ratio}} \tag{3.3}$$

where, J_{ec} is the coupled moment of inertia of engine and carrier gear, J_{gs} is the coupled moment of inertia of generator and sun gear, J_{mr} is the coupled moment of inertia of motor and ring gear. T_c, T_s and T_r are the carrier torque, sun gear torque, and ring gear torque, respectively. T_e is the engine torque, T_m is the motor torque, T_g is the generator toque and T_{sh} is the driveline shaft torque. ω_e, ω_g and ω_m are the engine speed, generator speed and motor speed, respectively. K_{ratio} is the gear ratio between the motor and the driveline shaft.

Besides the dynamic equations, based on the mechanical constraints inside the planetary gear set, the relationships between the speeds and torques are given by:

$$\omega_g S + \omega_m R = \omega_e \left(R + S\right) \tag{3.4}$$

Or,
$$\dot{\omega}_g S + \dot{\omega}_m R = \dot{\omega}_e \left(R + S\right) \tag{3.5}$$

$$T_s + T_r = T_c \tag{3.6}$$

$$T_s R = T_r S \tag{3.7}$$

where R and S are the radii of the ring gear and sun gear.

3.3.2 Driveline Dynamics

The vehicle driveline is closely connected with the shaft of the electric motor and ring gear. In order to fully describe the effect of the spring and damper in driveline to the driveline dynamics, the dynamic equations are represented by:

$$J_{sh}\dot{\omega}_{sh} = T_{sh} - T_{out} \tag{3.8}$$

$$f_{sh}\Delta\dot{\theta} = -K_s\Delta\theta + T_{out} \tag{3.9}$$

$$J_v\dot{\omega}_v = T_{out} - T_v \tag{3.10}$$

where,

$$\omega_{sh} = \frac{\omega_m}{K_{ratio}}$$

$$\Delta\dot{\theta} = \omega_{sh} - \omega_v$$

$$T_v = f_{tire}M_v g\cos\left(\phi_{road}\right)R_{tire} + 0.5\rho_a C_{drag}A_f\omega_v{}^2 R_{tire}{}^3 + M_v g\sin\left(\phi_{road}\right)R_{tire}$$

$$J_v = M_v R_{tire}{}^2$$

ω_{sh} is the driveline shaft speed, ω_v is the vehicle speed, and $\Delta\theta$ is the rotary angle of the driveline shaft. T_{sh} is the driveline shaft torque, T_{out} is the output torque to drive the vehicle, and T_v is the overall load torque of the vehicle. J_{sh} is the moment of inertia of the driveline and J_v is the moment of inertia of the whole vehicle. K_s and f_{sh} are spring constant and damping coefficient of the driveline shaft. f_{tire} is rolling friction coefficient

of the tires, M_v is the vehicle mass, g is the acceleration of gravity, ϕ_{road} is the grade angle of the road, R_{tire} is the tire radius, ρ_a is the mass density of the air, C_{drag} is the drag coefficient, and A_f is the vehicle frontal area.

Since the driveline shaft speed ω_{sh} is proportional to the motor speed ω_m, they are actually the same state variable. Thus, there is only one independent state ω_v in the driveline dynamics.

3.3.3 Generator/motor Dynamics

As the main alternative power sources in electric hybrid, the electric generator and motor are introduced to realize fuel efficiency improving, energy regeneration and electric-assistant or electric-only launching. The PM (permanent magnet) AC synchronous machines are usually employed for its high efficiency, high power density and high reliability. The dynamics of the PMAC machines are given as follows [85]-[87]:

$$L_d \dot{I}_d = U_d - R_s I_d + n_p L_q \omega_m I_q \tag{3.11}$$

$$L_q \dot{I}_q = U_q - R_s I_q - n_p L_d \omega_m I_d - \psi_m n_p \omega_m \tag{3.12}$$

$$T_m = \frac{3}{2} n_p \left[\psi_m I_q + \left(L_d - L_q \right) I_d I_q \right] \tag{3.13}$$

where, U_d and U_q are the direct and quadrature axis voltages respectively, which are used as the control inputs for the electric torques control. I_d and I_q are the direct and quadrature axis currents, respectively. L_d and L_q are the direct and quadrature axis inductances, respectively. ω_m is rotary speed of the electric motor (or generator). R_s is the series phase resistance, n_p is the numbers of pole pairs, and ψ_m is the permanent electric machine flux.

The power limiters for both motor and generator are also used to guarantee that their torque/speed profiles do not conflict with their electric constraints (maximum electric power).

3.3.4 Storage Battery Dynamics

The electric power to/from the storage battery is the product of the power conversion by the motor and generator. Hence, the battery power is calculated as follows:

$$P_{batt} = P_g + P_m = -T_g \omega_g \eta_g^{\,k1} + T_m \omega_m \eta_m^{\,k2} \tag{3.14}$$

where P_{batt} is the gross power that the battery transfers to the powertrain system; in other words, when P_{batt} is positive, the battery works in the "discharging" mode; or, the battery is charging. P_g and P_m are the electric power transferred from the battery to the generator and motor, respectively. η_g and η_m are the power conversion efficiency of the generator and motor, respectively. The exponents k_1 and k_2 are defined subject to the charge/discharge states of battery: $k_1 = 1$ when $T_g \omega_g$ is positive and $k_1 = -1$ when $T_g \omega_g$ is negative; $k_2 = -1$ when $T_m \omega_m$ is positive, and $k_2 = 1$ when $T_m \omega_m$ is negative.

Furthermore, the dynamics of the SOC (state of charge, in percent) of the storage battery is defined to reflect the storage energy status:

$$P_{batt} = V_{batt} I_{batt} - I_{batt}^{\,2} R_{batt} \tag{3.15}$$

$$\dot{SOC} = -\frac{I_{batt}}{Q_{batt}} \tag{3.16}$$

where, I_{batt} is the battery current, Q_{batt} is the rated capacity of the battery, R_{batt} is the internal resistance of the battery and V_{batt} is the open-loop voltage of the battery.

Substituting (3.14)-(3.15) into (3.16) yields the straight description of the SOC dynamics:

$$\dot{SOC} = -\frac{V_{batt}}{2Q_{batt}R_{batt}} + \frac{\sqrt{V_{batt}^{\,2} - 4\left[-T_g \omega_g \eta_g^{\,k1} + T_m \omega_m \eta_m^{\,k2}\right] R_{batt}}}{2Q_{batt}R_{batt}} \tag{3.17}$$

3.4 CONTROL DESIGN

Targeted at emulating the real-world hybrid powertrain operation, the control system is designed to generate and experimentally realize the optimal engine operating profile at

hybrid operation modes, under realistic driving scenarios.

3.4.1 Adaptive Driver Model Design

In the real-life driving scenarios, the desired vehicle speed is only concerned with the mind of the driver, and hence, cannot be directly accessed by the powertrain control system. Thus, the significance of the driver model design is to transfer the driver's desired vehicle speed to the command of the powertrain output power which is described by the commands on the accelerator/brake pedal. Given a specific vehicle speed trajectory, the driver model should not only mimic the real-life mechanism of the human behavior, but also be competent to precisely track the reference vehicle speed just like a real experienced driver, which will guarantee the accurate driving cycle testing on the hybrid powertrain research platform. Some PID based driver models have been conducted in [45],[82]. To improve the tracking accuracy without losing the similarity of the real human behavior, an adaptive driver model is built.

From (3.10), The vehicle driveline dynamics is given by:

$$J_v\dot{\omega}_v = \frac{PW_{out}}{\omega_v} - f_{tire}M_v g R_{tire} - 0.5\rho_a C_{drag} A_f \omega_v{}^2 R_{tire}{}^3 \tag{3.18}$$

where PW_{out} is the desired powertrain output power. Here we assume the road grade $\phi_{road} = 0$.

Further, (3.18) can be transformed to the error dynamics with the speed error $e_v = \omega_{v\_des} - \omega_v$, given by:

$$J_v\dot{e}_v = -\frac{PW_{out}}{\omega_v} + \sigma_1\dot{\omega}_{v\_des} + \sigma_2 + \sigma_3\omega_v{}^2 \tag{3.19}$$

where, $\sigma_1 = J_v$, $\sigma_2 = f_{tire}M_v g R_{tire}$, $\sigma_3 = 0.5\rho_a C_{drag} A_{tire} R_{tire}{}^3$

Since the variables e_v, ω_v and $\dot{\omega}_{v\_des}$ can be captured by the driver in real time, it is reasonable for the driver to give out the pedal commands with the corresponding power output:

$$PW_{out} = K_1 e_v \omega_v + \hat{\sigma}_1\dot{\omega}_{v\_des}\omega_v + \hat{\sigma}_2\omega_v + \hat{\sigma}_3\omega_v{}^3 \tag{3.20}$$

where, $\hat{\sigma}_1$, $\hat{\sigma}_2$ and $\hat{\sigma}_3$ are the driver's estimates for σ_1, σ_2 and σ_3. K_1 is a positive gain.

Substituting (3.20) into (3.19) yields:

$$J_v \dot{e}_v = -K_1 e_v + \tilde{\sigma}_1 \dot{\omega}_{v\_des} + \tilde{\sigma}_2 + \tilde{\sigma}_3 \omega_v^2 \tag{3.21}$$

where, $\tilde{\sigma}_1 = \sigma_1 - \hat{\sigma}_1$, $\tilde{\sigma}_2 = \sigma_2 - \hat{\sigma}_2$, $\tilde{\sigma}_3 = \sigma_3 - \hat{\sigma}_3$.

To enable the stability of the error dynamics, the adaptive parameter tuning dynamics are designed. Firstly, for nonlinear system in (3.21), a composite Lyapunov function is given by:

$$V(e_v, \sigma) = \frac{1}{2} J_v e_v^2 + \frac{1}{2} K_2 \tilde{\sigma}_1^2 + \frac{1}{2} K_3 \tilde{\sigma}_2^2 + \frac{1}{2} K_4 \tilde{\sigma}_4^2 \tag{3.22}$$

where K_2, K_3 and K_4 are all positive gains.

With the adaptive parameter error dynamics,

$$\dot{\hat{\sigma}}_1 = -\dot{\tilde{\sigma}}_1 = \frac{\dot{\omega}_{v\_des} e_v}{K_2} \qquad \dot{\hat{\sigma}}_2 = -\dot{\tilde{\sigma}}_2 = \frac{e_v}{K_3} \qquad \dot{\hat{\sigma}}_3 = -\dot{\tilde{\sigma}}_3 = \frac{\omega_v^2 e_v}{K_4} \tag{3.23}$$

The asymptotic stability of the nonlinear system in (3.21) is guaranteed due to the Barbalat's lemma. Thus, the vehicle speed error is eliminated by the adaptive driver dynamics. Fig. 3.4 shows the performance of the designed driver model.

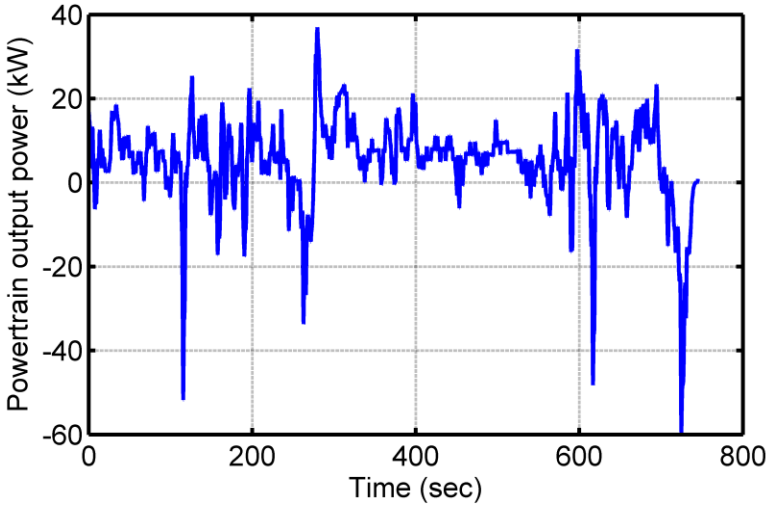

(a) Estimated powertrain output power

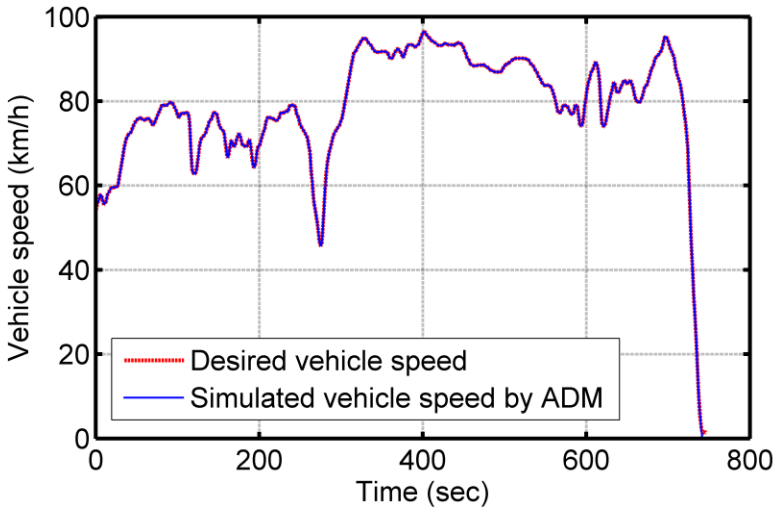

(b) Estimated vehicle speed

Fig. 3.4 Estimated powertrain output power and vehicle speed based on the adaptive driver model

3.4.2 High-level Control: Experiment-oriented DP-based Energy Optimization Strategy

As a typical optimization tool in the hybrid powertrain control, dynamic programming [12],[42], is utilized as the energy management strategy and specially designed for experiments.

Assumed that the driver model can track the vehicle speed very well, the dynamic equation describing the vehicle speed dynamics can be eliminated by replacing the state ω_v with the desired ω_{v_des} and replacing the input T_e with the output power PW_{out} and other inputs T_g and T_m [12]. Then, the remaining second-order system (engine speed dynamics and storage battery dynamics) with states ω_e and SOC, and inputs T_g and T_m, will be used as the system dynamics for DP computation.

The cost function used in the DP based energy management strategy is designed to minimize the fuel consumption and keep the SOC sustained in a limited bound, given by:

$$J = \sum_{k=0}^{N-1} \left\{ FC(k) + f_{\omega e}\left[\omega_e(k+1) - \omega_e(k)\right]^2 + f_{Te}\left[T_e(k+1) - T_e(k)\right]^2 \right\} + f_{soc}\left[SOC(N) - SOC(N)_{des}\right]^2 - m_{soc}\left[SOC(N) - SOC(N)_{des}\right] \quad (3.24)$$

where FC is the fuel consumption in a single sampling step, $SOC(N)$ and $SOC(N)_{des}$ are the actual and desired battery SOC at the final step, f_{soc} is the SOC sustaining factor and m_{soc} is the SOC variation compensation factor. In experiments, it is too challenging to directly apply the conventional DP optimized results because of the drastically oscillating speed and torque produced by DP. To meet the experimental requirement, an engine speed oscillation penalty factor $f_{\omega e}$ and an engine torque oscillation penalty factor f_{Te} are used to smooth the optimized operating trajectories.

3.4.3 Mid-level Control: Virtual Hybrid Torque Control and Electric Machine Control

In the mid-level system, the desired vehicle speed ω_v (or correspondingly, PW_{out}) and optimized engine operation T_e and ω_e will be tracked by controlling the commands for engine throttle and virtual hybrid torques T_{m_cmd} and T_{g_cmd}. Furthermore, to realize the torque commands T_{m_cmd} and T_{g_cmd}, the servo control for the electric machines should be achieved. Hence, the mid-level control system can be divided into two subsystems:

(1) Virtual Hybrid Torque Control

The principal objective for the mid-level control is to simultaneously realize the desired ω_v, T_e and ω_e, which depends on the precise torque control of the electric machines. In high-level control, the DP optimization strategy has generated the optimized trajectories T_{m_des} and T_{g_des}, which theoretically ensure the desired hybrid powertrain operation. However, experimental results show that the pure open-loop control using the optimized inputs T_{m_des} and T_{g_des} cannot guarantee the stability of the whole system. It can be attributed to the fact that the optimization is actually built on some simplified dynamic models (without the engine combustion dynamics) in the discrete time.

Therefore, it is significant to redesign the control of T_m and T_g to ensure both the system stability and precise tracking of the other important system variables.

Assumed that the engine throttle has been well controlled based on the engine map, the engine torque T_e are actually coupled with the engine speed ω_e. Thus, the control objective is formulated into a two-inputs (T_m, T_g), two-outputs (ω_v, ω_e) control problem. Here, a hybrid torque control strategy is designed to transfer it into two single-input, single-output controls: it utilizes the generator as a speed compensator to track the engine speed ω_e (and indirectly, T_e), to realize the optimal engine operation; simultaneously, the motor is used as a power compensator to track the power PW_{out} (equivalently, ω_v), to realize the desired vehicle operation [12],[38],[88].

The generator torque (engine speed) control is critical to realize the control target of the mid-level system. A torque/speed feedback control law plus pole placement is designed to address this issue. At first, for the planetary gear set, the transmission dynamics are given by:

$$\begin{aligned} J_{ec}\dot{\omega}_e &= T_e - T_c, \\ J_{gs}\dot{\omega}_g &= T_s - T_g, \\ T_s(R+S) &= T_c S \end{aligned} \tag{3.25}$$

If the high-bandwidth generator inertia dynamics is neglected compared with the low-bandwidth engine inertia dynamics, then the transmission dynamics can be rewritten as:

$$J_{ec}\dot{\omega}_e = T_e - \frac{R+S}{S}T_g \tag{3.26}$$

where the engine torque is a mapping of the engine speed and throttle opening, so that it cannot be directly controlled but can be measured. Thus, a torque/speed feedback control is given by:

$$T_{g\_cmd} = \frac{S}{R+S}T_{e\_des} - \frac{S}{R+S}J_{ec}\dot{\omega}_{e\_des} + K_p\left(\omega_e - \omega_{e\_des}\right) + K_I\int\left(\omega_e - \omega_{e\_des}\right)dt \tag{3.27}$$

where, K_p and K_I are both positive gains.

Substituting (3.27) into (3.26) yields:

$$J_{ec}\dot{e}_{\omega_e} + \frac{R+S}{S}K_p e_{\omega_e} + \frac{R+S}{S}K_I \int e_{\omega_e} dt = 0 \tag{3.28}$$

where, $e_{\omega_e} = \omega_e - \omega_{e\_des}$. In experiments, there always exist some errors for the torque control and hence, a disturbance term $dis(t)$ is introduced into (3.28):

$$J_{ec}\dot{e}_{\omega_e} + \frac{R+S}{S}K_p e_{\omega_e} + \frac{R+S}{S}K_I \int e_{\omega_e} dt = dis(t) \tag{3.29}$$

Or, in the *s*-domain (*s* is the Laplace operator),

$$\frac{E_{\omega_e}(s)}{Dis(s)} = \frac{s}{J_{ec}s^2 + \frac{R+S}{S}K_p s + \frac{R+S}{S}K_I} \tag{3.30}$$

It is obvious that this control law can eliminate the constant system disturbance or perturbation for engine speed control. Tuning of the gains K_P and K_I will produce a good pole placement for improving the system stability.

On this basis, with the torque command T_{g_cmd} in (3.27) as a time-varying parameter, the motor torque T_m can be used to compensate the powertrain output power, given by:

$$T_{m\_cmd} = \frac{PW_{out\_des} - \frac{R}{S}T_{g\_cmd}\omega_m}{\omega_m} \tag{3.31}$$

(2) Virtual Electric Machine Control

Given the torque commands T_{g_cmd} and T_{m_cmd}, the electric machine servo control will achieve the torque reference tracking by controlling the two-phase input voltages. Here, the two-phase currents, two-phase voltages and rotary speed are all measurable or can be calculated from the measured data.

Form the electric machine dynamics in (3.11)-(3.13), there is a nonlinear mapping between the motor torque T_m, the direct axis current I_d and quadrature axis current I_q. In order to simplify the electric torque control, I_d can be regulated to zero, so as to build a linear mapping between T_m and I_q, as:

$$I_{q\_des} = \frac{2T_{m\_cmd}}{3n_p\psi_m} \tag{3.32}$$

Then, the current-voltage error dynamics are given by:

$$\begin{aligned} L_d\dot{e}_{I_d} &= -R_s e_{I_d} - n_p L_q \omega_m I_q - U_d \\ L_q\dot{e}_{I_q} &= -R_s e_{I_q} + L_q\dot{I}_{q\_des} + R_s I_{q\_des} + n_p L_d \omega_m I_d + \psi_m n_p \omega_m - U_q \end{aligned} \tag{3.33}$$

where, the current errors $e_{I_d} = -I_d$, $e_{I_q} = I_{q\_des} - I_q$

The state-feedback control law for the two inputs is:

$$\begin{aligned} U_d &= -n_p L_q \omega_m I_q \\ U_q &= L_q\dot{I}_{q\_des} + R_s I_{q\_des} + n_p L_d \omega_m I_d + \psi_m n_p \omega_m \end{aligned} \tag{3.34}$$

Substituting the control law in (3.34) into (3.33) yields

$$\begin{aligned} L_d\dot{e}_{I_d} &= -R_s e_{I_d} \\ L_q\dot{e}_{I_q} &= -R_s e_{I_q} \end{aligned} \tag{3.35}$$

The controlled system is asymptotically stable, which ensures the electric motor (or generator) torque tracks the desired trajectories generated by the hybrid torque controllers.

In summary, the physics-based SISO middle level control described above can be interpreted in Fig. 3.5.

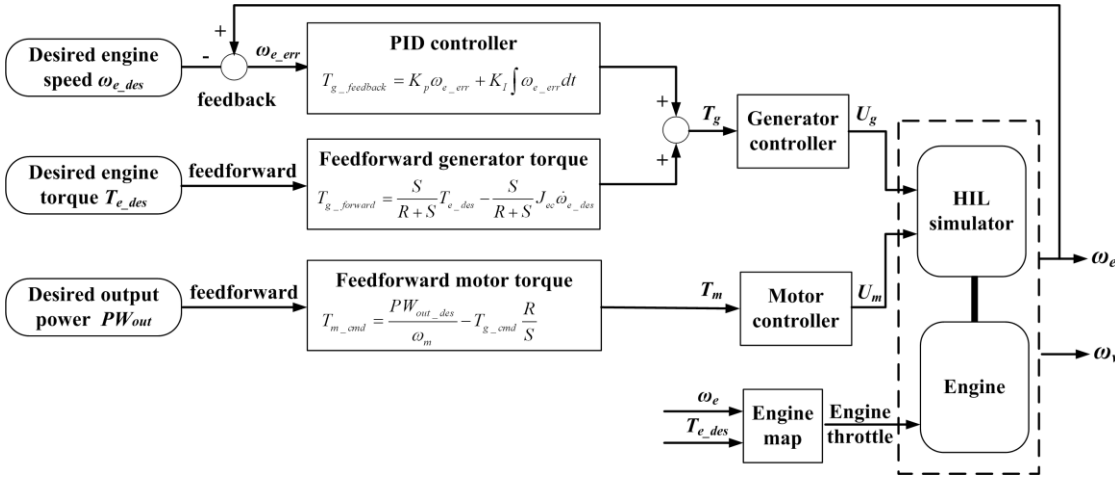

Fig. 3.5 SISO mid-level control architecture

3.4.4 Low-level Control: Feedback-Linearization Based Dynamometer Torque Control

With regards to the engine-dynamometer system in the low level, the control objective is to accurately manipulate the dynamometer torque T_d by controlling the input w_{HS} (i.e., the HSC valve opening) to mimic the torque behavior of the virtual hybrid powertrain (in other words, track the engine loading torque produced by the HIL simulation). For the nonlinear hydraulic dynamics, a feedback-linearization-based controller is designed [77].

First, since that there exists a direct mapping between the dynamometer torque T_d and outlet pressure P_{out}:

$$T_d = \frac{D_M}{2\pi}\left(1+C_f\right)P_{out} - \frac{D_M}{2\pi}\left(1-C_f\right)P_{in} + \frac{D_M}{2\pi}C_{da}\mu\omega_e \tag{3.36}$$

It is equivalent to track the outlet pressure P_{out} instead of dynamometer torque T_d, if only the variables P_{in} and ω_e are measureable. Thus, the outlet pressure - flow rate dynamics are presented for pressure tracking:

$$\begin{aligned}\dot{P}_{out} &= \frac{D_M\beta_e}{2\pi V_{t2}}\omega_e - \frac{\beta_e}{V_{t2}}\left(C_{im}+C_{em}\right)P_{out} + \frac{\beta_e}{V_{t2}}C_{im}P_{in} - \frac{\beta_e}{V_{t2}}C_d A_{HS}\sqrt{\frac{2}{\rho}P_{out}}\,w_{HS} \\ &= a\left(\omega_e, P_{out}, P_{in}, D_M\right) + b\left(P_{out}\right)w_{HS}\end{aligned} \tag{3.37}$$

where $a\left(\omega_e, P_{out}, P_{in}, D_M\right)$ and $b\left(P_{out}\right)$ are both functions of the state variables and measurable time-varying parameters.

Further, for a desired pressure P_{out_des}, (3.37) can be rewritten as the pressure error dynamics:

$$\dot{e}_{P_{out}} = a\left(\omega_e, P_{out}, P_{in}, D_M\right) + b\left(P_{out}\right)w_{HS} - \dot{P}_{out\_des} \tag{3.38}$$

where $e_{P_{out}} = P_{out} - P_{out\_des}$.

The feedback control law via feedback linearization should include a linearizing component $w_{HS} = \left(v - a + \dot{P}_{out\_des}\right)/b$ and a stabilizing component $v = -\lambda_1 e_{P_{out}}$.

Consequently, the nonlinear feedback control law is given by:

$$w_{HS} = \left(-\lambda_1 e_{P_{out}} - a + \dot{P}_{out\_des}\right)\Big/ b \tag{3.39}$$

where, the feedback gain λ_1 is positive.

Obviously, the state feedback control law in (3.39) ensures the transformed system in (3.38) globally is asymptotically stable. To further reduce the tracking error from some unmodeled dynamics, the feedback control law in (3.39) is modified by adding an integral term:

$$w_{HS} = \left(-\lambda_1 e_{P_{out}} - \lambda_2 \int e_{P_{out}} dt - a + \dot{P}_{out\_des}\right)\Big/ b \tag{3.40}$$

where, λ_2 is also a positive gain.

The desired output pressure P_{out_des} used in the above control law and its related variables can be derived via(3.36) with the pre-calculated desired dynamometer (engine loading) torque T_{d_des}:

$$e_{P_{out}} = \frac{2\pi\left(T_d - T_{d\_des}\right)}{D_M\left(1+C_f\right)} \tag{3.41}$$

$$\dot{P}_{out\_des} = \frac{2\pi\dot{T}_{d\_des} + D_M\left(1-C_f\right)\dot{P}_{in} - D_M C_{da}\mu\dot{\omega}_e}{D_M\left(1+C_f\right)} \tag{3.42}$$

Substituting (3.41)-(3.42) to the pressure tracking control law in (3.40) yields the final feedback control law for the dynamometer torque, given by:

$$\begin{aligned} w_{HS} = &-\lambda_1 \frac{2\pi\left(T_d - T_{d\_des}\right)}{D_M\left(1+C_f\right)b} - \lambda_2 \frac{2\pi\int\left(T_d - T_{d\_des}\right)dt}{D_M\left(1+C_f\right)b} - \frac{a}{b} \\ &+ \frac{2\pi\dot{T}_{d\_des} + D_M\left(1-C_f\right)\dot{P}_{in} - D_M C_{da}\mu\dot{\omega}_e}{D_M\left(1+C_f\right)b} \end{aligned} \tag{3.43}$$

3.5 EXPERIMENTS RESULTS (DRIVING CYCLES TESTS)

To demonstrate the capability and performance of the hybrid powertrain control system with the rapid prototyping hybrid powertrain research platform, extensive

experiments on the engine-dynamometer system have been conducted. As an example, the Highway Fuel Economy Test (HWFET) driving circle is chosen and slightly modified as the reference of the vehicle speed.

Test Case 1: Partial HWFET driving cycle, gasoline engine

First, the hybrid dynamics emulation has been tested on the low-inertia gasoline engine with part of the HWFET driving cycle. Figures 3.6-3.9 show the experimental trajectories of all the key variables (including the vehicle speed, the engine speed/torque, the motor and generator speed/torque and the SOC of the battery, etc). It is worth noting that all the experimental results are built on the system-decoupling-based, pole placement mid-level control proposed in Section 3.4.3.

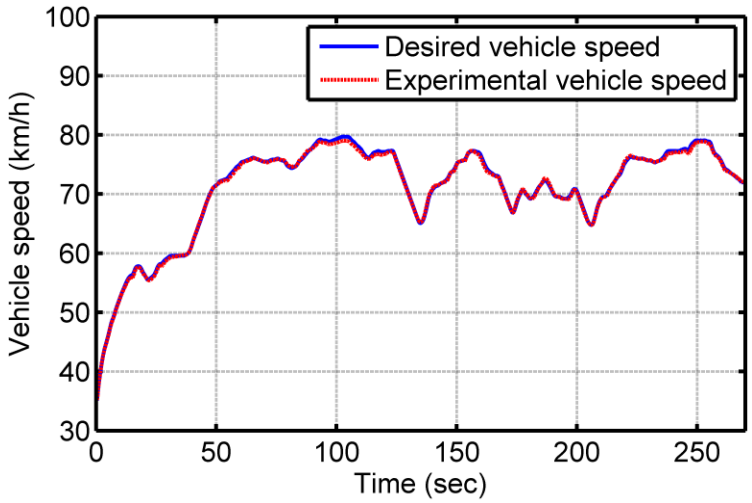

Fig. 3.6 HIL experiments (partial driving cycle): vehicle operation trajectories

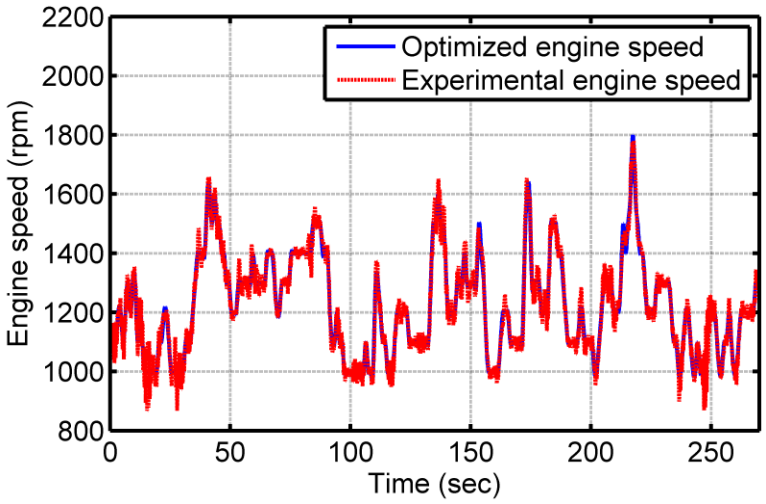

(a) Engine speed

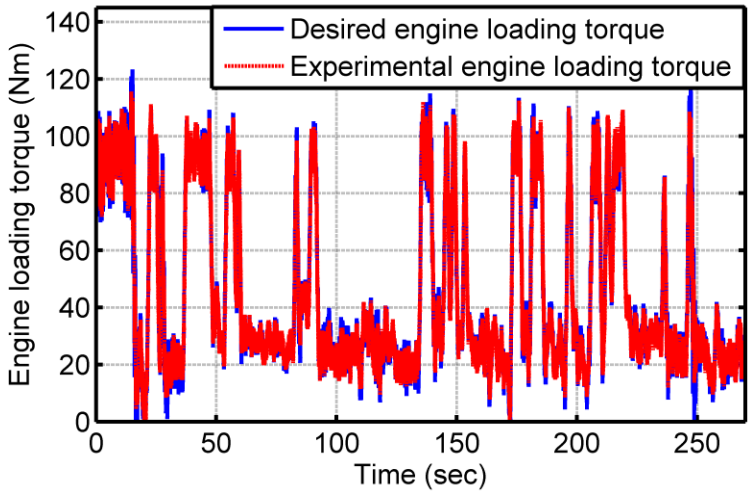

(b) Engine loading torque

Fig. 3.7 HIL experiments (partial driving cycle): engine operation trajectories

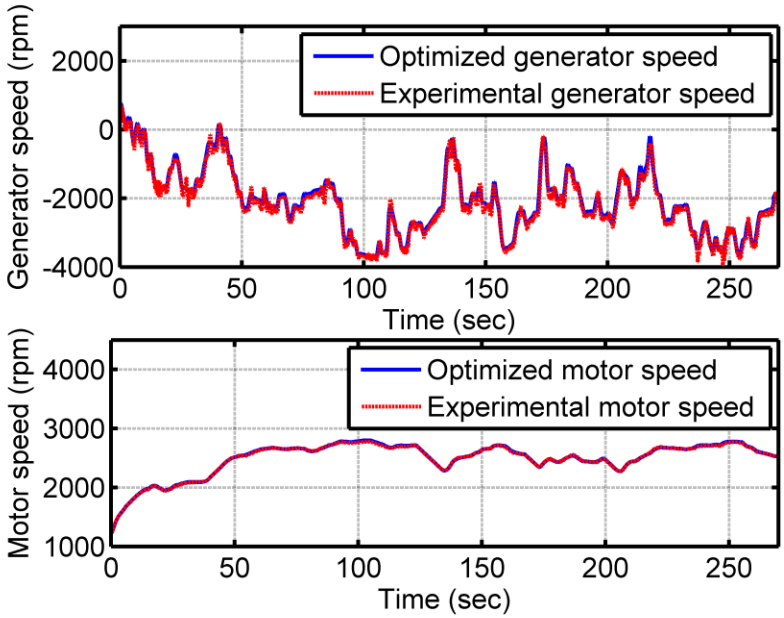

(a) Generator/motor speed

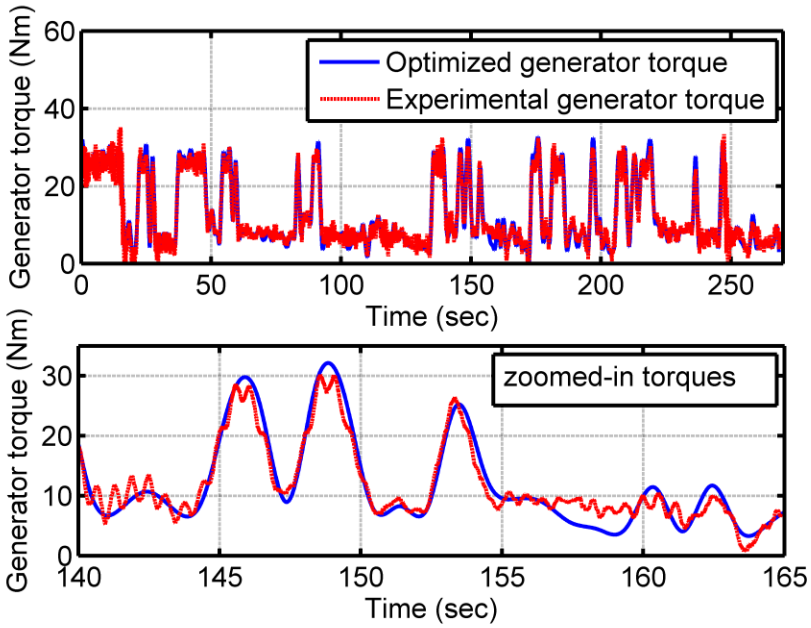

(b) Generator (zoomed-in) torque

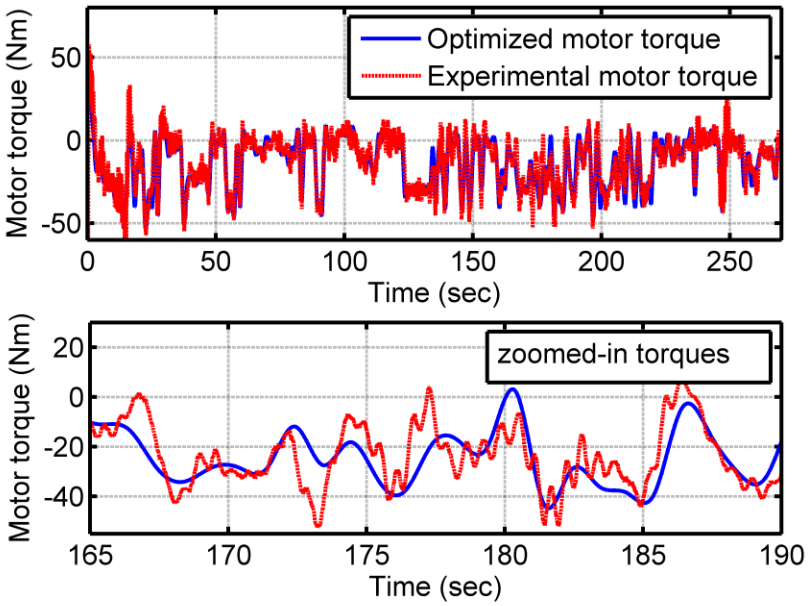

(c) Motor (zoomed-in) torque

Fig. 3.8 HIL experiments (partial driving cycle): generator/motor operation trajectories

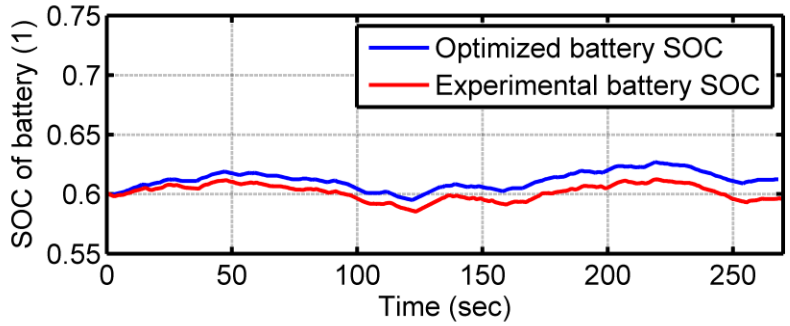

Fig. 3.9 Battery SOC trajectories

As shown in Fig. 3.6-3.9, the experimental results (vehicle speed, engine speed, engine loading torque and electric machine speeds) precisely track the desired trajectories. Especially for the engine loading torque tracking in Fig. 3.7(b), the accurate tracking fully demonstrates the performance of the torque-control based hybrid powertrain control system. Figure 3.8 shows the experimental generator/motor torques vs. the DP optimized generator/motor torques. As mentioned before, open loop control

with the DP optimized electric torques triggers the system instability. Thus, the feedback control for the electric torques is designed, which induces some differences in the high frequency domain. As a consequence, the experimental SOC of the battery shown in Fig. 3.9 is also different the optimized trajectory.

Test Case 2: Complete HWFET driving cycle, diesel engine

With the high-inertia diesel engine, the hybrid dynamics emulation experiments are also conducted with the complete HWFET driving cycle. Because of the different distributions of the BSFC (brake specific fuel consumption) in the engine efficiency maps as well as different engine coefficients (for example, engine inertias), the optimized diesel engine speed/torque trajectories are quite different from the case with the gasoline engine. However, the basic logics of the hybrid power management of the two cases are very similar: when the vehicle runs at the "accelerating" mode (which means that the demand power is very high), the DP energy management strategy intends to drive the engine running at some high torque - high BSFC areas to provide enough power for both providing the demand power and charging the battery; when the vehicle runs at the "cruising" or "near-cruising" mode (which means that the demand power is moderate), the DP energy management strategy intends to drive the engine running at some low torque - low speed areas (close to the "idle" state) and discharge the battery to compensate the demand power; when the vehicle runs at the "decelerating" mode, the battery will be charged to regenerate the braking energy.

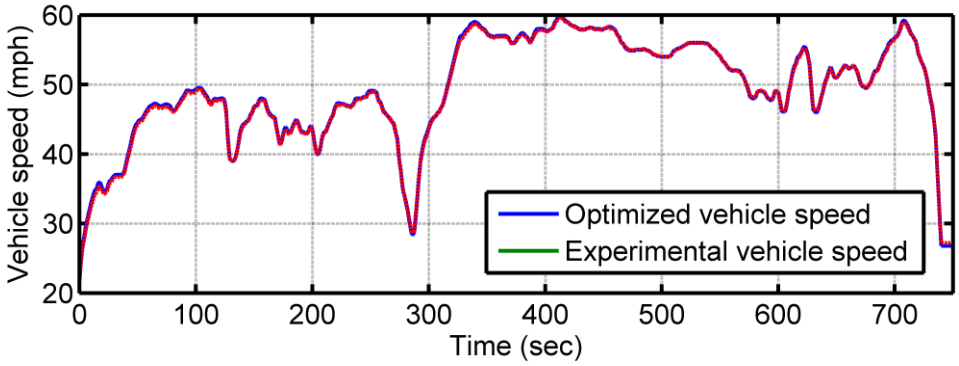

Fig. 3.10 HIL experiments (full driving cycle): vehicle operation trajectories

Figures 3.10-3.15 show the experimental trajectories of the important system

variables (including the hybrid powertrain variables, engine fuel consumption and some typical emission variables). For the engine torque shown in Fig. 3.11(b), some tracking errors can be observed because of the pure open-loop engine torque control used in SISO mid-level control.

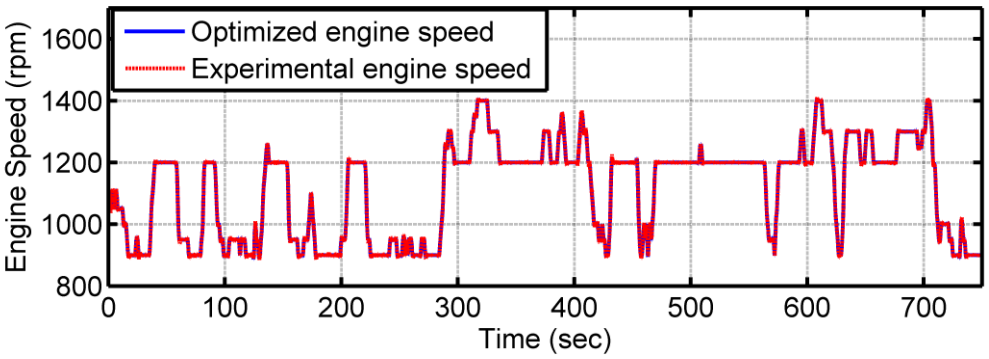

(a) Engine speed

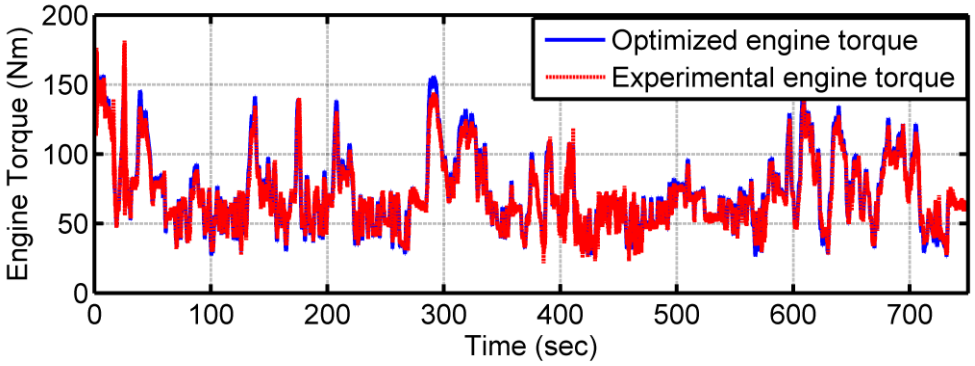

(b) Engine Torque

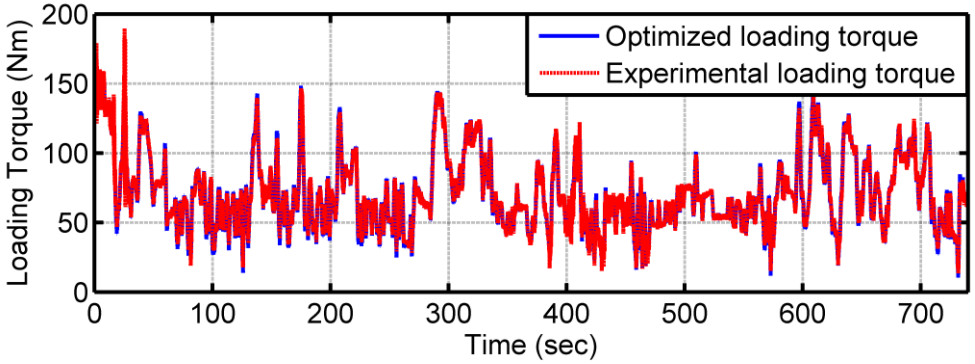

(c) Engine loading (dynamometer) torque

Fig. 3.11 HIL experiments (full driving cycle): engine operation trajectories

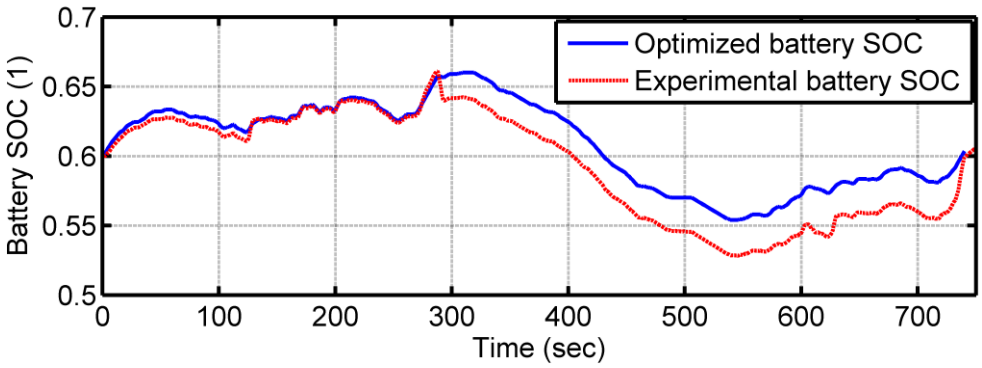

Fig. 3.12 HIL experiments (full driving cycle): battery SOC trajectory

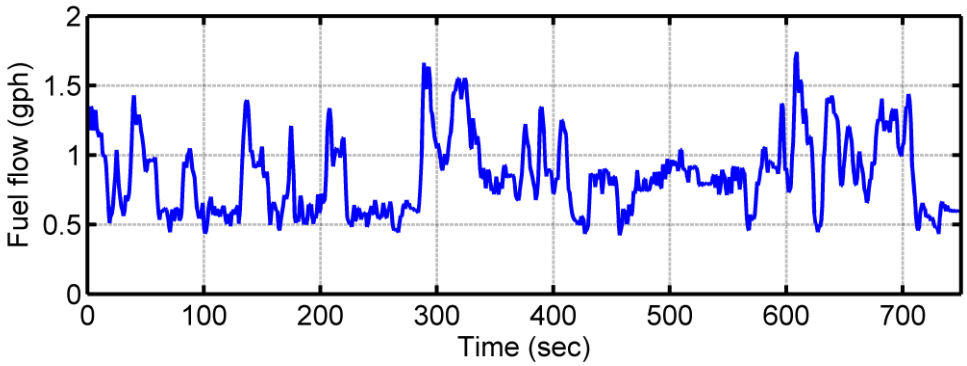

Fig. 3.13 HIL experiments (full driving cycle): fuel flow trajectory

Clearly, from Fig. 3.13-3.15, the engine fuel consumption, gaseous emissions (CO, NOx) and particulate emission are affected by the engine speed/torque to a very large extent. All of the measurements can be considered as the characterization of the emulated hybrid powertrain system with the current hardware sizing and energy management strategy design. The analysis of these experimental data will further support the energy management strategy design for comprehensive optimization of both fuel consumptions and emissions.

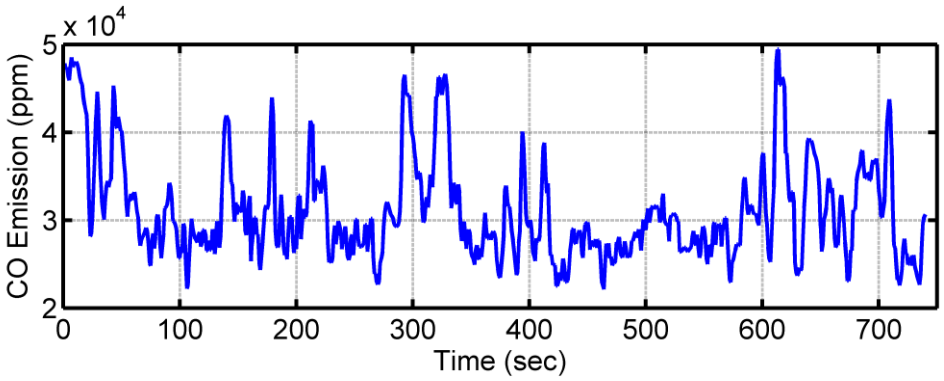

(a) CO emission

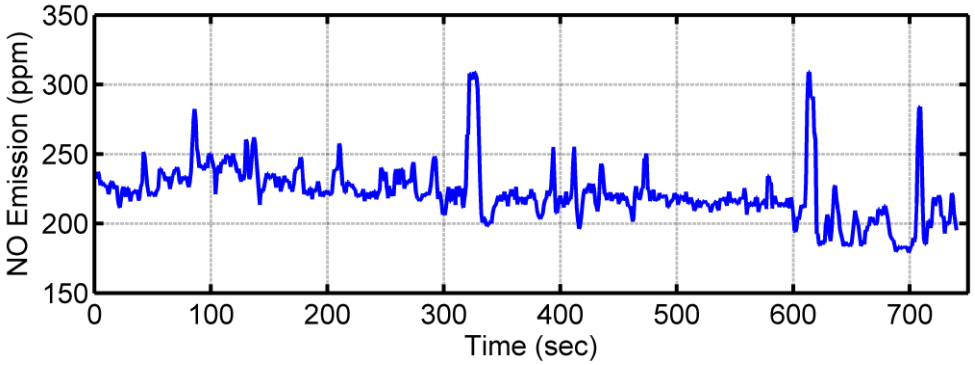

(b) NO emission

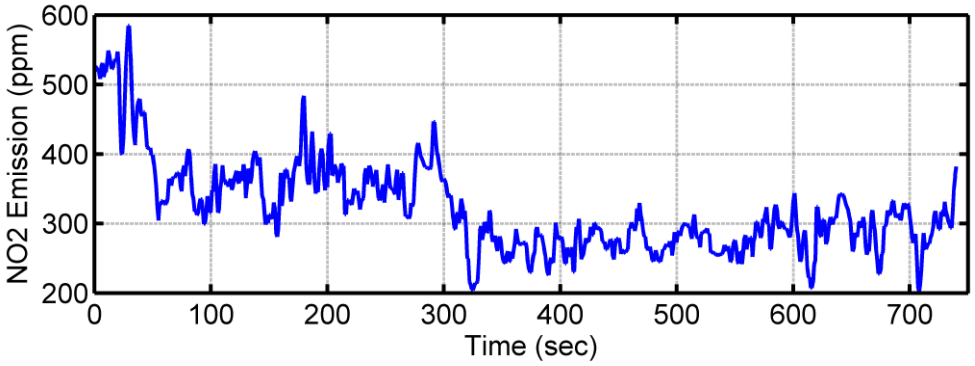

(c) NO_2 emission

Fig. 3.14 HIL experiments (full driving cycle): gaseous emissions trajectories

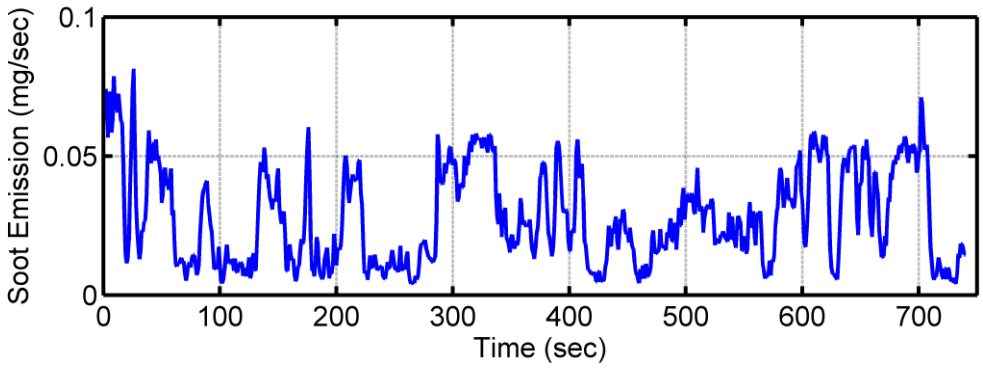

Fig. 3.15 HIL experiments (full driving cycle): micro soot trajectory

3.6 DYNAMIC ANALYSIS OF THE POWER-SPLIT HYBRID POWERTRAIN

Even with the experimental validation of the hybrid powertrain emulation, the inherent dynamic characteristics of the hybrid powertrain system will nevertheless induce the incompetency of the decoupling-based SISO mid-level control under some highly dynamic scenarios. In this section and thereafter, the dynamic characteristics of the hybrid powertrain system will be analyzed and on this basis, the capabilities and limitations of the SISO mid-level control will be unveiled.

3.6.1 Multi-inputs, Multi-outputs Dynamic Analysis

To better interpret the dynamics between the system outputs and control inputs, the dynamic models of the power-split HEV are transformed into a third-order compact form. At first, by neglecting the driveline spring/damping dynamics, the equations (3.1)-(3.17) can be simplified and transformed to a compact form, given by:

$$\begin{aligned}
\dot{\omega}_v &= \frac{a_2}{a_1}T_e + \frac{a_3}{a_1}T_g + \frac{a_4}{a_1}T_m - \frac{a_4}{a_1}\alpha\omega_v^{\,2} - \frac{a_4}{a_1}\beta \\
\dot{\omega}_e &= \frac{b_2}{b_1}T_e + \frac{b_3}{b_1}T_g + \frac{b_4}{b_1}T_m - \frac{b_4}{b_1}\alpha\omega_v^{\,2} - \frac{b_4}{b_1}\beta \\
S\dot{O}C &= -\frac{V_{batt}}{2Q_{batt}R_{batt}} + \frac{\sqrt{V_{batt}^{\,2} - 4\left[-T_g\omega_g\eta_g^{\,k1} + T_m\omega_m\eta_m^{\,k2}\right]R_{batt}}}{2Q_{batt}R_{batt}}
\end{aligned} \tag{3.44}$$

where $\left[\omega_v \quad \omega_e \quad SOC\right]^T$ are the system states and $\left[T_e \quad T_g \quad T_m\right]^T$ are the system inputs that can be directly controlled in hybrid powertrain. The parameters a_1 - a_4 and b_1 - b_4 will be explained in Appendix 1. For the sake of convenience, the storage battery dynamics are temporarily neglected and the remaining three-input (T_e, T_g, T_m), two-output (ω_v, ω_e) system will be investigated in the following sections [89].

Without losing generality, the dynamics of the engine and electric machines can be approximated using first-order systems with time constants τ_e, τ_g and τ_m, given by:

$$\begin{aligned}
\dot{T}_e &= \frac{1}{\tau_e}\left(T_{e_cmd} - T_e\right) \\
\dot{T}_g &= \frac{1}{\tau_g}\left(T_{g_cmd} - T_g\right) \\
\dot{T}_m &= \frac{1}{\tau_m}\left(T_{m_cmd} - T_m\right)
\end{aligned} \tag{3.45}$$

where the variables T_{e_cmd}, T_{g_cmd} and T_{m_cmd} are the torque commands for power sources.

To make use of the linear dynamic response analysis tool, the dynamic system linearization is realized. Around a steady-state $y_0 = x_0 = \left(\omega_{v0}, \omega_{e0}\right)$, the open-loop system dynamics in (3.44) and (3.45) are linearized and rewritten as the input-output transfer function matrix in the *s*-domain :

$$\begin{aligned}
Y(s) &= P(s)U(s) \\
P(s) &= \begin{bmatrix} P_{11}(s) & P_{12}(s) & P_{13}(s) \\ P_{21}(s) & P_{22}(s) & P_{23}(s) \end{bmatrix}
\end{aligned} \tag{3.46}$$

where

$$P_{11}(s)=\frac{\frac{a_2}{a_1}}{\left(s+2\frac{a_4}{a_1}\alpha\omega_{vo}\right)(\tau_e s+1)},\qquad P_{21}(s)=\frac{\frac{b_2}{b_1}s+2\left(\frac{b_2}{b_1}\frac{a_4}{a_1}-\frac{b_4}{b_1}\frac{a_2}{a_1}\right)\alpha\omega_{vo}}{s\left(s+2\frac{a_4}{a_1}\alpha\omega_{vo}\right)(\tau_e s+1)},$$

$$P_{12}(s)=\frac{\frac{a_3}{a_1}}{\left(s+2\frac{a_4}{a_1}\alpha\omega_{vo}\right)(\tau_g s+1)},\qquad P_{22}(s)=\frac{\frac{b_3}{b_1}s+2\left(\frac{b_3}{b_1}\frac{a_4}{a_1}-\frac{b_4}{b_1}\frac{a_3}{a_1}\right)\alpha\omega_{vo}}{s\left(s+2\frac{a_4}{a_1}\alpha\omega_{vo}\right)(\tau_g s+1)},$$

$$P_{13}(s)=\frac{\frac{a_4}{a_1}}{\left(s+2\frac{a_4}{a_1}\alpha\omega_{vo}\right)(\tau_m s+1)},\qquad P_{23}(s)=\frac{\frac{b_4}{b_1}}{\left(s+2\frac{a_4}{a_1}\alpha\omega_{vo}\right)(\tau_m s+1)}$$

where, $U(s)=\left[T_{e\_cmd}(s)\quad T_{g\_cmd}(s)\quad T_{m\_cmd}(s)\right]^T$ are the control inputs in the *s*-domain, and $Y(s)=\left[\omega_v(s)\quad \omega_e(s)\right]^T$ are the system outputs in the *s*-domain.

For the three-input, two-output system (3.46), the frequency responses of all the input-output transfer functions are shown in Fig. 3.16, where a typical vehicle speed ω_{v0} = 30 *mph* is applied. It is not difficult to find that, there are some considerable dynamic interactions between the vehicle speed output and every torque input (only the gain of $P_{11}(s)$ is lower than the other two by around 20 dB, which means that the dynamic effect of the engine torque to the vehicle speed is relatively small); while for the engine speed output, the interactions between the engine speed and engine/generator torque are obviously dominant, because the gain of $P_{23}(s)$ is lower than the other two by 40-50 dB, which means that the dynamic effect of the motor torque to the engine speed is small enough to be neglected).

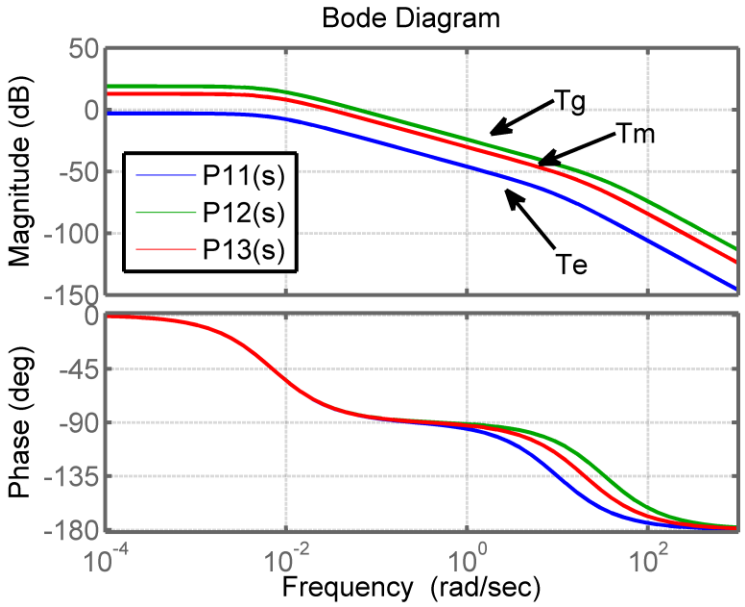

(a) Input-output transfer function elements P_{11}, P_{12} and P_{13}

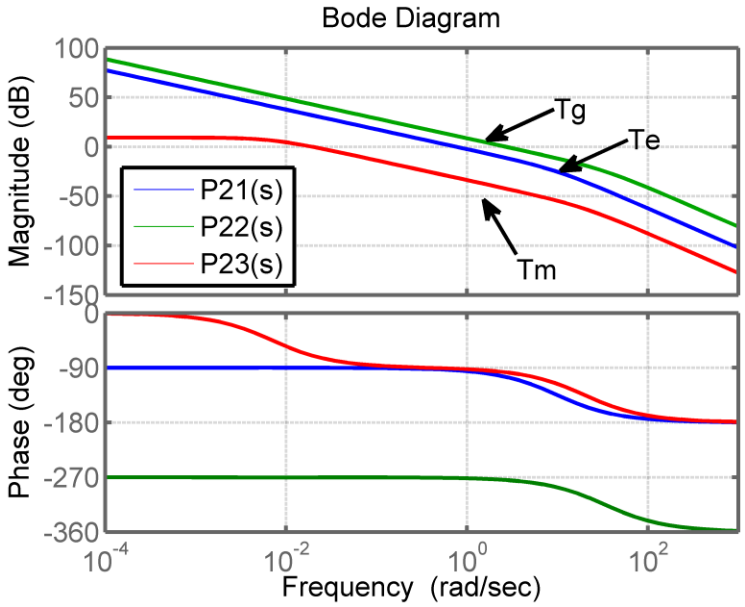

(b) Input-output transfer function elements P_{21}, P_{22} and P_{23}

Fig. 3.16 Bode plots of the open-loop transfer functions

Moreover, it is worth noting that the transfer function $P_{22}(s)$ which maps the generator torque to the engine speed is not a classic minimum-phase system, but with an

additional 180° phase lag. This is because the generator torque input opposes the engine speed output; or more straightforwardly, the parameter $\frac{b_3}{b_1}$ is negative in (3.44). In other words, the input T_{g_cmd} has a considerable negative interaction with output ω_e, as well as a positive interaction with output ω_v. As demonstrated in next sections, this fact may lead to the degradation of the engine speed tracking with a fast engine operation point switching (e.g., large step command) owing to a large vehicle acceleration/deceleration.

3.6.2 Theoretical Validation of the Physics-Based SISO Controls

With the linearized dynamics shown in the last section, the physics-based SISO control described in Section 3.4, which has been experimentally demonstrated in Section 3.5, can be further analytically validated.

In the physics-based SISO control, the engine throttle is dedicated to open-loop control the engine torque T_e based on a calibrated engine map, which implies theoretically the input T_{e_cmd} can be always equivalent to its desired value T_{e_des} if neglecting the inertia transient and steady-state error (which is a basic assumption of the SISO controls design). Consequently, the hybrid torque control is formulated into a two-inputs (T_{g_cmd} and T_{m_cmd}), two-outputs (ω_v and ω_e) problem. Here, two single-input, single-output controls are designed: the generator is used as a speed compensator to track ω_e; and simultaneously, the motor is used as a power compensator to track ω_v (equivalently, the power output), as described in (3.27) and (3.31).

By comparing the physics-based SISO controls with the dynamic analysis in the Section 3.6.1, it is not difficult to find out:

(1) The engine speed tracking control in (3.27) neglects the effect of input T_{m_cmd} to the output ω_e, which matches the conclusion of the dynamic analysis that the magnitude of transfer function $P_{23}(s)$ which maps T_{m_cmd} to ω_e is too small compared with the other two inputs. Also, the simplified steady-state ratio of T_{e_cmd} to T_{g_cmd} (which is,

$\frac{R+S}{S}=3.6$) is numerically close to the theoretically strict ratio (which is, $-\frac{b_3}{b_2}=3.5295$) from (3.44). Therefore, the simplified engine speed tracking in the SISO controls is effective.

(2) The vehicle speed tracking control in (3.31) comprehensively combines all the three inputs, but merges the collective effects of inputs T_{e_cmd} and T_{g_cmd} into one combined engine-driving torque $\frac{R}{S}T_{g\_cmd}$. Still, numerically the ratio of the combined torque to the generator torque (which is, $\frac{R}{S}=2.6$) is almost equal to the theoretically strict gain (which is, $\left(-\frac{a_2b_3}{b_2}+a_3\right)\Big/a_4=2.5886$) from (3.44). Also, the coefficient of the feedforward term (vehicle acceleration) in the motor torque T_{m_cmd} (which is, $\frac{J_v}{K_{ratio}}=31.9435$) is close to the strict one (which is, $\frac{a_1}{a_4}=32.5343$). Therefore, the simplified vehicle speed tracking is also verified to be precise enough.

3.7 DYNAMIC RESPONSE (TRANSIENT PERFORMANCE) OF THE POWER-SPLIT HYBRID SYSTEM

Although the physics-based SISO control has been proved of relatively high precision on reference tracking, there are still some concerns about its dynamic response under transients. In this section, two main dynamic issues are analyzed and investigated: one is the inverse transient dynamics issue, which has been unveiled in [90]-[91] to be of concerns with regards to some specific SISO controls; the other is the transient engine operation tracking issue (i.e., electric torque/power spike issue), which eventually drives us to further extend the current SISO control into the multivariable control.

3.7.1 Engine/Vehicle Inverse Transient Dynamics

Undesired inverse transient dynamic response describes the step response that starts

in the wrong direction and has initial undershoot during the short transient. This phenomenon was studied in [90] as an important issue linked with the non-minimum-phase zeros in the transfer functions of the continuously variable transmission (CVT) system. Since the power-split hybrid powertrain can be treated as a functionality-extended CVT system, a similar concern will intuitively emerge in the transient dynamic analysis of the hybrid powertrain system. Based on the analysis in Section 3.6.1, the transfer function $P_{22}(s)$ with the 180° phase lag (which maps the generator torque to the engine speed) may bring the non-minimum-phase zeros into the close-loop transfer functions from desired references (ω_{v_des}, ω_{e_des}) to the actual outputs (ω_v, ω_e), and hence, bring some potential possibilities of inverse transient dynamic response on the system outputs. To clarify it, some analysis based on the closed-loop system with the SISO mid-level control structure (with or without feedforward controls) are conducted.

To simplify the problem, let us limit the control analysis into a vehicle accelerating transient case, in which for a desired vehicle speed ω_{v_des} (or equivalently, the desired powertrain output power PW_{out}), the engine is manipulated to track the optimized reference (T_{e_des}, ω_{e_des}) produced by the hybrid energy management strategy. Theoretically, the DP/SDP optimized engine operating reference (T_{e_des}, ω_{e_des}) would be the step signal; while the vehicle speed command ω_{v_des} can be treated as a ramp signal due to the huge vehicle inertia in the real world (although the step reference ω_{v_des} is also discussed in this section for the purpose of performance comparisons).

In the high level controller, for a specific desired vehicle speed ω_{v_des} for acceleration, the DP/SDP based control law will correspondingly generate a specific desired engine operation point (ω_{v_des}, ω_{e_des}). Therefore, in the vehicle accelerating case study, the three reference variables ω_{v_des}, ω_{e_des} and T_{e_des} are bonded together. To simplify the dynamic analysis, it is reasonable to couple the two reference variables with some constant scales κ_T and κ_V as, $T_{e\_des} = \kappa_T \omega_{e\_des}$ and $\omega_{v\_des} = \kappa_V \omega_{e\_des}$ (when ω_{v_des} is a step signal) or $\dot{\omega}_{v\_des} = \kappa_V \omega_{e\_des}$ (when ω_{v_des} is a ramp signal). With this necessary

assumption, the engine speed closed-loop dynamics is analyzed first.

(1) Inverse transient dynamic analysis for the reference-input transfer function $f_1(s)=T_g(s)/\omega_{e\_des}(s)$ and reference-output transfer function $f_2(s)=\omega_e(s)/\omega_{e\_des}(s)$

From the dynamics(3.46), since the gain of $P_{23}(s)$ is much lower than other transfer function (i.e., the effect of the motor torque to the engine speed is small enough to be neglected), the simplified dynamic equation is given by:

$$\dot{\omega}_e=\frac{b_2}{b_1}T_e+\frac{b_3}{b_1}T_g \tag{3.47}$$

If we use a pure feedback controller

$$T_{g\_cmd}=-K_p\left(\omega_{e\_des}-\omega_e\right)-K_I\int\left(\omega_{e\_des}-\omega_e\right)dt \tag{3.48}$$

Then in the *s*-domain, we have

$$T_{g\_cmd}=K_p\omega_e-K_p\omega_{e\_des}+K_I\frac{\omega_{e\_des}}{s}-K_I\frac{\omega_{e\_des}}{s} \tag{3.49}$$

i.e.,
$$\omega_e=\frac{T_{g\_cmd}+K_p\omega_{e\_des}+K_I\dfrac{\omega_{e\_des}}{s}}{K_p+K_I\dfrac{1}{s}} \tag{3.50}$$

With the temporary assumption $T_e=T_{e\_des}$ and $T_g=T_{g\_cmd}$, substituting (3.50) into (3.47) yields :

$$f_1(s)=\frac{T_{g\_cmd}}{\omega_{e\_des}}=\frac{-K_ps^2+\left(\dfrac{b_2}{b_1}\kappa_TK_I-K_I\right)s+\dfrac{b_2}{b_1}\kappa_TK_I}{s^2-\dfrac{b_3}{b_1}K_ps-\dfrac{b_3}{b_1}K_I} \tag{3.51}$$

For (3.51), based on the initial value theorem, with a step reference ω_{e_des} , we have:

$$\dot{T}_{g\_cmd}(t=0)=s\lim_{s\to\infty}sf_1(s)\omega_{e\_des}(s)=\lim_{s\to\infty}s^2f_1(s)\frac{1}{s}=-\infty \tag{3.52}$$

This implies that at the very beginning of the transient process, theoretically the input T_g has infinite negative dynamic response with a step reference. Certainly, under the actual cases, we should consider the engine and electric machine inertia dynamics.

By introducing the inertia dynamics

$$T_e = \frac{T_{e\_des}}{\tau_e s + 1}, \quad T_g = \frac{T_{g\_cmd}}{\tau_g s + 1} \tag{3.53}$$

into the transfer function (3.52), we get

$$f_1(s) = \frac{T_g}{\omega_{e\_des}} = \frac{-K_p s^2 + \left(\frac{b_2}{b_1}\kappa_T K_I \frac{1}{\tau_e s + 1} - K_I\right)s + \frac{b_2}{b_1}\kappa_T K_I \frac{1}{\tau_e s + 1}}{\left(\tau_g s + 1\right)s^2 - \frac{b_3}{b_1}K_p s - \frac{b_3}{b_1}K_I} \tag{3.54}$$

Based on the initial value theorem and final value theorem, we have

$$\dot{T}_g(t=0) = s\lim_{s\to\infty} s f_1(s)\omega_{e\_des}(s) = \lim_{s\to\infty} s^2 f_1(s)\frac{1}{s} = -\frac{K_p}{\tau_g} < 0 \tag{3.55}$$

$$T_g(t=\infty) = \lim_{s\to 0} s f_1(s)\omega_{e\_des}(s) = \lim_{s\to 0} s f_1(s)\frac{1}{s} = -\frac{b_2}{b_3}\kappa_T > 0 \tag{3.56}$$

where it is worth noting that gain b_3 is negative and all the other gains are positive.

This implies that the final generator torque T_g will converge to a positive value from the original point, but at the initial stage T_g has large negative (i.e., inverse) transient dynamic response with a step reference, if we use a pure feedback controller in (3.48), even with the engine and generator inertia.

However, in the physics-based SISO control shown in Section 3.4.3, a feedforward term is utilized and added onto the feedback controller, which is given by:

$$T_{g\_cmd} = -\frac{b_2}{b_3}T_{e\_des} - K_p\left(\omega_{e\_des} - \omega_e\right) - K_I\int\left(\omega_{e\_des} - \omega_e\right)dt \tag{3.57}$$

The transfer function (3.54) will be modified as:

$$f_1(s) = \frac{T_g}{\omega_{e\_des}} = \frac{\left(-\frac{b_2}{b_3}\kappa_T - K_p\right)s^2 + \left(\frac{b_2}{b_1}\kappa_T K_I \frac{1}{\tau_e s + 1} - K_I\right)s + \frac{b_2}{b_1}\kappa_T K_I \frac{1}{\tau_e s + 1}}{\left(\tau_g s + 1\right)s^2 - \frac{b_3}{b_1}K_p s - \frac{b_3}{b_1}K_I} \tag{3.58}$$

Further, based on the initial value theorem, we have

$$\dot{T}_g(t=0) = s\lim_{s\to\infty} sf_1(s)\omega_{e\_des}(s) = \lim_{s\to\infty} s^2 f_1(s)\frac{1}{s} = -\frac{\frac{b_2}{b_3}\kappa_T + K_p}{\tau_g} \tag{3.59}$$

With the feedforward control, the transient dynamic response of T_g will depends on the quantitative comparisons between the torque-speed scale κ_T and proportional gain K_p. Generally in the hybrid powertrain, when the vehicle accelerates, both the engine torque and engine speed will sequentially goes up for providing the traction power, i.e., $\kappa_T > 0$ and $\frac{b_2}{b_3}\kappa_T < 0$; in these cases, the introduction of the feedforward term greatly reduces, if it does not fully eliminate, the inverse dynamic response of the reference-input transfer function $f_1(s) = T_g(s)/\omega_{e\_des}(s)$. Only in a few cases where for some special reasons (for example, the previously over-accumulated battery power needs to be consumed) the engine torque goes down while engine speed goes up, the feedforward term may boost up the inverse dynamic response since $\kappa_T < 0$ at that moment.

Compared with the torque input T_g, we actually care more about the transient dynamics of the system output ω_e with respect to the step reference (T_{e_des}, ω_{e_des}). Following the similar steps in the last section, if we use the pure feedback controller in (3.48), we get the reference-output transfer function:

$$f_2(s) = \frac{\omega_e}{\omega_{e\_des}} = \frac{-\frac{b_3}{b_1}K_p\tau_e s^2 + \left(\frac{b_2}{b_1}\kappa_T - \frac{b_3}{b_1}K_p - \frac{b_3}{b_1}K_I\tau_e\right)s - K_I\frac{b_3}{b_1}}{(\tau_e s+1)\left(s^2 - \frac{b_3}{b_1}K_p s - \frac{b_3}{b_1}K_I\right)} \tag{3.60}$$

Then, based on the initial value theorem, we have

$$\dot{\omega}_e(t=0) = s\lim_{s\to\infty} sf_2(s)\omega_{e\_des}(s) = \lim_{s\to\infty} s^2 f_2(s)\frac{1}{s} = -\frac{b_3}{b_1}K_p > 0 \tag{3.61}$$

Or, when we use the feedforward plus feedback controller in (3.57), the reference-output transfer function in (3.60) is modified as

$$f_3(s)=\frac{\omega_e}{\omega_{e\_des}}=\frac{-\frac{b_3}{b_1}K_p\tau_e s^2+\left(-\frac{b_3}{b_1}K_p-\frac{b_3}{b_1}K_I\tau_e\right)s-K_I\frac{b_3}{b_1}}{(\tau_e s+1)\left(s^2-\frac{b_3}{b_1}K_p s-\frac{b_3}{b_1}K_I\right)} \tag{3.62}$$

We still have the transient response

$$\dot{\omega}_e(t=0)=s\lim_{s\to\infty}sf_2(s)\omega_{e\_des}(s)=\lim_{s\to\infty}s^2 f_2(s)\frac{1}{s}=-\frac{b_3}{b_1}K_p>0 \tag{3.63}$$

This implies that no matter with or without feedforward term, there is actually not any concern of the transient inverse dynamic response for the system output ω_e.

In conclusion, for both the system input T_g and output ω_e, the potential inverse transient dynamics due to the undesired zeros can be fully or partially eliminated by the introduction of the feedforward control (except for some special cases in T_g). Especially for the system output ω_e that we concern more, the inverse transient dynamic effect theoretically never exists.

(2) Inverse transient dynamic analysis for the reference-output transfer function $f_3(s)=\omega_v(s)/\omega_{v\_des}(s)$

From the dynamics (3.46), although all the transfer functions $P_{11}(s)$, $P_{12}(s)$ and $P_{13}(s)$ are all minimum-phase systems, there is potential risk that the possible inverse transient dynamic response of T_g for engine speed control may be transferred into the vehicle speed control system and induce some transient dynamic issues. To clarify this concern, the similar transient dynamic analysis is taken for the vehicle speed control dynamics.

From the system dynamics in (3.44), the vehicle speed control dynamics is given by:

$$\dot{\omega}_v=\frac{a_2}{a_1}T_e+\frac{a_3}{a_1}T_g+\frac{a_4}{a_1}T_m-\frac{a_4}{a_1}\alpha\omega_v^{\,2}-\frac{a_4}{a_1}\beta \tag{3.64}$$

In the SISO controls, a pure feedforward controller is used,

$$T_{m\_cmd} = \frac{PW_{out\_des}}{K_{ratio}\omega_v} - \frac{R}{S}T_{g\_cmd} \tag{3.65}$$

where $PW_{out} = J_v\dot{\omega}_{v\_des}\omega_{v\_des} + f_{tire}M_v gR_{tire}\omega_{v\_des} + 0.5\rho_a C_{drag}A_f\omega_{v\_des}{}^3 R_{tire}{}^3$

Based on the analysis in Section 3.6.2, this feedforward controller can be considered to be approximately equivalent to:

$$T_{m\_cmd} = \frac{a_1}{a_4}\dot{\omega}_{v\_des} + \alpha\omega_v{}^2 + \beta - \frac{a_2}{a_4}T_{e\_des} - \frac{a_3}{a_4}T_{g\_cmd} \tag{3.66}$$

Then in the *s*-domain, we have

$$T_{m\_cmd} = \frac{a_1}{a_4}s\omega_{v\_des} + \alpha\omega_v{}^2 + \beta - \frac{a_2}{a_4}T_{e\_des} - \frac{a_3}{a_4}T_{g\_cmd} \tag{3.67}$$

i.e.,

$$T_m = \frac{a_1}{a_4}\frac{s}{\tau_m s+1}\omega_{v\_des} + \frac{1}{\tau_m s+1}\left(\alpha\omega_v{}^2 + \beta\right) - \frac{a_2}{a_4}\frac{1}{\tau_m s+1}T_{e\_des} - \frac{a_3}{a_4}\frac{1}{\tau_m s+1}T_{g\_cmd} \tag{3.68}$$

With introducing the inertia dynamics, substituting (3.68) into (3.64) yields:

$$s\omega_v = \frac{a_2}{a_1}\left(T_e - \frac{1}{\tau_m s+1}T_{e\_des}\right) + \frac{a_3}{a_1}\left(T_g - \frac{1}{\tau_m s+1}T_{g\_cmd}\right) + \frac{s}{\tau_m s+1}\omega_{v\_des} - \frac{a_4}{a_1}\frac{\tau_m s}{\tau_m s+1}\left(\alpha\omega_v{}^2 + \beta\right) \tag{3.69}$$

From the previous analysis, when we treat the desired vehicle speed ω_{v_des} as a step reference, it will be coupled with the desired engine speed with a constant scale as $\omega_{v\_des} = \kappa_V\omega_{e\_des}$.

Furthermore, (3.69) can be rewritten as:

$$s\omega_v = \frac{(\tau_m - \tau_e)s}{(\tau_e s+1)(\tau_m s+1)}\frac{a_2}{a_1}\frac{\kappa_T}{\kappa_V}\omega_{v\_des} + \frac{(\tau_m - \tau_g)s}{\tau_m s+1}\frac{a_3}{a_1}T_g + \frac{s}{\tau_m s+1}\omega_{v\_des} - \frac{a_4}{a_1}\frac{\tau_m s}{\tau_m s+1}\left(\alpha\omega_v{}^2 + \beta\right) \tag{3.70}$$

Substituting (3.58) into (3.70) yields the reference-output transfer function:

$$
\begin{aligned}
f_3(s) &= \frac{\omega_v}{\omega_{v\_des}} \\
&= \frac{\tau_m - \tau_e}{(\tau_e s+1)(\tau_m s+1)} \frac{a_2}{a_1} \frac{\kappa_T}{\kappa_V} + \frac{1}{\tau_m s+1} \\
&\quad + \frac{\tau_m - \tau_g}{\tau_m s+1} \frac{\left(-\frac{b_2}{b_3}\kappa_T - K_p\right)s^2 + \left(\frac{b_2}{b_1}\kappa_T K_I \frac{1}{\tau_e s+1} - K_I\right)s + \frac{b_2}{b_1}\kappa_T K_I \frac{1}{\tau_e s+1}}{(\tau_g s+1)s^2 - \frac{b_3}{b_1}K_p s - \frac{b_3}{b_1}K_I} \frac{a_3}{a_1} \frac{1}{\kappa_V}
\end{aligned}
\tag{3.71}
$$

where the nonlinear term $\frac{a_4}{a_1}\frac{\tau_m}{\tau_m s+1}\left(\alpha\omega_v^2 + \beta\right)$ in (3.70) has been neglected because it is not difficult to find that this team has almost no effect on the transient dynamics.

The transient vehicle speed response for a step reference will be given from (3.71) based on the initial value theorem,

$$
\dot{\omega}_v(t=0) = s\lim_{s\to\infty} s f_3(s)\omega_{v\_des}(s) = \lim_{s\to\infty} s^2 f_3(s)\frac{1}{s} = \frac{1}{\tau_m} > 0 \tag{3.72}
$$

Then, for an even more general case when the vehicle speed reference is a ramp signal, i.e., $\dot{\omega}_{v\_des} = \kappa_V \omega_{e\_des}$, then the reference-output transfer function will be given by:

$$
\begin{aligned}
f_3(s) &= \frac{\omega_v}{\omega_{v\_des}} \\
&= \frac{(\tau_m - \tau_e)s}{(\tau_e s+1)(\tau_m s+1)} \frac{a_2}{a_1} \frac{\kappa_T}{\kappa_V} + \frac{1}{\tau_m s+1} \\
&\quad + \frac{(\tau_m - \tau_e)s}{\tau_m s+1} \frac{\left(-\frac{b_2}{b_3}\kappa_T - K_p\right)s^2 + \left(\frac{b_2}{b_1}\kappa_T K_I \frac{1}{\tau_e s+1} - K_I\right)s + \frac{b_2}{b_1}\kappa_T K_I \frac{1}{\tau_e s+1}}{(\tau_g s+1)s^2 - \frac{b_3}{b_1}K_p s - \frac{b_3}{b_1}K_I} \frac{a_3}{a_1} \frac{1}{\kappa_V}
\end{aligned}
\tag{3.73}
$$

Then the transient vehicle speed response is given by for the ramp reference:

$$
\dot{\omega}_v(t=0) = s\lim_{s\to\infty} s f_3(s)\omega_{v\_des}(s) = \lim_{s\to\infty} s^2 f_3(s)\frac{1}{s^2} = 0 \tag{3.74}
$$

It is very obvious that no matter with a step reference and a ramp reference, there is actually not any concern of the transient inverse dynamic response for the system output ω_v. From the viewpoint of physics, this can be explained as the "torque compensation"

effect of the electric motor. The existence of the electric motor (with the storage battery) provides the hybrid system with an independent power/torque source. No matter what dynamic behaviors of the generator/engine are conducted for engine speed control, the motor can "absorb" the transferred transient generator/torque response and ideally inject an appropriate torque for desired vehicle operation. The introduction of the electric motor (second independent hybrid power source) into the power-split hybrid powertrain not only fully decouples the vehicle and engine operations at steady state, but also isolates the vehicle control from the transient disturbance generated from the engine control.

Further, let us discuss a new case if there is no storage battery in the power-split hybrid system, which is, actually an EVT (electric variable transmission) powertrain system. Without an energy storage element, the electric generator and motor powers $P_m = P_g$ if we assume there is no electric power transfer loss. Further, without considering the electric machine inertias, for a specific transient case it is reasonable to assume that there is a scale between the simultaneous generator operation point (ω_g, T_g) and motor operation point (ω_m, T_m), i.e., $T_m = \kappa_E T_g$ and $T_m = \frac{1}{\kappa_E} T_g$. Then, still with the previous assumptions, the vehicle operation dynamics are transformed to:

$$\dot{\omega}_v = \frac{a_2}{a_1} T_e + \left(\frac{a_3}{a_1} + \frac{a_4}{a_1} \kappa_E \right) T_g - \frac{a_4}{a_1} \alpha \omega_v^{\,2} - \frac{a_4}{a_1} \beta \tag{3.75}$$

Substituting (3.58) into (3.76) yields the new reference-output transfer function for a step vehicle speed reference,

$$\begin{aligned} f_3(s) &= \frac{\omega_v}{\omega_{v\_des}} \\ &= \frac{a_2}{a_1} \frac{1}{s(\tau_e s + 1)} \frac{\kappa_T}{\kappa_V} \\ &\quad + \left(\frac{a_3}{a_1} + \frac{a_4}{a_1} \kappa_E \right) \frac{\left(-\frac{b_2}{b_3} \kappa_T - K_p \right) s^2 + \left(\frac{b_2}{b_1} \kappa_T K_I \frac{1}{\tau_e s + 1} - K_I \right) s + \frac{b_2}{b_1} \kappa_T K_I \frac{1}{\tau_e s + 1}}{(\tau_g s + 1) s^3 - \frac{b_3}{b_1} K_p s^2 - \frac{b_3}{b_1} K_I s} \frac{1}{\kappa_V} \end{aligned} \tag{3.77}$$

The transient dynamic response for a step reference is given as:

$$\dot{\omega}_v(t=0) = s\lim_{s\to\infty} sf_3(s)\omega_{v\_des}(s) = \lim_{s\to\infty} s^2 f_3(s)\frac{1}{s} = \left(\frac{a_3}{a_1} + \frac{a_4}{a_1}\kappa_E\right)\left(-\frac{b_2}{b_3}\kappa_T - K_p\right)\frac{1}{\tau_g \kappa_V} \tag{3.78}$$

Then, still for a more general case when the vehicle speed reference is a ramp signal, the new reference-output transfer function is given by:

$$\begin{aligned} f_3(s) &= \frac{\omega_v}{\omega_{v\_des}} \\ &= \frac{a_2}{a_1}\frac{s}{s(\tau_e s+1)}\frac{\kappa_T}{\kappa_V} \\ &\quad + \left(\frac{a_3}{a_1} + \frac{a_4}{a_1}\kappa_E\right)\frac{\left(-\frac{b_2}{b_3}\kappa_T - K_p\right)s^3 + \left(\frac{b_2}{b_1}\kappa_T K_I \frac{1}{\tau_e s+1} - K_I\right)s^2 + \frac{b_2}{b_1}\kappa_T K_I \frac{s}{\tau_e s+1}}{(\tau_g s+1)s^3 - \frac{b_3}{b_1}K_p s^2 - \frac{b_3}{b_1}K_I s}\frac{1}{\kappa_V} \end{aligned} \tag{3.79}$$

The transient vehicle speed response is given by:

$$\dot{\omega}_v(t=0) = s\lim_{s\to\infty} sf_3(s)\omega_{v\_des}(s) = \lim_{s\to\infty} s^2 f_3(s)\frac{1}{s^2} = 0 \tag{3.80}$$

In this special case (EVT powertrain system), with a step reference of vehicle speed, the possible inverse dynamics (depends on the quantitative relationship of the variables in the term $-\frac{b_2}{b_3}\kappa_T - K_p$) from the transfer function $P_{22}(s)$ is transferred into the vehicle control dynamics. In other words, only an independent (decoupled with the electric generator) motor can absolutely prevent the transient dynamic disturbance from degrading the transient vehicle operations, no matter what the vehicle speed reference is.

In summary, the transfer function $P_{22}(s)$ with the 180° phase lag does not really induce the serious inverse transient dynamics for both the two system outputs ω_e and ω_v in the current power-split hybrid powertrain.

3.7.2 Transient Engine Operation Tracking (Transient Electric Torques/Power Spike Issue)

It has been clearly explained that the input-output transfer function $P_{22}(s)$ with the 180° phase lag in the hybrid powertrain system will not induce the inverse transient dynamics of the system outputs (ω_e and ω_v); however, it may bring in another dynamic response issue in the power-split hybrid powertrain control, which is, the engine operation (mainly, engine speed) dynamic response issue (or, from another viewpoint, transient electric torques/power spike issue).

This problem is especially obvious when we take some transient engine operation tracking with the SISO controls at the vehicle acceleration/deceleration scenarios, just like the case we discussed in the last section. For a typical vehicle acceleration case, the transient need of the high traction power usually drives the high-level hybrid powertrain control to assign a sudden engine operating "jump-up" (both engine speed and torque rising up) as well as a surge of the electric power as an assistant for vehicle accelerating. This sharp engine operation is even further amplified by the discrete-time dynamic analysis that the DP/SDP usually uses. In the hybrid operation emulation experiments shown in Section 3.5, the engine operating jump-up are actually "smoothed" within the whole DP sampling period (which are actually, the ramp responses), which in turns triggers a relatively moderate surge of the electric torque/power within an acceptable threshold.

However, in the real testing scenario, the pursuit of the optimality of the engine operations during transient will always ask for an as-rapid-as-possible engine jump-up (ideally, the pure step responses). In this fast transient case, i.e., when the proportional gain K_p is very large and $-\frac{b_2}{b_3}\kappa_T - K_p < 0$, the dynamics described by the transfer function $f_1(s) = T_g(s)/\omega_{e\_des}(s)$ will trigger an "inverse" dynamics in the system input T_g, and in turns a large motor torque spike T_m for compensating this transient inverse T_g. This spike will be added on the high motor torque surge that is originally used to speed

up the vehicle. Eventually, this combined high motor torque/power spike during transients may induce the extra challenges on the designed electric power/torque capacity.

As the other side of a coin, the electric torque/power spike issue can be also treated as an engine transient operation tracking issue. If the electric power/torque capacity is strictly limited and an extra large motor torque spike is truncated, the large generator torque inverse cannot be compensated any longer. In order to ensure the good track of the vehicle speed (which is the first-priority target for the hybrid power train control), the large generator torque inverse has to be abandoned (partly because of the electric torque/power limitation of the generator itself), i.e., a smaller gain K_p should be used. Consequently, the rapid engine speed dynamic response (the short rise time for a step reference) will be sacrificed. In a word, rejecting the electric power/torque spike will simultaneously trigger the engine speed transient tracking issue.

It is worth noting that in these discussions the large generator torque inverse will never induce any undesired inverse dynamics of the both engine speed and vehicle speed, as proved in Section 3.7.1. The existence of the large generator torque inverse will always support the fast engine speed tracking for step reference, but will slow down the vehicle speed tracking.

The above arguments are verified by the simulation results shown in Fig. 3.17-3.20, where the electric torques/powers are unlimited. Here various SISO controls with different control gains from the most conservative one to the most aggressive one are used to achieve different transient engine operation tracking. From Fig. 3.17, with various SISO controls the vehicle speeds are all relatively precisely tracked. Then, Figure 3.18 shows the engine transient control effects by the same feedforward but different PI control gains, with a step change between different engine operating (speed) points. Very obviously, the high control gains bring on the fast and accurate engine operating points tracking; however, the payment of the fast transient engine response is the overuse of the generator/motor torques. From Fig. 3.19, with the high PI gains the transient peak torque for the generator and motor exceed -100 *Nm* and 200 *Nm* respectively, which further induces the huge electrical power spike for the battery shown in Fig 3.20.

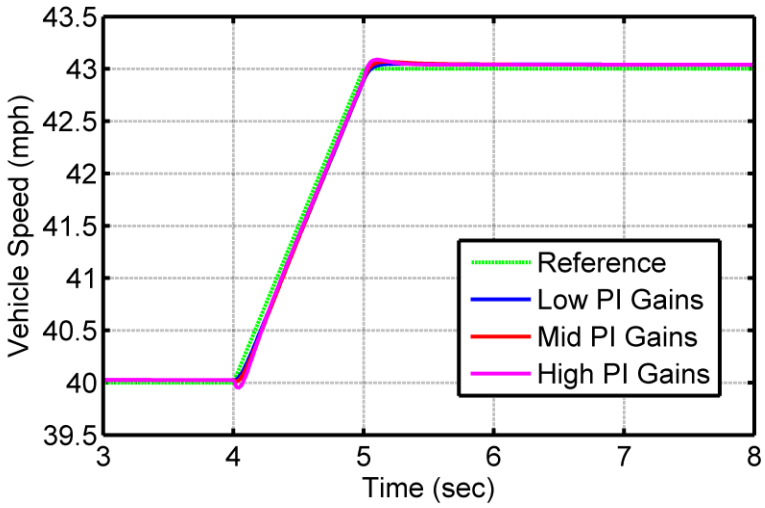

Fig. 3.17 Transient control simulations (SISO): vehicle operation trajectories

For the (ramp) vehicle speed tracking, there is actually not any significant excitation that may trigger a huge transient torque peak. The large "spike" on the motor torque is essentially from the interaction between T_g and ω_v. Because of the step command of the engine speed, a large negative generator torque peak is excited due to the negative interaction between T_g and ω_e. Further, the positive interaction between T_g and ω_v transfer this torque peak into the vehicle motion dynamics. Based on feedforward control law in (3.31), the system has to generate a positive motor torque peak to offset the effect of the generator torque peak.

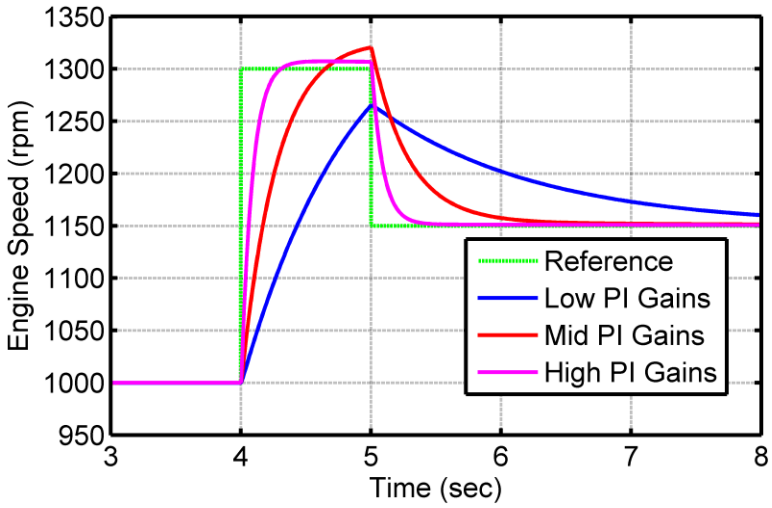

(a) Engine Speed

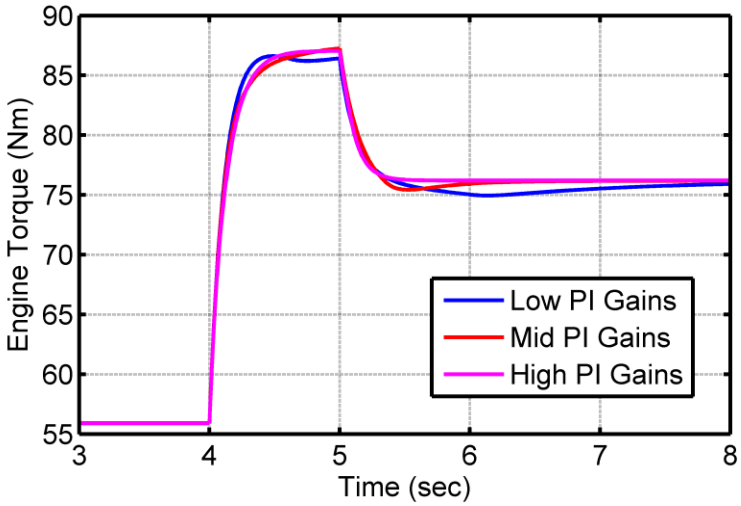

(b) Engine Torque

Fig. 3.18 Transient control simulations (SISO): engine operation trajectories

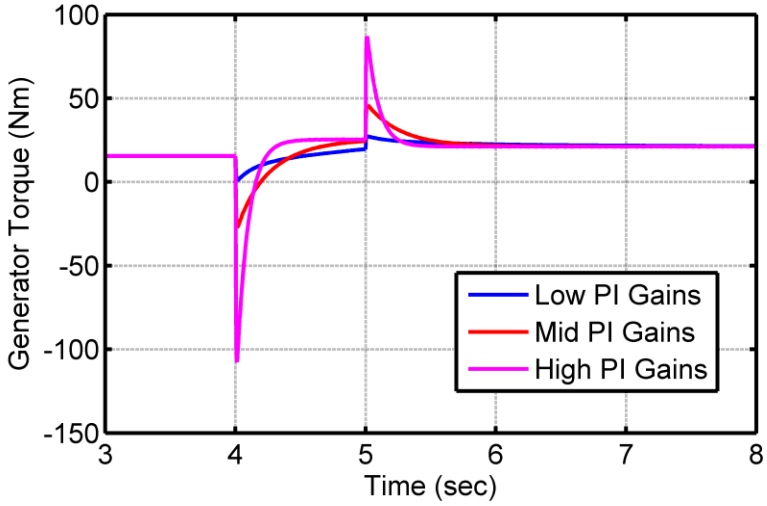

(a) Generator Torque

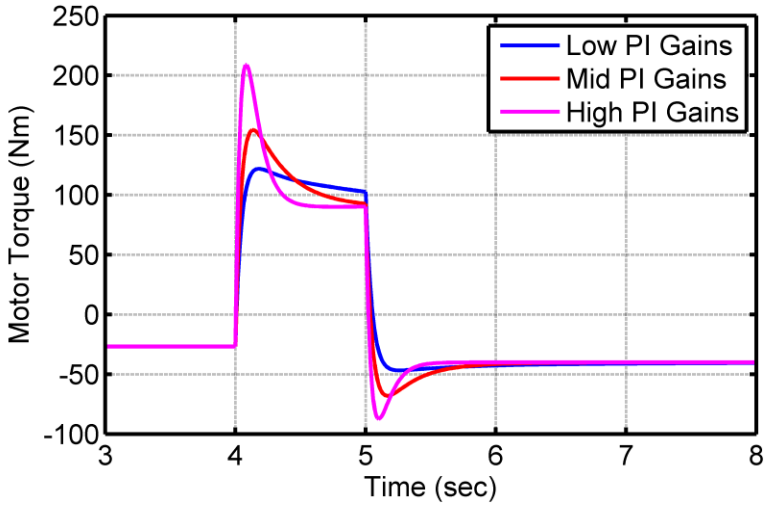

(b) Motor Torque

Fig. 3.19 Transient control simulations (SISO): electric machines operation trajectories

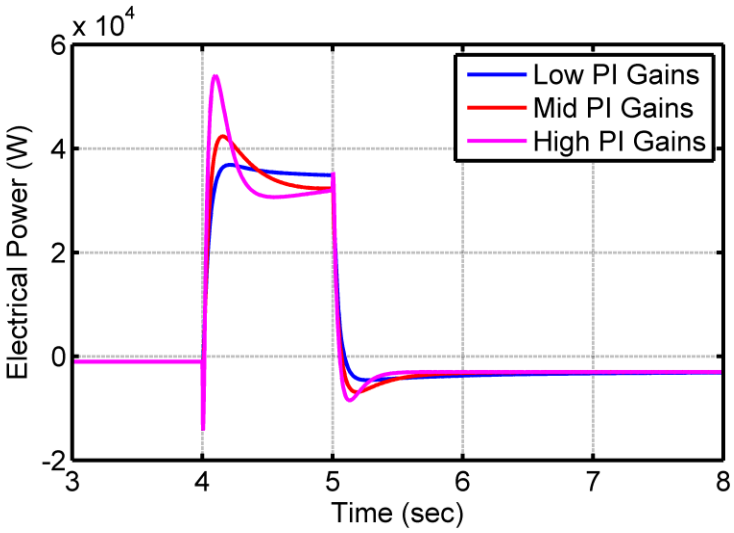

(a) Electric Power

Fig. 3.20 Transient control simulations (SISO): battery operation trajectories

The inherent conflict between the rapid engine operation tracking and high electric torques/power spikes naturally asks for a balance between the engine transient controls and the vehicle acceleration/deceleration power consumption (with the consideration of the electrical capacity constraints). With the highest priority, the driver's demands for the vehicle acceleration must be guaranteed by the hybrid powertrain system. Thus, with the SISO controls, due to the lack of the accurate control of the transient engine torque, we have to sacrifice the transient engine speed tracking to some extent to realize the moderate usage of the electrical power sources.

3.7.3 Engine Torque Dynamic Response and Steady-State Error

Except for pursuing an appropriate trade-off between the fast engine speed tracking and moderate electric torque/power usage, the desire of a good balance of the transient engine speed and torque tracking also asks for an accurate feedback-based engine torque control, instead of the purely feedforward control used in the current SISO middle level controls. The experimental results showed that the real-world engine torque/speed mapping is actually very sensitive to the environmental parameters such as temperature, humidity, frictions and so on. In many cases, the purely feedforward engine control (via the engine throttle/ fuel injection control) based on the engine map cannot drive the

engine torque to the desired points, which inevitably leads to the steady-state error. Owing to the dynamic interactions between engine speed and torque, the steady-state torque error will further degrade the dynamic response of the engine speed control. Therefore, how to introduce the feedback control into the engine torque, and maintain a good coordination of the engine transient speed and torque rather than trigger the instability issue of the multivariable control system, will be critical for the redesign of the middle-level control system.

3.8 MULTIVARIABLE MIDDLE-LEVEL CONTROLLER DESIGN

Based on the analysis in the last section, it is of interest to investigate if a multivariable middle-level control can improve the engine operation transient tracking performance. The main idea of the multivariable middle-level control is to introduce the feedback control into the engine torque control so as to:

(1) mitigate or eliminate the transient torque spike issue of the generator/motor by increasing the engine torque to compensate the saturated generator/motor torque by the electric constraints.

(2) more significantly, reach a good balance of the transient engine speed tracking and torque tracking, to generate faster and more accurate engine operation tracking for better realizing the optimal trajectory generated by the high-level energy control strategy, especially for realizing the more complicated and advanced high-level controls that will be introduced in Chapter 4.

First, since that the decoupling in (3.27) and (3.31) has been proved to be effective and precise enough for the vehicle speed control, this idea will be maintained in the new multivariable control design. In other words, the vehicle speed control is still realized by manipulating the motor torque T_m with the feedforward control design (3.31).

On this basis, the system dynamics of interest will be only the engine speed/torque dynamics, which are already simplified by neglecting the effect of the motor torque and

vehicle speed based on the analysis in Section 3.7.1,

$$\begin{aligned}\dot{\omega}_e &= \frac{b_2}{b_1}T_e + \frac{b_3}{b_1}T_g \\ \dot{T}_e &= \frac{1}{\tau_e}\left(T_{e\_cmd} - T_e\right)\end{aligned} \tag{3.81}$$

where the system outputs are ω_e and T_e and inputs are T_g and T_{e_cmd} . T_{e_cmd} is the corresponding engine torque of the real system input - engine throttle control command. The time constant of the engine torque dynamics $\tau_e = g\left(\omega_e, T_e\right)$ is a nonlinear function of the system states, which are not precisely identified but can be estimated within a range. It is worth noting that T_e used to be an input in the original system dynamics analysis in Section 3.6.1, but now become an output as the result of the introduction of the engine torque dynamics. More importantly, this change reflects the fact that the engine torque T_e is essentially also an important control target of the engine operation tracking, which cannot be simply treated as an open-loop mapping of the pre-defined engine throttle if we consider both the dynamic and static torque mapping errors. Because of the existence of the engine torque steady-state errors, physically even in the steady-state the engine torque control input T_{e_cmd} is not equal to the steady-state reference T_{e_des}.

To further unveil the limitation of the SISO-based mid-level control, let us still use the original feedforward plus feedback generator torque control, given by

$$T_{g\_cmd} = -\frac{b_2}{b_3}T_{e\_des} - K_p\left(\omega_{e\_des} - \omega_e\right) - K_I\int\left(\omega_{e\_des} - \omega_e\right)dt$$

Neglecting the generator torque dynamics since it is much quicker than the engine torque dynamics, and substituting this control into (3.81) yields:

$$\begin{aligned}\left(\dot{\omega}_e - \dot{\omega}_{e\_des}\right) &= \frac{b_3}{b_1}K_p\left(\omega_e - \omega_{e\_des}\right) + \frac{b_3}{b_1}K_I\int\left(\omega_e - \omega_{e\_des}\right)dt + \frac{b_2}{b_1}\left(T_e - T_{e\_des}\right) \\ \dot{T}_e - \dot{T}_{e\_des} &= \frac{1}{\tau_e}\left(T_{e\_cmd} - T_e\right)\end{aligned} \tag{3.82}$$

where the desired engine operation (ω_{e_des} , T_{e_des}) are treated as step reference.

Then, in the *s*-domain, we get

$$s^2\left(\omega_e-\omega_{e\_des}\right)-\frac{b_3}{b_1}K_p s\left(\omega_e-\omega_{e\_des}\right)-\frac{b_3}{b_1}K_I\left(\omega_e-\omega_{e\_des}\right)-\frac{b_2}{b_1}\frac{1}{\tau_e}\left(T_{e\_cmd}-T_e\right)=0 \tag{3.83}$$

In the original SISO mid-level control, the engine torque control is designed based on the open-loop mapping, which implies namely $T_{e\_cmd}=T_{e\_des}$; however, because there always exists the steady-state torque error owning to the inaccurate map, and torque deviation due to the speed tracking error, the corresponding engine torque of the engine throttle control command will be given by:

$$T_{e\_cmd}=T_{e\_des}+T_{e\_err}+m_{T_e}\left(\omega_e-\omega_{e\_des}\right) \tag{3.84}$$

where T_{e_err} is the engine torque error induced by the map inaccuracy, and m_{T_e} is the conversion factor from the speed tracking error to the corresponding engine torque deviation. Here m_{T_e} is time-varying as the engine speed varies during transients.

Substituting (3.84) into (3.83) yields the closed-loop system dynamics (without considering the other system disturbances):

$$s^2\left(\omega_e-\omega_{e\_des}\right)-\frac{b_3}{b_1}K_p s\left(\omega_e-\omega_{e\_des}\right)=\left(\frac{b_3}{b_1}K_I+\frac{b_2}{b_1}\frac{m_{T_e}}{\tau_e}\right)\left(\omega_e-\omega_{e\_des}\right)+\frac{b_2}{b_1}\frac{1}{\tau_e}\left(T_{e\_des}+T_{e\_err}-T_e\right) \tag{3.85}$$

For the engine speed tracking, it is obvious that we may need a very large integral gain K_I (in turn, a large proportional gain K_p) to keep the coefficient $\frac{b_3}{b_1}K_I+\frac{b_2}{b_1}\frac{m_{T_e}}{\tau_e}$ always negative and eliminate the effect of the engine torque error, so as to maintain the system stability and the relatively fast speed convergence; however, the large K_p and K_I will easily induce both the transient system vibrations and the electric power spike issue (as explained in Section 3.7). For the engine torque tracking, the mapping-based open-loop control can neither improving the dynamic response nor reducing the steady-state errors.

In order to improve both the engine speed and torque tracking, the mid-level control will be re-designed by introducing the feedback control into the engine torque controller,

as interpreted as follows.

At first, the system in (3.82) is re-written in the state space form:

$$\begin{aligned}\dot{x}_0 &= x_1 \\ \dot{x}_1 &= \frac{b_3}{b_1} K_p x_1 + \frac{b_3}{b_1} K_I x_0 + \frac{b_2}{b_1} x_2 \\ \dot{x}_2 &= -\frac{1}{\tau_e} x_2 + \frac{1}{\tau_e} u\end{aligned} \tag{3.86}$$

where the states $x_0 = \int \left(\omega_e - \omega_{e\_des} \right) dt$, $x_1 = \omega_e - \omega_{e\_des}$ and $x_2 = T_e - T_{e\_des}$, the input $u = T_{e\_cmd} - T_{e\_des}$, which presents the feedback part of the engine torque control command. The states-space system seems to be of a form of linear system; however, the existence of the nonlinear function of the system states $\tau_e = g\left(\omega_e, T_e \right)$ makes the system a nonlinear system with some uncertainty, since $g\left(\omega_e, T_e \right)$ cannot be precisely identified.

In this system, the control objective is transferred to stabilize the states $\left(x_1, x_2 \right)$ to the origins by manipulating the only input *u* with a state feedback control law. The special system dynamics in (3.86) inspire us to leverage the design of the sliding-mode based nonlinear control to realize the system stabilization with enough robustness to cover the system uncertainty.

Making use of the sliding mode control design, a sliding manifold is defined as

$$S = k x_1 + \frac{b_2}{b_1} x_2 = 0 \qquad (k > 0) \tag{3.87}$$

In this sliding manifold, we actually have the dynamics

$$k x_1 + \dot{x}_1 - \frac{b_3}{b_1} K_p x_1 - \frac{b_3}{b_1} K_I x_0 = 0$$

$$\text{i.e., } \dot{x}_1 + \left(k - \frac{b_3}{b_1} K_p \right) x_1 - \frac{b_3}{b_1} K_I x_0 = 0 \tag{3.88}$$

which can eventually drive the state x_1 to asymptotically converge to the origin, as well as the state x_2.

Then, a state feedback control law is designed to bring the trajectory to this manifold

and maintain it there. A Lyapunov function candidate $V = \frac{1}{2}S^2$ is generated and we have

$$\begin{aligned}\dot{V} = S\dot{S} &= S\left(k\dot{x}_1 + \frac{b_2}{b_1}\dot{x}_2 \right) = S\left(k\frac{b_3}{b_1}K_p x_1 + k\frac{b_3}{b_1}K_I x_0 + k\frac{b_2}{b_1}x_2 - \frac{1}{\tau_e}\frac{b_2}{b_1}x_2 + \frac{1}{\tau_e}\frac{b_2}{b_1}u \right) \\ &= S\left(k\frac{b_3}{b_1}K_p x_1 + k\frac{b_3}{b_1}K_I x_0 + k\frac{b_2}{b_1}x_2 - \frac{1}{\tau_e}\frac{b_2}{b_1}x_2 \right) + S\frac{1}{\tau_e}\frac{b_2}{b_1}u \\ &\le |S|\left| k\frac{b_3}{b_1}\left(K_p x_1 + K_I x_0 \right) \right| + |S|\left| \frac{b_2}{b_1}\left(k - \frac{1}{\tau_e} \right)x_2 \right| + S\frac{1}{\tau_e}\frac{b_2}{b_1}u\end{aligned} \tag{3.89}$$

Now we can design the feedback control law

$$u = -\mathrm{sgn}(S)\left[\left| k\frac{b_3}{b_1}\left(K_p x_1 + K_I x_0 \right) \right| |\tau_e| + \left| (k\tau_e - 1)x_2 \right| + \beta_0 \right] \tag{3.90}$$

where β_0 is a small positive constant.

When $x_1 \to 0$ and $x_2 \to 0$, the feedback control

$$u \approx -\mathrm{sgn}(S)\beta_0 \tag{3.91}$$

In the experimental implementation, in order to mitigate the chattering, instead of the sign function $\mathrm{sgn}(S)$, a saturation function is used,

$$\mathrm{sat}(S) = \begin{cases} \dfrac{S}{p} & if\ |S| < p < 1 \\ \mathrm{sgn}(s) & if\ |S| > p \end{cases} \tag{3.92}$$

Actually, the ratio *k* can be treated as a weighting factor that adjusts the tradeoff between the simultaneous engine speed error and engine torque error. A smaller *k* will produce a relatively slower engine speed tracking but smaller transient engine torque spike. Rising *k* will increase the sensitivity of the engine speed error in this sliding surface, which may result in that the transient engine speed control other than the torque control dominates the mid-level controls.

Essentially, the multivariable middle-level controller leverages both the system-decoupling thinking of the SISO controls and the robust stabilization methodology from the Lyapunov-based Sliding-Mode control. For both the vehicle and engine control dynamics, the multivariable middle-level controller inherits the system-decoupling-based

electric motor and generator controls, but introduces the feedback control into the engine torque control design. For the engine torque feedback control, the Sliding-Mode control logic is utilized to stabilize both the engine torque and speed (i.e., realize the stable engine torque and speed tracking). Physically, the design of the sliding mode manifold is equivalent to the dynamic weighting of the engine speed and torque dynamic responses, and hence, by selecting a proper ratio gain k, a good compromise of the engine speed/torque tracking can be reached to better realize the optimal control targets generated by the high-level energy management strategy. Further, coordinating the sliding mode ratio k and generator PI control gains K_p and K_I will give us more flexibilities to pursue a good balance of fast engine transient operation and moderate electric torque/power usage.

3.9 EXPERIMENTS RESULTS (TRANSIENT CONTROL TESTS)

With this state feedback control law designed in Section 3.8, the experimental comparisons between a SISO mid-level control system and multivariable (MV) middle-level controllers (with relatively low ratio gain k and high ratio gain k) at a typical vehicle acceleration case are shown in Fig. 3.21-3.26. From Fig. 3.21 both the SISO and MV mid-level controls can achieve excellent tracking for the vehicle speed, but the MV mid-level control achieves an obviously better transient tracking for both the engine speed and engine torque in Fig. 3.22. Especially in Fig. 3.22(b), the utilization of the MV control not only realizes the faster engine transient dynamics, but also eliminates the steady-state torque errors that the SISO controls cannot avoid. In addition, Figure 3.22 presents that the multivariable mid-level controller with the high k can achieve even better engine speed transient tracking than the one with relatively low k; however, the engine torque spike at the starting stage of transient torque tracking induced by the former one is also larger than the latter one.

Even with the better transient engine speed tracking performance, the MV controls do not overuse the generator and motor torque/power and battery power, compared with

the SISO control in Fig. 3.24-3.26. This should attribute to the surge of the engine torque in the starting stage that meets the torque demand for the engine acceleration. Actually, because the SISO control and the MV controls used the same PI control gains K_p and K_I in these experiments, all of these controllers eventually trigger the similar electric torque/power spikes. If even smaller electric torque/power spikes are expected, the combination of the smaller PI control gains (K_p and K_I) and a large ratio gain k will be a good choice, for holding a relatively fast engine transient operation when the electric torque/power spikes are further mitigated.

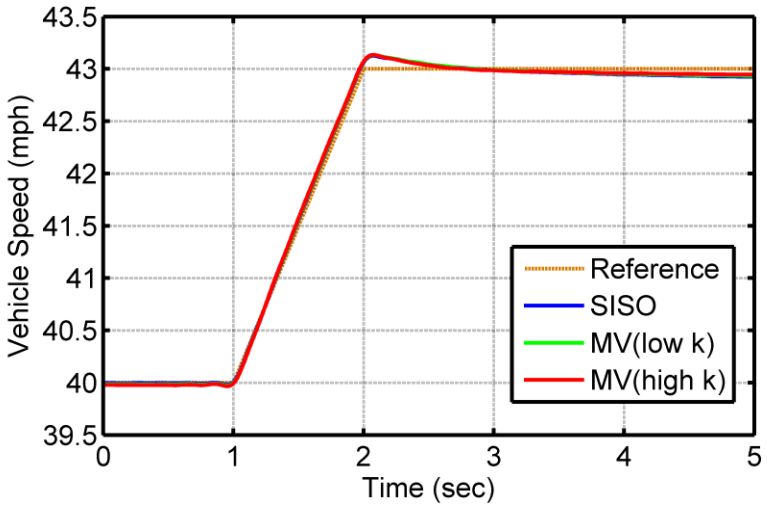

Fig. 3.21 Transient control experiments (SISO vs MV): vehicle operation trajectories

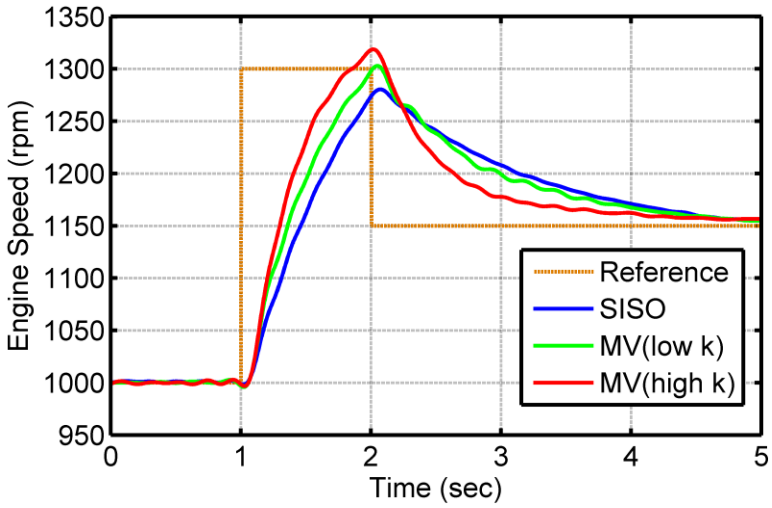

(a) Engine Speed

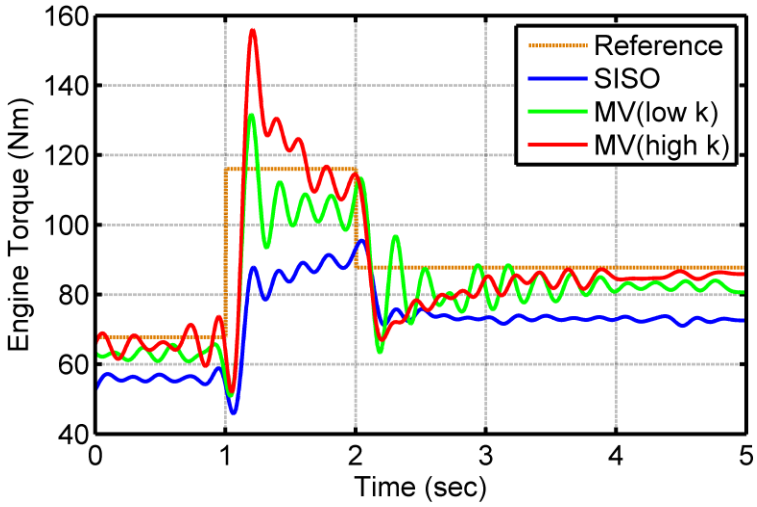

(b) Engine Torque

Fig. 3.22 Transient control experiments (SISO vs MV): engine operation trajectories

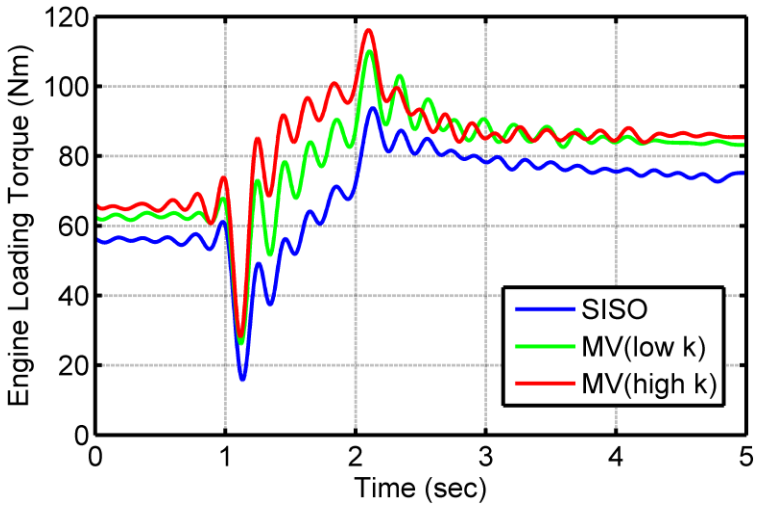

Fig. 3.23 Transient control experiments (SISO vs MV): dynamometer operation trajectories

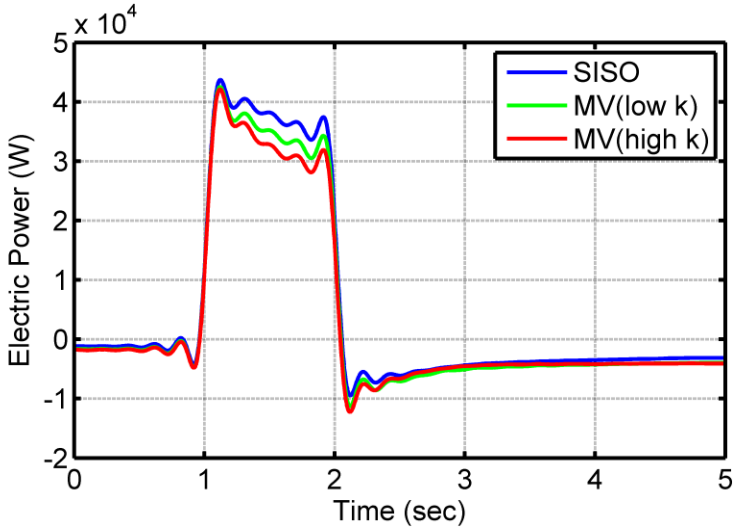

Fig. 3.24 Transient control experiments (SISO vs MV): battery operation trajectories

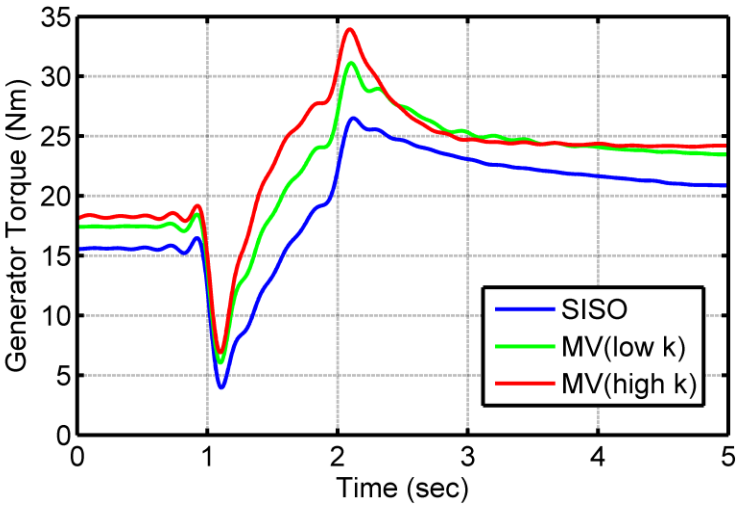

(a) Generator Torque

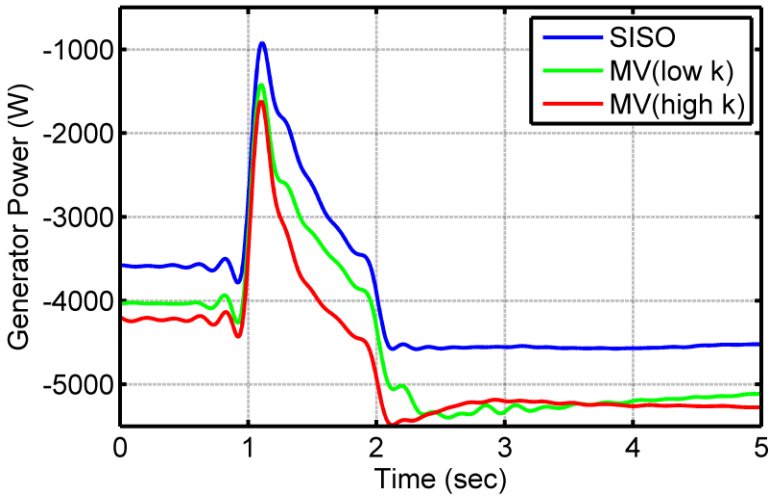

(b) Generator Power

Fig. 3.25 Transient control experiments (SISO vs MV): generator operation trajectories

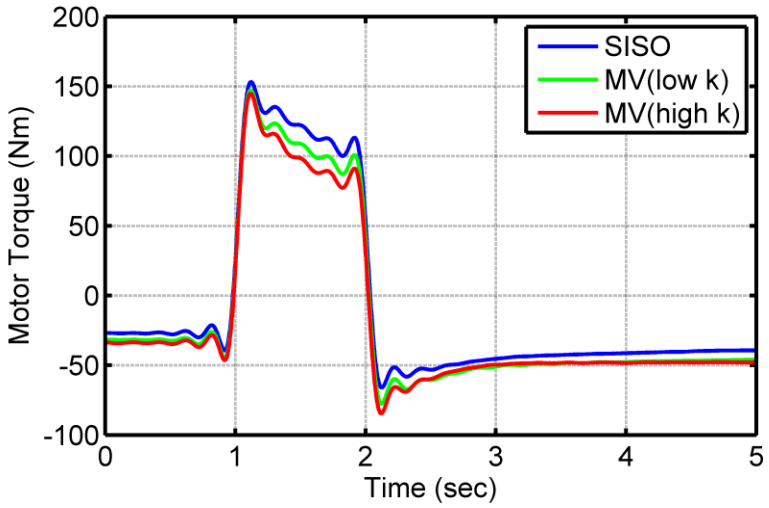

(a) Motor Torque

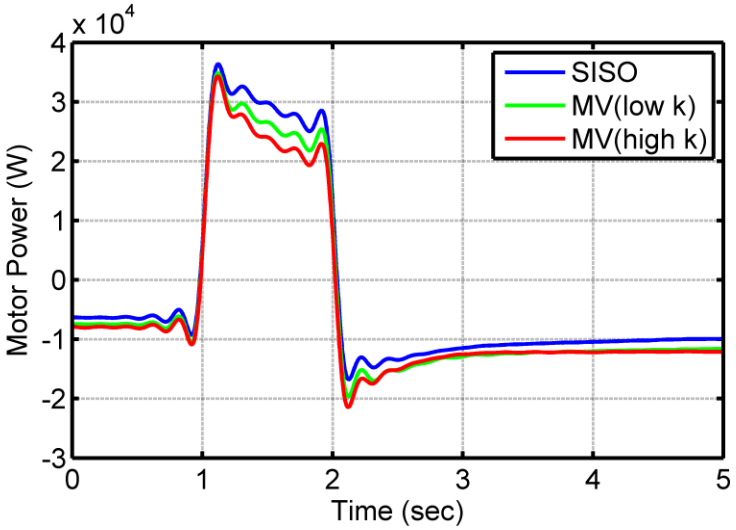

(b) Motor Power

Fig. 3.26 Transient control experiments (SISO vs MV): motor operation trajectories

All in all, except for the advantage of eliminating the electric torques/power spikes, from the viewpoint of experimental implementation, the multivariable middle-level controller also provides us a more accurate engine torque control with rejection of the possible engine torque shifts from the static engine speed-torque map. With the multivariable middle-level controller, the transient engine speed and torque tracking are well-coordinated, and on this basis, a faster and optimal engine operation tracking will be

accomplished for better realizing the optimal trajectory generated by the DP/SDP-based high level control.

3.10 CONCLUSION

This chapter presents the design and experimental investigation of the hybrid powertrain control within a rapid prototyping hybrid powertrain research platform. Based on a transient hydrostatic dynamometer, the research platform can mimic the dynamic behaviors of any kind of hybrid power sources and various hybrid architectures. To facilitate the control design, the detailed dynamic models of the virtual hybrid powertrain system are built. On this basis, with an adaptive driver model, various controllers corresponding to the three levels of the research platform, which combines a DP based energy management strategy, a SISO hybrid powertrain control and a feedback linearization based dynamometer torque control, are designed and integrated. The experimental results demonstrate the capability of the proposed hybrid powertrain control system for the hybrid operation emulation for both the low-inertia gasoline engine and the high-inertia diesel engine. In order to better improve the transient performance of the whole control system, the transient dynamics of the power-split hybrid powertrain is comprehensively analyzed and the engine speed/torque dynamic response issue (equivalently, the transient electric torque/power spike issue) is unveiled. Based on the dynamic analysis, a multivariable mid-level (hybrid powertrain) controller is designed to pursue a good balance of fast transient engine speed/torque tracking and moderate usage of the electric torque/power within the electrical capability. The experimental results demonstrate that this multivariable control can achieve faster engine speed tracking and more accurate engine torque tracking, with similar transient electric torques/power spikes as the SISO mid-level control.

Chapter 4

Real-Time Optimal Control of the Fuel Efficiency with a SDP-ES Hybrid Energy Management Strategy

4.1. RESEARCH OBJECTIVE

By optimizing the dynamic operations of the ICE and the alternative energy sources at every time instant, the hybrid energy management strategies play a crucial role which decides to what extent to what extent the hybrid powertrain is able to improve the fuel efficiency and reduce emissions. In essential, the hybrid energy management is a global optimization problem that strongly depends on the given operating paths and time horizon, but asks for a real-time control with instantaneous decisions based on some local feedbacks. This in turn brings on a series of challenges for the energy management strategy design, including:

1) In terms of the optimal control target, how to attain a good balance between the "absolute" global optimality for some specific driving cycles and the instantaneous control actions which are capable to realize the optimizations for the uncertain driving cycles (usually from a statistic viewpoint) ;

2) In terms of the optimal control accuracy, how to obtain a trade-off between the high optimization accuracy which inevitably asks for the precise system models and the huge computational burden that is extremely sensitive to the model dimensions and grid size;

3) In terms of the controller implementation, how to combine the offline control design based on the engine efficiency maps and the online control design based on the

real-time measurement of the system outputs.

The existing hybrid energy optimization algorithms, including rule-based control, dynamic programming/ stochastic dynamic programming (DP/SDP), the adaptive equivalent consumption minimization (A-ECMS), the model predictive control (MPC), and so on all contribute to address one or more aspects of the hybrid energy optimization problem. However, how to get a good balance among all the aspects of the hybrid energy optimization problem still remains inaccessible.

As an attempt to further investigate a fast and accurate hybrid energy management strategy, a Stochastic Dynamic Programming – Extremum Seeking (SDP-ES) optimization algorithm is proposed and developed in this chapter. This algorithm synthesizes the offline stochastic dynamic programming to ensure the approximate global optimality and battery SOC sustainability, and employs the extremum seeking in real-time to provide a better local optimization. The SDP-ES combines the advantages of both the SDP and ES algorithms, but "loosens" the limitations for each method and hence, reduces their disadvantages. This algorithm is characterized by two notable properties:

1) State-plus-output feedback: not only the system states (engine speed, vehicle speed and battery SOC) but also the system outputs (fuel consumptions and emissions) can be fed back to generate the control actions. Particularly, the states are sent to the SDP control law, and the outputs are sent to the ES control law. This state-plus-output feedback can be realized with the rapid prototyping hybrid powertrain research platform that has been designed and built in the Chapter 2 and 3. In this research platform, the state-of-the-art fuel consumption and emission measurement instruments are employed for system output measurements, as shown in Fig. 4.1;

2) Semi-Model-Based Control: although the system inputs-states models (which consist of the hybrid powertrain dynamics, energy storage dynamics of the alternative power sources and vehicle driveline dynamics) can be attained to generate the SDP state-feedback control law, it is difficult to obtain the accurate models between the inputs/states and outputs (which consist of the engine combustion dynamics and efficiency maps). The extremum seeking is essentially a non-model-based adaptive control, which will on-line search the local optimal point by means of output feedback.

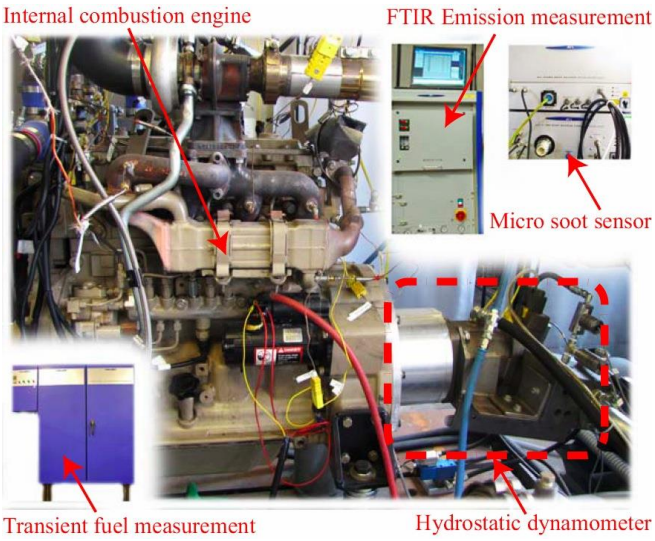

Fig. 4.1 The complete real-time measurement instruments in the research platform

In this chapter, for the need of the analysis, the complete dynamic models of the power-split powertrain are first formulated in Section 4.2. Section 4.3 analyzes the existing optimization algorithms for the power-split application, and summarizes the current challenges for further improving the optimization performance based on these algorithms (mainly, SDP). Targeted at overcoming these challenges, in Section 4.4, a SDP-ES optimization algorithm is proposed and designed. The detailed designs of its two main components (SDP controller and ES controller) are introduced respectively, and their combination and cooperation are further described. In Section 4.5, the simulation results show that this proposed SDP-ES algorithm is capable of producing better fuel efficiency than the original SDP, without loss of the battery SOC sustainability.

4.2. HYBRID POWERTRAIN MODELING

To meet the demands of the energy optimization algorithm design, the dynamic model of the power-split HEV built in Section 3.3 needs to be simplified and transformed to the compact form(3.44), which is:

$$\dot{\omega}_v = \frac{a_2}{a_1}T_e + \frac{a_3}{a_1}T_g + \frac{a_4}{a_1}T_m - \frac{a_4}{a_1}\alpha\omega_v^{\,2} - \frac{a_4}{a_1}\beta$$
$$\dot{\omega}_e = \frac{b_2}{b_1}T_e + \frac{b_3}{b_1}T_g + \frac{b_4}{b_1}T_m - \frac{b_4}{b_1}\alpha\omega_v^{\,2} - \frac{b_4}{b_1}\beta \qquad (4.1)$$
$$\dot{SOC} = -\frac{V_{batt}}{2Q_{batt}R_{batt}} + \frac{\sqrt{V_{batt}^{\,2} - 4\left[-T_g\omega_g\eta_g^{\,k1} + T_m\omega_m\eta_m^{\,k2}\right]R_{batt}}}{2Q_{batt}R_{batt}}$$

Or, simply,

$$\dot{x}_{HV} = f_{HV}\left(x_{HV}, u_{HV}\right) \qquad (4.2)$$

where, $x_{HV} = \left[\omega_v \quad \omega_e \quad SOC\right]^T$ are the system states and $u_{HV} = \left[T_e \quad T_g \quad T_m\right]^T$ are the system inputs. f_{HV} is the nonlinear time-invariant system dynamics.

Further, with the fuel consumption $\dot{m}_f$, micro soot emission $\dot{m}_{ms}$ and gaseous emissions $\dot{m}_{gas}$ (or some integrated performance index of the three variables with some weighting factors) as the system outputs, the dynamics between the system outputs and inputs/states are given by:

$$\dot{y}_{ICE} = g_{ICE}\left(y_{ICE}, x_{HV}, u_{HV}\right) \qquad (4.3)$$

where, $y_{ICE} = \left[\dot{m}_f \quad \dot{m}_{ms} \quad \dot{m}_{gas}\right]^T$ is the system outputs and g_{ICE} is the dynamics between the system outputs (fuel consumption and emissions), and inputs (engine torque) and states (engine speed). Based on our knowledge of the engine combustion, the dynamic system in (4.3) is asymptotically stable with respect to a group of equilibrium points. Hence, in many cases, it is also simplified to a static mapping between the inputs/states and outputs, given by:

$$y_{ICE} = \bar{g}_{ICE}\left(x_{HV}, u_{HV}\right) \qquad (4.4)$$

where $\bar{g}_{ICE}$ denotes the static mapping relationship between these output equilibrium points and the corresponding states and inputs.

4.3. ANALYSIS OF THE REAL-TIME ENERGY MANAGEMENT STRATEGIES

With regards to the engine operating optimization in the high-level system, extensive investigations have been conducted, as mentioned in Section 1.5.1. Dynamic programming is usually not capable of real-time optimizing arbitrary vehicle operating paths, in spite of its capacity in terms of absolute global optimality of a pre-known path. With respect to the real-time optimization of the unknown vehicle operating paths, some real-time optimization approaches have been studied. The rule-based control [46] employs a set of event-triggered rules to on-line manipulate the operation of the hybrid powertrain to realize relatively high fuel efficiency; however, it does not provide any guarantee on the global optimality; the A-ECMS [57]-[58] converses the instantaneous electric power into estimated equivalent fuel consumption to realize the instantaneous minimization of the gross fuel consumptions, which effectively simplifies the optimization problem. The optimality of A-ECMS only depends on the choice (or, adaption) of the precise energy conversion factor which is very difficult to be attained for implementation, albeit existent in theory [58]. The MPC algorithm [54]-[55] formulates the global optimization problem into an optimization problem over a finite time window based on predictive models, and further, reduces the nonlinear optimization into a linear quadratic program problem for which the analytical real-time solutions exist. The optimality of the MPC algorithm is limited by the assumption about the future vehicle speed (or, power demand) in the prediction horizon. Compared with the above algorithms, the SDP [47]-[52], which globally optimizes the fuel efficiency by searching through all feasible control actions along an infinite time period (with a cost discounting factor) for all the possible states (with the corresponding probabilities), presents some distinguished advantages in spite of the associated huge offline computation. Theoretically, with the precise statistic knowledge of the future paths, the SDP is able to produce the optimal control from the statistic viewpoint. Therefore, the SDP algorithm can be chosen as a method to approach the path with the global energy optimality and battery SOC sustainability. The characteristics of every optimization algorithm are

summarized in Table 4.1.

TABLE 4.1 Characteristics of the existing real-time optimization algorithm

Algorithm	Optimality	Computation Burden
Rule-Based	Relatively low: without any guarantee of the global optimization	Very low
A-ECMS	Relatively high: depends on the choice (or, adaption) of the precise energy conversion factor	Relatively high
MPC	Relatively high: limited by the assumption of the future vehicle speed (or, power demand) in the prediction horizon.	Relatively low
SDP	High: theoretically can produce the global optimal control in the statistic viewpoint	High: with the high model dimension and small step size for discretization

Even with a good expectation for the global energy optimality, there are some limitations that degrade the theoretical advantages of the SDP algorithm, including:

1) The “curse of dimensionality”: when the state variables increase in number, the offline computation load will increases exponentially. This greatly compounds the difficulty of the implementation of the SDP. However, along with the increase of the degree of freedom of the hybrid vehicle, the increase of the state variable numbers of the dynamic models cannot be avoided. Especially, the application of the power-split hybrid vehicle, which is a 3rd-order dynamic system as shown in (4.1), increases the system state variables and induces serious computation problems. To address the computation problems, some trade-offs are introduced to simplified the system models, for example, limiting the engine power on a pre-defined operating curve. However, it will inevitably

sacrifice the global optimality of the SDP to some extent.

2) The negative effect of the large grid size: similarly, with purpose of reducing the computation load, the state variables and inputs (engine power, battery SOC and vehicle speed) will be discretized with large grid size. It will result in the generated optimal controls deviate from the actual optimal points due to the rough interpolations in implementation

3) The lack of the precise system output model: because of the lack of the complicated engine combustion dynamics $g_{ICE}\left(x_{HV},u_{HV}\right)$, instead an engine map $\bar{g}_{ICE}\left(x_{HV},u_{HV}\right)$ that represents the static relation between the engine torque, speed and fuel consumption/ emissions, is usually used for the offline SDP optimization. This simplification also leads to some optimization deviations, because it is very difficult to obtain the accurate engine maps, especially for the transient emissions.

Because of the above deficiencies of the SDP algorithm, the accumulated control errors may degrade its optimality.

4.4. DESIGN OF THE STATE-PLUS-OUTPUT-FEEDBACK SDP-ES OPTIMIZATION ALGORITHM

To make up the inherent deficiencies of the SDP algorithm, an output-feedback based optimization tool, extremum seeking (ES) is introduced to locally compensate the SDP optimal control, so as to drive the operating points towards the direction that further reduces the fuel consumption. Extremum seeking, is a real-time optimization method which makes use of a periodic perturbation to dynamically search a maximum/minimum from an uncertain reference-to-output equilibrium map of a dynamic system. This dynamic system can be a general nonlinear system if only its reference-to-output equilibrium map has a maximum/ minimum, and all the equilibria are locally stable [62]-[64], [92]-[95].

4.4.1 SDP-ES optimization Algorithm Design

The SDP-ES algorithm utilizes a SDP-based state-feedback control as a reference term and injects a "local" feedback term via ES to compensate the control commands from SDP. The basic schematic of the SDP-ES optimization is shown in Fig.4.2.

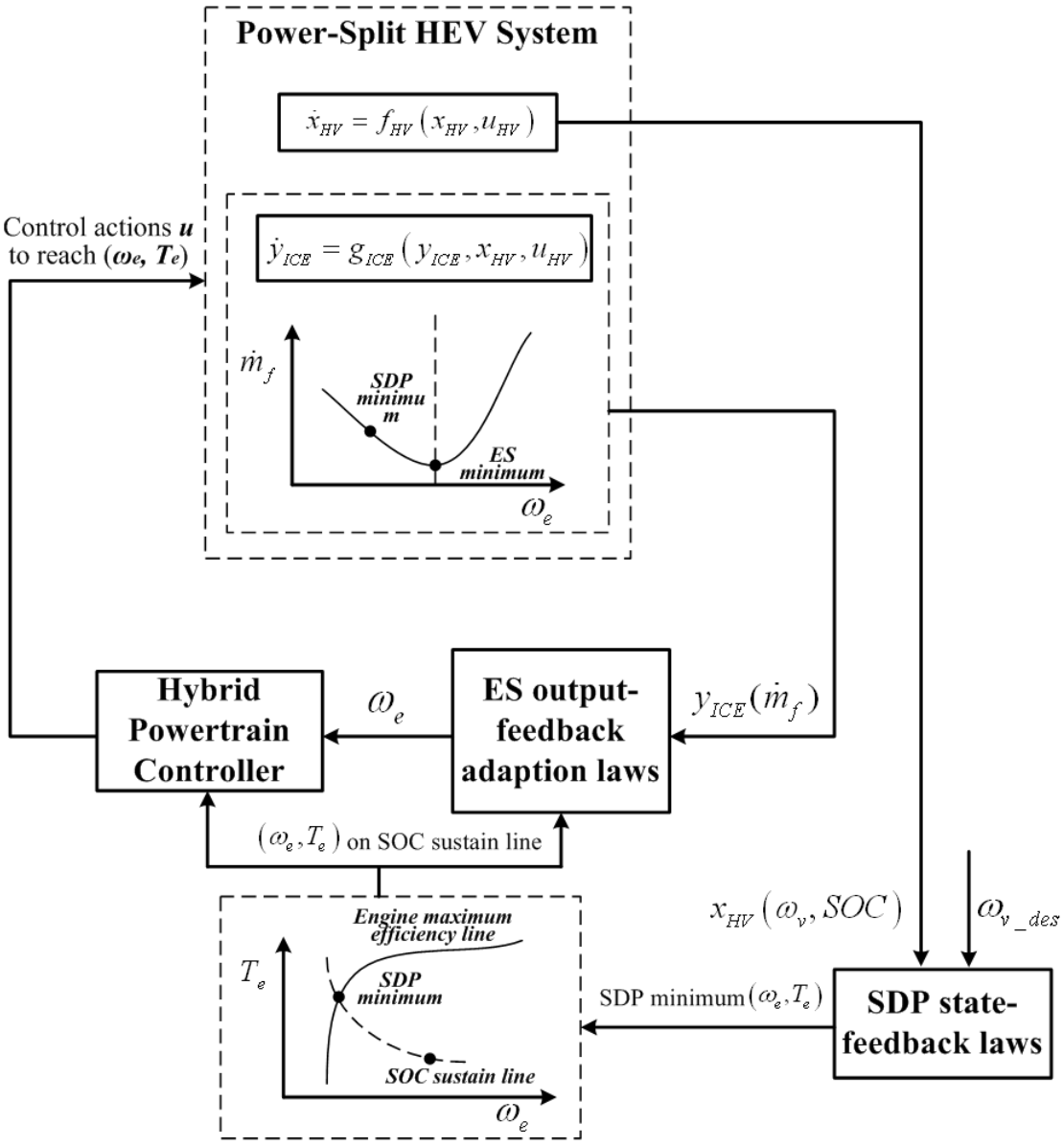

Fig. 4.2 The schematic of the SDP-ES energy optimization algorithm

With the state feedbacks from the HEV system and speed (or power) demands

ω_{v_des} from the driver model, the SDP will search through the control laws in an offline look-up table, to find a corresponding optimal engine power P_e, which further corresponds an operating point $\left(\hat{\omega}_e, \hat{T}_e\right)$ on a pre-defined curve. Here, we call $\left(\hat{\omega}_e, \hat{T}_e\right)$ the "SDP minimum" that means the minimal fuel consumption point calculated by the SDP. Based on a known SDP minimum, a SOC sustaining line can be generated based on the hybrid vehicle model. The battery SOC of all the points along this line can be maintained the same as the SDP minimum. From (4.1), the SOC sustaining line is the collection of the operating points that satisfy:

$$P_{elec} = -T_g \omega_g \eta_g^{\ k1} + T_m \omega_m \eta_m^{\ k2} = -\hat{T}_g \hat{\omega}_g \eta_g^{\ k1} + \hat{T}_m \hat{\omega}_m \eta_m^{\ k2} \tag{4.5}$$

where $T_g \omega_g$ and $T_m \omega_m$ are the electric generator/motor powers of the arbitrary points on the SOC sustaining line, and $\hat{T}_g \hat{\omega}_g$ and $\hat{T}_m \hat{\omega}_m$ are the electric generator/motor powers of the SDP minimum. The detailed procedure to generate the operating points along the SOC sustaining line is given by:

To formulate the SOC sustaining line, the electric torques corresponding to the given vehicle speed ω_{v_des} and SDP minimum $\left(\hat{\omega}_e, \hat{T}_e\right)$ are first given by:

$$\begin{aligned} \hat{T}_g &= \left[-\frac{a_1}{a_4} \dot{\omega}_{v\_des} + \frac{b_1}{b_4} \dot{\hat{\omega}}_e + \left(\frac{a_2}{a_4} - \frac{b_2}{b_4} \right) \hat{T}_e \right] \Big/ \xi_1 \\ \hat{T}_m &= \left[-\frac{a_1}{a_3} \dot{\omega}_{v\_des} + \frac{b_1}{b_3} \dot{\hat{\omega}}_e + \left(\frac{a_2}{a_3} - \frac{b_2}{b_3} \right) \hat{T}_e + \xi_2 \left(\alpha \omega_{v\_des}^{\ 2} + \beta \right) \right] \Big/ \xi_2 \end{aligned} \tag{4.6}$$

where, $\xi_1 = b_3/b_4 - a_3/a_4$, $\xi_2 = b_4/b_3 - a_4/a_3$.

Further, the electric power defined by the SDP minimum is:

$$P_{elec} = -\hat{T}_g \left[\frac{R+S}{S} \hat{\omega}_e - \frac{R}{S} K_{ratio} \omega_{v\_des} \right] \eta_g^{\ k1} + \hat{T}_m K_{ratio} \omega_{v\_des} \eta_m^{\ k2} \tag{4.7}$$

Solving (4.1), (4.5) and (4.7) yields the relationship between ω_e and T_e along the SOC sustaining line:

$$T_e = \frac{\left[\begin{array}{l} -P_{elec} - \sigma_1 \xi_2 \left(-\frac{a_1}{a_4}\dot{\omega}_{v\_des} + \frac{b_1}{b_4}\dot{\omega}_e \right) \\ +\sigma_2 \xi_1 \left[-\frac{a_1}{a_3}\dot{\omega}_{v\_des} + \frac{b_1}{b_3}\dot{\omega}_e + \xi_2 \left(\alpha {\omega_{v\_des}}^2 + \beta \right) \right] \end{array}\right]}{\sigma_1 \xi_2 \left(\frac{a_2}{a_4} - \frac{b_2}{b_4} \right) - \sigma_2 \xi_1 \left(\frac{a_2}{a_3} - \frac{b_2}{b_3} \right)} \tag{4.8}$$

where, $\sigma_1 = \left[\omega_e \left(R+S \right)/S - K_{ratio}\omega_{v\_des} R/S \right] {\eta_g}^{k1}$, $\sigma_2 = K_{ratio}\omega_{v\_des}{\eta_m}^{k2}$

Equation (4.8) is a continuous function that formulates every engine operating point $\left(\omega_e, T_e\right)$ along the SOC sustaining line. Here, to ensure the SOC sustaining line is unique for a specific engine power, the engine torque T_e should be and only be the function of ω_e. To satisfy this condition, the term $\dot{\omega}_e$ in (4.8) must be neglected [96]-[97], which is equivalent to neglecting the engine motion dynamics. This simplification may induce some slight SOC deviations in the extremum seeking process from the SDP generated SOC. To compensate these deviations, some penalty terms about the transient power consumption for accelerating/decelerating the engine can be added onto the static fuel consumption, as part of the system output feedback.

Then, between two successive SDP commands, with the system outputs as the feedback, the ES control will adapt the optimal speed ω_e to minimize the fuel consumption (or emissions) along the calculated SOC sustaining line. Here, a hybrid powertrain controller introduced in Chapter 3 is designed to generate the control *u* (engine throttle and torques T_m and T_g) to realize any engine operating point $\left(\omega_e, T_e\right)$ caught by the ES. After a short adaptive transient, the ES optimal control can find a new minimum point $\left(\omega_e^*, T_e^*\right)$, along the fuel consumption curve defined by the SDP (i.e., the SOC sustaining line).

In summary, different form the state-feedback and model- based SDP, the improved SDP-ES is a state-plus-output-feedback, semi-model-based optimization, which combines SDP and ES into one feedback controller. Essentially, the SDP can be treated as a "reference" component in the feedback control that gives a control action profile based on the large amount of statistical data. This control profile at least can produce an

approximate global optimal path from the statistic view and sustains the battery SOC. On this basis, without asking for any knowledge about the output dynamics g_{ICE} or the engine map $\overline{g}_{ICE}$, the ES compensates this SDP control profile using the instantaneous output measurement, to generate even better control actions. This is simply interpreted as follows:

In the discrete time form, because the battery SOC generated by the SDP-ES is almost equal to the one from the SDP in every sampling step, the two accumulated SOC deviations at the final states will keep the same. Then, given a specific vehicle cycle, for the global cost function

$$J = \sum_{k=0}^{N-1} \left\{ FC(k) \right\} + f_{soc} \Delta SOC(N)^2 - m_{soc} \Delta SOC(N) \tag{4.9}$$

where FC is the fuel consumption in every sampling step, $\Delta SOC(N)$ is the error between the actual and desired SOC at the final step, f_{soc} is the SOC sustaining factor and m_{soc} is the SOC variation compensation factor. Only $FC(k)$ is concerned about the cost difference between SDP-ES and SDP.

Based on the optimal target of the ES control, for each step:

$$FC_{SDP-ES}(k) \le FC_{SDP}(k), k \in [0, N-1] \tag{4.10}$$

where FC_{SDP-ES} and FC_{SDP} are the instantaneous fuel consumptions given by the SDP-ES and SDP algorithm .

From (4.9)-(4.10), it is not difficult to conclude:

$$\sum_{k=0}^{N-1} \left\{ FC_{SDP-ES}(k) \right\} \le \sum_{k=0}^{N-1} \left\{ FC_{SDP}(k) \right\} \Rightarrow J_{SDP-ES} \le J_{SDP} \tag{4.11}$$

Thus, the SDP-ES improve the optimality of the original SDP algorithm, which can be approximately shown in Fig. 4.3 (in the real case, the shape of the fuel consumption contours are not necessarily round). Compared with the SDP strategy, the SDP-ES method will produce less fuel consumption along the whole driving cycle.

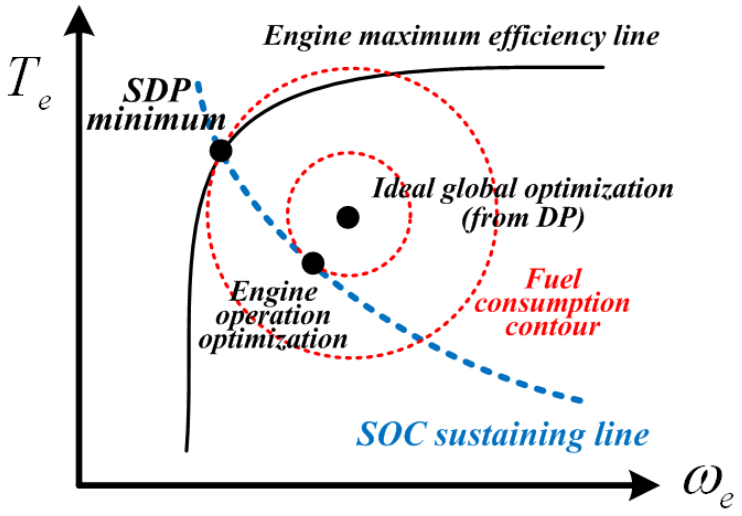

Fig. 4.3 Better optimality of the SDP-ES algorithm

4.4.2 Design of the SDP Control Laws

The SDP algorithm is designed to generate the stationary optimal control policy π which will directly map the driver's command (vehicle acceleration) and system states (SOC and vehicle speed ω_v) at the current time *t*, to the control actions (engine power P_e) at time *t*, without any concerns about the states in any other time [98]. Based on various driving cycles, a Markov model is first designed to quantify the transition probability P_{ij} between different accelerations $\dot{\omega}_{v,j}$ and $\dot{\omega}_{v,i}$ with respect to a specific speed ω_v.

Although the plant model is a 3rd-order system in (4.1), the engine speed is coupled with the engine torque on a pre-defined operating line for model simplification and the engine dynamics is eliminated. With the driver's command and current states (SOC, ω_v), a control P_e (or equivalently, T_e) can be chosen and, all the states at the next step can be solved with some transition probabilities. Then, the cost function from state *j* to state *i* is:

$$\begin{aligned} J_{\pi,i} &= R\left(x_{HV}, u_{HV}\right)_i + \alpha \sum_j P_{ij} J_{\pi,j} \\ R\left(x_{HV}, u_{HV}\right)_i &= FC\left(\omega_e, T_e\right)_i + f_{soc} \Delta SOC_i^{\,2} - m_{soc} \Delta SOC_i \end{aligned} \tag{4.12}$$

where, $0 < \alpha < 1$ is the discount factor which determines the converge speed of the

accumulated cost.

The SDP algorithm can be achieved through the policy iteration [98]. Starting with an initial policy, the cost at state j will be calculated and then, for the policy improvement, a new policy at state i will be generated by:

$$\pi_i = \arg\min\left[R\left(x_{HV}, u_{HV}\right)_i + \alpha \sum_j P_{ij} J_{\pi,j} \right] \tag{4.13}$$

Then, with the new policy, the cost will be updated and this algorithm will be performed iteratively, until π converges within an acceptable tolerance level due to the discount factor. Figure 4.4 shows a map of control law for a specific vehicle acceleration demand.

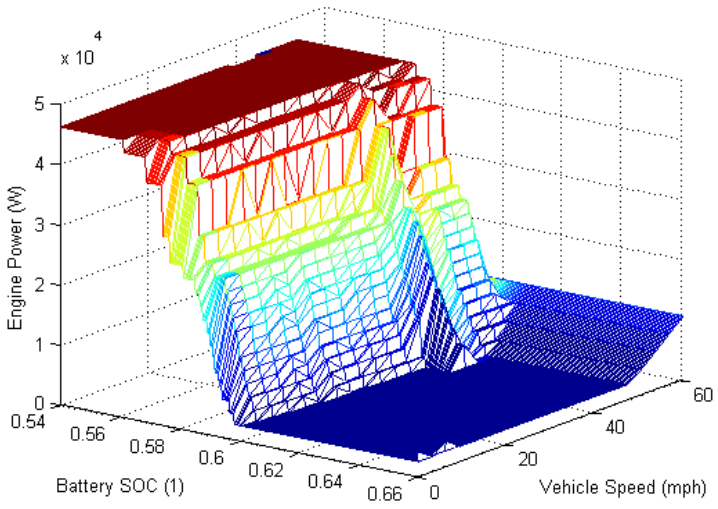

Fig. 4.4 The engine optimal control law generated by SDP
(when vehicle acceleration demand = 1.08 mph/sec)

4.4.3 Design of the ES Output-Feedback Control Laws

Since any point $\left(\omega_e, T_e\right)$ on the SOC sustaining line can be positioned by one scalar parameter ω_e (or, T_e), for the overall system that includes the hybrid powertrain and the controller:

$$\dot{x}_{HV} = f_{HV}\left(x_{HV}, u_{HV}\right),\ \dot{y}_{ICE} = g_{ICE}\left(y_{ICE}, x_{HV}, u_{HV}\right)\ ,$$

we can use the control inputs u_{HV} (electric torques) to achieve the fast and precise track of desired state ω_e, and correspondingly produce a locally stable equilibrium y_{ICE} (fuel consumption). On this basis, our optimization objective is to develop a feedback mechanism which adapts the optimal point ω_e which minimizes the steady-state value of y_{ICE}, without asking for any knowledge of either f_{HV} and g_{ICE}. With this objective, a self-optimal ES control schematic is built, as shown in Fig. 4.5. The basic design logic is interpreted below:

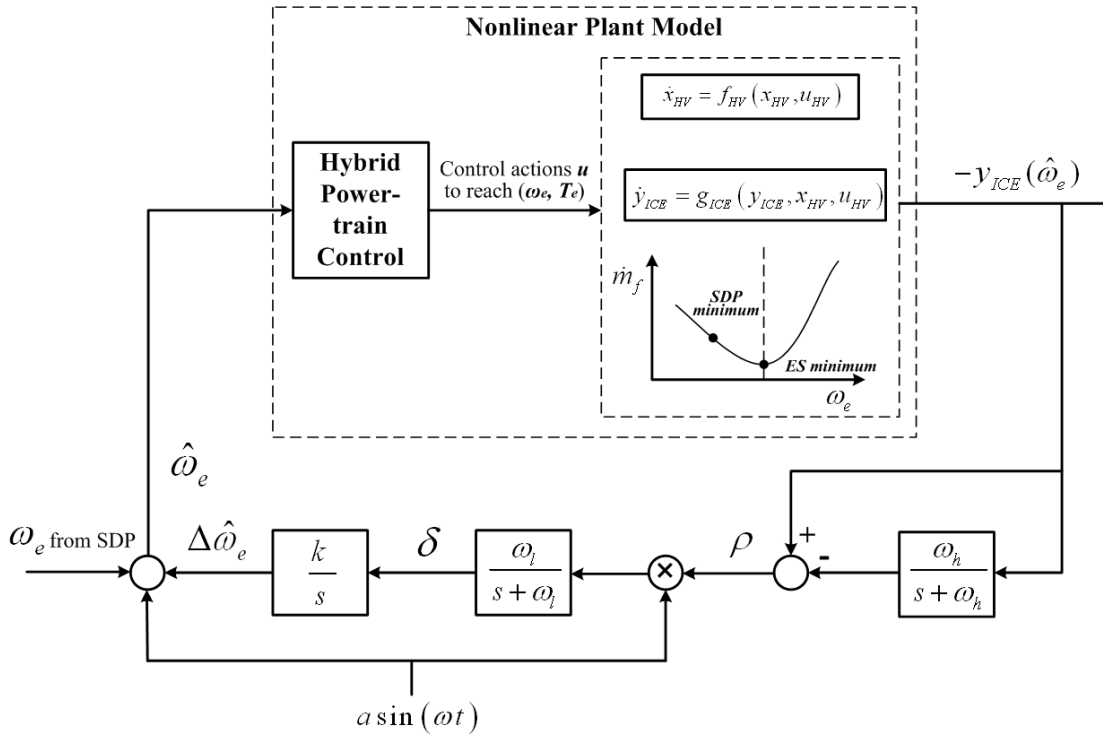

Fig. 4.5 The control schematic of the ES real-time optimization

If we define the optimal speed corresponding to the minimal fuel consumption y_{ICE}^* as ω_e^*, then the estimate of ω_e^* can be defined as $\hat{\omega}_e$. For every $\hat{\omega}_e$ in the adaptive process, a periodic perturbation $a\sin(\omega t)$ is added onto the reference signal [62]-[63]. This perturbation is designed slower than the plant dynamics (with the hybrid powertrain controller), so that the plant dynamics can be approximately treated as a static map

$y_{ICE} = \phi(\omega_e)$ which will not seriously disturb the minimum seeking mechanism. When the simultaneous $\hat{\omega}_e$ is on the left side of the optimum ω_e^* ($\hat{\omega}_e < \omega_e^*$), the perturbation $a\sin(\omega t)$ will trigger a periodic response of $-y_{ICE}$ (here, "-" is added to cope with the minimum seeking problem) which is in phase with $a\sin(\omega t)$; vice versa, when $\hat{\omega}_e$ is on the right side of the optimum ω_e^*, the triggered periodic output response will be out of phase with $a\sin(\omega t)$. Then, to avoid the "DC" component of $-y_{ICE}$ to interfere with the adaptive process, a high-pass filter $\frac{s}{s+\omega_h}$ is first designed to extract the high-frequency periodic components of $-y_{ICE}$. As a result, $\frac{s}{s+\omega_h} a\sin(\omega t)$ and $-\frac{s}{s+\omega_h} y_{ICE}$ will be approximately two sinusoidal signals which still satisfy: when $\hat{\omega}_e < \omega_e^*$, in phase; when $\hat{\omega}_e > \omega_e^*$, out of phase (here, we also add a high-pass filter for the perturbation $a\sin(\omega t)$ to compensate the phase deviation). Based on the trigonometric functions, the product of these two sinusoidal signals will have a "DC" component δ which satisfies: when $\hat{\omega}_e < \omega_e^*$, $\delta > 0$; when $\hat{\omega}_e > \omega_e^*$, $\delta < 0$. Particularly, the DC component δ will be approximately in the form of

$$\delta = -\frac{a^2}{2}\phi'(\hat{\omega}_e) \tag{4.14}$$

After we extract δ by a low-pass filter $\frac{\omega_l}{s+\omega_l}$ [62]-[63], the adaptive law to generate the speed compensation $\Delta\hat{\omega}_e$ can be given by:

$$\Delta\dot{\hat{\omega}}_e = k\delta = -\frac{ka^2}{2}\phi'(\hat{\omega}_e) \tag{4.15}$$

Finally, the estimate $\hat{\omega}_e$ is generated by adding the ES compensation $\Delta\hat{\omega}_e$ and $a\sin(\omega t)$ onto a reference speed ω_e provided by the SDP. This adaptive control law can finally make the estimate $\hat{\omega}_e$ converge to the optimal point ω_e^*. Here, a reference ω_e is introduced for reducing the ES control efforts and make the adaptation converge quickly.

4.5. SIMULATION RESULTS

To demonstrate the performance of the proposed SDP-ES energy optimization algorithm, extensive simulation studies have been conducted. In these studies, the SDP-ES optimization results are compared and analyzed with the original SDP optimization results along the Highway Fuel Economy Test (HWFET) driving cycle. Currently, to simplify the problem, we use the engine fuel consumption as the only system output and also, the only optimization target. An experimental verified engine fuel efficiency map of a 4.5L, 4 cylinders John Deere[@] diesel engine is employed to produce the system outputs, as shown in Fig. 4.6. The SDP controller will produce a new engine power command every one second based on the current system states. For the ES optimal controller, a sinusoidal perturbation of $\sin(10\pi t)$ is used to trigger the minimum seeking. The high pass filter and low pass filter are designed with time constant $\omega_h = 100$ and $\omega_l = 2$. The adaptive gain is set as $k = 10000$ with some constrains to speed up the seeking process.

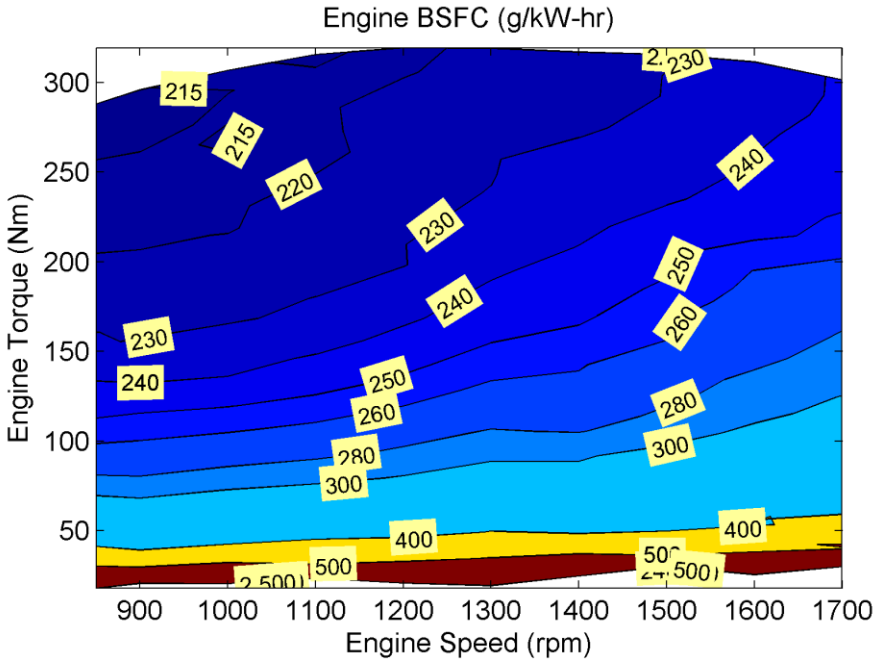

Fig. 4.6 Steady-state fuel efficiency map

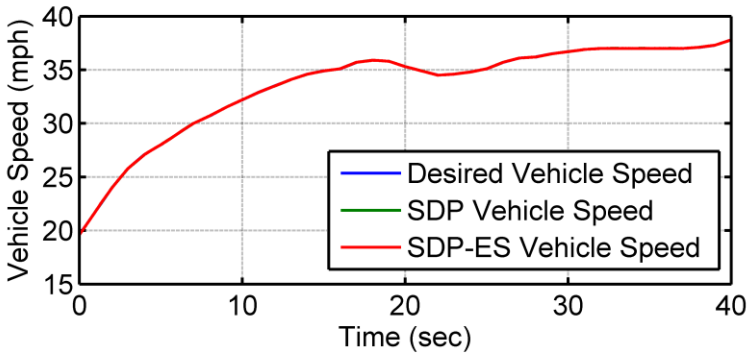

(a) vehicle speed

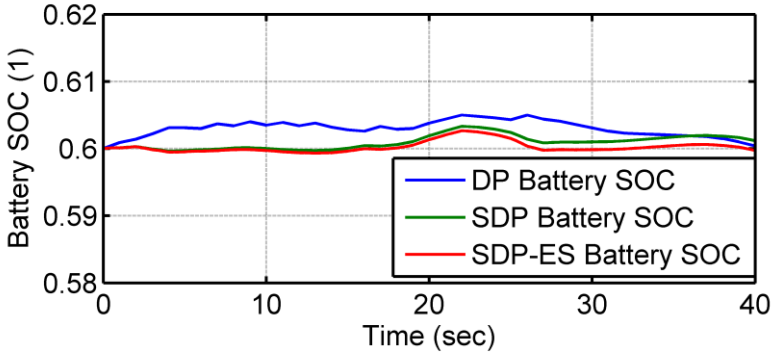

(b) battery SOC

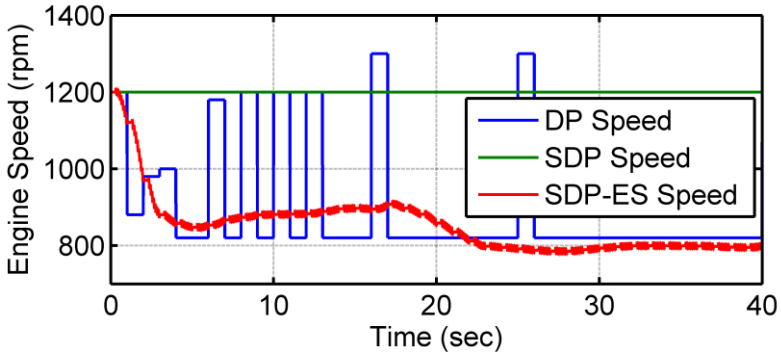

(c) engine speed

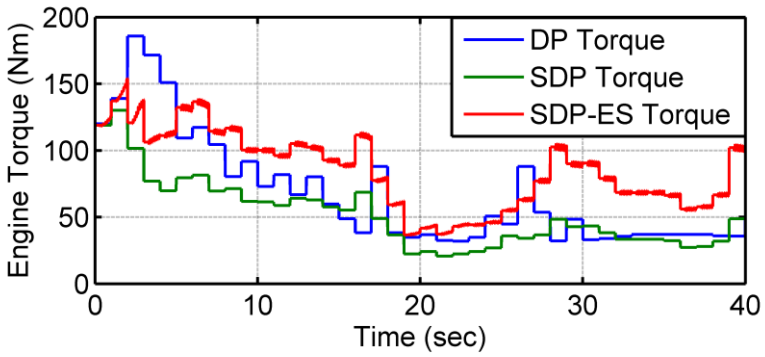

(d) engine torque

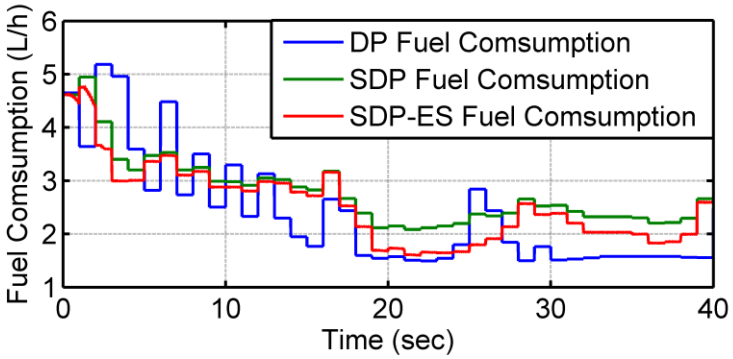

(e) fuel consumption

Fig. 4.7 Comparisons between the optimized results by DP, SDP and SDP-ES

The simulation results demonstrate, for some driving scenarios where the SDP algorithm cannot produce the best results (e.g., an "accelerating" phase in the HWFET cycle shown in Fig. 4.7), the ES can provide the notable improvement on fuel efficiency compared with the original SDP. Here the offline global optimization results from the DP are also shown for reference. From the Fig. 4.7(a)-(b), it is obvious that both the SDP and SDP-ES can precisely track the vehicle speed and maintain the SOC at almost the same level (but different from the DP). Figure 4.7(c)-(d) show the engine operating profiles (engine speed and torque) generated by the SDP and SDP-ES are quite different, which induces the difference on their fuel consumptions in Fig. 4.7(e). Particularly the SDP-ES improves the fuel efficiency at almost every time instant and finally achieves a 10%

improvement based on the SDP (during this scenario, the fuel economy generated by the SDP and SDP-ES are 45.72 *mpg* and 50.14 *mpg*, respectively; and the theoretical optimal fuel economy from the DP is 53.63 *mpg*).

4.6. CONCLUSION

This chapter presents the design of a new SDP-ES hybrid energy management strategy that leverages the nature of the SDP on the global optimality and SOC sustainability, and compensates its optimal control errors by introducing the real-time ES (extremum seeking) output feedback. This design actually "loosens" the precision limitations of the SDP, so as to offer larger space to reduce the computation burden by model simplification.

Chapter 5

Optimal Control of the Transient Emissions and Fuel Efficiency with a Two-Mode Hybrid Energy Management Strategy

5.1 RESEARCH OBJECTIVE

As it is well known, by virtue of its high compression ratio, the compression-ignition (CI) diesel engines have higher fuel efficiency than the spark-ignition (SI) gasoline engines. Therefore, the diesel HEV, with even better energy-saving performance compared with the gasoline HEV, has been considered as an important alternative solution to address the energy issue. However, due to its inherent disadvantage of high NOx and soot emissions [65], the wide application of the diesel HEV is still seriously limited. In particular, the diesel engine emissions will deteriorate under transient operations, such as engine start-up and abrupt vehicle acceleration/deceleration. During engine transients, the low-bandwidth air flow dynamics of the diesel engine (which is, mainly concerned with the time lag introduced by the turbocharger) will cause the air supply to mismatch with the rapidly increasing/decreasing fuel injection. Consequently, it will lead to the undesirable in-cylinder air-fuel ratio and hence, the deteriorated combustion conditions. The transient dynamic responses of the exhaust gas recirculation (EGR) mechanism and the fuel injection mechanism can also contribute to the local high concentration of emissions (especially the soot emission). In addition, the slow thermal dynamics make the various transient engine temperatures (in-cylinder temperature, exhaust gas temperature, intake manifold temperature and so on) quite different from the steady state cases. As a result, the transient engine operations will create higher emission concentration than the steady-state cases [65]-[66]. Unfortunately, along the typical

operating trajectories of the HEV, the engine will frequently encounter the abrupt torque transients that usually induce high emissions, albeit may be beneficial for the fuel efficiency improvement.

Targeted at achieving both the global energy optimization and transient emissions control, a two-mode hybrid powertrain energy management strategy is proposed in this paper. First, dynamic programming (DP) is employed to ensure the global fuel efficiency optimization and battery state of charge (SOC) sustainability for any given driving cycles. On this basis, during selected "emissions reducing" modes, the management strategy locally modifies the engine operations into another trajectory with the purpose of reducing the high transient emissions; and more significantly, at the end of every "emissions reducing" mode, the locally optimized engine operating trajectory will be driven back to match the globally optimized trajectory generated by the DP for the succeeding operation. This design ensures the global optimization of the fuel efficiency (albeit with some slight deviations in some areas) and battery SOC sustainability since the DP optimized engine/battery operations are recovered after every local emission optimization. Specifically, in the "fuel efficiency improving" mode, the management strategy makes use of the DP algorithm to seek the global optimization of the fuel efficiency over the entire driving cycle; while in the "emission reducing" mode, this strategy utilizes a linear quadratic regulator (LQR) to locally optimize the operating trajectory in a short time horizon, to suppress the surging emissions due to the sudden engine torque transients. Here, it is worth noting that we avoid directly adding the transient emission optimization task into the DP global optimization algorithm, which will otherwise significantly increase the computational burden of DP. Because the complicated transient emission model will considerately increase the order of the dynamic models used in DP, the introduction of the emission dynamics into the DP optimization problem may greatly increase the computational burden.

This chapter is organized as follows. A control-oriented transient (micro-soot) emission model of a diesel engine is first introduced by the AR algorithm and simplified into a proper form in Section 5.2. In Section 5.3, the two-mode hybrid energy management strategy is proposed and designed. Finally, the experimental results are

shown in Section 5.4, which demonstrate that the proposed optimization algorithm is capable of reaching a good balance between energy-saving and emission-reduction, without losing the battery SOC sustainability.

5.2 CONTROL-ORIENTED EMISSION MODEL

Targeted at realizing simultaneous fuel consumption and emission control, both the engine fuel consumption and emission models are needed. Different from the static-mapping-based fuel consumption model, the emission model must involve higher-order transient dynamics. Ideally, to precisely describe the complex thermodynamics and chemistry of the engine combustion, the complete engine transient emissions model should contain as many high-fidelity physics-based submodels as possible that can catch the various engine processes (in-cylinder processes, inlet/exhaust manifold operation, EGR operation, Turbocharger operation and so on) and identify the effects of all the key operating parameters (engine speed, fuel injection mass, inlet air pressure, exhaust gas temperature, EGR opening and so on). However, to implement the transient emission control in real-time, a simplified, control-oriented model with well-selected input variables is required.

Various control-oriented emission models have been reported. A dynamic model composed of steady state emission and transient emission correction was adopted in Ref [99] here some process variables that present the engine combustion or cylinder charge characteristics are used as inputs to characterize the transient emission effects. Otherwise, actual EGR opening rate, fresh air mass flow and fuel/air ratio are also commonly used for transient correction [100]-[101]. However, the previous emission models are commonly used for improving the engine operation within the engine control unit (ECU), but not for the vehicle-level energy management strategy. Recently, some studies on the emission models that are suitable for the vehicle-level control are also reported. In Ref [102], a Volterra series based model with fuel flow rate and engine speed as the inputs, is presented.

Aiming at developing a hybrid vehicle energy management strategy that can optimize the fuel consumption over the entire driving cycle and reduce local transient

emissions, a data-driven emission model that is capable to predict the transient emission is built and identified by experiments. The modeling and validation process consists of two steps:

5.2.1 Input Parameters Selection

Although empirical data have shown that the engine internal variables (inlet air pressure, exhaust gas temperature, EGR opening, etc.) are closely concerned with both NOx and soot emissions, including those variables will increase the dimension of the emission model and consequently the computational burden of the vehicle-level energy management. Therefore, the proposed model chooses the engine external variables (driver's control inputs): engine speed ω_e and engine torque T_e as the inputs. Such selection is based on the observation that the other key variables (such as the inlet air pressure, exhaust temperature and so on) are ultimately determined by the current engine speed and torque command (or, their derivatives).

As a result, this input parameters selection brings us two advantages. Firstly, the engine torque and speed are more accessible and controllable than the engine internal variables (i.e., ECU control actions); and secondly, these control inputs can directly determine the engine fuel consumption in the static-mapping model, which is advantageous for coordinating the optimal controls of both the fuel consumption and emissions in the energy management strategy (albeit for emissions, more obvious transient effects also need to be taken into consideration). The experimental data of a diesel engine (John Deere® 4045HF, Tier IV, 4 cylinders, 4.5L) demonstrate the steady state relationship between the engine fuel consumption/emissions and engine torque/speed, as shown in Fig 5.1 (a)-(c), where the engine loads corresponds to different engine torques.

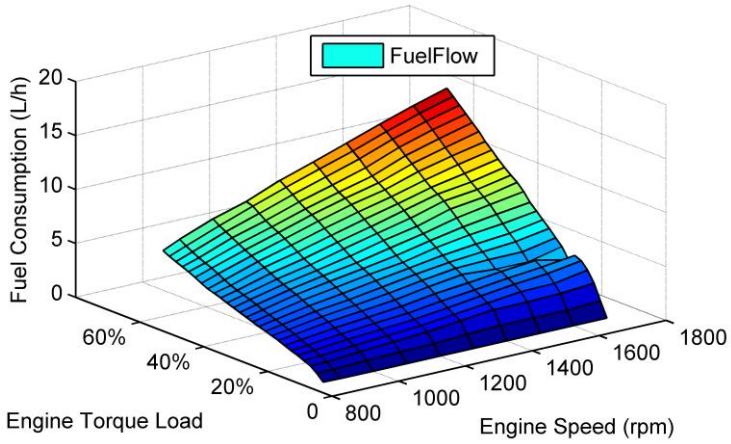

(a) Fuel consumption

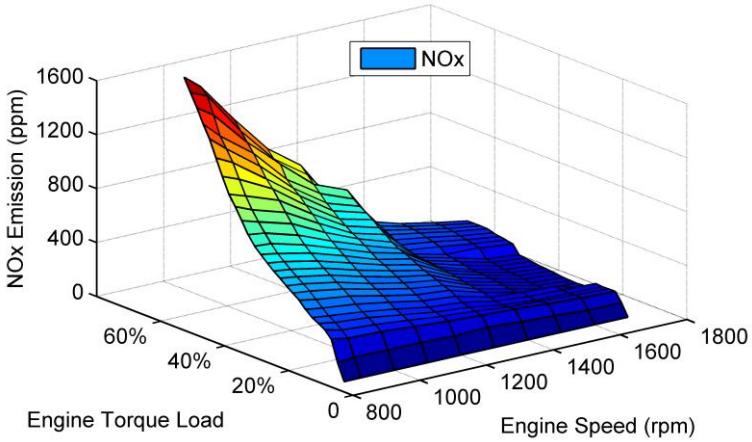

(b) NOx emission

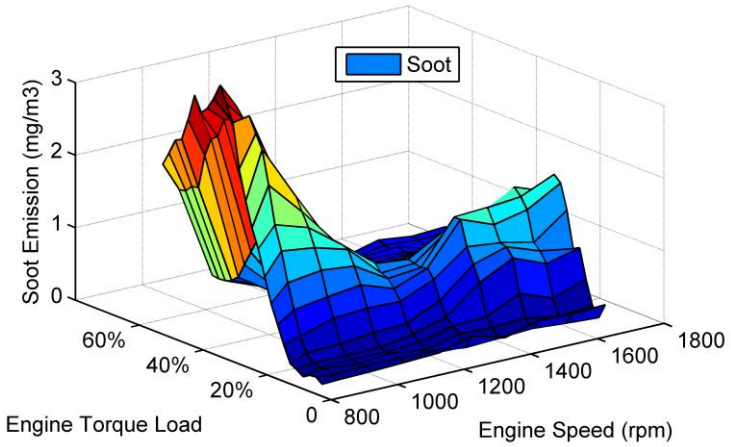

(c) Soot emission

Fig. 5.1 Steady state fuel efficiency and emissions maps

In addition, to capture the transient emission dynamics without introducing new independent variables, the derivatives of engine speed $\dot{\omega}_e$ and engine torque $\dot{T}_e$ are used as additional inputs. The physical explanation of $\dot{\omega}_e$ and $\dot{T}_e$ as additional input to capture the transient emission dynamics is illustrated in Fig.5.2-5.3. Under different engine load transient conditions (different torque derivatives), the fuel injection flow rate will present different transients which in turn affects the transient air/fuel ratio and hence, the emission output. The faster the engine load changes, i.e., the larger the torque derivative $\dot{T}_e$ is, the higher the transient fuel flow rate becomes, as shown in Fig.5.2. However, the inlet air flow rate is limited by the air pressure dynamics. Eventually, the transient air/fuel ratio that can directly cause undesired emission output, is coupled with the torque derivative $\dot{T}_e$, as shown in Fig.5.3.

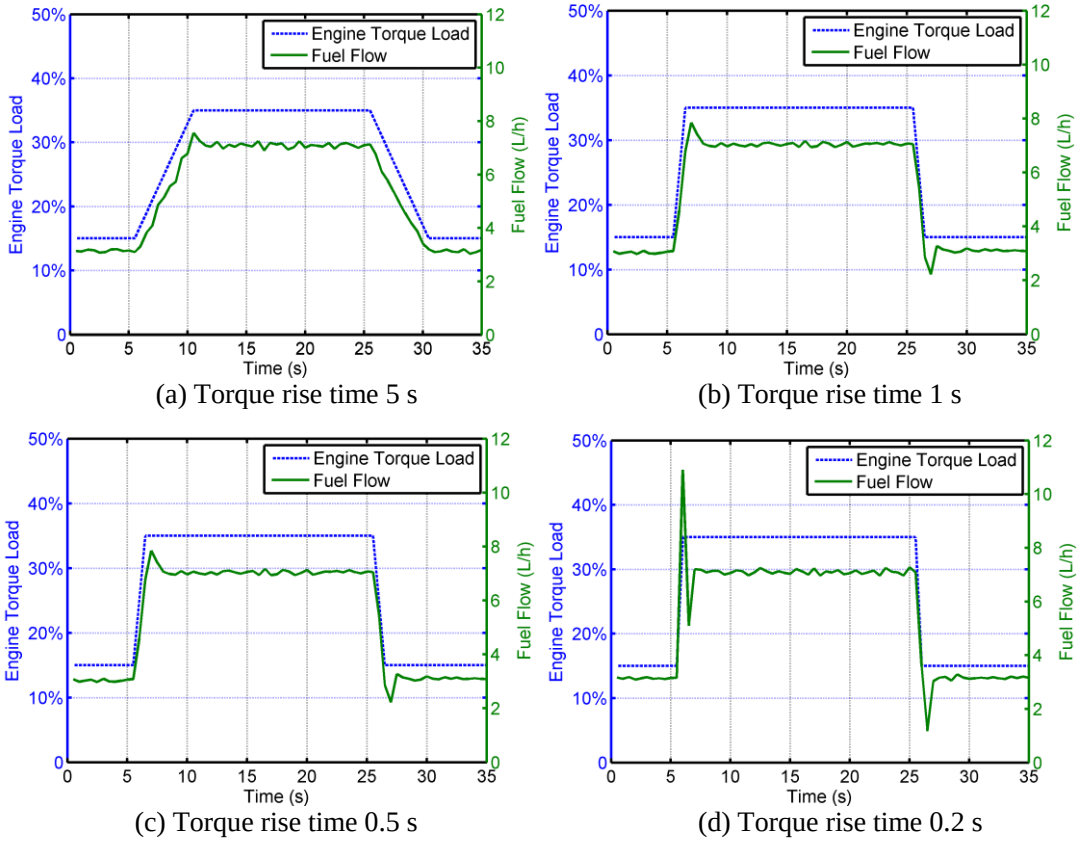

(a) Torque rise time 5 s (b) Torque rise time 1 s

(c) Torque rise time 0.5 s (d) Torque rise time 0.2 s

Fig. 5.2 Engine fuel injections under different torque transients

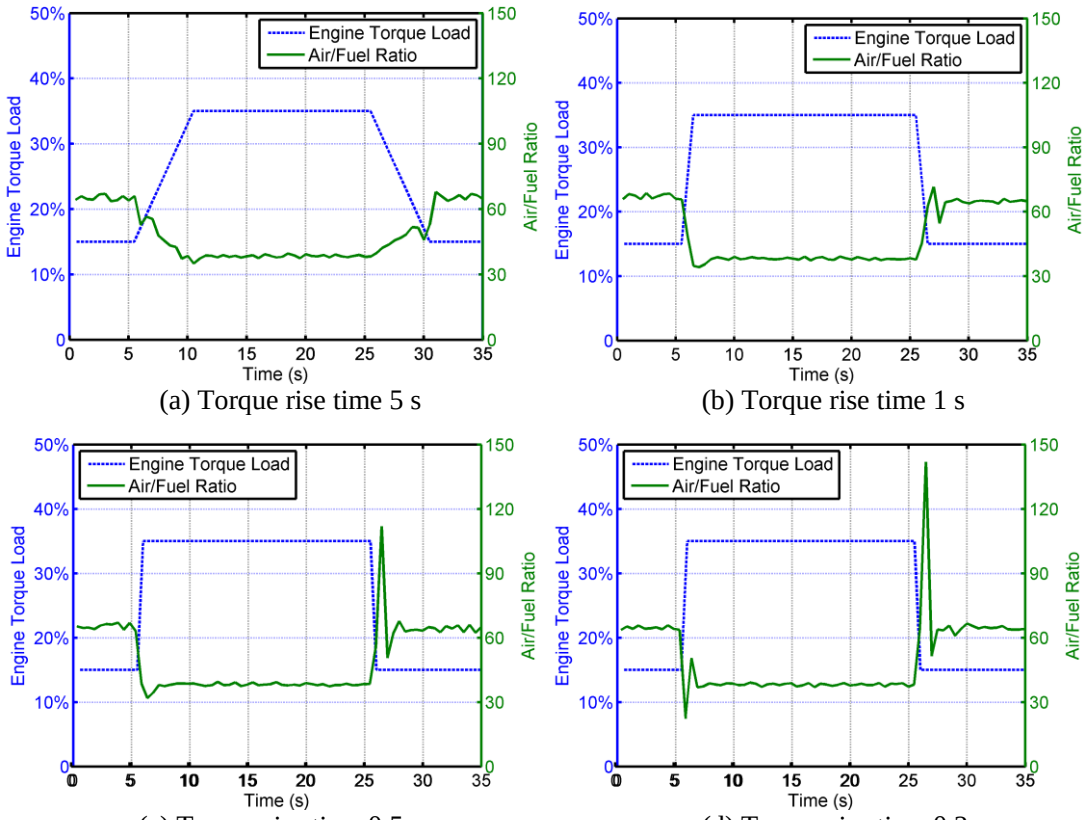

(a) Torque rise time 5 s (b) Torque rise time 1 s

(c) Torque rise time 0.5 s (d) Torque rise time 0.2 s

Fig. 5.3 Engine air/fuel ratios under different torque transients

5.2.2 Control-oriented Model Development and Validation

With the well-selected input variables, a proper mathematic model should be constructed to describe the nonlinear emission dynamics with relatively compact structure. To capture the nonlinear relationship and maintain a relatively simple structure, the Hammerstein model structure [103]-[104] that contains a static nonlinearity in series with a linear dynamic system, is utilized for emission modeling. A general Hammerstein model can be described in the discrete-time form, where the static nonlinearity is approximated as a finite polynomial expansion:

$$\begin{aligned} & y(K)+m_1 y(K-1)+m_2 y(K-2)+\ldots+m_N y(K-N) \\ & \quad = n_1 x(K-1)+n_2 x(K-2)+\ldots+n_N x(K-N) \\ & x(K)=\gamma_1 u(K)+\gamma_2 u^2(K)+\gamma_3 u^3(K)+\ldots+\gamma_M u^M(K) \end{aligned} \tag{5.1}$$

where u, x and y are the system inputs, states and outputs respectively, $M, N \in \mathrm{N}$, $m_1 ... m_N$ and $n_1 ... n_N$ are constant.

The block diagram of the proposed control oriented emission model is shown in Fig 5.4. The static nonlinearity is presented by a third-order polynomial that consist of four input variables, which are proved to be sufficient to describe the relatively smooth ramp and saddle surfaces of the steady state emissions shown in Fig 5.1 (b)-(c). Besides, the linear dynamics are all set to be of first-order, based on the autoregressive analysis of experimental data shown in the next section. Although there are multiple gaseous and particulate emissions, here we focus on the micro soot emission and other emissions can be treated in a similar fashion.

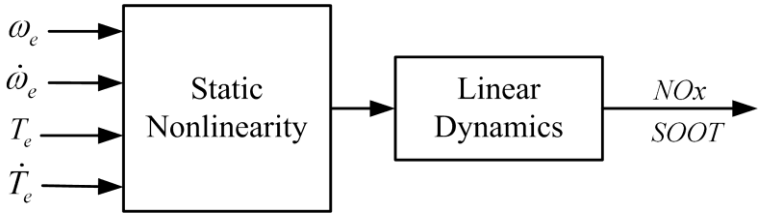

Fig. 5.4 Hammerstein model structure

The control-oriented soot emission model is shown as:

$$\dot{S}oot = -\frac{1}{\tau} Soot + \frac{1}{\tau}\left[\lambda_1 T_e + \lambda_2 \omega_e T_e + \lambda_3 \dot{\omega}_e T_e + \lambda_4 {\omega_e}^2 T_e + \lambda_5 {\dot{\omega}_e}^2 T_e + \cdots + \lambda_{34} \omega_e {\dot{T}_e}^2\right] \quad (5.2)$$

where the time constant τ and parameters $\lambda_1, \cdots, \lambda_{34}$ are all constants. If necessary, different time constants can be assigned to different terms of the input and the energy management strategy proposed in the thesis can still work.

Further, the Hammerstein emission model is identified by the experimental data with the autoregressive (AR) algorithm. AR model is a kind of random process usually used to model and predict various types of natural phenomena. The general AR model is one or a group of linear prediction formulas to predict the future system outputs from the previous outputs. To meet the specific need of the linear prediction formulas, we use the sequence of the measured emissions outputs and all the polynomial expansions of the measured engine speed/torque as the inputs for regression. All the parameters $\tau, \lambda_1, \cdots, \lambda_{34}$ in the emission model (5.2) are identified using experimental measurement of the input

variables and soot emission. Figure 5.5 shows the comparison of the micro soot emissions measured in experiments and predicted by the emission model, along a predefined engine operation trajectory. It is obvious that the predictions based on the dynamic model match the experimental data very well.

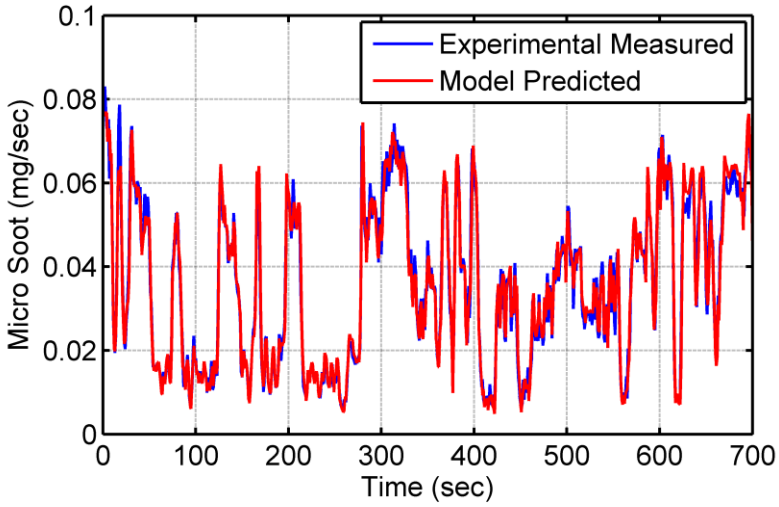

Fig. 5.5 Experimental and model predicted emissions

In order to apply the proposed real-time optimal control to reduce local emissions, the emission model in (5.2) needs to be further simplified. As will be shown in Section 5.3, the engine torque T_e and torque rate $\dot{T}_e$ are treated as state and control variables respectively. Thus, the polynomials that contain the crossing terms of T_e and $\dot{T}_e$, and the polynomials that only contain the speed ω_e or acceleration $\dot{\omega}_e$ but without T_e or $\dot{T}_e$, should be avoided. Consequently, we simplify the soot emission model into the form given by:

$$\begin{aligned}\dot{S}oot = & -\frac{1}{\tau} Soot \\ & + \frac{1}{\tau}\left[\lambda_1 T_e + \lambda_2 \omega_e T_e + \lambda_3 \dot{\omega}_e T_e + \lambda_4 {\omega_e}^2 T_e + \lambda_5 {\dot{\omega}_e}^2 T_e + \lambda_6 \omega_e \dot{\omega}_e T_e\right] \\ & + \frac{1}{\tau}\left[\lambda_7 \dot{T}_e + \lambda_8 \omega_e \dot{T}_e + \lambda_9 \dot{\omega}_e \dot{T}_e + \lambda_{10} {\omega_e}^2 \dot{T}_e + \lambda_{11} {\dot{\omega}_e}^2 \dot{T}_e + \lambda_{12} \omega_e \dot{\omega}_e \dot{T}_e\right]\end{aligned} \tag{5.3}$$

where the parameters $\tau, \lambda_1, \cdots, \lambda_{12}$ are constant.

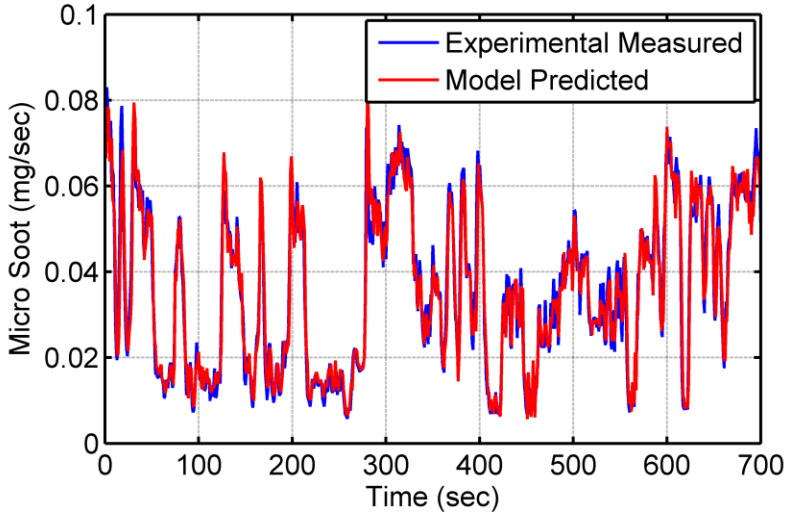

Fig. 5.6 Experimental and simplified model predicted emissions

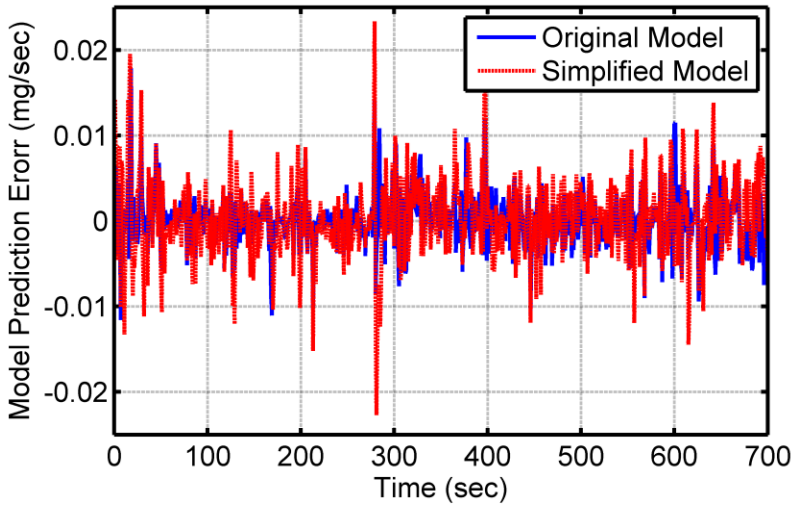

Fig. 5.7 Original and simplified model prediction errors

Compared with the original model, the performance of the simplified emission model is degraded to some extent, but still acceptable as shown in Fig. 5.6-5.7.

5.3 TWO-MODE HYBRID ENERGY MANAGEMENT STRATEGY

To reduce the transient engine emissions without losing the global fuel efficiency

optimization and battery SOC sustainability, a two-mode hybrid energy management strategy is proposed, as shown in Fig.5.8.

Along the predefined driving cycle, most of the time the hybrid vehicle is running in the "fuel efficiency improving" mode, where both the engine speed and torque will be optimized by the DP optimal control algorithm. The cost of the DP optimization is calculated based on the steady-state fuel efficiency map (or the weighted fuel efficiency and emission map, if needed), so as to ensure the global optimization of the steady-state fuel consumption. However, since the DP optimization does not take the transient emissions into consideration, the optimized control may sacrifice the emission performance to a large extent, especially when the engine torque changes abruptly. To reduce the transient emission concentration, when the control commands from the DP optimization exceed some predefined threshold (i.e., the engine torque is forced to change abruptly), the "emission reducing" mode is triggered and a local linear quadratic regulator (LQR) optimal control will override the global DP optimization by modifying the engine torque commands (i.e., fuel injection commands) but still holding the speed commands calculated by the DP (See Fig. 5.8). Generally the LQR control will smooth the surging engine torque to reduce the high local emission concentration. This approach fully takes advantage of the hybrid powertrain system where the electric torques can be flexibly controlled to compensate the deficit engine torque at any time instant so as to keep tracking the predefined engine speed trajectory. At the end of the time horizon, the battery SOC of the hybrid vehicle will be driven back to the globally optimized point, so that the global fuel efficiency optimization and battery SOC sustainability can still be maintained. The design of the two mode hybrid energy management strategy is shown in details as follows:

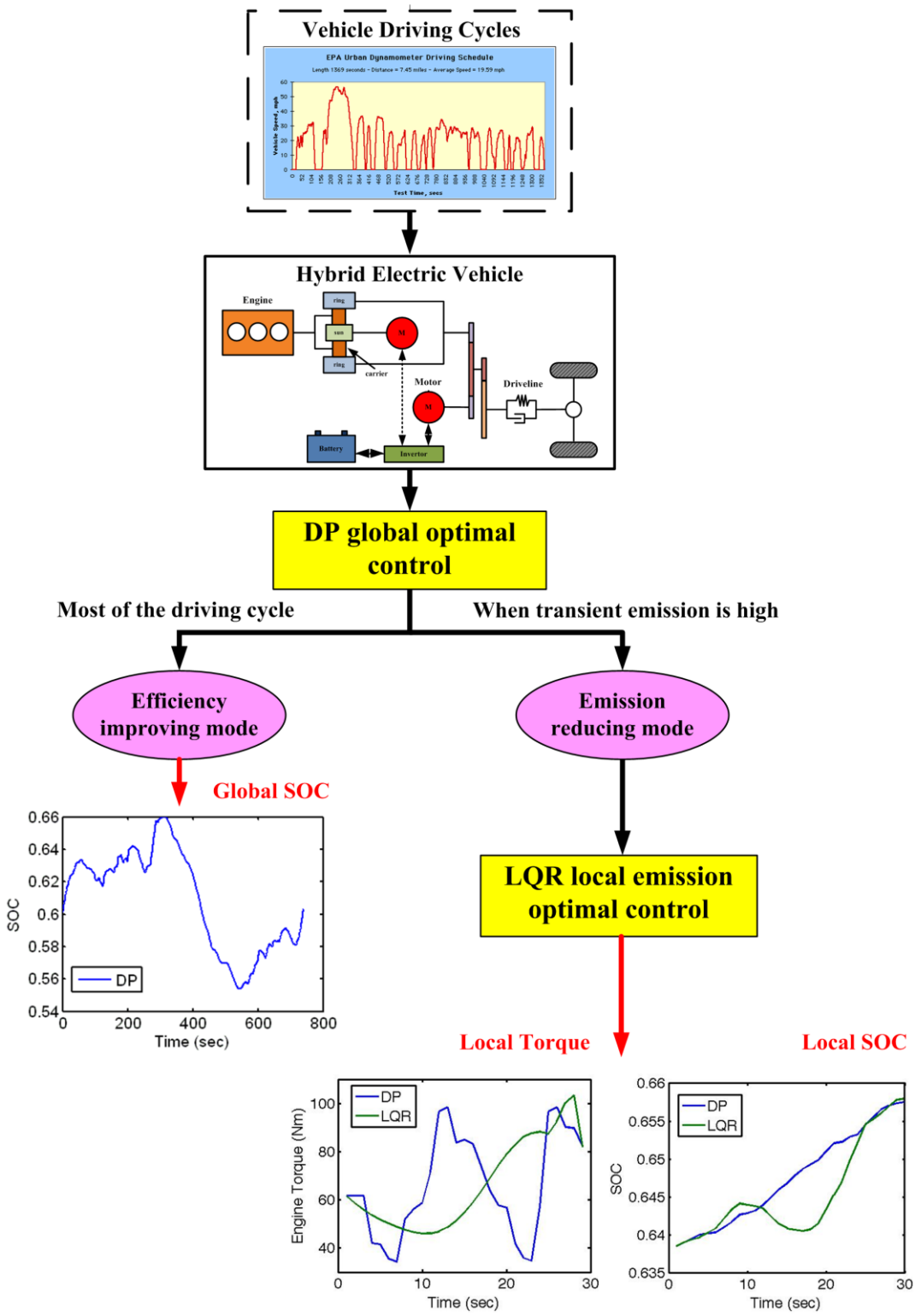

Fig. 5.8 Two-mode fuel efficiency and emissions optimal control

5.3.1 Efficiency Improving Mode: Global DP Optimization

In efficiency improving mode, dynamic programming, which has been widely investigated in the hybrid powertrain control area [43]-[45], is utilized as the energy management strategy. DP is a global optimization algorithm that backwards searches all the possible states and feasible control actions along a predefined path, so as to find the optimal operation trajectory to meet the specific optimization objective (cost function).

The cost function used in the DP optimization is designed to minimize the fuel consumption and keep the SOC sustained in a limited bound, given by:

$$J = \sum_{k=0}^{N-1} \left\{ FC(k) \right\} + f_{soc} \left[SOC(N) - SOC(N)_{des} \right]^2 - m_{soc} \left[SOC(N) - SOC(N)_{des} \right] \tag{5.4}$$

where FC is the fuel consumption in a single sampling step, $SOC(N)$ and $SOC(N)_{des}$ are the actual and desired battery SOC at the final step, f_{soc} is the SOC sustaining factor and m_{soc} is the SOC variation compensation factor.

5.3.2 Emission Reducing Mode: Local LQR Optimal Control

In the emission reducing mode, a local optimal control algorithm is required to realize two tasks:

1) modifying the engine torque trajectory to realize the local emission optimization, without changing the engine speed during the local time horizon;

2) at the end of the local time horizon, the battery SOC should be driven back to the trajectory defined by the DP, so that the SOC sustainability provided by the DP can still be maintained.

To meet the above requirements, a linear quadratic regulator is utilized in the emission reducing mode. LQR is a linear state feedback optimal control along some finite time period [105]. Thus, the linearization and necessary simplification of the nonlinear plant model which includes the powertrain dynamics in (4.1) and emission dynamics in (5.3) is necessary.

For the engine and vehicle dynamics, the engine speed and vehicle speed will be maintained the same as the DP optimized results; in other words, both ω_e and ω_v as well as their time derivative can be treated as known terms in the LQR control. Then, the nonlinear terms involved with ω_e and ω_v in (4.1) are actually eliminated and we can rewrite the engine and vehicle dynamics as:

$$\begin{aligned} T_m &= -\frac{a_2 b_3 - b_2 a_3}{a_4 b_3 - b_4 a_3} T_e + \frac{a_1 b_3 \dot{\omega}_v - b_1 a_3 \dot{\omega}_e}{a_4 b_3 - b_4 a_3} + \left(\alpha \omega_v^{\,2} + \beta\right) \\ &= r_{m1} T_e + r_{m2} \\ T_g &= -\frac{a_2 b_4 - b_2 a_4}{a_3 b_4 - b_3 a_4} T_e + \frac{a_1 b_4 \dot{\omega}_v - b_1 a_4 \dot{\omega}_e}{a_3 b_4 - b_3 a_4} \\ &= r_{g1} T_e + r_{g2} \end{aligned} \tag{5.5}$$

For the battery dynamics, if we neglect the internal resistance of the battery (which is reasonable since the internal resistance is usually small so that the energy consumption induced by the internal resistance is also small), then the nonlinear dynamics can be transformed into a linear form:

$$\begin{aligned} \dot{SOC} &= -\frac{P_{batt}}{V_{batt} Q_{batt}} = -\frac{-T_g \omega_g \eta_g^{\,k1} + T_m \omega_m \eta_m^{\,k2}}{V_{batt} Q_{batt}} \\ &= \frac{\left(r_{g1} T_e + r_{g2}\right)\left(\dfrac{\omega_e \left(R+S\right) - \omega_v K_{ratio} R}{S}\right)\eta_g^{\,k1} - \left(r_{m1} T_e + r_{m2}\right)\left(\omega_v K_{ratio}\right)\eta_m^{\,k2}}{V_{batt} Q_{batt}} \end{aligned} \tag{5.6}$$

For the micro soot emission model shown in (5.3), since the engine speed and its time derivative are both considered as known parameters, the emission dynamics can be expressed by a more compact equation:

$$\begin{aligned} \dot{Soot} = -\frac{1}{\tau} Soot + \frac{1}{\tau}\left[f_1\left(\omega_e, \dot{\omega}_e\right) + \cdots + f_6\left(\omega_e, \dot{\omega}_e\right)\right] T_e \\ + \frac{1}{\tau}\left[f_7\left(\omega_e, \dot{\omega}_e\right) + \cdots + f_{12}\left(\omega_e, \dot{\omega}_e\right)\right] dT_e \end{aligned} \tag{5.7}$$

where the functions $f_1, \cdots, f_6$ are λ_1, $\lambda_2 \omega_e$, $\lambda_3 \dot{\omega}_e$, $\lambda_4 \omega_e^{\,2}$, $\lambda_5 \dot{\omega}_e^{\,2}$ and $\lambda_6 \omega_e \dot{\omega}_e$ respectively, and the functions $f_7, \cdots, f_{12}$ are λ_7, $\lambda_8 \omega_e$, $\lambda_9 \dot{\omega}_e$, $\lambda_{10} \omega_e^{\,2}$, $\lambda_{11} \dot{\omega}_e^{\,2}$ and $\lambda_{12} \omega_e \dot{\omega}_e$ respectively.

Further, combining the (5.5) - (5.7) yields a complete description of the engine soot

emission dynamics (here a discrete-time form is used for the discrete-time LQR control):

$$x(K+1)=A(K)x(K)+B(K)u(K)+G(K),$$

or,
$$x(K+1)=\begin{bmatrix}1 & 0 & 0\\ A_{21}(K) & A_{22}(K) & 0\\ A_{31}(K) & 0 & 1\end{bmatrix}x(K)+\begin{bmatrix}1\\ B_2(K)\\ 0\end{bmatrix}u(K)+\begin{bmatrix}0\\ 0\\ G_3(K)\end{bmatrix} \tag{5.8}$$

where, the states $x(k)=\left[T_e(k)\quad Soot(k)\quad SOC(k)\right]^T$ and the input $u(k)=dT_e(k)$, which is the torque change from the K_{th} step to the $(K+1)_{th}$ step. Other parameters are interpreted as:

$$\begin{aligned}
A_{21} &= \frac{1}{\tau}\left[f_1(\omega_e,\dot{\omega}_e)+\cdots+f_6(\omega_e,\dot{\omega}_e)\right]\\
A_{22} &= 1-\frac{1}{\tau}\\
A_{31} &= \frac{(r_{g1})\left(\dfrac{\omega_e(K)(R+S)-\omega_v(K)K_{ratio}R}{S}\right)\eta_g^{\,k_1}-(r_{m1})(\omega_v(K)K_{ratio})\eta_m^{\,k_2}}{V_{batt}Q_{batt}}\\
B_2 &= \frac{1}{\tau}\left[f_7(\omega_e,\dot{\omega}_e)+\cdots+f_{12}(\omega_e,\dot{\omega}_e)\right]\\
G_3 &= \frac{(r_{g2})\left(\dfrac{\omega_e(K)(R+S)-\omega_v(K)K_{ratio}R}{S}\right)\eta_g^{\,k_1}-(r_{m2e})(\omega_v(K)K_{ratio})\eta_m^{\,k_2}}{V_{batt}Q_{batt}}
\end{aligned} \tag{5.9}$$

After transforming the original nonlinear plant model into the linear from in (5.8), he LQR optimal control algorithm can be designed. The optimal objective of the LQR control is to minimize the cost function within a predefined time period (in the discrete-time form, correspondingly, $k=0\cdots N$):

$$J=\frac{1}{2}x^T(N)Hx(N)+\frac{1}{2}\sum_{K=0}^{N-1}\left[x^T(K)Q(K)x(K)+u^T(K)Ru^T(K)\right] \tag{5.10}$$

where, the gain matrices H, Q and R can be customized to meet the specific optimal target.

With the objective of minimizing the soot emission by smoothing the torque change,

as well as maintaining the battery SOC the same as the DP result at the final stage, the gain matrices H, Q and R are designed as follows:

$$H = \begin{bmatrix} h_1 & & \\ & h_2 & \\ & & h_3 \end{bmatrix},\ Q = \begin{bmatrix} 0 & & \\ & q_2 & \\ & & 0 \end{bmatrix},\ R = r_1$$

These gain matrices need to tuned to produce a good balance of the soot emission minimization and battery SOC sustainability. Usually, h_3 is much larger than h_1 and h_2 for driving the SOC convergence to the predefined value; q_2 needs to be tuned carefully to reduce the soot emission during this time horizon; and r_1 can be quite small (since the effect of the torque transients on the soot emission have been contained in the dynamics of state x_2 and penalized by matrix Q). For example, a group of typical parameters are given by: $h_1 = 0.01$, $h_2 = 1$, $h_3 = 1\text{e}^7$, $q_2 = 5000$, and $r_1 = 0.01$.

Then, the LQR state-feedback control law u^* can be generated as:

$$u^*(N-K) = F(N-K)\left\{ x(N-K) + \begin{bmatrix} 0 \\ 0 \\ G_3(N-K) \end{bmatrix} \right\} \tag{5.11}$$

where,

$$\begin{aligned} F(N-K) &= -\left[R + B^T(N-K)P(K)B(N-K) \right]^{-1} \times B^T(N-K)P(K)A(N-K) \\ P(K+1) &= \left[A(N-K) + B(N-K)F(N-K) \right]^T P(K) \times \left[A(N-K) + B(N-K)F(N-K) \right] \\ &\quad + F^T(N-K)RF(N-K) + Q \end{aligned} \tag{5.12}$$

The generated LQR optimal control law is not the same as the standard form because of the existence of the known time-varying term G. However, the special form of the matrices A, G and Q (which satisfies that, $AG = G$ and $G^TQG = 0$) allows us to modify the control law without violating the derivation of the closed-loop form of the LQR control law.

Remark: The plant model (9) is linear but time-varying; there are limited options on achieving optimal control of such plants. LQR is selected due to its systematic approach and compact form for implementation.

5.4 EXPERIMENTAL RESULTS AND ANALYSIS

To demonstrate the performance of the proposed two-mode hybrid energy management strategy, large amount of experimental studies have been conducted with the rapid prototyping hybrid powertrain research platform designed in the Chapter 3. With the hardware-in-the-loop (HIL) engine testing architecture, this research platform utilizes a high-bandwidth hydrostatic dynamometer to precisely mimic the dynamic behaviors of the tested hybrid powertrain system to interact with a real-world John Deere® 4045HF Tier IV diesel engine, so as to create the high-fidelity engine operations as if it is under the actual HEV dynamic environment. On this basis, the state-of-the-art transient fuel consumption and emission measurement instruments (including the AVL® P402 Fuel Measurement System, AVL® Micro Soot Sensing System, AVL® FTIR Emission Sampling and Measurement System,) are employed for system output measurements, as shown in Fig. 4.1.

5.4.1 Model Switching Rule in Experiments

The basic principle of switching between the two operation modes is: since the fuel efficiency is not considered in the LQR control, both the local time horizon and the accumulative time proportion of the emission reducing mode in the whole driving cycle should be limited. In our experiments, when the DP optimized engine torque changes rapidly above a threshold (>35Nm/s), and the electric power usage is lower than its physical threshold (< 20kW), the "emission reducing" mode is triggered; otherwise the HEV will be operated in the "fuel efficiency improving" mode. For each occurrence of the "emission reducing" mode, the time duration will be in a range of 10sec-30sec.

5.4.2 Emissions/Fuel Efficiency Optimization in Highway Cycles

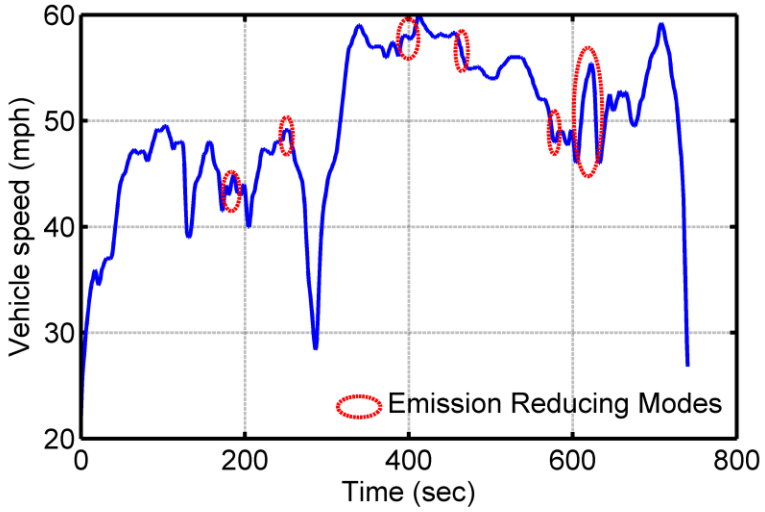

(a) HWFET driving cycle

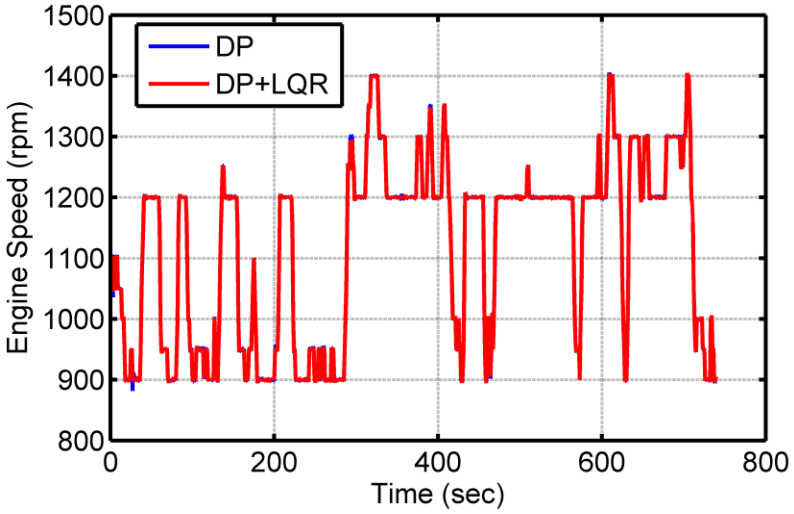

(b) Engine speed

Fig. 5.9 Desired vehicle speed and DP optimized engine speed

Along a typical highway fuel efficiency testing (HWFET) cycle, the hardware-in-the-loop hybrid powertrain testing experiments with both the single mode (DP only) and two mode (DP plus LQR) energy management strategies are conducted. The experimental results, as shown in Fig. 5.9-5.11, demonstrate that the proposed two-mode

energy management strategy can provide an improvement on the soot emission compared with the single-mode strategy, without any significant loss on the fuel economy.

Figure 5.9(a) the number of occurrence of the “emission reducing” mode along the HWFET driving cycle, which is determined by the switching rule and marked with the dash circle. Totally we get six “emission reducing” events that will be named by Emission Reducing Event 1, Event 2, … , and Event 6. Figure 5.9(b) shows the DP optimized engine speed trajectory that will be tracked by both the single-mode and two-mode energy management strategies.

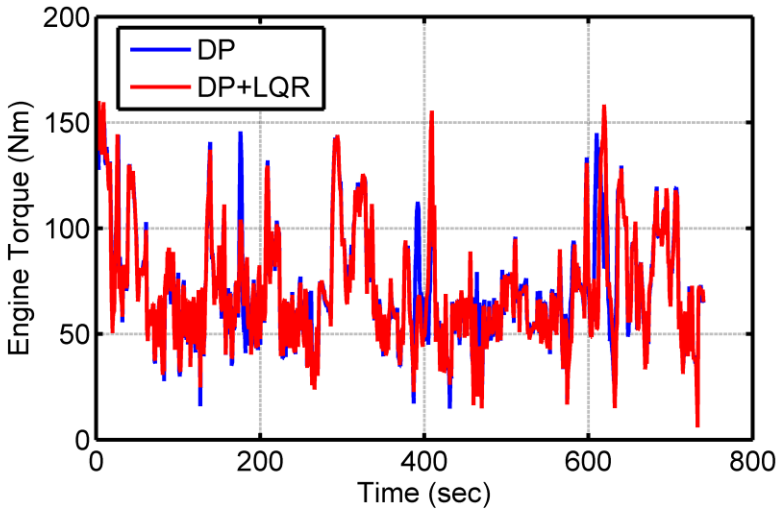

(a) Engine torques

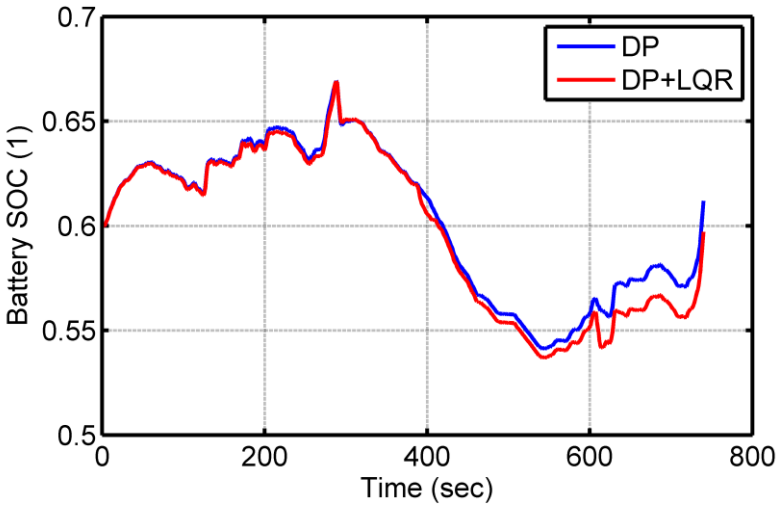

(b) Battery SOC

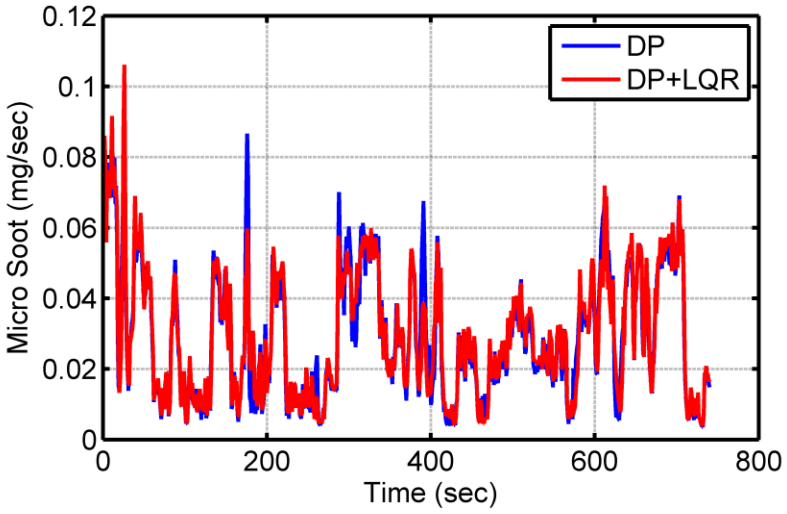

(c) Micro soot emission

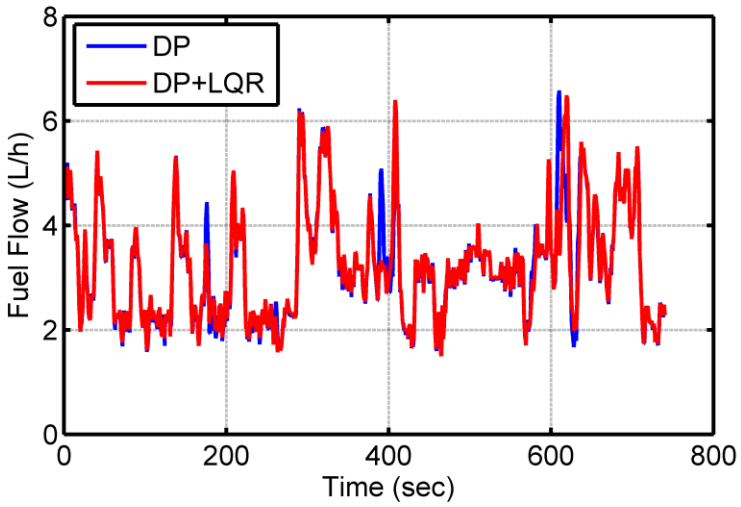

(d) Fuel flow

Fig. 5.10 Globally and locally optimized trajectory along the HWFET cycle

From Fig. 5.10(a), the engine torque trajectory in the "emission reducing" mode is quite different from the one generated directly by the DP. However, due to the LQR optimal control, the battery SOC will converge to the DP optimized point at the final step as shown in Fig.5.10 (b), so that the battery SOC is maintained in a sustainable fashion. The difference in the engine torque trajectories leads to the difference in the micro-soot emissions and fuel consumption, as shown in Fig. 5.10(c)-(d), which are further zoomed

in Fig. 5.11.

From Fig 5.11 (c)-(d), in the "emission reducing" mode 3 (387-410 seconds), the soot emission is obviously reduced by the LQR, while the fuel consumption is maintained in a similar level with the DP optimized trajectories.

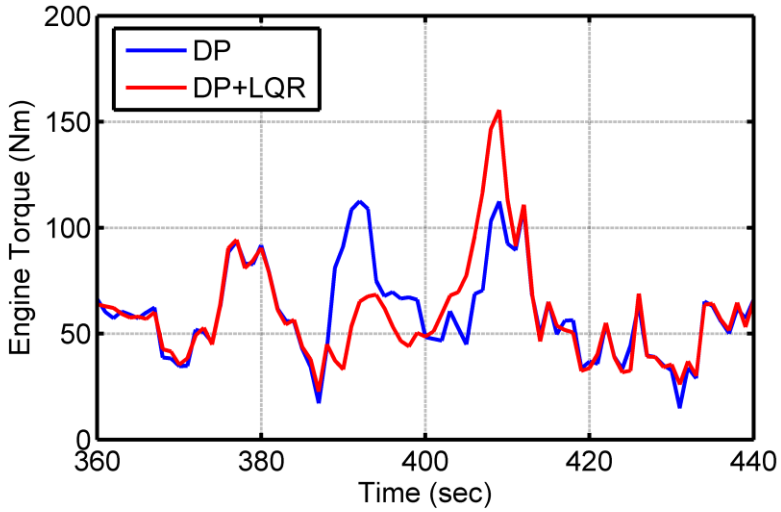

(a) Engine torques

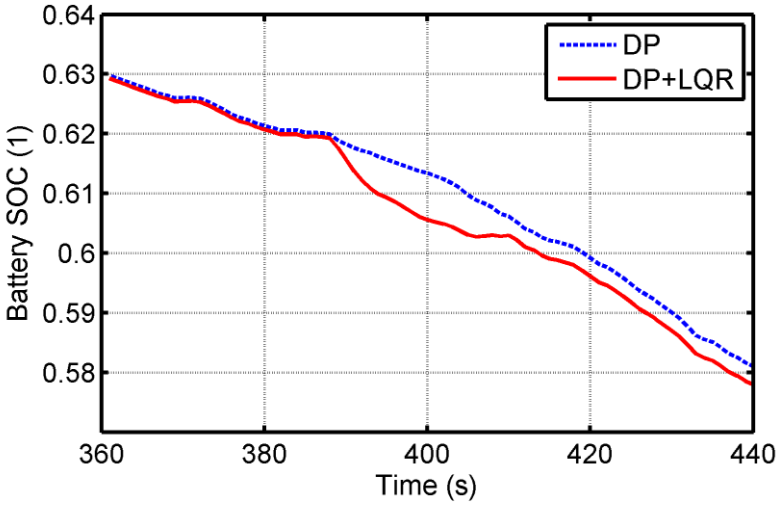

(b) Battery SOC

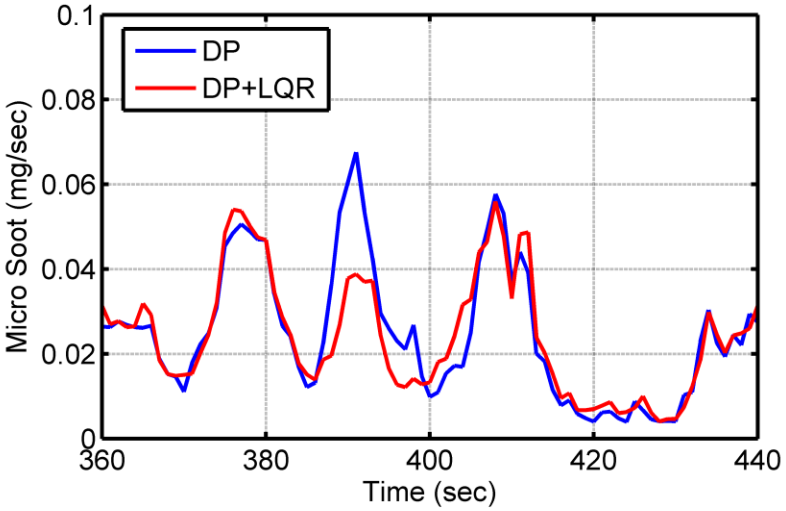

(c) Micro soot emission

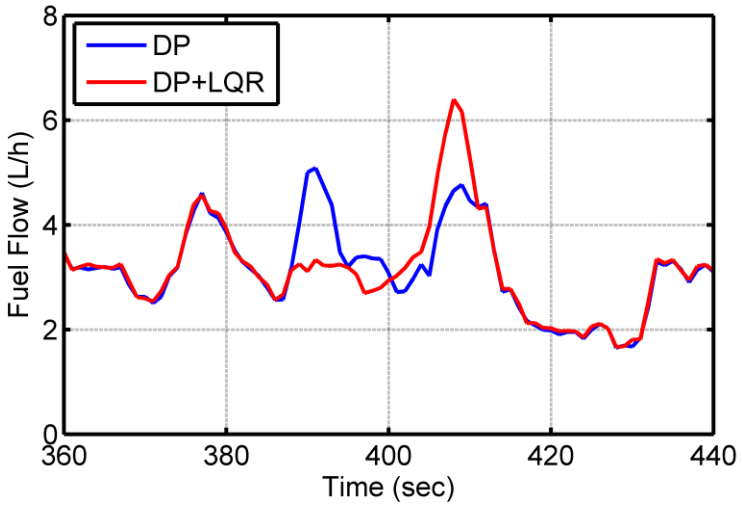

(d) Fuel Flow

Fig. 5.11 Zoomed-in globally and locally optimized trajectory between the 360th-440th sec

Tables 5.1-5.4 further show the detailed data of the soot emissions, fuel consumptions and battery SOC of all the "emission reducing" modes. From Table 5.1, the soot emission is reduced in every "emission reducing" mode, and a total of 11.56% emission reduction is realized compared with the "DP-only" modes. Theoretically, the corresponding fuel consumption in the "emission reducing" modes can be slightly higher than the "DP-only" cases, since the LQR control does not include the fuel efficiency into

the optimization cost function. However, the experimental fuel consumptions in the "emission reducing" modes are even lower than the "DP-only" case, as shown in Table 5.2. That can be explained by the deviations of battery SOC shown in Table 5.3. Because of the unavoidable model uncertainty and disturbance during experiments, the battery SOC cannot be maintained in the absolutely same level as the "DP-only" cases. Eventually for the "emission reducing" modes, the loss in the battery SOC will offset the gains in the fuel saving. In order to better evaluate the fuel consumptions with different management strategies, the SOC losses in Table 5.2 are transferred into the equivalent fuel consumptions by:

$$FC_{equ} = \kappa_{trans} E_{elec} \Delta SOC \eta_{batt} \eta_{elec} / Q_{LHV} \tag{5.13}$$

where, E_{elec} is the full-charging electric energy of the storage battery, ΔSOC is the SOC loss, η_{batt} is the battery charging efficiency, η_{elec} is the electric machine efficiency, Q_{LHV} is the lower heating value of the diesel fuel (which is, 43.4 *MJ/kg*). κ_{trans} is the transfer factor from the mechanical energy to the fuel energy, i.e., the reciprocal of the conversion efficiency from the fuel energy (based on the lower heating value) to the real-world mechanical energy. It is not difficult to understand that the unpredictable distribution of the engine operations (torque/speed) in the engine map will introduce significant difficulty to accurately estimate the transfer factor. Therefore, instead of using a constant but inaccurate transfer factor, we use a range of transfer factor (corresponding to the largest/smallest engine conversion efficiencies in the engine operation area) to quantify the equivalent fuel consumption due to the SOC deviation. With an experimentally validated engine efficiency map, the transfer factor is calculated within the range 2.9-6.0. Then, Equation (5.14) will provide a range of the equivalent fuel consumption FC_{equ}.

The equivalent fuel consumptions, as shown in Table 5.4, indicate that the LQR control introduces a little more fuel consumption than the DP based control (within 1.13% - 6.03%), which is acceptable compared with the more significant emission reduction shown in Table 5.1. In conclusion, with the two-mode energy management strategy, the soot emission is significantly reduced without significant loss on the fuel economy.

TABLE 5.1 Emission analysis of all the “emission reducing” modes

Emission Reducing Events	Micro Soot (DP) /mg	Micro Soot (LQR) /mg	Soot Reduction (by LQR) /%
1 (173sec-188sec)	0.4739	0.4581	3.33%
2 (256sec-266sec)	0.1150	0.0828	27.97%
3 (387sec-410sec)	0.8115	0.6742	16.92%
4 (462sec-472sec)	0.1249	0.1054	15.59%
5 (573sec-583sec)	0.2739	0.2239	18.24%
6 (606sec-636sec)	1.1715	1.0830	7.55%
Total	2.9707	2.6274	11.56%

TABLE 5.2 Fuel consumption analysis of all the “emission reducing” modes

Emission Reducing Events	Fuel Flow (DP) /mL	Fuel Flow (LQR) /mg	Fuel Flow Reduction (by LQR) /mL
1 (173sec-188sec)	11.7827	11.6668	0.1159
2 (256sec-266sec)	6.3150	5.8398	0.4752
3 (387sec-410sec)	24.7273	24.4847	0.2426
4 (462sec-472sec)	7.2152	6.7792	0.436
5 (573sec-583sec)	9.6822	8.9170	0.7652
6 (606sec-636sec)	34.9750	33.8021	1.1729
Total	94.6974	91.4896	3.2078

TABLE 5.3 Battery SOC analysis of all the “emission reducing” modes

Emission Reducing Events	SOC variation (DP) /1	SOC variation (LQR) /1	SOC Loss (by LQR) /1
1 (173sec-188sec)	-0.0034	-0.0043	0.0009
2 (256sec-266sec)	0.0047	0.0037	0.0010
3 (387sec-410sec)	-0.0140	-0.0165	0.0025
4 (462sec-472sec)	-0.0020	-0.0028	0.0008
5 (573sec-583sec)	0.0041	0.0021	0.0019
6 (606sec-636sec)	0.0078	0.0002	0.0077
Total	-0.0028	-0.0176	0.0148

Note: since the battery SOC varies between 0 (fully empty) to 1(fully charged), its unit is set as “1” (i.e., normalized fully-charged electric energy).

TABLE 5.4 Equivalent fuel consumptions of all the “emission reducing” modes

Emission Reducing Events	Transferred Fuel Flow from SOC Loss (by LQR) /mL	Equivalent Fuel Flow Increase (by LQR) /mL	Equivalent Fuel Flow Increase (by LQR) /%
1 (173sec-188sec)	0.2603 ~ 0.5422	0.1444 ~ 0.4263	1.23% ~ 3.62%
2 (256sec-266sec)	0.2892 ~ 0.6024	-0.186 ~ 0.1272	-2.95% ~ 2.01%
3 (387sec-410sec)	0.7229 ~ 1.5061	0.4803 ~ 1.2635	1.94% ~ 5.11%
4 (462sec-472sec)	0.2313 ~ 0.4819	-0.2047 ~ 0.0459	-2.83% ~ 0.64%
5 (573sec-583sec)	0.5494 ~ 1.1446	-0.2158 ~ 0.3793	-2.23% ~ 3.92%
6 (606sec-636sec)	2.2266 ~ 4.6388	1.0497 ~ 3.4659	3.00% ~ 9.90%
Total	4.2797 ~ 8.9161	1.0719 ~ 5.7083	1.13% ~ 6.03%

5.4.3 Comparisons between the Cost-weighted DP Optimization and the Two-Mode Optimization

In order to further demonstrate the performance of the two-mode energy management strategy, another cost-weighted DP optimization algorithm is designed as a counterpart. In the cost-weighted DP optimization algorithm, the FC term in (5.4) is replaced by the cost term which consists of the weighted fuel consumption and soot emission, given by:

$$\begin{aligned} J = & \sum_{k=0}^{N-1} \left\{ w_{fc} FC(k) + w_{soot} SOOT(k) \right\} \\ & + f_{soc} \left[SOC(N) - SOC(N)_{des} \right]^2 - m_{soc} \left[SOC(N) - SOC(N)_{des} \right] \end{aligned} \tag{5.15}$$

where, $SOOT$ is the steady state soot emission from the emission map. w_{fc} and w_{soot} are the weighting factors for fuel consumption and soot emission respectively.

For the convenience of the comparison, the costs-weighted DP optimization is only conducted in the areas at the "emission reducing mode" of the two-mode optimization. The experimental comparison results are shown in Fig 5.12-5.13. Similar with the previous cases, the zoomed-in plots are chosen to show the performance difference.

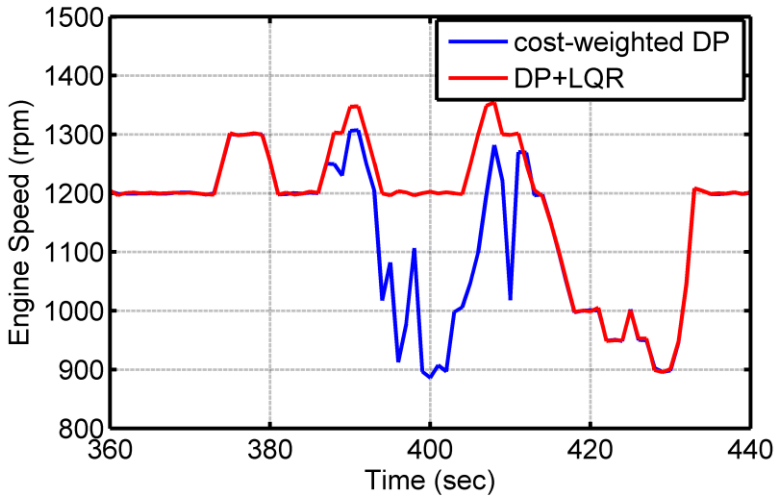

(a) Engine speed

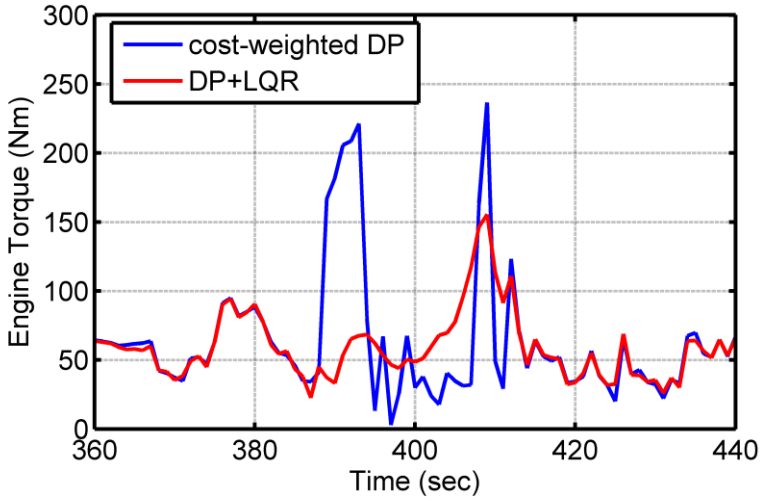

(b) Engine torque

Fig. 5.12 Engine operations by the costs-weighted DP and two-mode strategy between the 360th-440th sec

From Fig. 13 (a)-(c), the soot emission produced by the two-mode energy management strategy is higher than the cost-weighted DP; however, the cost-weighted DP optimization induces more fuel consumption than the two-mode strategy as well as more battery SOC loss. Eventually the two optimization methods produce similar performance if we pursue a good balance between the fuel efficiency and emissions. However, the two-mode energy management takes the transient emission dynamics into the consideration, which may make it more advantageous if other Tier II or Tier III diesel engines (in which, the transient emission concentrations due to the torque transients are even much more significant) are used. On the other hand, if we attempt to add the transient emission dynamics into the cost-weighted DP, then the two-mode energy management strategy can save a lot of computation time compared with the cost-weighted DP.

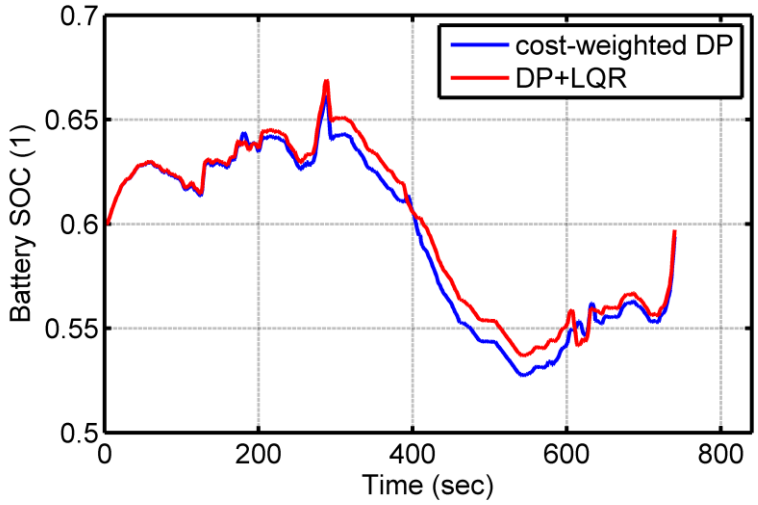

(a) Battery SOC

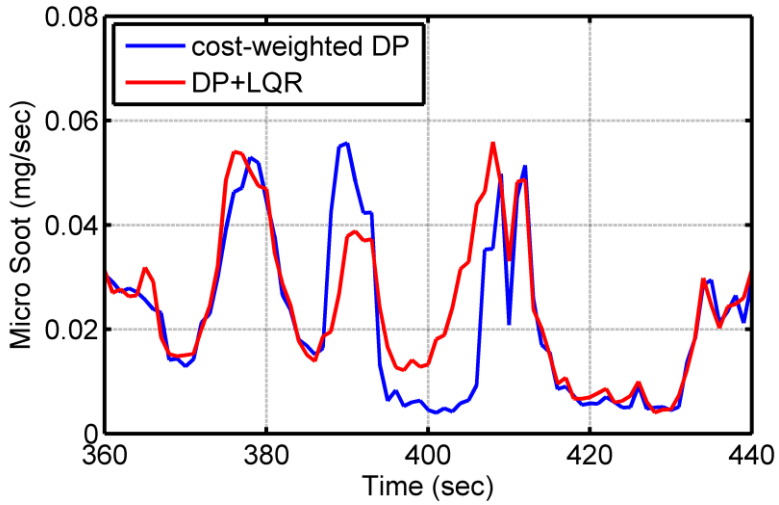

(b) Micro soot emission

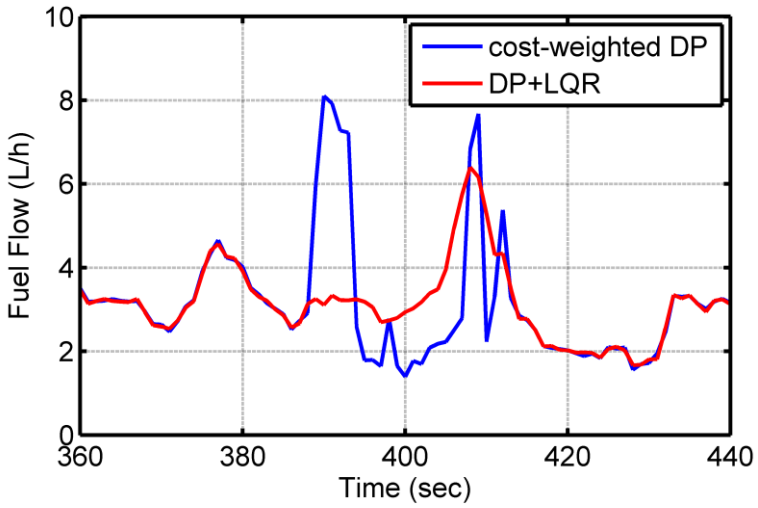

(c) Fuel flow

Fig. 5.13 Engine performances by the costs-weighted DP and two-mode strategy between the 360th-440th sec

5.5 CONCLUSION

This chapter presents a two-mode hybrid energy management strategy which can achieve both the global energy optimization and transient emissions reduction. In the "fuel efficiency improving" mode, the management strategy makes use of a dynamic programming (DP) algorithm to seek the global optimization of the fuel efficiency over any given driving cycles, while in the "emission reducing" mode, the management strategy utilizes a linear quadratic regulator (LQR) to locally reduce the surging emissions due to the sudden engine transients. The two modes are seamlessly integrated by driving the system states back to the globally optimized point at the end of each "emission reducing" mode. This design methodology combines the advantages of both the offline DP (i.e., global fuel efficiency optimization and battery SOC sustainability) and online LQR optimization (i.e., local emissions reduction), and eliminates their disadvantages, especially the "curse of dimensionality" of the DP along with the complicated emission dynamic model. The experimental results demonstrate the optimal

capability of the proposed energy management strategy.

Chapter 6
Conclusion and Future Work

6.1 RESEARCH SUMMARY

This thesis focuses on the architecture design, dynamic modeling and system control of a rapid-prototyping hybrid powertrain research platform and on this basis, conducts a series of research work on the powertrain control and energy/emissions optimization of the hybrid powertrain system. This hybrid powertrain research platform leverages the fast dynamic response of a transient hydrostatic dynamometer to mimic the dynamics of various hybrid power sources and hybrid architectures and therefore, creates an accurate and highly flexible emulation tool for hybrid powertrain operations. This design will greatly speed up the research progress and reduce the economic cost of the study on various hybrid architectures and control methodologies. The design, control and optimization of this research platform include the detailed research achievements in three levels of the proposed system:

1) Low-level system (hydrostatic dynamometer) design and control

With regards to the low-level system, the design, modeling, control and experimental validation of a transient hydrostatic dynamometer are accomplished, which provides the hardware ingredient for the research platform and ensures the dynamics emulation capability of the system. For the dynamotor system modeling, a 9^{th}-order nonlinear model of the hydraulic system is built, with experimental identification and validation for the system parameters. To simplify the control design, the dynamometer system decoupling is realized by leveraging the unique system architecture, which transfers the high-order, multivariable nonlinear system control issue into low-order nonlinear control. For the system control design, model-based nonlinear controllers (nonlinear model-based inversion plus PID controller and the state feedback controller

via feedback linearization) and a Kalman-filter-based observer are designed to enable the transient tracking capability. The experimental results demonstrate that the combination of the system design and control ensures that the hydrostatic dynamometer are capable of fast and precise tracking of the desired engine speed profile.

2) Mid-level system (hybrid powertrain system) design and control

With regards to the mid-level system, the design and experimental investigation of the hybrid powertrain control within the hybrid powertrain research platform are achieved; on this basis, the systematic integration and coordination of the energy optimization, powertrain control, hardware-in-the-loop vehicle simulation and hybrid torque emulation are conducted within a closed-loop architecture.

In the first research stage, the research contributions focus on the overall hybrid powertrain control system design and functionality (i.e., hybrid powertrain dynamics emulation) realization. To facilitate the control design, the virtual hybrid powertrain system models are built and the hardware-in-the-loop hybrid vehicle operation simulation is realized, which produces the high-fidelity, real-time hybrid dynamic responses as the tracking targets of the hybrid powertrain emulator. Around this virtual hybrid powertrain system, a three-level hybrid powertrain optimization and control system, which combines a DP based energy management strategy, a SISO hybrid powertrain control and a feedback linearization based dynamometer torque control, is designed and coordinated. The experimental results demonstrate the capability of the proposed hybrid powertrain optimization and control system for the hybrid operation emulation for both the low-inertia gasoline engine and the high-inertia diesel engine.

In the second research stage, the research achievements include the comprehensive analysis of the transient dynamics of the hybrid powertrain system, and the design of the advanced multivariable hybrid powertrain (mid-level) controller. In order to better improve the transient performance of the hybrid powertrain control system, the potential engine/vehicle inverse transient dynamics are analyzed and the engine speed/torque transient tracking issue (transient electric torque/power spike issue) are unveiled. By introducing the transient engine torque control to affect the engine operation and compensate the electric torque/power spike, a multivariable mid-level controller is

designed to achieve the balance of fast transient engine speed/torque tracking and moderate usage of the electric torque/power within the electrical capability.

3) High-level system (hybrid energy and emission management) control and optimization

The high-level system design objectives consist of the fuel efficiency optimization and transient emission optimization, which are not only the advanced studies in the core area of the hybrid powertrain technology development, but also can be considered as the functionality demonstrations of the designed hybrid powertrain research platform.

For the fuel efficiency optimization, a new SDP-ES hybrid energy management strategy is designed to combine the global optimality and SOC sustainability of the SDP (stochastic dynamic programming) optimization strategy, and the real-time model-independent optimization capability of the ES (extremum seeking) algorithm. This design actually "loosens" the precision limitations of the SDP, so as to offer larger space to reduce the computation burden by model simplification. More significantly, this SDP-ES algorithm design potentially provides the possibility of releasing the hybrid energy management from the constraint of the model-based optimization by making use of the real-time measurement of the hybrid system outputs.

For the transient emission optimization, a two-mode hybrid energy management strategy which can achieve both the global energy optimization and transient emissions reduction is designed. In the "fuel efficiency improving" mode, the management strategy makes use of a dynamic programming (DP) algorithm to seek the global optimization of the fuel efficiency over any given driving cycles, while in the "emission reducing" mode, the management strategy utilizes a linear quadratic regulator (LQR) to locally reduce the surging emissions due to the sudden engine transients. The two modes are seamlessly integrated by driving the system states back to the globally optimized point at the end of each "emission reducing" mode. This design methodology combines the advantages of both the offline DP (i.e., global fuel efficiency optimization and battery SOC sustainability) and online LQR optimization (i.e., local emissions reduction), and eliminates their disadvantages, especially the "curse of dimensionality" of the DP along with the complicated emission dynamic model. The experimental results demonstrate the

optimal capability of the proposed energy management strategy, and also validate the functionality of the hybrid powertrain research platform design.

6.2 FUTURE WORK

In the future, following the current tracks on transient fuel efficiency and emission optimization objectives, some tasks can be further conducted including:

(1) Introduce the iterative learning to develop the current SDP-ES algorithm. Particularly, we will dynamically update the SDP control laws based on the ES seeking results. This updating process will be running iteratively, to continuously optimize the control laws. More importantly, the optimal control laws that fit the specific driver behaviors can be attained by learning from a selected driver. This algorithm can provide us a chance to reduce the dependence of the SDP on the Markov chain model from the statistic data of general driving cycles.

(2) Improve and utilize the LQR based emission control algorithm to enable the online learning/optimization of the hybrid powertrain control, so as to further reduce the dependence of the hybrid energy optimization on the complete knowledge of the driving cycles.

References

[1] C. C. Chan, “The state of the art of electric and hybrid vehicles,” *Proceeding of the IEEE*, 2002, 90(2), pp. 247–275.

[2] M. Ehsani, Y. Gao, J. M. Miller “Hybrid electric vehicles: architecture and motor drives,” *Proceeding of the IEEE*, 2007, 95(4), pp. 719–728.

[3] M. Ehsani, Y. Gao, A. Emani, *Modern electric, Hybrid electric and fuel cell vehicles, fundamentals, theory and design (2nd edition)*. Florida: CRC Press, 2010.

[4] J. Miller, “Hybrid electric vehicle propulsion system architectures of the e-CVT type”, *IEEE Transactions on Power Electronics*, 2006, 21(3), pp.756-767.

[5] J. Van de Ven, M. W. Olson, P. Y. Li, "Development of a hydro-mechanical hydraulic hybrid drive train with independent wheel torque control for an urban passenger vehicle", *IFPE 2008*, Las Vegas, NV, 2008.

[6] J. Meisel. “An analytical foundation for the Toyota Prius THS-II powertrain with a comparison to strong parallel hybrid-electric powertrain”, *2006 Society of Automobile Engineer Technical Paper*, Detroit, Michigan, 2006-01-0666.

[7] T. Grewe, B. Conlon, A. Holmes. “Defining the General Motors 2-mode hybrid transmission”, *2007 Society of Automobile Engineer Technical Paper*, Detroit, Michigan, 2007-01-0273.

[8] K. A. Stelson, J. J., Meyer, A. G. Alleyne, B. Hencey, “Energy saving control of a hydraulic hybrid passenger vehicle,” *Proceedings of the 7th Japan Society of Fluid Power International Symposium on Fluid Power*, Toyama, Japan, 2008, pp. 143-148

[9] Z. Filipi, and Y. J. Kim, “Hydraulic hybrid propulsion for heavy vehicles: combining the simulation and engine-in-the-loop techniques to maximize the fuel economy and emission benefits,” *Oil & Gas Science and Technology*, 2010, 65(1), pp.155-178.

[10] C. Tai, T.-C. Tsao, M. B. Levin, G. Barta, et al, "Using camless valvetrain for air hybrid optimization," *2003 Society of Automobile Engineer Technical Paper*, Detroit, Michigan, 2003-01-0038.

[11] C. Donitz, I. Vasile, C. Onder, L. Guzzella, “Dynamic programming for hybrid pneumatic vehicles,” *Proceedings of the 2009 American Control Conference*, St Louis, MO, 2009, pp. 3956-3963.

[12] J. Liu, H. Peng. “Modeling and control of a power-split hybrid vehicle”, *IEEE Transactions on Control Systems Technology*, 2008, 16(6), pp. 1242-1251.

[13] A. Sciarretta, L. Guzzella. “Control of hybrid electric vehicles”, *IEEE Control Systems Magazine*, 2007, 27(2), pp. 60-70.

[14] S. Tomura, Y. Ito, K. Kamichi, and A. Yamanaka, “Development of vibration reduction motor control for series-parallel hybrid system”. *2006 Society of Automobile Engineer Technical Paper*, Detroit, Michigan, 2006-01-1125.

[15] Y. Wang, Z. Sun, K. Stelson. “Modeling and tracking control of a hydrostatic dynamometer”, *Proceedings of the American Control Conference*, St. Louis, Missouri, 2009, pp. 1391-1396.

[16] Y. Wang, Z. Sun, K. A. Stelson, “Nonlinear tracking control of a transient hydrostatic dynamometer for hybrid powertrain research”, *Proceedings of the ASME Dynamic System and Control Conference*, DSCC2010-4171, Cambridge, Massachusetts, 2010.

[17] Y. Wang, Z. Sun, K. A. Stelson, “Modeling, control and experimental validation of a transient hydrostatic dynamometer”, *IEEE Transactions on Control Systems Technology*, 2011, 19(6), pp. 1578-1586..

[18] B. J. Bunker, M. A. Franchek, B. E. Thomason. “Robust multivariable control of an engine-dynamometer system”, *IEEE Transactions on Control Systems Technology*, 1997, 5(2), pp. 189-199.

[19] J. C. Longstreth, F.A. Sanders, S.P. Seaney, et al. “Design and construction of a high bandwidth hydrostatic dynamometer”, *1993 Society of Automobile Engineer Technical Paper*, Detroit, Michigan, 930259.

[20] R.E. Dorey, D. Wang. “A hydrostatic dynamometer for engine testing” *Proceedings of 2th Bath International Fluid Power Workshop*, University of Bath, UK, 1989, pp. 153-175.

[21] Schenck Pegasus. “Automatic control behavior of driveline and loading machines for dynamic engine testing”, *Schenck Pegasus Technical literature L3920e*, Darmstadt, Germany, 1990.

[22] G. R. Babbitt. “Transient engine test system for hardware-in-the-loop powertrain development”, *Ph.D. dissertation*, University of Wisconsin-Madison, 1999.

[23] H. Ghaffarzadeh, M. Guebeli, N. D. Vaughan. “Linear model identification of a hydrostatic dynamometer through dynamic simulation”, *Proceedings of 5th Bath International Fluid Power Workshop*, University of Bath, UK, 1992, pp. 416-430.

[24] G. R. Babbitt, R. L. R. Bonomo, J. J. Moskwa. “Design of an integrated control and data acquisition system for a high-bandwidth, hydrostatic, transient engine dynamometer”, *Proceedings of the American Control Conference*, Albuquerque, New Mexico, 1997, pp. 1157-1161.

[25] G. R. Babbitt, J. J. Moskwa. “Implementation details and test results for a transient engine dynamometer and hardware in the loop vehicle model”, *Proceedings of International Symposium on Computer Aided Control System Design*, Hawaii, 1999, pp. 569-574.

[26] J. L. Lahti, J. J. Moskwa. “A transient hydrostatic dynamometer for testing single-cylinder prototypes of multi-cylinder engines”, *2002 Society of Automobile Engineer Technical Paper*, Detroit, Michigan, 2002-01-0616.

[27] J. L. Lahti, J. J. Moskwa. “A transient test system for single cylinder research engines with real time simulation of multi-cylinder crankshaft and intake manifold dynamics”, *2004 Society of Automobile Engineer Technical Paper*, Detroit, Michigan, 2004-01-0305.

[28] J. J. Moskwa, J. L. Lahti, M.W. Snyder. “Single cylinder engine transient test system”, *International Journal on Vehicle Design*, 2006, 40(1/2/3), pp. 196-211

[29] M. A. Holland, K. Harmeyer, J. H. Lumkes. “Design of a high- bandwidth, low-cost hydrostatic absorption dynamometer with electronic load control”, *2009 Society of Automobile Engineer Technical Paper*, Detroit, Michigan, 2009-01-2846.

[30] J. Arellano-Padilla, G.M. Asher, M. Sumner. “Control of an AC dynamometer for dynamic emulation of mechanical loads with stiff and flexible shafts”, *IEEE Transactions on Industrial Electronics*, 2006, 53(4), pp. 1250-1260.

[31] N. Sureshbabu, M. T. Dunn. “Hub-coupled dynamometer control”, *Proceedings of the 37th IEEE Conference on Decision & Control*, Tampa, Florida, 1998, pp. 1516-1521.

[32] D. U. Campos-Delgado, D. R. Espinoza-Trejo, E. Palacios. “Closed-loop torque control of an absorbing dynamometer for a motor test-bed”, *Proceedings of International Symposium on Industrial Electronics*, 2007, pp. 2113-2118.

[33] Y. Wang, Z. Sun, “A hydrostatic dynamometer based hybrid powertrain research platform”, *Proceedings of the International Symposium on Flexible Automation*, UPS-2739, Tokyo, Japan, 2010.

[34] Y. Wang, X. Song, and Z. Sun, "Hybrid powertrain control with a rapid prototyping research platform", *Proceedings of the 2011 American Control Conference*, San Francisco, California, 2011, pp. 997-1002.

[35] M. Ducusin, S. Gargies, and C. Mi, "Modeling of a series hybrid electric high-mobility multipurpose wheeled vehicle," *IEEE Transactions on Vehicular Technology*, 2007, 56(2), pp. 557-565.

[36] Y. J. Kim, and Z. Filipi, "Series Hydraulic Hybrid Propulsion for a Light Truck - Optimizing the Thermostatic Power Management", *2007 Society of Automobile Engineer Technical Paper*, Detroit, Michigan, 2007-24-0080.

[37] C. C. Lin, H. Peng, J. W. Grizzle, and J. Kang, "Power management strategy for a parallel hybrid electric truck", *IEEE Transactions on Control Systems Technology*, 2003, 11(6), pp. 839-849.

[38] A. Kimura, T. Abe, S. Sasaki, "Drive force control of a parallel-series hybrid system", *J.SAE Review*, 1999, 20, pp337-341.

[39] S. Liu, A. Stefanopoulou. "Effects of control structure on performance for an automotive powertrain with a continuously variable transmission", *IEEE Transactions on Control Systems Technology*, 2002, 10(5), pp. 701-708.

[40] Q. Wang, F. Syed, R. McGee, M. Kuang, A.Phillios, "Centralized torque controller for a nonminimum phase phenomenon in a powersplit HEV," *2012 Society of Automobile Engineer Technical Paper*, Detroit, Michigan, 2012-01-1026.

[41] Y. Wang, Z. Sun, "SDP-based extremum seeking energy management strategy for a power-split hybrid electric vehicle", *Proceedings of the 2012 American Control Conference*, Montreal, Canada, 2012, pp. 553-558.

[42] P. Pisu, G. Rizzoni. "A comparative study of supervisory control strategies for hybrid electric vehicles", *IEEE Transactions on Control Systems Technology*, 2007, 15(3), pp. 506-518.

[43] C. C. Lin, "Modeling and control strategy development for hybrid vehicles", *Ph.D. dissertation*, University of Michigan, 2004.

[44] E. D. Tate, "Techniques for hybrid electric vehicle controller synthesis", *Ph.D. dissertation*, University of Michigan, 2007.

[45] J. Liu, "Modeling, configuration and control optimization of power-split hybrid vehicles", *Ph.D. dissertation*, University of Michigan, 2007.

[46] H. Banvait, S. Anwar, Y. Chen. "A rule-based energy management strategy for plug-in hybrid electric vehicle (PHEV)", *Proceedings of the American Control Conference*, St. Louis, Missouri, 2009, pp. 3938-3943.

[47] I. Kolmanovsky, I. Siverguina, B. Lygoe. "Optimization of powertrain operating policy for feasibility assessment and calibration: stochastic dynamic programming approach", *Proceedings of the American Control Conference*, Anchorage, Alaska, 2002, pp. 1425-1430

[48] C. C. Lin, H. Peng, J. Grizzle, "A stochastic control strategy for hybrid electric vehicles," *Proceedings of the American Control Conference*, Boston, MA, 2004, pp. 4710-4715.

[49] J. Meyer, K. A. Stelson, A. Alleyne, and T. Deppen, "Energy management strategy for a hydraulic hybrid vehicle using stochastic dynamic programming", *Proceedings of the 6th FPNI-PhD Symposium*, West Lafayette, Indiana, 2010, pp. 55-68.

[50] S. Moura, H. Fathy, D. Callaway, and J. Stein, "A stochastic optimal control approach for power management in plug-in hybrid electric vehicles", *IEEE Transactions on Control Systems Technology*, 2011, 19(3), pp. 545 - 555.

[51] E. D. Tate, J. Grizzle, H. Peng. "Shortest path Stochastic control for hybrid electric vehicles", *International Journal of Robust and Nonlinear Control*, 2008, 18, pp. 1409-1429.

[52] E. D. Tate, J. Grizzle, H. Peng. "SP-SDP for fuel consumption and tailpipe emissions minimization in an EVT hybrid ", *IEEE Transactions on Control Systems Technology*, 2010, 18(3), pp. 673-687.

[53] D. F. Opila, "Incorporating drivability metrics into optimal energy management strategies for hybrid vehicles", *Ph.D. dissertation*, University of Michigan, 2010.

[54] H. Borhan, A.Vahidi, A. M. Phillips, at el, "Predictive energy management of a power-split hybrid electric vehicle", *Proceedings of the American Control Conference*, Saint Luis, Missouri, 2009, pp. 3970-3976.

[55] T. Deppen, A. Alleyen, K. A. Stelson, et al., "A model predictive control approach for a parallel hydraulic hybrid powertrain", *Proceedings of the 2011 American Control Conference*, San Francisco, California, 2011, pp. 2713-2718.

[56] G. Paganelli, Y. Guezennec, G. Rizzoni, "Optimizing control strategy for hybrid fuel cell vehicle", *2002 Society of Automobile Engineer Technical Paper*, Warrendale, PA, 2002-01-0102.

[57] C. Musardo, G. Rizzoni, Y. Guezennec, B. Staccia. “A-ECMS: An adaptive algorithm for hybrid electric vehicle energy management ”, *European Journal of Control*, 2005, 11, pp. 509-524.

[58] L. Serrao, S. Onori, G. Rizzoni. “ECMS as a realization of Pontryagin’s minimum principle for HEV control”, *Proceedings of the American Control Conference*, St. Louis, Missouri, 2009, pp. 3964-3969.

[59] X. Wei, , L. Guzzella, V. I.Utkin, G. Rizzoni, “Model-based fuel optimal control of hybrid electric vehicle using variable structure control systems”, *ASME Journal of dynamic system, measurement and control*, 2007, 129, pp. 13-19.

[60] B. Baumann, G. Washington, B. Glenn, G. Rizzoni.”Mechatronics design and control of hybrid electric vehicles”, *IEEE Transactions on Mechatronics*, 2000, 5, pp. 58-72.

[61] J. Momoh, Y. Wang, M. Elfayoumy. “Artificial neural network based load forecasting”, *Proceedings of IEEE International Conference on computational Cybernetics and Simulation*, 1997, pp. 3443-3451.

[62] K. Ariyur, and M. Krstic. *Real time optimization by extremum seeking control*. New York: John Wiley and Sons, 2003, pp. 3-20.

[63] M. Krstic, H. Wang. “Stability of extremum seeking feedback for general nonlinear dynamic systems”, *Automatica*, 2000, 36, pp. 595-601

[64] D. Popovic, M. Jankovic, S. Magner, A. R. Teel “Extreme seeking methods for optimization of variable cam timing engine operation”, *IEEE Transactions on Control Systems Technology*, 2006, 14(3), pp. 398-407

[65] C.D. Rakopoulos, E.G. Giakoumis, *Diesel engine transient operation*. London: Springer, 2009.

[66] J.R. Hagena, Z.S. Filipi, D.N. Assanis, “Transient diesel emissions: analysis of engine operation during a tip-in”, *2006 Society of Automobile Engineer Technical Paper*, Detroit, Michigan, 2006-01-1151.

[67] Y. Wang, H. Zhang, Z. Sun, “ Optimal control of the transient emissions and fuel consumption of a diesel hybrid electric vehicle”, *Proceedings of the 2012 International Conference on Advanced Vehicle Technologies and Integration (VTI),* Changchun, China, 2012, 0461.

[68] N. Lindenkamp, C. Stöber-Schmidt, P. Eilts, "Strategies for reducing NOx- and particulate matter emissions in diesel hybrid electric vehicles", *2009 Society of Automobile Engineer Technical Paper*, Detroit, Michigan, 2009-01-1305.

[69] S. Tian, "Optimal control of ISG hybrid system with diesel engines in transient state", *Ph.D dissertation*, Tsinghua University, China, 2008.

[70] R. Johri, A. Salvi, Z.S. Filipi, "Optimal energy management for a hybrid vehicle using neuro-dynamic programming to consider transient engine operation", *Proceedings of the 2011 ASME Dynamic Systems and Control Conference*, 2011, DSCC2011-6138.

[71] T. Nuesch, M. Wang, C. Voser, L. Guzzella, "Optimal energy management and sizing for hybrid electric vehicles considering transient emissions", *Proceedings of the 2012 IFAC Workshop on Engine and Powertrain Control, Simulation and Modeling*, Rueil-Malmaison, France, 2012, pp. 278-285.

[72] O. Grondin, L. Thibault, C. Querel, "Transient torque control of a diesel hybrid powertrain for NOx limitation", *Proceedings of the 2012 IFAC Workshop on Engine and Powertrain Control, Simulation and Modeling*, Rueil-Malmaison, France, 2012, pp 286-295.

[73] H. E. Merritt. *Hydraulic control systems*. New York: John Wiley & Sons, 1967, pp. 65-72.

[74] J. Chen. "Speed and acceleration filters/estimators of powertrain and vehicle controls", *2007 Society of Automobile Engineer Technical Paper*, Detroit, Michigan, 2007-01-1599.

[75] B. D. O. Anderson, J. B. Moore. *Optimal filtering*. Mineola, New York: Dover Publications, 1995, pp. 36-45.

[76] S. Devasia, D. Chen, and B. Paden, "Nonlinear inversion-based output tracking," *IEEE Transactions on Automatic Control*, 1996, 41(7), pp. 930–942.

[77] A. Isidori. *Nonlinear control system*. London: Springer, 1995, pp. 137-211.

[78] G. Vossoughi, M. Donath. "Dynamic feedback linearization for electrohydraulically actuated control systems", *Journal of Dynamic Systems, Measurement, and Control*, 1995, 117(4), pp. 468-477.

[79] A. Alleyne, M. Pomykalski. "Control of a class of nonlinear systems subject to periodic exogenous signals", *IEEE Transactions on Control Systems Technology*, 2000, 8(2), pp. 279-287.

[80] Y. Bin, K. Li, N. Feng. "Feedback linearization tracking control of vehicle longitudinal acceleration under low-speed conditions", *Journal of Dynamic Systems, Measurement, and Control*, 2008, 130(5), pp. 189-199.

[81] H. K. Khalil. *Nonlinear systems*. Beijing: Pearson Education, 2007, pp. 540-544.

[82] Z. Filipi, H. Fathy, J. Hagena, et al., "Engine-in-the-loop testing for evaluating hybrid propulsion concepts and transient emissions – HMMWV case study", *2006 Society of Automobile Engineer Technical Paper*, Detroit, Michigan, 2006-01-0443.

[83] M. Duoba, H. Ng, R. Larsen, "Characterization and compassion of two hybrid electric vehicles (HEVs) – Honda Insight and Toyota Prius", *2001 Society of Automobile Engineer Technical Paper*, Detroit, Michigan, 2001-01-1335.

[84] J. D. Halderman, T. Martin. *Hybrid alternative fuel vehicles*. New York: Prentice Hall, 2010, pp. 283-300.

[85] X. Chen, S. Shen, "Comparison of two permanent-magnet machines for a mild hybrid electric vehicle application", *2008 Society of Automobile Engineer Technical Paper*, Detroit, Michigan, 2008-01-1552.

[86] F. Syed, M. Kuang, J. Czubay, "Derivation and experimental validation of a power-split hybrid electric vehicle model", *IEEE Transactions on Vehicular Technology*, 2006, 55(6), pp. 1731-1741

[87] S. Bogosyan, M. Gokasan, D. Goering, "A novel model validation and estimation approach for hybrid serial electric vehicles", *IEEE Transactions on Vehicular Technology*, 2006, 56(4), pp. 1485-1497

[88] X. Ai, S. Anderson, "An electro-mechanical infinitely variable transmission for hybrid electric vehicles", *2005 Society of Automobile Engineer Technical Paper*, Detroit, Michigan, 2005-01-0281.

[89] S. Skogestad, I. Postlethwaite. *Multivariable Feedback Control Analysis and Design*. New York: John Wiley and Sons, 1996, pp. 385-420.

[90] S. Liu, A. G. Stefanopoulou, "Effects of control structure on performance for an automotive powertrain with a continuously variable transmission", *IEEE Transactions on Control Systems Technology*, 2002, 10(5), pp. 701-708.

[91] Q. Wang, F. Syed, R. McGee, M. Kuang, A. Philips, "Centralized torque controller for a nonminimum phase phenomenon in a powersplit HEV", *2012 Society of Automobile Engineer Technical Paper*, Detroit, Michigan, 2012-01-1026.

[92] M. Krstic, "Performance improvement and limitations in extremum seeking control", *System and Control Letters*, 2000, 39, pp. 313-326.

[93] P. Binetti, K. Ariyur, M. Krstic, F. Bernelli, "Formation flight optimization using extremum seeking feedback", *Journal of Guidance, Control and Dynamics*, 2003, 26(1), pp. 132-142.

[94] K. Ariyur, M. Krstic, "Slope seeking: a generation of extremum seeking", *International Journal of Adaptive Control and Signal Processing*, 2004, 18, pp. 1-22.

[95] R. Oldenburger. *Optimal and Self-Optimizing Control*. Cambridge, Massachusetts: The M.I.T. Press, 1966, pp. 1-50.

[96] P.Y. Li, F. Mensing, "Optimization and control of a hydro-mechanical transmission based hybrid hydraulic passenger vehicle", *Proceedings of the 7th international fluid power conference*, Aachen, Germany, 2010.

[97] C.T. Li, H. Peng, "Optimal configuration design for hydraulic split hybrid vehicles", *Proceedings of the 2010 American Control Conference*, Baltimore, Maryland, 2010, pp. 5812-5817.

[98] S. Ross, *Introduction to stochastic dynamic programming*. London: Academic Press Inc, 1982, pp. 29-44.

[99] M. Benz, C. H. Onder, L. Guzzella , "Engine emission modeling using a mixed physics and regression approach", *Journal of Engineering for Gas Turbines & Power*, 2010, 132(4), 042803.

[100] Y. Wang, Y. He, S Rajagopalan, "Design of engine-out virtual NOx sensor using neural networks and dynamic system identification", *SAE International Journal of Engines*, 2011, 4(1), pp.837-849.

[101] C. Ericson, B. Westerberg, "Transient emission prediction with quasi stationary models," *2005 Society of Automobile Engineer Technical Paper*, Detroit, Michigan, 2005-01-3852.

[102] R. Ahlawat, J.R. Hagena, Z.S. Filipi, J.L. Stein, H.K. Fathy, "Volterra series estimation of transient soot emissions from a diesel engine," *2010 IEEE Vehicle Power and Propulsion Conference (VPPC)*, 2010, pp. 1-7.

[103] M. Adlouni, "Modeling of soot emission for heavy-duty diesel engines in transient operation", *Master dissertation*, Lund University, Sweden, 2011.

[104] E.Eskinat, S. Johnson, W. Luyben, (1991), “Use of Hammerstein models in identification of nonlinear systems”, *AlChE Journal*, 1991, 37(2), pp. 255-268.

[105] D. Kirk, *Optimal control theory: An introduction*. New Jersey: Prentice Hall, 1970, pp. 78-86.

Appendix 1

The hybrid powertrain plant model (3.1)-(3.17) built in Chapter 3 (not includes the battery model) is a tenth-order model (including second-order engine torque dynamics, fourth-order generator and motor torque dynamics, second-order planetary gear set dynamics and second-order driveline dynamics). Aiming at realizing the tracking control in such a high order system, we need to reduce the order of the plant model for simplifying the controller design.

Since that the bandwidths of the engine/generator/motor torque dynamics are all far less than the engine/vehicle dynamics, these related dynamics can be eliminated from the control model; in addition, the stiffness of the driveline shaft is usually high, so that we can also neglect the shaft dynamics in the control model. In this case, the control model will only be concerned with the planetary gear set and vehicle dynamics.

From (3.1)-(3.17), the simplified planetary gear set dynamics can be rewritten as:

$$\left[(J_e + J_c) + \frac{(R+S)^2}{S^2}(J_g + J_s)\right]\dot{\omega}_e - \frac{R(R+S)}{S^2}(J_g + J_s)\dot{\omega}_m = T_e - \frac{R+S}{S}T_g \qquad \text{(A1.1)}$$

$$\left[(J_m + J_r) + \frac{R^2}{S^2}(J_g + J_s)\right]\dot{\omega}_m - \frac{R(R+S)}{S^2}(J_g + J_s)\dot{\omega}_e = \frac{R}{S}T_g + T_m - \frac{T_{sh}}{K_{ratio}} \qquad \text{(A1.2)}$$

In addition, the simplified vehicle dynamics is given by:

$$\frac{\dot{\omega}_m}{K_{ratio}}J_v = T_{sh} - f_{tire}M_v g\cos(\phi_{load})R_{tire} - 0.5\rho C_d A_f \frac{\omega_m^{\ 2}}{K_{ratio}^{\ 2}}R_{tire}^{\ 3} - M_v g\sin(\phi_{load})R_{tire} \qquad \text{(A1.3)}$$

Substituting (A1.3) into (A1.1) and (A1.2) yields the simplified hybrid powertrain dynamic model:

$$\dot{\omega}_v = \frac{a_2}{a_1}T_e + \frac{a_3}{a_1}T_g + \frac{a_4}{a_1}T_m - \frac{a_4}{a_1}\alpha\omega_v{}^2 - \frac{a_4}{a_1}\beta$$
$$\dot{\omega}_e = \frac{b_2}{b_1}T_e + \frac{b_3}{b_1}T_g + \frac{b_4}{b_1}T_m - \frac{b_4}{b_1}\alpha\omega_v{}^2 - \frac{b_4}{b_1}\beta \qquad \text{(A1.4)}$$
$$S\dot{O}C = -\frac{V_{batt}}{2Q_{batt}R_{batt}} + \frac{\sqrt{V_{batt}{}^2 - 4\left[-T_g\omega_g\eta_g{}^{k1} + T_m\omega_m\eta_m{}^{k2}\right]R_{batt}}}{2Q_{batt}R_{batt}}$$

Where,

$$a_1 = b_1 = J_{ec}J_{mr} + \frac{(R+S)^2}{S^2}J_{gs}J_{mr} + \frac{R^2}{S^2}J_{ec}J_{gs} + \frac{1}{K_{ratio}{}^2}J_{ec}J_v + \frac{(R+S)^2}{K_{ratio}{}^2S^2}J_{gs}J_v$$

$$a_2 = \frac{R(R+S)}{K_{ratio}S^2}J_{gs},$$

$$a_3 = J_{ec}\frac{R}{K_{ratio}S}$$

$$a_4 = \frac{J_{ec}}{K_{ratio}} + \frac{(R+S)^2}{K_{ratio}S^2}J_{gs},$$

$$b_2 = J_{mr} + \frac{R^2}{S^2}J_{gs} + \frac{1}{K_{ratio}{}^2}J_v,$$

$$b_3 = -\frac{R+S}{S}J_{mr} - \frac{R+S}{SK_{ratio}{}^2}J_v$$

$$b_4 = \frac{R(R+S)}{S^2}J_{gs},$$

$$\alpha = \frac{0.5\rho_a C_{drag}A_f R_{tire}{}^3}{K_{ratio}},$$

$$\beta = \frac{f_{tire}M_v g\cos(\phi_{load})R_{tire}}{K_{ratio}} + \frac{M_v g\sin(\phi_{load})R_{tire}}{K_{ratio}}$$

J_{ec} is the coupled inertia of engine and carrier gear, J_{gs} is the coupled inertia of generator and sun gear, J_{mr} is the coupled inertia of motor and ring gear. f_{tire} is rolling friction

coefficient of the tires, M_v is the vehicle mass, g is the acceleration of gravity, ϕ_{road} is the grade angle of the road, R_{tire} is the tire radius, ρ_a is the air mass density, C_{drag} is the drag coefficient, and A_f is the vehicle frontal area. In the simplified system, the output ω_m is replaced with the state ω_v, since in the power-split hybrid powertrain system the motor speed ω_m can be always expressed as a linear function of the vehicle speed ω_v.